# Charge and ion dynamics in light-emitting electrochemical cells : understanding the operational mechanism from electrical transport to light generation

*Citation for published version (APA):*
Reenen, van, S. (2014). *Charge and ion dynamics in light-emitting electrochemical cells : understanding the operational mechanism from electrical transport to light generation*. [Phd Thesis 1 (Research TU/e / Graduation TU/e), Applied Physics and Science Education]. Technische Universiteit Eindhoven.
https://doi.org/10.6100/IR776754

*DOI:*
10.6100/IR776754

*Document status and date:*
Published: 01/01/2014

*Document Version:*
Publisher's PDF, also known as Version of Record (includes final page, issue and volume numbers)

*Please check the document version of this publication:*

• A submitted manuscript is the version of the article upon submission and before peer-review. There can be important differences between the submitted version and the official published version of record. People interested in the research are advised to contact the author for the final version of the publication, or visit the DOI to the publisher's website.
• The final author version and the galley proof are versions of the publication after peer review.
• The final published version features the final layout of the paper including the volume, issue and page numbers.

Link to publication

*General rights*
Copyright and moral rights for the publications made accessible in the public portal are retained by the authors and/or other copyright owners and it is a condition of accessing publications that users recognise and abide by the legal requirements associated with these rights.

- Users may download and print one copy of any publication from the public portal for the purpose of private study or research.
- You may not further distribute the material or use it for any profit-making activity or commercial gain
- You may freely distribute the URL identifying the publication in the public portal.

If the publication is distributed under the terms of Article 25fa of the Dutch Copyright Act, indicated by the "Taverne" license above, please follow below link for the End User Agreement:

www.tue.nl/taverne

*Take down policy*
If you believe that this document breaches copyright please contact us at:

openaccess@tue.nl

providing details and we will investigate your claim.

Download date: 16. Nov. 2023

# Charge and ion dynamics in light-emitting electrochemical cells

## Understanding the operational mechanism from electrical transport to light generation

PROEFSCHRIFT

ter verkrijging van de graad van doctor aan de
Technische Universiteit Eindhoven, op gezag van de
rector magnificus prof.dr.ir. C.J. van Duijn, voor
een commissie aangewezen door het College voor
Promoties, in het openbaar te verdedigen
op dinsdag 23 september 2014 om 16:00 uur

door

Stephan van Reenen

geboren te Eindhoven

Dit proefschrift is goedgekeurd door de promotoren en de samenstelling van de promotiecommissie is als volgt:

| | |
|---|---|
| voorzitter: | prof.dr.ir. G.M.W. Kroesen |
| 1e promotor: | prof.dr.ir. M. Kemerink |
| 2e promotor: | prof.dr.ir. R.A.J. Janssen |
| leden: | prof.dr. L. Edman (Umeå University) |
| | prof.dr.ir. P.W.M. Blom (Max Plank Institute for Polymer Research, Mainz) |
| | prof.dr. R. Coehoorn (Philips Research & Eindhoven University of Technology) |
| | prof.dr. B. Koopmans |
| adviseur: | dr. H.J. Bolink (Universidad de Valencia) |

A catalogue record is available from the Eindhoven University of Technology Library

ISBN: 978-90-386-3667-2

Printed by Universiteitsdrukkerij Technische Universiteit Eindhoven

nanonextnl
innovating with micro and nanotechnology

This thesis is part of NanoNextNL, a micro and nanotechnology innovation programme of the Dutch Government and 130 partners from academia and industry. More information on www.nanonextnl.nl

# Contents

**Chapter 1 Low-cost lighting by light-emitting electrochemical cells ........................... 5**
1.1 Low-cost lighting from organic semiconductors ........................................................ 6
1.2 Organic light-emitting electrochemical cells ............................................................ 7
1.3 Aim and outline of thesis ...................................................................................... 11
**Chapter 2 A unifying model for the operation of polymer LECs ............................... 17**
2.1 Introduction .......................................................................................................... 18
2.2 Material and methods ........................................................................................... 19
2.3 Results and discussion .......................................................................................... 21
2.4 Conclusions .......................................................................................................... 27
**Chapter 3 Salt concentration effects ........................................................................ 31**
3.1 Introduction .......................................................................................................... 32
3.2 Material and methods ........................................................................................... 33
3.3 Results and discussion .......................................................................................... 34
3.4 Conclusions .......................................................................................................... 44
**Chapter 4 Doping dynamics in light-emitting electrochemical cells ......................... 47**
4.1 Introduction .......................................................................................................... 48
4.2 Material and methods ........................................................................................... 49
4.3 Results and discussion .......................................................................................... 50
4.4 Conclusions .......................................................................................................... 59
4.5 Supplemental figures ............................................................................................ 60
**Chapter 5 Dynamic processes in stacked polymer LECs ........................................... 65**
5.1 Introduction .......................................................................................................... 66
5.2 Material and methods ........................................................................................... 67
5.3 Results and discussion .......................................................................................... 68
5.4 Conclusions .......................................................................................................... 80
**Chapter 6 Dynamic doping in planar iTMC-LECs ..................................................... 83**
6.1 Introduction .......................................................................................................... 84
6.2 Material and methods ........................................................................................... 84
6.3 Results and discussion .......................................................................................... 86
6.4 Conclusions .......................................................................................................... 95
**Chapter 7 Universal transients in polymer- and iTMC-LECs ..................................... 97**
7.1 Introduction .......................................................................................................... 98
7.2 Material and methods ........................................................................................... 98
7.3 Results and discussion .......................................................................................... 100
7.4 Conclusions .......................................................................................................... 106
**Chapter 8 Photoluminescence quenching by electrochemical doping ..................... 109**
8.1 Introduction .......................................................................................................... 110
8.2 Materials and methods ......................................................................................... 110
8.3 Experimental results ............................................................................................. 111
8.4 Discussion ............................................................................................................ 117
8.5 Conclusions .......................................................................................................... 126

8.6 Supplemental figures ........ 126
**Chapter 9 Understanding the efficiency in LECs ........ 131**
9.1 Introduction ........ 132
9.2 Materials and methods ........ 133
9.3 Results and discussion ........ 135
9.4 Conclusions ........ 144
**Chapter 10 Large magnetic field effects in electrochemically doped polymer LECs... 147**
10.1 Introduction ........ 148
10.2 Materials and methods ........ 148
10.3 Experimental results ........ 150
10.4 Discussion ........ 152
10.5 Conclusions ........ 165
**Chapter 11 Origin of work function modification by electrolytes ........ 169**
11.1 Introduction ........ 170
11.2 Materials and methods ........ 172
11.3 Results and discussion ........ 174
11.4 General considerations ........ 186
11.5 Conclusion ........ 186
**Chapter 12 Perspective on the future of LECs ........ 191**
12.1 Current view on operational mechanism of LECs ........ 192
12.2 Future directions to improve LECs ........ 194
**Appendix ........ 199**
A Numerical model to describe operation of LECs ........ 200
**Summary ........ 211**
**Samenvatting ........ 217**
**About the author ........ 227**
**List of publications ........ 229**
**Dankwoord ........ 231**

# **Chapter 1** Low-cost lighting by light-emitting electrochemical cells

---

*Light-emitting electrochemical cells (LECs) are potential candidates for next-generation, low-cost, large-area lighting applications. LECs consist of a single, solution-processed active layer which consists of an organic semiconductor admixed with mobile ions. Its merits are excellent processing characteristics without a large compromise in performance. Understanding of the fundamental device operation of LECs is however limited. This thesis aims to understand the transient and steady-state operation of LECs by investigating electronic carrier injection, transport and recombination in the presence of mobile ions. This understanding is utilized to assess the limits in device performance and to determine routes for optimization.*

## 1.1 Low-cost lighting from organic semiconductors

Artificial lighting is a crucial part of everyday life, providing illumination in absence of sufficient daylight or to convey information by displays. The aesthetic function of lighting is becoming increasingly important as well. These functions add up to a large global market, which requires durable and energy efficient lighting technologies. The fastest growing and promising lighting technologies at this moment are based on inorganic and organic semiconductors. State-of-the-art lighting from inorganic semiconductors already outperforms older technologies like incandescent and fluorescent lighting in efficiency, while development of lighting from organic semiconductors is still in progress.[1-2] Inorganic light emitting diodes (LEDs) are already widely used in televisions, lamps, and signage applications. Also organic light emitting diodes (OLEDs) have recently hit the market and are mainly employed as decorative lighting sources and in displays.

OLEDs promise revolutionary properties like transparency, color tunability and flexibility while being low-cost. Opposed to LEDs, OLEDs have a superior response time, viewing angle, contrast ratio, and color rendering index, while being less thick and heavy. However, lifetime, efficiency, cost, and resolution are so far mainly in favor of LEDs.

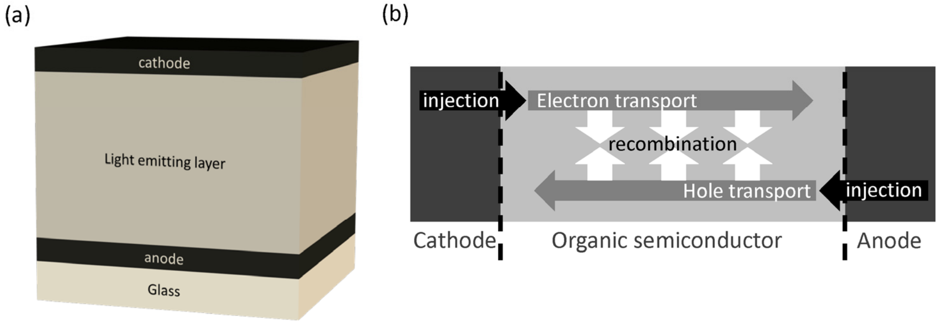

**Figure 1.1 (a) Schematic device layout of a single-layer OLED. (b) Schematic of the conversion of electricity in light with subsequently charge injection (black arrows), transport (gray arrows), and recombination (white arrows).**

In its most basic form, an OLED consists of two electrodes which sandwich a thin semiconducting film as shown in Figure 1.1a. This film consists of either a polymer or small molecule semiconductor. One of the advantages of organic semiconductors is that they can be deposited from solution.[3-7] This makes OLEDs promising for low-cost production like printing in a roll-to-roll process. Next to low production costs, also a sufficient efficiency is required to compete with inorganic lighting technologies. For an efficient device the conversion of electrical energy into light needs to be optimized. In (O)LEDs this conversion follows the chain carrier injection, transport, and recombination as shown in Figure 1.1b. Optimization of all these processes in one and the same material is not at all straight-forward as e.g. improvement of transport by modification of the material may lead to a reduction in recombination efficiency. In addition, optoelectronic processes in solution-processed OLEDs can suffer from contaminations which are introduced during the fabrication by solvents or the atmosphere.[8] Batch-to-batch variation in polymers is also known to lead to irreproducibility.

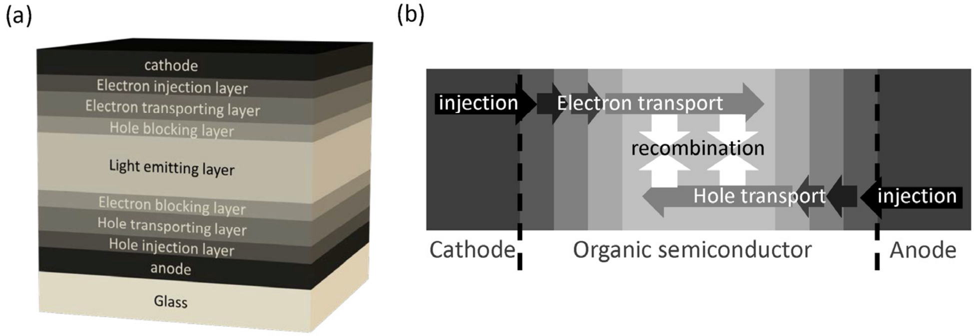

**Figure 1.2 (a) Schematic device layout of a multilayer OLED. (b) Schematic of the conversion of electricity in light with subsequently charge injection (black arrows), transport (gray arrows), and recombination (white arrows).**

Rather than optimizing a single layer, multilayer stacks as shown in Figure 1.2a can be used. In efficient OLEDs, the different functionalities related to injection, transport, recombination and blocking of charge carriers are distributed over multiple layers (see Figure 1.2b) so each layer needs only to be optimized for a limited number of functionalities. The fabrication of such a device is however more challenging compared to the single layered device shown in Figure 1.1a. The fabrication of multilayer OLEDs from solution, see e.g. Ref. 9, is challenging as dissolution of previous layers must be avoided. Therefore multilayer OLEDs are typically deposited in vacuum by thermal evaporation of small organic molecules. Besides the ability to fabricate multilayer OLEDs, other advantages of thermal evaporation in vacuum are good control over the layer thickness and the avoidance of contaminations in the bulk and at the interfaces. This is part of the reason that the highest efficiencies in OLEDs reported to date are obtained in vacuum evaporated small molecule OLEDs. This type of OLEDs is already commercially available. The cost of these devices is however relatively high compared to competing and more mature technologies like LEDs. A lowering of the price is still expected as costs will scale with the production volume. However, to make lighting from organics compete with e.g. LEDs, more innovation is required.

## 1.2 Organic light-emitting electrochemical cells

Light-emitting electrochemical cells (LECs) promise a combination of the advantages in performance of multilayer OLEDs and the advantages in processability of single-layered

OLEDs. LECs consist of a single medium which allows the simultaneous transport of anions/cations and electrons/holes. When a bias voltage is applied to turn the device on, the ions redistribute in such a way that different regions are created within the single layer as shown in Figure 1.3. These different regions take subsequently care of carrier injection, transport and recombination. Opposed to the many layers typically encountered in vacuum deposited OLEDs, the single, solution-processable layer in LECs furthermore allows facile, cheap, large-scale production techniques like printing. Roll-to-roll deposition of LECs was for example recently demonstrated by Edman et al.[10]

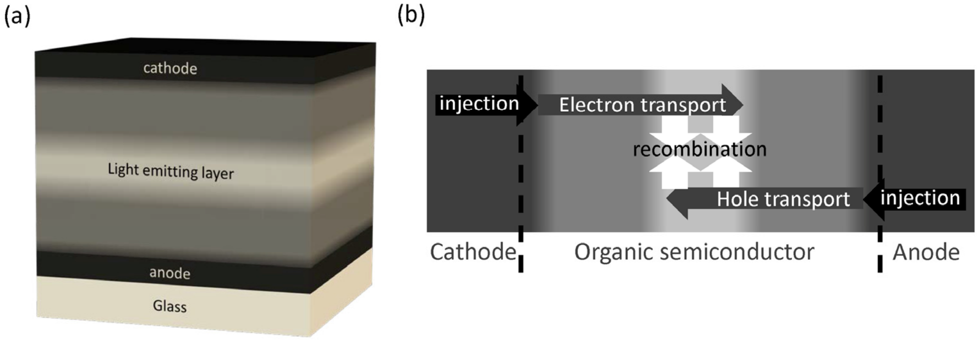

**Figure 1.3 (a) Schematic device layout of an LEC, consisting of a single material which upon biasing has in-situ formed multiple layers. (b) Schematic of the conversion of electricity in light with subsequently charge injection (black arrows), transport (gray arrows), and recombination (white arrows).**

LECs can be operated efficiently in forward and reverse bias,[11] which indicates that the electrode material is not so crucial for efficient carrier injection, unlike in standard OLEDs (as shown in Figure 1.1). This allows the use of cheap and/or air-stable electrode materials. Furthermore LECs boast efficient carrier transport properties highlighted by efficient operation with an active layer thickness between $10^{-7}$ m and $10^{-6}$ m.[10, 12-13] Devices with a thickness of ~$10^{-3}$ m moreover still generate light that is detectable by eye.[14-15] This weak relation between efficiency and active layer thickness provides a relatively large tolerance for large scale production of LECs, which is favorable for the final costs. For comparison, in OLEDs small tolerances of ~$10^{-9}$ m in layer thicknesses are required.

The question which remains is at which price the above advantages of LECs come. Currently, LECs have a slow response time above a millisecond.[16-17] Although this is substantial, the technology is still sufficient for applications like signage or ambient lighting. The peak efficiency of white LECs currently lies around 20 lm $W^{-1}$.[18-19] To give an indication of the currently reached lifetimes, the LECs reported in Ref. 16 can run over 4000 h before their luminance is reduced to half the initial luminance of 670 cd $m^{-2}$.

Solution-processed OLEDs achieve similar efficiencies[20] but still require multiple layers with well-defined thicknesses.[4-6] In Table 1.1 an overview is given of the highest reported brightness, efficiency and lifetime in *white* lighting technologies based on small molecule OLEDs, solution-processed OLEDs and LECs (small molecule and polymer).

**Table 1.1 Performance of organic white lighting technologies**

| Technology | Brightness (cd m$^{-2}$) | Efficiency (%; lm W$^{-1}$; cd A$^{-1}$) | Lifetime (hours) |
|---|---|---|---|
| **Small molecule LECs** | 115 (at 4 V) [21] | 11; 20; 20 [18-19] | 24000 (at 100 cd m$^{-2}$) [16] |
| **Polymer LECs** | 6240 (at ~9.5 V) [22] | 2.4 [23]; 1.2; 3.8 [22] | 6000 (at 100 cd m$^{-2}$) [22] |
| **Solution-processed OLEDs** | 30000 (at ~9 V) [24] | 28.8; 40 ; 60 [25] | 1000 (at 100 cd m$^{-2}$) [26] |
| **Small molecule OLEDs** | 48000 (at ~12 V) [27] | 50 [28]; 139 [29]; - | 100000 (at 1000 cd m$^{-2}$) [30] |

The active layer of LECs basically consists of a semiconducting as well as ionically conductive material. In literature mainly two types of LECs can be distinguished, either based on semiconducting polymers mixed with ions, or based on semiconducting small molecules which are ionic by themselves. In the next paragraphs both types are discussed in more detail.

### 1.2.1 Polymer semiconductors

Polymer LECs were first introduced by Pei *et al.*[11] and typically consist of a semiconducting polymer blended with a solid electrolyte, e.g. poly(ethylene oxide) (PEO) admixed with potassium triflate (KTf or $KCF_3SO_3$) (see Figure 1.4).[31] In these devices the semiconductor facilitates transport of electronic carriers, whereas ionic carrier transport is facilitated by the PEO. Phase separation of the different components must be prevented and therefore must be taken into account in the choice of material. In general some poly(p-phenylene vinylene) (PPV) derivatives (see e.g. Figure 1.4) are found to mix well with the typically used PEO.

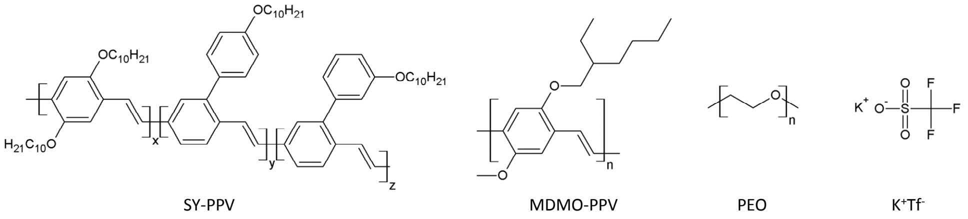

**Figure 1.4 Structural formulae for typical constituents of polymer LECs.**

The PPV derivatives used for the work in this thesis are poly[2-methoxy-5-(3',7'-dimethyloctyloxy)-p-phenylene vinylene] (MDMO-PPV, American Dye Source) and a phenyl-substituted poly(p-phenylene vinylene) copolymer (SY-PPV, Merck, catalogue number PDY-132), commonly termed "Super Yellow". The oxidation and reduction levels of PPV and PEO furthermore favor injection of electronic charge carriers in PPV over injection in PEO, preventing undesired oxidation or reduction of the PEO.[32] In addition, p- and n-type transport in PPV is relatively balanced.[33] Alternatives for the electrolyte are ionic liquids like methyltrioctylammonium trifluoromethanesulfonate (MATS).[34]

### 1.2.2 Small molecule semiconductors

A year after the first report on polymer LECs another type of LEC, based on small molecules, was introduced.[35-37] These small molecules are semiconducting transition metal complexes which are intrinsically ionic. When used as active layer in LECs such an ionic transition metal complex (iTMC) takes care of both ionic and electronic transport. An example of an iTMC is the cationic iridium complex bis(2-phenylpyridine-C,N)(2,2'-bipyridine-N,N')iridium(III) hexafluorophosphate $[Ir(ppy)_2(bpy)]^+$ $(PF_6^-)$ shown in Figure 1.5.[38] Variation in iTMCs are possible by modification of the ligands or the central metal atom. Complexes based on ruthenium[39] or copper[40] have also been reported but are not as stable and efficient as iridium-based iTMCs.[37] The advantage of Ir-iTMC-LECs compared to polymer LECs is that the Ir-iTMCs are triplet emitters, resulting in a larger radiative recombination efficiency after exciton formation. The response time of LECs based on Ir-iTMCs is however very low, i.e. several hours,[38] but can be enhanced by admixing with PEO, as has been shown for Ru-based iTMCs in Ref. 41, or an ionic liquid like 1-butyl-3-methylimidazolium hexafluorophosphate $(BMIM^+PF_6^-)$ to a turn-on time of a few minutes.[38] Use of a constant current driving approach can even reduce the turn-on time to roughly $10^{-5}$ s.[16] iTMCs dissolve in benign solvents allowing for environmentally friendly processing. Another benefit is the ease of color tunability in iridium(III) ionic transition metal complexes (Ir-iTMCs) which enables a color range covering the entire visible spectrum, including white.[18, 21, 37, 42-45]

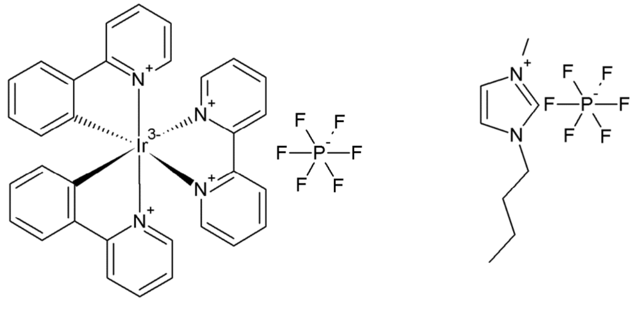

$[Ir(ppy)_2(bpy)]^+PF_6^-$ $BMIM^+PF_6^-$

**Figure 1.5 Structural formulae for typical constituents of ionic transition metal complex (iTMC) LECs.**

## 1.3 Aim and outline of thesis

Although LECs offer promising features regarding processing and performance, significant research is still required to assess their limits and to maximize their performance. Fundamental and quantitative understanding of the LEC device operation are crucial to address loss processes affecting the performance and to give direction to materials synthesis. The aim of this thesis is to conceptually and quantitatively understand the dominant processes in LEC operation. The full line of events from carrier injection, doping/ion dynamics, charge transport until the (non-)radiative recombination processes is therefore investigated in LECs based on polymer and iTMC semiconductors. Both the turn-on and steady-state operation will be addressed. Moreover the potential and limits of LEC devices in their current form are assessed in terms of performance. An outline of the thesis is given below.

For a decade the device operation of LECs was described by two competing models, the electrochemical doping model and the electrodynamic model. In **Chapter 2** experimental, numerical and analytical methods are combined on planar ($\sim10^{-4}$ m interelectrode gap) polymer LECs to establish a universal model for the operation of LECs. The model unifies both previous models. The electrochemical doping model is found to describe the operation of optimized LECs, whereas the electrodynamic model arises in case charge injection is limited. According to the electrochemical doping model, a light-emitting p-i-n junction forms in between electrochemically doped p- and n-type regions. Chapter 2 also serves as a more specific introduction to the (processes involved in the) operation of LECs.

In **Chapter 3** the effects of ion density on the device operation is studied in planar polymer LECs. A large ion density is found to enhance carrier injection and transport by increased electrochemical doping. To optimize LECs for charge transport, while ignoring the effects of doping on the radiative efficiency, an as high as possible ion density is found to be preferred, provided electronic carrier injection can follow the enhanced bulk conductivity.

In **Chapter 4** the dynamics of electrochemical doping in planar polymer LECs is investigated. During turn-on doping fronts are observed to sweep through the device towards each other, subsequently forming a light-emitting p-i-n junction. Numerical drift diffusion modeling proves that such doping fronts arise from the combination of a strong doping dependence in the electronic carrier mobility and an ion mobility which is comparable to the undoped electronic carrier mobility. These results give insight in the origin of the turn-on time in LECs.

In order to generalize the results obtained on planar cells in previous chapters, **Chapter 5** investigates the operational behavior of stacked ($\sim10^{-7}$ m interelectrode gap) polymer LECs by impedance spectroscopy. Steady-state characteristics observed in planar cells are found to be also present in stacked cells: electric double layers improving carrier injection and electrochemical doping leading to the formation of a light-emitting p-i-n junction. In addition, the long turn-on time typical for LECs is found to be limited by salt dissociation into ions rather than by ion migration.

In **Chapter 6** the operation of iTMC-LECs is investigated in planar cell configuration (~$10^{-5}$ m interelectrode gap). Scanning Kelvin probe microscopy and UV excited photoluminescence experiments show that reversible electrochemical doping takes place in this type of materials. A dynamic light-emitting p-i-n junction is observed away from the contacts which proves without doubt that the electrochemical doping model not only applies to polymer LECs, but also iTMC-LECs.

In **Chapter 7** the temperature dependent transient behavior of the current, luminance and efficacy of stacked iTMC and polymer LECs are studied and compared. These results show highly similar transient behavior in both types of LECs. This demonstrates that no fundamental difference exists between charge transport and quenching processes in small molecule and mixed polymeric active materials.

Attention is then switched from charge transport to the conversion of electronic carriers in photons in **Chapter 8**. Here exciton quenching in electrochemically doped polymer semiconductors is studied. Photoluminescence quenching is observed to arise at carrier densities between $10^{18}$ and $10^{19}$ $cm^{-3}$. The doping dependence of the PL quenching can be described by Förster resonance energy transfer and by charge transfer, both between diffusing excitons and ion-compensated polarons.

The quenching relations found in the previous chapter are used in **Chapter 9** to describe experimental results which evidence quenching by electrochemical doping. Enhancing the admixed salt density was found to lead to reduced luminescent efficiency. Numerical modeling, including doping-induced exciton quenching (Chapter 8), was successfully used to model the experiments qualitatively and quasi-quantitatively. This shows that all the major processes describing operational PPV-based LECs are known and taken into account in the model, highlighting the current understanding of LEC operation. The relatively low efficiency in LECs, compared to OLEDs, is found to be intrinsically related to the use of dopants to improve charge transport.

In **Chapter 10** magnetic field effects in an electrochemically doped polymer LEC are studied. Large magneto-resistance is observed simultaneous with positive magneto-electroluminescence. These effects are related to competition between spin mixing and exciton formation leading to an enhanced singlet:triplet ratio at nonzero magnetic field. The resultant reduction in triplet exciton density is argued to reduce detrapping of polarons in the recombination zone at low bias voltages, explaining the observed magneto-resistance. At high electric fields a negative magneto-electroluminescence effect is observed which is rationalized by triplet-triplet annihilation that leads to delayed fluorescence. In the studied devices delayed fluorescence enhances the efficiency of singlet emitter-based (polymer) LECs by at most 17 %.

Thin ionic interface layers have been reported to modify electrode work functions, improving electronic carrier injection into organic electronic devices. To determine whether LEC-type ion-induced doping is the underlying mechanism, such interface layers are studied in **Chapter 11**. Conversely, work function modification is found to originate from interfacial dipole formation, induced by image charges in the contacting material. Asymmetry in the ionic constituents, i.e. in size and ability to approach the interface, is shown to lead to the formation of a net dipole for a wide range of materials.

# References

[1] S. Reineke, M. Thomschke, B. Lussem, K. Leo, Rev. Mod. Phys. 85 (2013) 1245.

[2] Y. Narukawa, M. Sano, T. Sakamoto, T. Yamada, T. Mukai, Phys. Status Solidi A 205 (2008) 1081.

[3] D. H. Lee, J. S. Choi, H. Chae, C. H. Chung, S. M. Cho, Displays 29 (2008) 436.

[4] L. A. Duan, L. D. Hou, T. W. Lee, J. A. Qiao, D. Q. Zhang, G. F. Dong, L. D. Wang, Y. Qiu, J. Mater. Chem. 20 (2010) 6392.

[5] T. Chiba, Y. J. Pu, H. Sasabe, J. Kido, Y. Yang, J. Mater. Chem. 22 (2012) 22769.

[6] H. Zheng, Y. N. Zheng, N. L. Liu, N. Ai, Q. Wang, S. Wu, J. H. Zhou, D. G. Hu, S. F. Yu, et al., Nat. Commun. 4 (2013) 1971.

[7] Y. T. Hong, J. Kanicki, IEEE Trans. Electron Devices 51 (2004) 1562.

[8] D. M. Taylor, IEEE Trans. Dielectr. Electr. Insul. 13 (2006) 1063.

[9] L. C. Ko, T. Y. Liu, C. Y. Chen, C. L. Yeh, S. R. Tseng, Y. C. Chao, H. F. Meng, S. C. Lo, P. L. Burn, et al., Org. Electron. 11 (2010) 1005.

[10] A. Sandstrom, H. F. Dam, F. C. Krebs, L. Edman, Nat. Commun. 3 (2012) 1002.

[11] Q. B. Pei, G. Yu, C. Zhang, Y. Yang, A. J. Heeger, Science 269 (1995) 1086.

[12] P. Matyba, H. Yamaguchi, M. Chhowalla, N. D. Robinson, L. Edman, ACS Nano 5 (2011) 574.

[13] P. Matyba, H. Yamaguchi, G. Eda, M. Chhowalla, L. Edman, N. D. Robinson, ACS Nano 4 (2010) 637.

[14] P. Matyba, K. Maturova, M. Kemerink, N. D. Robinson, L. Edman, Nat. Mater. 8 (2009) 672.

[15] J. Gao, J. Dane, J. Appl. Phys. 98 (2005) 063513.

[16] D. Tordera, S. Meier, M. Lenes, R. D. Costa, E. Orti, W. Sarfert, H. J. Bolink, Adv. Mater. 24 (2012) 897.

[17] S. van Reenen, R. A. J. Janssen, M. Kemerink, Adv. Funct. Mater. 22 (2012) 4547.

[18] T. Hu, L. He, L. Duan, Y. Qiu, J. Mater. Chem. 22 (2012) 4206.

[19] Y. P. Jhang, H. F. Chen, H. B. Wu, Y. S. Yeh, H. C. Su, K. T. Wong, Org. Electron. 14 (2013) 2424.

[20] http://www.printedelectronicsworld.com/articles/latest-progress-on-solution-processed-oleds-00004752.asp?sessionid=1

[21] L. He, J. Qiao, L. Duan, G. F. Dong, D. Q. Zhang, L. D. Wang, Y. Qiu, Adv. Funct. Mater. 19 (2009) 2950.

[22] S. Tang, J. Pan, H. A. Buchholz, L. Edman, J. Am. Chem. Soc. 135 (2013) 3647.

[23] Y. Yang, Q. B. Pei, J. Appl. Phys. 81 (1997) 3294.

[24] Q. Fu, J. S. Chen, H. M. Zhang, C. S. Shi, D. G. Ma, Opt. Express 21 (2013) 11078.

[25] J. H. Zou, H. Wu, C. S. Lam, C. D. Wang, J. Zhu, C. M. Zhong, S. J. Hu, C. L. Ho, G. J. Zhou, et al., Adv. Mater. 23 (2011) 2976.

[26] A. Kohnen, M. Irion, M. C. Gather, N. Rehmann, P. Zacharias, K. Meerholz, J. Mater. Chem. 20 (2010) 3301.

[27] M. F. Lin, L. Wang, W. K. Wong, K. W. Cheah, H. L. Tam, M. T. Lee, M. H. Ho, C. H. Chen, Appl. Phys. Lett. 91 (2007) 073517.

[28] K. Yamae, H. Tsuji, V. Kittichungchit, N. Ide, T. Komoda, J. Soc. Inf. Display 21 (2014) 529.

[29] http://olednet.com/eng/sub02.php?mid=1&r=view&uid=154&ctg1=12

[30] http://panasonic.co.jp/corp/news/official.data/data.dir/2013/05/en130524-6/en130524-6.html

[31] Q. J. Sun, Y. F. Li, Q. B. Pei, J. Disp. Technol. 3 (2007) 211.

[32] P. Matyba, M. R. Andersson, L. Edman, Org. Electron. 9 (2008) 699.

[33] L. Bozano, S. A. Carter, J. C. Scott, G. G. Malliaras, P. J. Brock, Appl. Phys. Lett. 74 (1999) 1132.

[34] Y. Shao, G. C. Bazan, A. J. Heeger, Adv. Mater. 19 (2007) 365.

[35] J. K. Lee, D. S. Yoo, E. S. Handy, M. F. Rubner, Appl. Phys. Lett. 69 (1996) 1686.

[36] K. M. Maness, R. H. Terrill, T. J. Meyer, R. W. Murray, R. M. Wightman, J. Am. Chem. Soc. 118 (1996) 10609.

[37] R. D. Costa, E. Orti, H. J. Bolink, F. Monti, G. Accorsi, N. Armaroli, Angew. Chem. Int. Ed. 51 (2012) 8178.

[38] R. D. Costa, A. Pertegas, E. Orti, H. J. Bolink, Chem. Mater. 22 (2010) 1288.

[39] J. D. Slinker, J. A. DeFranco, M. J. Jaquith, W. R. Silveira, Y. W. Zhong, J. M. Moran-Mirabal, H. G. Craighead, H. D. Abruna, J. A. Marohn, et al., Nat. Mater. 6 (2007) 894.

[40] R. D. Costa, D. Tordera, E. Orti, H. J. Bolink, J. Schonle, S. Graber, C. E. Housecroft, E. C. Constable, J. A. Zampese, J. Mater. Chem. 21 (2011) 16108.

[41] C. H. Lyons, E. D. Abbas, J. K. Lee, M. F. Rubner, J. Am. Chem. Soc. 120 (1998) 12100.

[42] A. B. Tamayo, S. Garon, T. Sajoto, P. I. Djurovich, I. M. Tsyba, R. Bau, M. E. Thompson, Inorg. Chem. 44 (2005) 8723.

[43] F. Kessler, R. D. Costa, D. Di Censo, R. Scopelliti, E. Orti, H. J. Bolink, S. Meier, W. Sarfert, M. Gratzel, et al., Dalton Trans. 41 (2012) 180.

[44] H. C. Su, H. F. Chen, F. C. Fang, C. C. Liu, C. C. Wu, K. T. Wong, Y. H. Liu, S. M. Peng, J. Am. Chem. Soc. 130 (2008) 3413.

[45] L. He, L. A. Duan, J. A. Qiao, G. F. Dong, L. D. Wang, Y. Qiu, Chem. Mater. 22 (2010) 3535.

# **Chapter 2** A unifying model for the operation of polymer LECs

---

*For a long time two distinct models were used to describe the operational behavior of LECs: the electrochemical doping model and the electrodynamic model. Both models are supported by experimental data and numerical modeling in literature. Here, we show that these models are essentially limits of one master model, separated by different rates of carrier injection. For ohmic non-limited injection, a dynamic p-i-n junction is formed, which is absent in injection limited devices. This unification is demonstrated by both numerical simulations and measured surface potentials as well as light emission and doping profiles in operational devices. An analytical analysis yields an upper limit for the ratio of drift and diffusion currents, having major consequences on the maximum current density through this type of device*.

*Part of the work presented in this chapter has been published: S. van Reenen, P. Matyba, A. Dzwilewski, R. A. J. Janssen, L. Edman, M. Kemerink, J. Am. Chem. Soc. 132 (2010) 13776.

## 2.1 Introduction

Years after the invention of the light-emitting electrochemical cell (LEC) by Pei *et al.*[1], the underlying device physics was still far from fully understood. Measurements have been interpreted in either of two models: the electrodynamic model (EDM)[2-6] and the electrochemical doping model (ECDM).[7-12] These models are best distinguished by regarding the predicted steady-state operation of LECs as shown in Figure 2.1.

The EDM states that nearly all applied potential drops at two sheets of accumulated and uncompensated ions positioned in close proximity to the electrode interfaces (see Figure 2.1b). Next to the enhancement of carrier injection, these electric double layers (EDLs) screen the bulk polymer from the external electric field, resulting in a diffusion dominated electronic current in the bulk. The electronic carriers in the bulk are electrostatically compensated by a difference between the anion and cation concentrations to prevent the formation of net space charge.[2]

The ECDM predicts EDL formation as well, but only as much of the applied potential is dissipated at the EDLs as is needed to form ohmic contacts (see Figure 2.1a). The build-up of bulk space charge by the enhanced injection of electronic charge carriers is minimized by the response of the anions and cations. Anions (cations) move away from the electron (hole) injecting contact. Hence, regions are formed in which electrons (holes) are electrostatically compensated by cations (anions). Because of the similarity to the (static) situation encountered in doped inorganic semiconductors, this process is commonly referred to as (electrochemical) doping of the conjugated polymer: in both cases a (relatively) immobile ionic species forms a neutral complex with an electronic charge. Since the amount of ions is limited and the amount of injected electrons and holes is not, anions and cations eventually become completely separated.[11] In between the p- and n-type regions, a narrow intrinsic region arises where the remainder of the applied potential drops and where electron-hole recombination takes place: a light-emitting p-i-n junction is formed. Also in the EDM ‘partial’ doping occurs, in the sense that the electronic charges on both sides of the recombination zone are compensated by (a difference in the concentration of) anions and cations.

Both models are supported by experimental data. Regarding the electrostatic potential, results have been obtained favoring either of the two models.[5, 8, 13] Electrochemical doping has been mainly advocated in support of the ECDM, and has been visualized in planar LECs under UV-illumination by monitoring the doping-induced quenching of photoluminescence (PL).[9, 14] Also modeling studies favoring the EDM[2, 5] as well as the ECDM[11, 15-16] have appeared. It is clear that the inability of the current models in vogue to explain all experimental and numerical data impedes the further development of LECs.

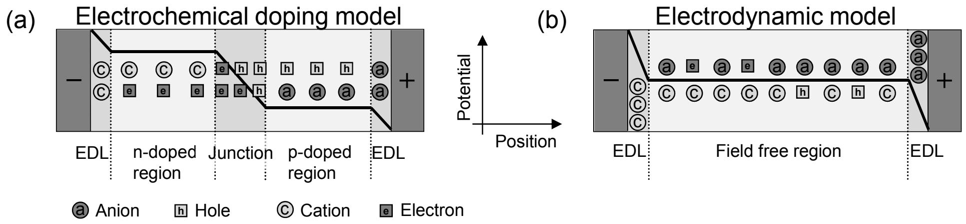

**Figure 2.1 Schematic diagrams illustrating the potential profile and the electronic and ionic charge distribution in an LEC during steady-state operation following (a) the ECDM and (b) the EDM. The thick black line represents the potential profile (in eV) and the electronic and ionic charge distribution is illustrated by the dark gray (negatively charged) and light gray (positively charged) symbols. The high and low field regions in the bulk are accentuated by dark and light shading respectively. In the low field regions, charges are mutually compensated, e.g. cations by anions or cations by electrons.**

Here, we present a unified description of LECs. Both the EDM and the ECDM are shown to be limiting situations of this master model, distinguished by the injection rate at the contacts. The numerical modeling results are confirmed by dedicated experiments and rationalize previous observations. An analytical evaluation of the steady-state situation shows that in the doped regions of LECs the electric field-driven drift current cannot exceed the diffusion current, which constrains the maximum device current.

## 2.2 Material and methods

*Device preparation*: For the fabrication of devices, one of the following two conjugated polymers was used: poly[2-methoxy-5-(3’,7’-dimethyloctyloxy)-p-phenylene vinylene] (MDMO-PPV, $M_w > 1 \cdot 10^6$ g mol$^{-1}$, American Dye Source) or phenyl-substituted poly(p-phenylene vinylene) copolymer (SY-PPV, Merck, catalogue number PDY-132); the latter is commonly termed “Super Yellow”. Poly(ethylene oxide) (PEO, $M_w = 5 \cdot 10^5$ g mol$^{-1}$, Aldrich) was used as received and the salt potassium trifluoromethanesulfonate ($KCF_3SO_3$, 98 %, Aldrich) was dried at 473 K under vacuum before use. The conjugated polymer (CP) SY-PPV was dissolved in cyclohexanone (> 99 %, anhydrous, Aldrich) at a concentration of 5 mg ml$^{-1}$, and the CP MDMO-PPV was dissolved in chloroform (> 99.8 %, anhydrous, Aldrich) at a concentration of 10 mg ml$^{-1}$. PEO and $KCF_3SO_3$ were dissolved separately in cyclohexanone (> 99 %, anhydrous, Aldrich) at 10 mg ml$^{-1}$ concentration. These solutions were mixed together in a mass ratio of CP: PEO: $KCF_3SO_3$ = 1:1.35:0.25. This blend solution was thereafter stirred on a magnetic hot plate at a temperature $T$ = 323 K for 5 h. Glass substrates (1×1 cm$^2$) were cleaned by subsequent ultrasonic treatment in detergent, distilled water, acetone and isopropanol.

The glass substrates were spin-coated with the blend solution (at 800 rpm for 60 s, followed by 1000 rpm for 10 s) after which they were dried at $T$ = 323 K for at least 1 h on a hot plate. The thickness of the active material film was ~230 nm, as determined by profilometry. AFM images show the presence of phase-separated regions with an average diameter in the order of $10^2$ nm.[17] For the non-injection limited devices, Au electrodes capped with a layer of Al were deposited by thermal evaporation under high vacuum ($p \sim 1 \cdot 10^{-6}$ mbar) on top of the spin-coated films. For injection limited devices, purposely oxidized Al electrodes were utilized instead. The oxidation procedure comprised preparing the spin-coated films in a glove box under $N_2$ atmosphere in the presence of a small amount of oxygen ($[O_2] \sim 20$ ppm) before evaporation of Al, and the subsequent storage of the devices for ~5 days before testing to allow the formation of an $AlO_x$ injection barrier. A thin wire-based shadow mask was used to create an inter-electrode gap of approximately 100 µm. All of the above mentioned procedures, save for the cleaning of the substrates and the oxidation of the Al electrodes, were done in a glove box under $N_2$ atmosphere ($[O_2] < 1$ ppm and $[H_2O] < 1$ ppm) or in an integrated thermal evaporator.

*Scanning Kelvin probe microscopy*: SKPM images were recorded in a glove box under $N_2$ atmosphere ($[O_2] < 1$ ppm and $[H_2O] < 1$ ppm) with a Veeco Instruments MultiMode AFM with Nanoscope IV controller, operating in lift mode with a lift height of 25 nm. Ti-Pt coated silicon tips (MikroMasch NSC36/Ti-Pt, $k \sim 1.75$ N m$^{-1}$) were employed. All measurements were carried out at $T = 333$ K.

*UV-excited photoluminescence detection*: Optical probing was performed in an optical-access cryostat under high vacuum ($p < 10^{-5}$ mbar), using a single-lens reflex camera (Canon EOS50) equipped with a macro lens (focal length: 65 mm) and a teleconverter (× 2). In parallel with the optical probing, the current was measured with a computer-controlled source-measure unit (Keithley 2612). The electro-optical probing was carried out at $T = 333$ K.

*Computational details*: For the numerical simulations, the 1-dimensional model was used which is described in detail in Appendix A. Here an active layer is modeled with length $L = 350$ nm, divided in $N = 81$ discrete, equidistant points. Devices with a bandgap $E_g = 1$ eV were simulated during operation at a bias voltage $V_{bias} = 2$ V until steady-state had been reached, recognized by a zero ion current. Initially, ions were homogeneously distributed at a density of $1.25 \cdot 10^{25}$ m$^{-3}$ as used by deMello.[4] No binding energy was assumed between anions and cations. Electrons and holes were injected from the contacts by use of different injection models, e.g. Fowler-Nordheim tunneling or Emtage O'Dwyer. The main difference between the various models is the resulting charge injection rate and its dependence on electric field, as described in Appendix A. The injection barriers were set at 0.5 eV for both electrons and holes to simulate a symmetric device. The Fowler-Nordheim tunneling model was used to achieve limited carrier injection. Non-limited carrier injection was achieved by use of the "modified Boltzmann" injection model with the same parameters. The following additional parameters were used: The relative dielectric constant $\varepsilon_r = 3$, $T = 300$ K, the electron and hole mobility $\mu_{p/n} = 10^{-6}$ m$^2$ V$^{-1}$ s$^{-1}$. A relatively high anion and cation mobility could be chosen ($10^{-7}$ m$^2$ V$^{-1}$ s$^{-1}$) to speed up convergence since this parameter does not affect the outcome at steady-state. It was checked that neither the magnitude of $E_g$ and $V_{bias}$ nor the thickness of the active layer affects the outcome of the simulations in a non-trivial manner, as long as $V_{bias} > E_g$.

## 2.3 Results and discussion

Simulations were done for different injection models, effectively altering the carrier injection rate. Consequently, the steady-state current of one device is limited by the injection process, whereas the other device is allowed to form a non-limiting ohmic contact. In the latter case the current is limited by the bulk resistivity. Figure 2.2 shows the resulting potential profiles. In the non-injection limited case, two EDLs have formed near the electrodes, dissipating as much potential as needed to overcome the injection barriers of 0.5 eV. The rest of the potential is dropped over a p-i-n junction formed in the bulk, in agreement with the ECDM. In contrast, when injection is limited, two large EDLs are formed, dissipating nearly all applied potential in accordance with the EDM. The electric field profiles shown in the inset clearly indicate that the electric field in the bulk is strongly reduced in the injection limited case as compared to the non-limited device.

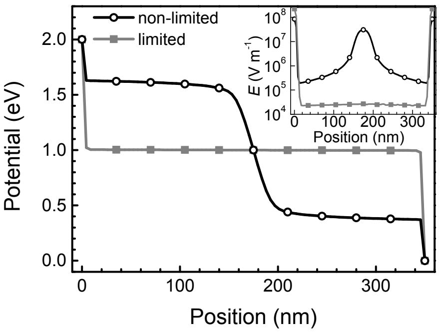

**Figure 2.2 Simulation results for the potential profile in an LEC during steady-state operation. The electrostatic potential profile $V(x)$ of the device that has (no) injection limitation corresponds to the gray (black) line with squares (circles). The corresponding electric field $E = -\mathrm{d}V/\mathrm{d}x$ is shown in the inset.**

The carrier distributions from both simulations at steady-state are shown in Figure 2.3. In the non-limited device (Figure 2.3a) the dopant anions and cations have been spatially separated, either for EDL formation or for doping of the polymer, i.e. for electrostatically compensating injected charge carriers. Due to the symmetry of the simulated device the p-i-n junction is centered. In the central intrinsic region the charge of the electrons and holes is not compensated due to the absence of dopant ions. Hence, their space charge causes the potential drop observed in this region. This sets organic LECs apart from inorganic p-i-n junctions in which the space charge results from the ionized dopants.[11] The resulting large electric field compensates for the low conductivity in this region, so a constant current density is maintained throughout the device. In contrast, in the injection limited device (Figure 2.3b) the dopant anions and cations are not fully spatially separated. Still, the ions are used to form EDLs as well as to do some minor doping. However, the doping is much less prominent due to the relatively low concentration of injected charge carriers. Consequently, a large fraction of ions remains paired to their counter ion, instead of to an electron or hole, as in the non-injection limited case. The (ionic and total) conductivity is therefore roughly constant throughout the device and no distinct raise of the electric field in the recombination zone is necessary to warrant a constant current density throughout the device. Hence, no p-i-n junction is formed.

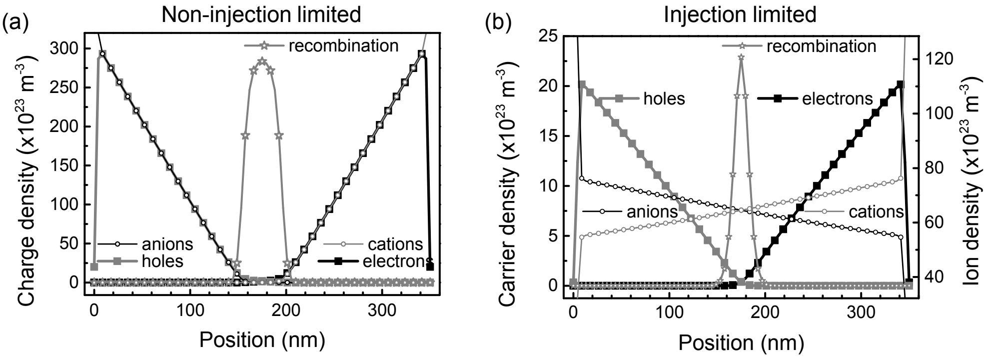

**Figure 2.3 Simulation results for electronic and ionic charge carriers and recombination distributions in an LEC. Electron, hole, anion and cation densities and recombination profile are indicated by the legends. No vertical axis is shown corresponding to the recombination. The distribution profiles for an LEC in (a) the non-injection limited regime and (b) the injection limited regime are shown.**

The calculated integrated recombination rate of the modeled LECs (see Figure 2.3) at steady-state is approximately one decade larger in the ohmic regime than in the injection limited regime. This difference is strongly dependent on the degree of injection limitation and may therefore become even more significant when injection becomes more problematic.

One characteristic that distinguishes LECs from other light emitting devices like organic and inorganic LEDs with fixed doping is that upon reversing the polarity of the applied potential the device still functions the same: the mobile ions redistribute so that n- and p-doped regions exchange positions.[1, 8-9] The p-i-n junction is dynamic. This behavior is evidently reproduced in our numerical modeling.

In order to substantiate the numerical results presented above, experiments were done on planar LECs by scanning Kelvin probe microscopy (SKPM) and electro-optical probing under UV-light. The former technique provides the electrostatic potential profile, whereas the latter indicates doping formation via doping-induced quenching of the UV-excited photoluminescence (PL), as well as a map of the light emission. The active layer comprised a conjugated polymer (either MDMO-PPV or SY-PPV), mixed with the salt $KCF_3SO_3$ and the ion-dissolving polymer PEO. The active layer is positioned amid two electrodes, defining an interelectrode gap of approximately 100 μm. Both types of measurement were performed on nominally identical devices under very similar, controlled circumstances. Devices were prepared in two manners to obtain cells with and without injection limitations as described in paragraph 2.2.

The experimental results are shown in Figure 2.4, with the electrode interfaces marked by vertical dashed lines. Figure 2.4a shows the steady-state potential profile of an LEC, with Au/Al top electrodes and SY-PPV as the conjugated polymer, that is not injection limited. The background shows the corresponding optical micrograph. Similar graphs have been obtained for MDMO-PPV-based active layers. In between the two electrodes, two doped regions, where PL is quenched, are visible, sandwiching a narrow junction region where light emission is observed (see Figure 2.4c). At the electrode interfaces potential drops of ~1.5 and ~1.0 eV are observed, indicating the presence of EDLs. In contrast to previous results on similar devices,[8] the potential drop over the EDLs is visible in our SKPM measurements. This is attributed to the use of an Al capping layer on top of the Au layer, which blocks the diffusion of ion-containing material through the electrode.[8] Note that equal electrodes are used, so that in order to form ohmic contacts the sum of the potential drops over both EDLs should be approximately equal to the bandgap of SY-PPV, i.e. 2.4 eV.[18] This is indeed the case. In the doped regions the potential is more or less constant, whereas a large potential drop is observed in a narrow region in the bulk: the light-emitting p-i-n junction. This behavior is fully consistent with the above simulations for a non-injection limited device in the ECDM limit (see black line marked by open circles in Figure 2). The final steady-state current through this device during operation was ~1.5 μA. The time dependence of the current will be discussed below.

Injection limitation was achieved by using Al electrodes that were allowed to oxidize slightly. Figure 2.4b shows the steady-state potential profile of an LEC with Al electrodes that shows all the attributes of being injection limited, as indicated by the large EDLs and the low electric field throughout the entire bulk. Furthermore, no significant doping was observed, as concluded from the absence of PL quenching in the optical micrograph, in line with the EDM. No light emission was observed during operation as shown in Figure 2.4d. The final steady-state current measured through this device was ~0.2 nA, being four orders of magnitude smaller than the current through the device operating in the non-injection limited regime. Hence, the recombination rate and the light-emission intensity will be reduced by a similar factor, beyond the detection limit of the measurement system.

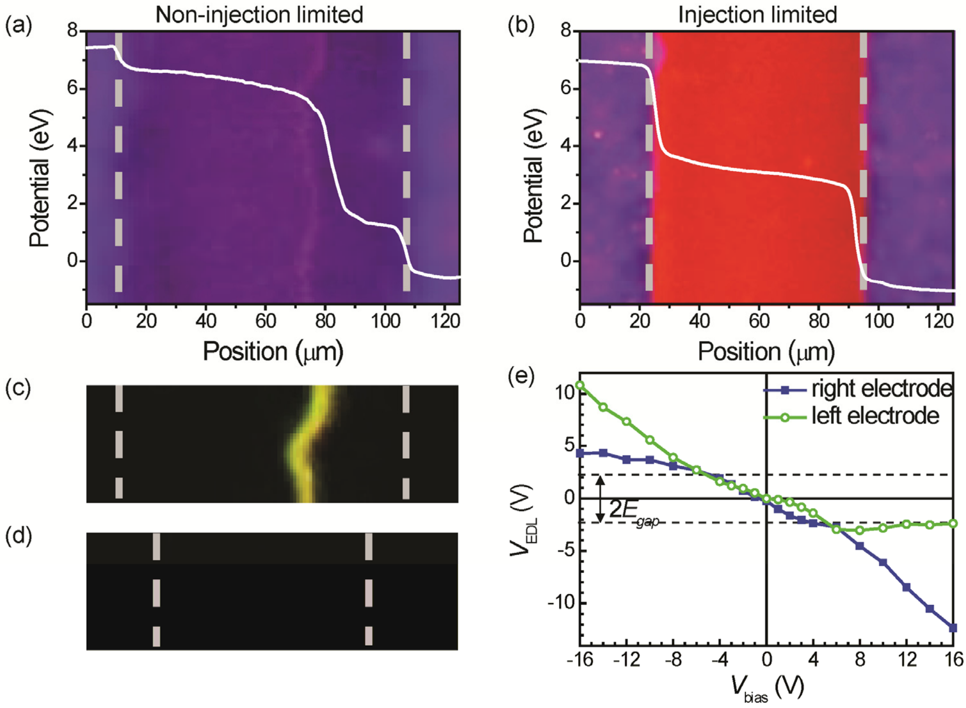

**Figure 2.4 Electrostatic potential and light-emission profiles in planar LECs during operation and voltage dependence on the interfacial potential drop. (a) and (b) typical steady-state potential profiles of an LEC during operation at $V_{bias}$ = 8 V in (a), the non-injection limited and (b), the injection limited regime. The pictures behind the graphs are UV/PL images in steady-state, on the same horizontal scale. (c) and (d) micrographs showing the presence or absence of light emission during steady-state operation at $V_{bias}$ = 8 V in (c), the non-injection limited and (d), the injection limited regime. The electrode interfaces are indicated by the white dashed lines in all micrographs. (e) The voltage dependent potential drop over the interfacial regions for an injection limited LEC. For positive bias voltages, the green line marked by open circles refers to the positive electrode.**

These experimental observations are in very good agreement with the numerical results for an injection limited LEC (see gray line marked by solid squares in Figure 2.2 and Figure 2.3b). Note, however, that care should be taken not to confuse a non-injection limited device with a p-i-n junction close to one of the electrodes with an injection limited device, since both may have similar potential profiles. Therefore, the interfacial potential drop of the injection limited LEC was determined as a function of bias voltage, see Figure 2.4e. The interfacial potential drop increases similarly at both electrodes for biases up to ±8 V. More important, at $|V_{bias}|$ = 6 V this potential drop surpasses the MDMO-PPV bandgap of ~2.3

eV at *both* electrode interfaces. A p-i-n junction that has formed right next to an electrode in a non-injection limited device can result in an interfacial potential drop larger than $E_g$. However, this cannot occur at both electrodes at the same time, as there can only be a single p-i-n junction in the device. Since the magnitude of the potential drop at a non-limiting contact in the ECDM is at most equal to $E_g$, the data in Figure 2.4e allow us to conclude that the device is truly injection limited and behaves according to the EDM.

Another major difference between the EDM and ECDM is that the EDM alleges the electronic bulk transport to diffusion rather than drift, since the ions screen the bulk from the external electric field. From the numerical results shown in Figure 2.2 and Figure 2.3, the ratio of the drift and diffusion contributions was determined, as shown in Figure 2.5. For the non-limited case, the drift and diffusion contributions are equal in the doped regions. In the injection limited case, diffusion dominates the total electronic current.

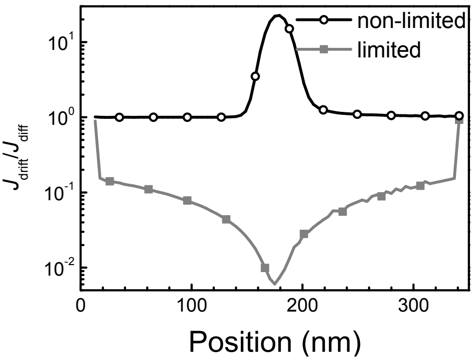

**Figure 2.5 Drift-diffusion current ratio profile in simulated LEC devices in steady-state. The profile of the device that has (no) injection limitation corresponds to the gray (black) line with squares (circles).**

We will now rationalize these observations. First, consider only the ionic current. In steady-state, the total ionic current must be zero, because of the ion-blocking electrodes and the absence of generation and recombination of ions. Thus, in the bulk, the drift and diffusion components of the ion current, $J_{i,drift}$ and $J_{i,diff}$ respectively, for both anions (*i* = *a*) and cations (*i* = *c*), must be equal but oppositely directed to obtain a zero total current: $J_{i,drift} = -J_{i,diff}$. A few steps are required to show that for a device in the ECDM limit (i.e. a non-injection limited device) this implies that $J_{p,drift} = J_{p,diff}$ holds for the hole current contributions in the p-doped region, and similar for electrons in the n-doped region. First, charge neutrality applies in the p-doped region, see Figure 2.3a, so hole and anion densities and their density gradients are equal. Second, holes experience the same electric field as anions. Therefore, the hole and anion drift currents, which are proportional to the product of density and field, are equal in magnitude, apart from a correction factor accounting for the difference in mobility. Also the hole and anion diffusion currents, proportional to the density gradient, are equal in magnitude, again apart from a correction factor accounting for the difference in diffusion constant. According to the Einstein relation the diffusion constant is proportional to the mobility, hence both correction factors are identical and $J_{p,drift} = J_{p,diff}$ follows from $J_{i,drift} = -J_{i,diff}$. The sign difference is due to the charge difference between holes and anions. A somewhat more elaborate derivation along these lines provides a general relation, valid for both injection limited and non-injection limited devices, between the electronic drift and diffusion currents at a position *x* in the doped region (See Ref. 19 for a detailed derivation):

$$\left.\frac{J_{p,drift}}{J_{p,diff}}\right|_{x} = \tanh\left(\frac{q}{kT}\left(V(x) - V(x_1)\right)\right), \tag{2.1}$$

for holes and

$$\left.\frac{J_{n,drift}}{J_{n,diff}}\right|_{x} = \tanh\left(-\frac{q}{kT}\left(V(x) - V(x_1)\right)\right), \tag{2.2}$$

for electrons, with *q* the absolute electronic charge, *k* the Boltzmann constant, *T* the absolute temperature, *V* the electrostatic potential and $x_1$ the position of the center of the recombination zone. Since tanh(*y*) is in between -1 and 1 for any value of *y*, these relations limit the drift current in steady-state to the diffusion current. The drift-diffusion current ratios in both injection regimes can now be identified. A large value of $\frac{q}{kT}\left(V(x) - V(x_1)\right)$, e.g. due to the presence of a p-i-n junction – $q/kT \approx 40$ V$^{-1}$ at 300 K – results in equal drift and diffusion currents. Without a junction, this value becomes smaller, effectively making the diffusion contribution dominant, c.f. Figure 2.5.

During the simulations of both devices acting in different injection regimes, also the current vs. time and recombination rate vs. time curves were recorded as shown in Figure 2.6. Starting from *t* = 0, a large current is observed due to anions and cations moving in opposite directions. The electrodes block the ions, resulting in EDL formation, which reduces the field in the bulk and hence the current goes down. After EDL formation, electrons and holes are injected and move through the active layer until they reach each other and recombine as denoted in Figure 2.6 with 1. The LEC in the injection limited EDM regime in Figure 2.6b shows a decreasing current after this point due to further screening of the electric field by increase of the EDLs. In contrast, the LEC in the non-injection limited ECDM regime in Figure 2.6a first shows a strong increase in current, which is electronic in nature and is due to doping formation in the bulk. This doping is then maximized, effectively reducing the electric field in the doped regions so that a p-i-n junction forms, as denoted by 2 in Figure 2.6a. After junction formation, the ions must adapt to the altered potential profile to reach steady-state. Concomitant with this adaptation, the electronic drift current becomes limited to the diffusion current and thus decreases, as discussed at Equations (2.1) and (2.2). Because of this, a strong current drop after junction formation is observed in Figure 2.6a.

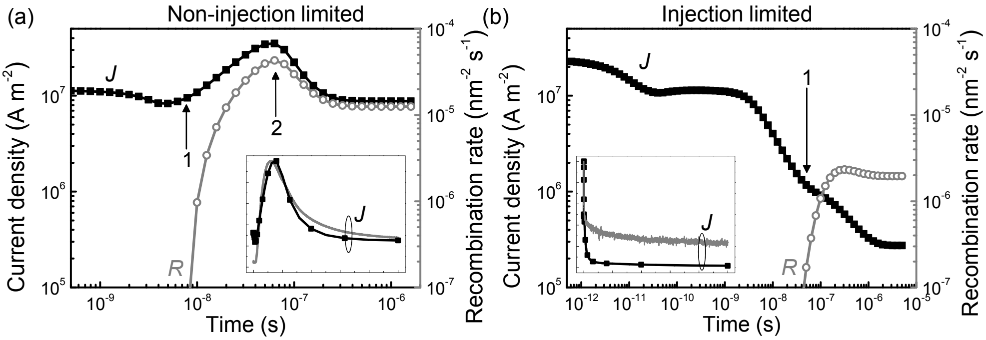

**Figure 2.6 Transient current density and recombination rate in a simulated LEC device. Both devices started identically at *t* = 0 and were simulated until steady-state was reached. The transient current density (black squares) and recombination rate (gray circles) for (a) a non-injection limited LEC and (b) an injection limited LEC are shown. The numbers 1 and 2 mark the initiation of recombination and junction formation, respectively. In the insets the calculated current density (black squares) is shown on a linear scale along with the experimental current trace (gray line). To enable comparison, horizontal and vertical axes have been normalized.**

Comparison of the results of simulations and experiments in the insets of Figure 2.6 reveals that the characteristic features of the current transients are well reproduced by the model in both injection regimes. The quantitative differences in current densities and time scales can be attributed to the significantly different device lengths used, i.e. 350 nm in the simulations vs. 100 µm in experiments, in combination with differences in applied bias and mobility values. Nonetheless, the similarity between the results from simulations and experiments convincingly constitutes the physical relevance of the numerical modeling results presented here.

## 2.4 Conclusions

Two operating regimes in LECs have been identified; their occurrence depends on the ability of the device to form non-injection limited ohmic contacts. In the case ohmic contacts are formed, the LEC follows the electrochemical doping model, characterized by the formation of a dynamic p-i-n junction in the bulk of the device. Anions and cations then become fully spatially separated across the junction at steady-state, forming electric double layers at the contacts and doped regions in the bulk. In the case injection of electronic charge carriers is limited, doping becomes less pronounced and the ion redistribution increases the electric double layers until the bulk is screened from the external electric field. In this injection limited regime, the device follows the electrodynamic model and the electronic current is dominated by diffusion. In contrast, in the ohmic regime drift and diffusion contribute equally. Numerical studies as well as experiments confirm these findings.

These results imply that the electrochemical doping operation mode, i.e. without contact limitations, is the preferred operational mode for LECs, as it gives the highest current densities and the highest electron-hole recombination rates. They also imply that any degradation in the contact area, either by electrochemical side reactions[20-21] or by contact oxidation[22] may cause a transition to the electrodynamic operation mode and hence a reduction in current and light output. The often stated independence of LEC operation on contact material should thus be reconsidered.[23] Finally, our results show that the operational mode of an LEC-type device may be concluded from the shape of the current transient, and does not per se require elaborate SKPM experiments.

# References

[1] Q. B. Pei, G. Yu, C. Zhang, Y. Yang, A. J. Heeger, Science 269 (1995) 1086.

[2] J. C. deMello, N. Tessler, S. C. Graham, R. H. Friend, Phys. Rev. B 57 (1998) 12951.

[3] J. C. deMello, J. J. M. Halls, S. C. Graham, N. Tessler, R. H. Friend, Phys. Rev. Lett. 85 (2000) 421.

[4] J. C. deMello, Phys. Rev. B 66 (2002) 235210.

[5] J. D. Slinker, J. A. DeFranco, M. J. Jaquith, W. R. Silveira, Y. W. Zhong, J. M. Moran-Mirabal, H. G. Craighead, H. D. Abruna, J. A. Marohn, et al., Nat. Mater. 6 (2007) 894.

[6] G. G. Malliaras, J. D. Slinker, J. A. DeFranco, M. J. Jaquith, W. R. Silveira, Y. W. Zhong, J. M. Moran-Mirabal, H. G. Craighead, H. D. Abruna, et al., Nat. Mater. 7 (2008) 168.

[7] C. V. Hoven, H. P. Wang, M. Elbing, L. Garner, D. Winkelhaus, G. C. Bazan, Nat. Mater. 9 (2010) 249.

[8] P. Matyba, K. Maturova, M. Kemerink, N. D. Robinson, L. Edman, Nat. Mater. 8 (2009) 672.

[9] J. Gao, J. Dane, Appl. Phys. Lett. 84 (2004) 2778.

[10] Q. Pei, A. J. Heeger, Nat. Mater. 7 (2008) 167.

[11] D. L. Smith, J. Appl. Phys. 81 (1997) 2869.

[12] D. J. Dick, A. J. Heeger, Y. Yang, Q. B. Pei, Adv. Mater. 8 (1996) 985.

[13] L. S. C. Pingree, D. B. Rodovsky, D. C. Coffey, G. P. Bartholomew, D. S. Ginger, J. Am. Chem. Soc. 129 (2007) 15903.

[14] J. H. Shin, L. Edman, J. Am. Chem. Soc. 128 (2006) 15568.

[15] I. Riess, D. Cahen, J. Appl. Phys. 82 (1997) 3147.

[16] J. A. Manzanares, H. Reiss, A. J. Heeger, J. Phys. Chem. B 102 (1998) 4327.

[17] S. van Reenen, P. Matyba, A. Dzwilewski, R. A. J. Janssen, A. Edman, M. Kemerink, Adv. Funct. Mater. 21 (2011) 1795.

[18] S. R. Tseng, Y. S. Chen, H. F. Meng, H. C. Lai, C. H. Yeh, S. F. Horng, H. H. Liao, C. S. Hsu, Synth. Met. 159 (2009) 137.

[19] S. van Reenen, P. Matyba, A. Dzwilewski, R. A. J. Janssen, L. Edman, M. Kemerink, J. Am. Chem. Soc. 132 (2010) 13776.

[20] T. Johansson, W. Mammo, M. R. Andersson, O. Inganas, Chem. Mater. 11 (1999) 3133.

[21] J. Fang, P. Matyba, N. D. Robinson, L. Edman, J. Am. Chem. Soc. 130 (2008) 4562.

[22] J. H. Shin, P. Matyba, N. D. Robinson, L. Edman, Electrochim. Acta 52 (2007) 6456.

[23] D. B. Rodovsky, O. G. Reid, L. S. C. Pingree, D. S. Ginger, ACS Nano 4 (2010) 2673.

# **Chapter 3** Salt concentration effects

*Incorporation of ions in the active layer of organic semiconductor devices leads to attractive device properties like enhanced injection and improved carrier transport. Here the effects the salt concentration has on the operation of light-emitting electrochemical cells are investigated using experiments and numerical simulations. The current density and light emission are shown to increase monotonously with increasing ion concentration over a wide range of concentrations. The increasing current is accompanied by an ion redistribution leading to a narrowing of the recombination zone. Hence, in absence of detrimental side reactions and doping-related electroluminescence quenching the ion concentration should be as high as possible.*

---

*Part of the work presented in this chapter has been published: S. van Reenen, P. Matyba, A. Dzwilewski, R. A. J. Janssen, L. Edman, M. Kemerink, Adv. Funct. Mater. 21 (2011) 1795.

## 3.1 Introduction

Charge carrier transport in organic semiconductors is often limited by poor injection and/or a low conductivity. The latter typically results from a low carrier mobility and a low charge density that is limited by the build-up of space charge. The effects of space charge are relatively severe due to the low dielectric constant in organic semiconductors, resulting in relatively weak screening of charge carriers. In light-emitting electrochemical cells (LECs),[1-3] these transport limitations are strongly reduced by electrochemical doping of the active layer as was shown in the previous chapter. This electrochemical doping process prevents the formation of space charge when electrons or holes are injected from the contacts into the semiconductor. The resultant enhanced carrier density (and mobility when the mobility is density dependent)[4] is concomitant with increased conductivity and enables enhanced device currents and light output.[5-6]

Next to improving carrier transport, the ions also improve the injection of charge carriers past relatively large injection barriers for bias voltages ($V_{\mathrm{bias}}$) exceeding the bandgap of the active layer ($E_g$). This is done by the formation of electric double layers (EDLs) at the interfaces as shown in the previous chapter. Oppositely charged ions are attracted by the positive and negative electrodes and accumulate at the electrode interfaces forming charged sheets. The large electric fields in the EDLs strongly reduce the barrier widths for carrier injection.[7-11]

All of the advantages (e.g. insensitivity to contact material and device length) and disadvantages (e.g. large turn-on time) of LECs as explained in chapter 1.2 are directly related to the presence of ions in the active layer. Therefore it is of utmost importance to understand the influence of the ion concentration on the LEC characteristics. Ideally an LEC contains sufficient ions to facilitate efficient carrier injection and conduction, but insufficient to suffer from detrimental effects like short operational life times and decreased efficiency. A few studies have already aimed at understanding the influence of the ion concentration in LECs. Fang et al.[12] have shown that in planar LECs with a relatively low ion concentration the doping fronts come to a halt before making contact, so no sharp p-i-n junction is formed. Other work on sandwich cell LECs with relatively low ionic content has shown improved lifetimes in combination with efficient injection.[13-16]

Here, we present the results of transient experiments carried out on planar polymer LECs. The salt concentration was varied to study its effect on the device operation of the LEC. SKPM was performed to study the evolution of the electrostatic potential, complemented by UV-excited photoluminescence (PL) measurements to monitor the electrochemical doping progression. In addition, numerical simulations were used to interpret the effects of a reduced ion concentration on the measured current, potential and doping transients. The results show that in an ideal LEC, i.e. in absence of electroluminescence quenching and side reactions, the current density and light output at fixed bias are linearly proportional to the ion concentration over many orders of magnitude.

## 3.2 Material and methods

*Device preparation*: For the conjugated polymer in the active layer we used a phenyl-substituted poly(p-phenylene vinylene) copolymer (SY-PPV, Merck, catalogue number PDY-132), commonly termed “Super Yellow”. Poly(ethylene oxide) (PEO, $M_w = 5{\cdot}10^5$ g mol$^{-1}$, Aldrich) was used as received. The salt potassium trifluoromethanesulfonate ($KCF_3SO_3$, 98 %, Aldrich) was dried at 473 K under vacuum before use. SY-PPV was dissolved (5 mg ml$^{-1}$) in cyclohexanone (> 99 %, anhydrous, Aldrich). PEO and $KCF_3SO_3$ were dissolved separately (10 mg ml$^{-1}$) in cyclohexanone (> 99 %, anhydrous, Aldrich). These solutions were mixed together in a weight ratio of SY-PPV:PEO:$KCF_3SO_3$ = 1:1.35:0.25. For the fabrication of ion-poor devices, a weight ratio of 1:1.35:0.06 was used. These blend solutions were thereafter stirred on a magnetic hot plate at a temperature $T$ = 323 K for 5 h. Glass substrates (1×1 cm$^2$) were cleaned by subsequent ultrasonic treatment in detergent, distilled water, acetone and isopropanol.

The glass substrates were spin-coated with the blend solution at 800 rpm for 60 s, followed by 1000 rpm for 10 s after which they were dried at $T$ = 323 K for at least 1 h on a hot plate. The resulting active layer thickness was ~230 nm, as determined by profilometry. Au electrodes capped with a layer of Al were deposited by thermal evaporation under high vacuum ($p \approx 1 \times 10^{-6}$ mbar) on top of the spin-coated films. A thin wire-based shadow mask was used to create an inter-electrode gap of approximately 100 µm. All the above procedures, save for the cleaning of the substrates, were done in a glove box under $N_2$ atmosphere ($[O_2] < 1$ ppm and $[H_2O] < 1$ ppm) or in an integrated thermal evaporator.

*Scanning Kelvin probe microscopy*: SKPM images were recorded in a glove box under $N_2$ atmosphere ($[O_2] < 1$ ppm and $[H_2O] < 1$ ppm) with a Veeco Instruments MultiMode AFM with Nanoscope IV controller, operating in lift mode with a lift height of 25 nm. Ti-Pt coated silicon tips (MikroMasch NSC36/Ti-Pt, $k$ ~1.75 N m$^{-1}$) were employed. All measurements were carried out at $T$ = 333 K.

*UV-excited photoluminescence detection*: Optical probing was performed in an optical-access cryostat under high vacuum ($p < 10^{-5}$ mbar), using a single-lens reflex camera (Canon EOS50) equipped with a macro lens (focal length 65 mm) and a ×2 teleconverter. In parallel with the optical probing, the current was measured with a computer-controlled source-measure unit (Keithley 2612). Also the electro-optical probing was carried out at $T$ = 333 K.

*Computational details*: The 1-dimensional model as described in Appendix A was used to model a planar LEC. An active layer of length $L$ = 20 µm was used, divided in $N$ = 81 discrete, equidistant points. Devices with a bandgap $E_g$ = 2 eV were simulated during operation at a bias voltage $V_{bias}$ = 5 V until steady-state had been reached, recognized by a zero ion current. Simulations were run for devices with initial ion concentrations $c_0$ varying between $1\cdot10^{-6}$ nm$^{-3}$ and $1\cdot10^{-1}$ nm$^{-3}$. No binding energy was assumed between anions and cations. Electrons and holes were injected from the contacts according to a self-designed injection model that gives rise to field dependent injection. The model is described in detail in Appendix A and has the advantage that injection is not affected by grid-point spacing. The hole and electron injection barriers were set at 0.5 and 1.5 eV respectively to simulate an asymmetric device. Such an asymmetry is realistic for the actual LECs studied in this chapter, which use Au for both the anode and cathode. Additional settings are the relative dielectric constant $\varepsilon$ = 3, the temperature $T$ = 300 K and the hole and electron mobility $\mu_{p/n}$ = $5\cdot10^{-11}$ m$^2$ V$^{-1}$ s$^{-1}$. The anion and cation mobility were chosen to be $5\cdot10^{-12}$ m$^2$ V$^{-1}$ s$^{-1}$. It was checked that the inter-electrode gap did not affect the outcome of the calculations in any non-trivial manner.[17]

## 3.3 Results and discussion

### 3.3.1 Experimental characterization

Two sets of planar LECs with different SY-PPV:PEO:$KCF_3SO_3$ weight ratios were prepared: ion-rich devices (1:1.35:0.25) and ion-poor devices (1:1.35:0.06). To study the difference in doping during device operation, PL measurements were carried out under UV illumination of the active layer. As both p- and n-type doping quench the UV-excited PL, the doped regions appear darker than undoped regions. The photographs are shown in Figure 3.1a and b. In Figure 3.1c-e schematic drawings of the anion and cation concentration distributions in LECs are shown before operation (Figure 3.1c), during doping front progression (Figure 3.1d) and in steady-state (Figure 3.1e). In unbiased, pristine devices the anions and cations are homogeneously distributed across the active layer (see Figure 3.1c). After application of a bias voltage, charges are injected. The injection initiates doping of the active layer, starting from the electrodes. The p- ($a^-p^+$) and n-type ($c^+p^-$) doping fronts propagate towards each other while splitting the available paired ions ($a^-c^+$) for the doping process (see Figure 3.1d). Ultimately, all of the anions and cations are used for doping of the polymer and are separated from each other (see Figure 3.1e).[11] In Figure 3.1a and b, this doping process was investigated in ion-rich and ion-poor LECs. At $t$ = 0, a bias voltage of 8 V was applied to the pristine devices. In the ion-rich device (Figure 3.1a) p- and n-type doping initiate from the anode and cathode respectively. These doping fronts then propagate towards each other and meet at $t$ = 9 s. After that light emission is observed, originating from electroluminescence (last picture of Figure 3.1a). In the ion-poor device, doping fronts form as well (Figure 3.1b). However, the doping fronts never meet as the n-type doping front only moves a short distance away from the negative contact and the p-type doping front stops at the centre of the active layer (*t* = 600 s). Eventually, the p-type doping front seems to retract somewhat towards the anode and the boundary between the p-doped and undoped region becomes less sharp. No electroluminescence was observed in the ion-poor LEC.

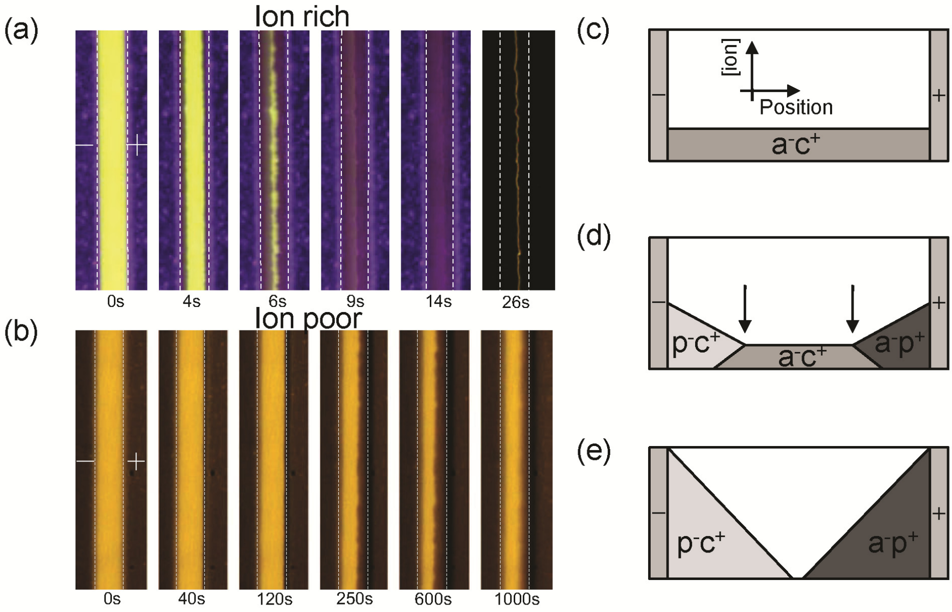

**Figure 3.1 Photographs of planar Au/SY-PPV:PEO:KCF$_3$SO$_3$/Au LECs with an interelectrode gap of ~90 µm during operation at $V_{bias}$ = 8 V and *T* = 333 K. Two different SY-PPV:PEO:KCF$_3$SO$_3$ weight ratios were used: 1:1.35:0.25 – ion-rich (a) and 1:1.35:0.06 – ion-poor (b). The ionic redistribution and doping process is schematically shown in (c-e). $a^-$ (dark gray area), $c^+$ (light gray area), $p^-$ and $p^+$ refer to anions, cations, reduced polymer and oxidized polymer respectively. The arrows in (d) indicate the position of the doping fronts.**

To obtain better insight into these characteristic results, SKPM was performed on similar devices. SKPM monitored the electrostatic potential in the active layer during operation of the LEC. Potential profiles of ion-rich and ion-poor devices operating at steady-state are shown in Figure 3.2a and b. The device was alleged to be at steady-state when the potential profile did not significantly evolve anymore. The UV-excited PL measurements during steady-state operation on similar devices have been added to the background of the graphs to enable comparison. The corresponding electrostatic field profiles are shown in Figure 3.2c and d for the ion-rich and ion-poor device, respectively.

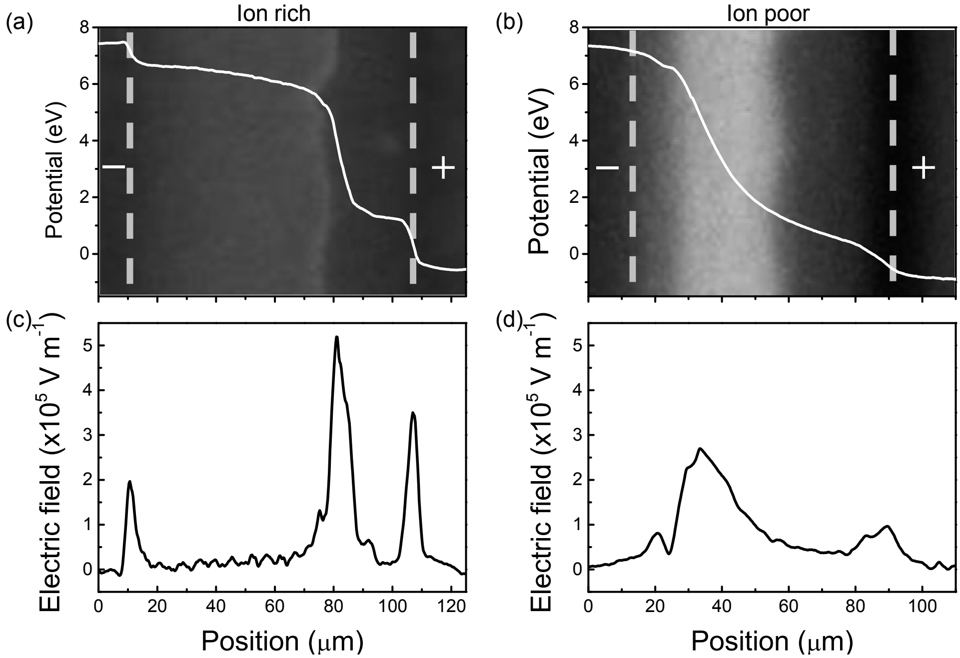

**Figure 3.2 (a,b) Electrostatic potential and (c,d) field profiles in planar LECs during operation at $V_{bias}$ = 8 V with weight ratios SY-PPV:PEO:$KCF_3SO_3$ (a,c) 1:1.35:0.25 and (b,d) 1:1.35:0.06. The photographs behind the graphs (a,b) are UV-excited PL images recorded at steady-state, on the same horizontal scale. The electrode interfaces are indicated by the gray dashed lines.**

Doping strongly decreases the resistivity of the semiconductor. Consequently a smaller electric field is necessary in stronger doped regions to conduct the same amount of current. The intrinsic junction separating the p- and n-doped regions has a basically constant, higher resistivity and hence requires a larger electric field to maintain a constant current at steady-state. The resulting peak in the electric field profile is clearly observed in Figure 3.2c and d, with the p-i-n junction located around $x$ = 85 and $x$ = 40 µm, respectively. These positions clearly correlate with the UV-excited PL measurements in the background of Figure 3.2a and b, with the p-i-n junction coinciding with the emission zone for the ion-rich device and with the bright, unquenched region for the ion-poor device. Furthermore, in Figure 3.2a and c, regions of relatively large electric field are observed at the electrode interfaces ($x$ = 10 and 110 µm): the electric double layers. Similar high-field regions were identified in the ion-poor LEC (see Figure 3.2b and d) at $x$ = 20 and $x$ = 90 µm.

Comparison of Figure 3.2a,c and b,d reveals the following changes in the LEC due to a decreased ion concentration: i) the junction region width has increased, concomitant with a decreased electric field in the junction; ii) the electric field in the doped regions has increased and iii) the potential drop at the electrode interfaces has decreased. A detailed discussion of these observations is given later in this chapter.

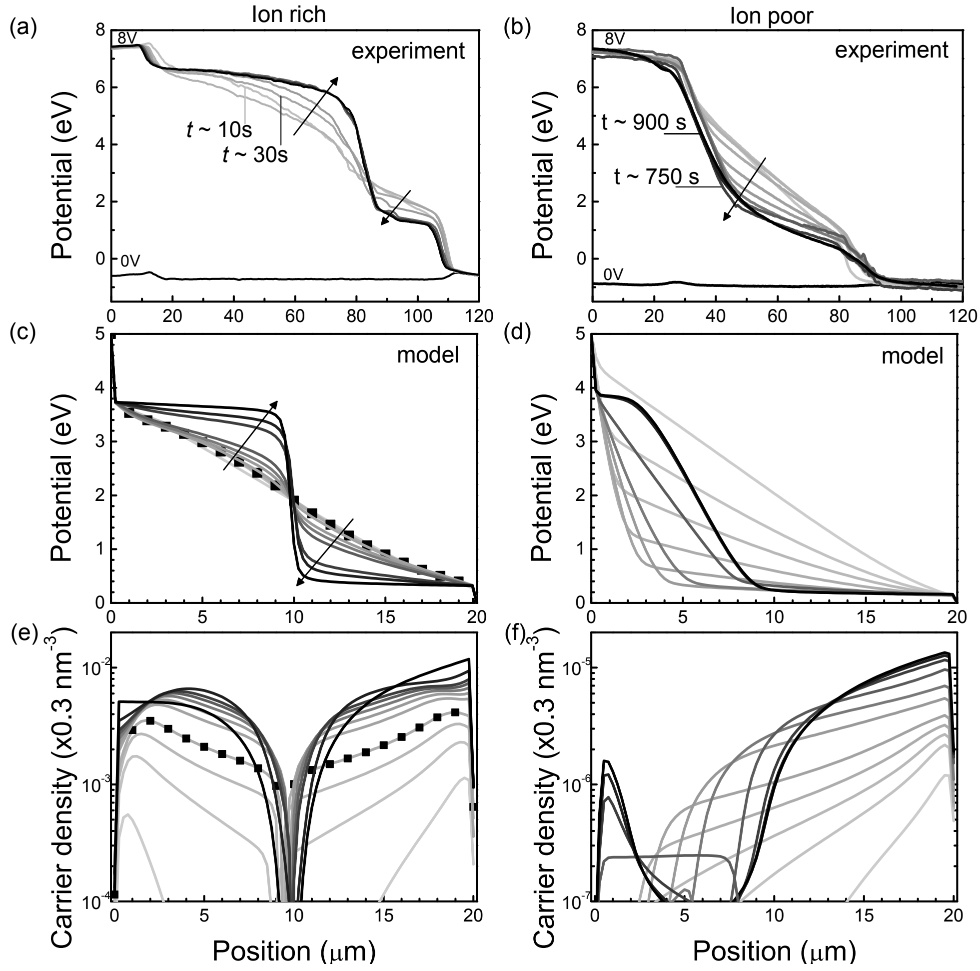

**Figure 3.3 Transient potential profiles (evolution from light gray to black) from experiments and simulations as well as simulated charge carrier density profiles. The experimentally determined profiles are from LECs with a SY-PPV:PEO:KCF$_3$SO$_3$ weight ratio of (a) 1:1.35:0.25 – ion-rich and (b) 1:1.35:0.06 – ion-poor. The numerically determined profiles are from LECs with an ion concentration of (c,e) 1.5·10$^{-3}$ ions nm$^{-3}$ and (d and f) 1.5·10$^{-6}$ ions nm$^{-3}$. The black lines denote the steady-state potential profile. In (a,b) the potential profiles at $V_{\text{bias}}$ = 0 V are included as well. The black arrows accentuate the change of the profiles in time. The lines marked by black squares in (c,e) indicate the profiles when the n-type and p-type doping fronts have met.**

In addition to the steady-state potential profiles, transient potential profiles were measured, as shown in Figure 3.3a and b for the ion-rich and ion-poor device, respectively. The arrows indicate the temporal trend of the potential profile evolution. In the ion-rich device, the EDLs form faster than the time resolution of the SKPM experiment of 10 s. Moreover, during the first potential measurement at *t* = 10 s light emission was already observed in a similar device (see Figure 3.1a). Therefore we may assume that the potential profile evolution shown here mainly reflects the saturation of doping after collision of the doping fronts, which is consistent with the observation that the light emission intensity from the p-i-n junction increases with time *after* the initial junction formation, as shown in Figure 3.1a and Ref. 18. This saturation is further indicated by the decreasing electric field (-dV/dx) in the doped regions and the increasing field in the junction region. Importantly, a comparison of Figure 3.1a and Figure 3.3a indicates that light emission already takes place from a narrow region even before the sharp potential drop has arisen. Moreover, if recombination does take place in the adjacent doped regions, the resultant light emission could be quenched by doping and therefore not observed.

In case the LEC contains relatively few ions (Figure 3.3b), small EDLs are formed and mainly p-type doping is observed. For this device, the potential profiles could be measured in similar time intervals as the PL measurements shown in Figure 3.1b. The junction region is broader and includes the region close to the negative contact, indicating the absence of significant n-type doping. Comparison of the last two potential traces shown in black indicates that the transition from the p-doped region to the junction region becomes less sharp in time. A similar transition was already observed in the final two pictures in Figure 3.1b.

### 3.3.2 Numerical simulations

In order to complement these experimental findings, numerical simulations were carried out to gain insight into the physical processes underlying the observed trends. The model described above was used to calculate the potential profile evolution for LECs with a high and low ion density of $1.5 \cdot 10^{-6}$ and $1.5 \cdot 10^{-3}$ ions $nm^{-3}$ respectively. The results are shown in Figure 3.3c and d. Corresponding carrier density profiles are shown in Figure 3.3e and f for the high and low ion density simulations respectively. In the bulk the carrier density equals the difference between the anion and cation density because of charge neutrality in the doped regions.

First consider the ion-rich LEC. The modeled potential profiles show that after formation of EDLs, no significant change occurs in the potential profile during progression of doping through the active layer (light gray lines in Figure 3.3c and e). After both doping regions make contact (the corresponding profiles are indicated by black squares), doping continues to saturate via the continued redistribution of ions. As a consequence, a thin high-field region, the p-i-n junction, forms in the bulk. The modeling shows that progression of doping is not necessarily visible in the potential evolution throughout the LEC. Furthermore, it indicates that the typical steady-state potential profile (see Figure 3.2a) only appears when doping reaches its saturation point and not when the doping fronts meet, highlighted by the initiation of light-emission (compare Figure 3.3c and e). This is in agreement with the observed experimental behavior (see Figure 3.3a and Figure

3.1a). In the model, the formation of a sharp potential drop in the junction region is related to removal of ions from the junction region. The time needed for this removal is given by the speed of depletion of anions (cations) from the n-type (p-type) doped region (see Figure 3.1c-e).

Further comparison of experiment and model shows a difference in junction position. In the model the junction is positioned in the center of the active layer, in contrast with the experiment. The asymmetry of the injection barriers hardly affects the junction position in the model. The discrepancy with the experiment is attributed to the absence of charge traps and side-reactions[19] and/or to the fact that the mobilities of holes and electrons were set equal in the model. Apart from the junction position, the simulation of an ion-rich LEC shows a qualitatively similar potential profile evolution as the real device.

The potential profile evolution in ion-poor LECs as determined by modeling (Figure 3.3d) and experiments (Figure 3.3b) also shows qualitatively similar behavior. In the model, the device has difficulty to form a good, i.e. a non-limiting or Ohmic contact at the negative electrode, as can be seen from the delayed formation of an n-type doped region ($x$ = 0-3 μm; see Figure 3.3f). This is due to the small amount of cations available to form an EDL at the negative contact, which has the largest injection barrier. Consequently, hole injection and subsequent p-type doping start far ahead of electron injection and n-type doping, as also experimentally observed (Figure 3.1b). In addition to this effect, the occurrence of side-reactions in real devices, which are known to predominantly occur at the negative electrode,[20] are a probable additional reason for the difficult injection of electrons that is observed in Figure 3.1b and Figure 3.3b. In both the model and the experiment, a moderately high-field junction region arises over a broad region relatively close to the negative contact.

To gain more insight into the effects of a reduced ion concentration in LECs, simulations were performed for ion densities ranging from $2\cdot10^{-6}$ nm$^{-3}$ to $1\cdot10^{-1}$ nm$^{-3}$. The steady-state potential and electric field profiles are shown in Figure 3.4a and b, respectively. In Figure 3.4c, the absolute difference between anion and cation density is shown throughout the active layers. In the bulk, this difference is directly related to the doping density since charge neutrality demands that differences in ionic concentrations are compensated by electrons or holes. At the electrode interfaces the ion density also comprises unpaired ions, which do not contribute to doping, but rather are responsible for EDL formation.

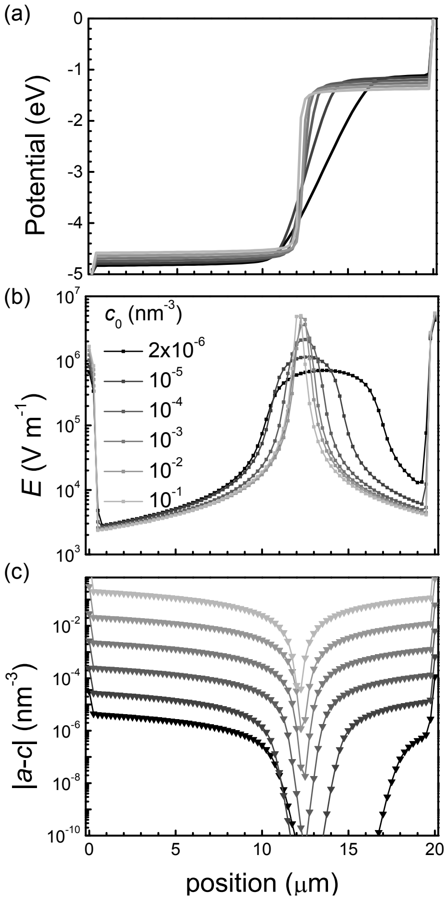

**Figure 3.4 (a) Electrostatic potential, (b) field and (c) ionic density profiles in modeled LECs during operation in steady-state for different initial ion concentrations ($c_0$), as indicated in the legend in (b).**

For each value of $c_0$ the LEC operates according to the electrochemical doping model: at the interfaces ($x$ = 0 and 20 μm) EDLs are identified, closing in p- and n-type doping regions with a p-i-n junction in between.[11] Multiple trends can be discerned for decreasing $c_0$, which can be identified also in the experimental data in Figure 3.2 and Figure 3.3. First of all, the p-i-n junction region width increases, whereas the potential drop at this junction shows only a minor increase. The result is that the electric field in this region decreases (see Figure 3.4b). Secondly, the width of the doped regions as well as the degree of doping decreases, while the electric field in these regions is enhanced. Lastly, the EDLs are affected, as the potential drop at the interfaces decreases for decreasing $c_0$. These phenomena are interconnected. Since the majority of ions is used for doping, the doping density and concomitantly the conductivity in the doped regions decreases almost linearly upon lowering of $c_0$. Hence, the current density also declines linearly, as shown in Figure

3.5. Because of current continuity this decline implies that the injection of charges must be decreased as well -otherwise a surplus of injected carriers would form behind the EDLs. To this end, the strength of the EDLs is decreased, which results in larger effective injection barriers and lower charge injection. Finally, the fact that the width of the junction region increases is also related to current continuity: the electric field, being proportional to the current through the junction, needs to be decreased by increasing the width of the junction region when the device current goes down. The mechanism outlined above shows that in LECs, the availability of ions to dope the conjugated polymer determines the potential profile both in the bulk and at the interfaces.

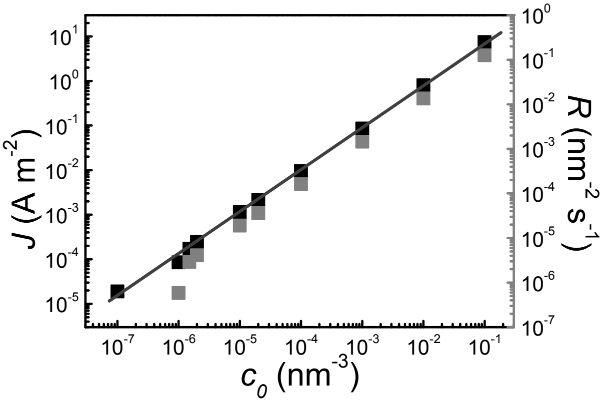

**Figure 3.5 The steady-state current density *J* (black) and recombination rate *R* (gray) for different ion concentrations $c_0$. The gray line follows the relation $J = A \cdot c_0$ for an arbitrary value of *A*, serving as a guide to the eyes.**

Another important result of the modeling presented here is the monotonous increase of the current density for increasing $c_0$, as shown in Figure 3.5. In principle, this implies that the presence of as much ions as possible is favorable for device performance. This is only true if all injected charge carriers recombine. In the modeling, the internal quantum efficiency is 100% as all carriers recombine in between the doped regions. In contrast to real devices, the model ignores doping induced exciton quenching and spatial competition between the conjugated polymer, the electrolyte and the ions. At some ion concentration, these two processes will start to adversely affect the radiative recombination efficiency, resulting in an upper limit for the allowable ion concentration.

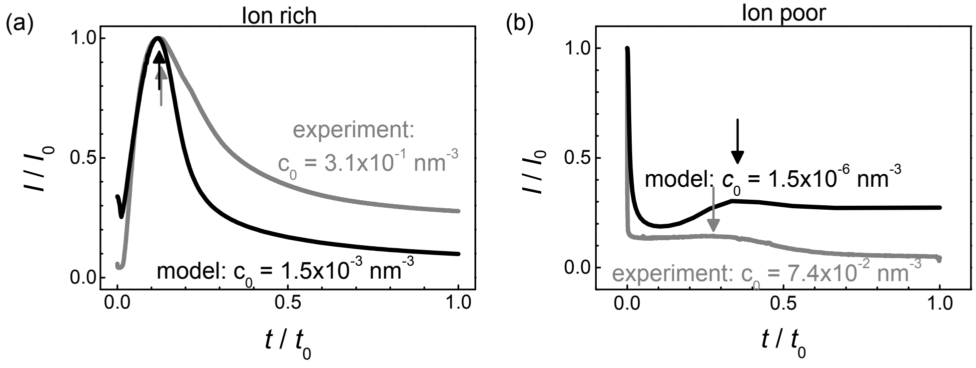

**Figure 3.6 Current transients of planar Au/SY-PPV:PEO:$KCF_3SO_3$/Au LECs with an interelectrode gap of ~90 µm during operation at $V_{bias}$ = 8 V. Two different SY-PPV:PEO:$KCF_3SO_3$ weight ratios were used: (a) 1:1.35:0.25 – ion-rich and (b) 1:1.35:0.06 – ion-poor. The modeled current transients are from LECs with an initial homogeneous ion concentration ($c_0$) as specified in the figures. [$I_0$, $t_0$] in (a) is [5 µA, 150 s] for the experiment and [1.8 A $m^{-2}$, 54 s] for the model and in (b) [5 nA, 1200 s] for the experiment and [0.15 mA $m^{-2}$, 300 s] for the model.**

In order to further determine the similarity between model and experiment, the measured and modeled current transients are presented in Figure 3.6. Characteristic features in both the high- and low-ion density curves can be decomposed in an ionic and electronic contribution. Since the contacts are initially non-injecting, the current density at *t* = 0 can be attributed to the redistributing ions in the active layer. Thereafter, this contribution continuously declines due to ion pile-up at the electrodes and a decrease of the bulk field because of the resulting EDL formation. When EDLs are being formed, injection of electrons and holes is enhanced, resulting in an increasing electronic current. This rise is observed in all four current transients and the resulting maximum in current is marked by the arrows in Figure 3.6. Following this rise, a second decrease of the current density, now related to a decrease of the electronic current, is observed. After the onset of current injection from the contacts, a large fraction of the electronic current is 'consumed' for doping the device, i.e. used to compensate space charges resulting from the further separation of anions and cations. When this doping process is completed, the electronic current decreases. At steady-state, anions and cations have been fully separated into p- and n-type doped regions, separated by a relatively sharp potential drop in the junction region; see Figure 3.1, Figure 3.3, and Figure 3.6. In the modeled LECs, the steady-state current consists of an electronic contribution only; the ionic current has vanished due to the ion-blocking electrodes and the absence of generation and recombination of ions. In principle the same holds for the real LECs, although a minor ionic contribution from regions outside the inter-electrode gap, having a longer settling time due to the larger distances involved, cannot be excluded.

One of the major setbacks of LECs is the relatively long response time. The present experimental results, as well as those by Fang *et al.*,[12] show that a decrease of $c_0$ leads to an increase of the response time in LECs. The same is observed in modeled LECs (Figure 3.6) in which the ion concentration becomes so low that the formation of EDLs is affected and delayed. This is observed at the cathode in Figure 3.3d. However, current transients accompanying the simulations presented in Figure 3.4 reveal that when EDL formation is not hindered, the response time is independent of $c_0$; see also Figure 3.7. This difference between model and experiment suggests that processes omitted in the model cause the longer response time of low ion concentration LECs. In the model, the redistribution of ions is limited by the cations (anions) being transported from the p-type (n-type) doped region to the n-type (p-type) doped region. The latter is only controlled by the (field driven) drift current, and should therefore be independent of concentration, unless e.g. side reactions hinder the movement of ions. Alternatively, it is conceivable that the ionic mobility is concentration dependent. In either case, these results indicate that the use of a high ion density decreases the turn-on time.

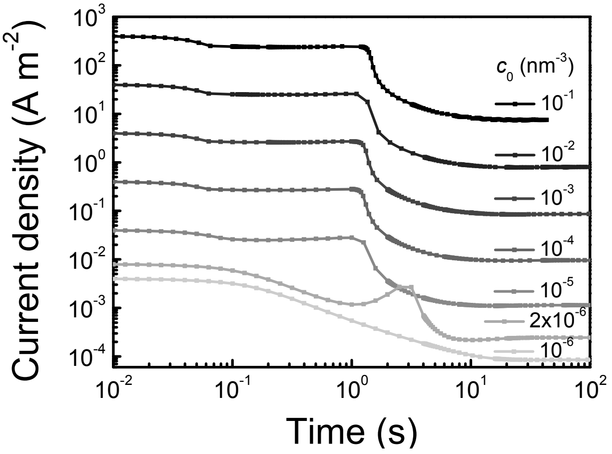

**Figure 3.7 Current transients of modeled LECs (c.f. Figure 3.4) for different values of the initial ion concentration $c_0$.**

So far, no comments have been made regarding the discrepancy between the ion concentration used in the model and the nominal salt concentration in the active layer during experiments. In the transient modeling presented in Figure 3.3c,d and Figure 3.6a,b, the initial ion concentrations were chosen to be $1.5 \cdot 10^{-3}$ and $1.5 \cdot 10^{-6}$ nm$^{-3}$ for the high- and low-ion density device, respectively. The nominal salt concentrations in the experiments were $3.0 \cdot 10^{-1}$ and $0.7 \cdot 10^{-1}$ nm$^{-3}$, respectively. The latter concentration difference of a factor of ~4 resulted in a decrease of the steady-state current by a factor ~$10^3$: 1.5 μA for the ion-rich device and 0.4 nA for the ion-poor device. As shown in Figure

3.5, changing the initial ion concentration by a factor $10^3$ in the model leads to a change in the calculated current density by the same factor $10^3$. Additionally, the only way to achieve qualitatively similar current transients and potential profiles in the model and the experiment is by using three orders of magnitude difference between high and low ion concentrations in the model. These results imply that the effective initial *mobile* ion density in a real LEC is a highly nonlinear function of the salt concentration. We speculate that this behavior is related to the effective loss of ions in side-reactions[19, 21] and/or to the existence of immobile ions locked up in crystalline PEO phases.[22-23]

## 3.4 Conclusions

By combination of experiments and numerical modeling insight is gained regarding the function of ions in planar light-emitting electrochemical cells. An increase of the initial ion concentration results in an increased steady-state current density and recombination rate in the LEC due to the enhanced conductivity of the active layer by electrochemical doping. Concomitant, injection is enhanced and the recombination zone is narrowed. Hence, from a device modeling point of view, optimal performance in terms of light output at given bias requires the use of an as high as possible ion concentration. In real devices adverse effects like doping-induced exciton quenching, side-reactions and a finite solubility may put an upper limit to the optimal ion concentration.

# References

[1] Q. B. Pei, G. Yu, C. Zhang, Y. Yang, A. J. Heeger, Science 269 (1995) 1086.

[2] J. M. Leger, Adv. Mater. 20 (2008) 837.

[3] L. Hu, G. Xu, Chem. Soc. Rev. 39 (2010) 3275.

[4] H. Shimotani, G. Diguet, Y. Iwasa, Appl. Phys. Lett. 86 (2005) 022104.

[5] Q. J. Sun, Y. F. Li, Q. B. Pei, J. Disp. Technol. 3 (2007) 211.

[6] O. Inganas, Chem. Soc. Rev. 39 (2010) 2633.

[7] L. He, L. A. Duan, J. A. Qiao, G. F. Dong, L. D. Wang, Y. Qiu, Chem. Mater. 22 (2010) 3535.

[8] C. Y. Lin, A. Garcia, P. Zalar, J. Z. Brzezinski, T. Q. Nguyen, J. Phys. Chem. C 114 (2010) 15786.

[9] Z. Chen, X. D. Dang, A. Gutacker, A. Garcia, H. P. Li, Y. H. Xu, L. Ying, T. Q. Nguyen, G. C. Bazan, J. Am. Chem. Soc. 132 (2010) 12160.

[10] G. Latini, G. Winroth, S. Brovelli, S. O. McDonnell, H. L. Anderson, J. M. Mativetsky, P. Samori, F. Cacialli, J. Appl. Phys. 107 (2010) 124509.

[11] R. Marcilla, D. Mecerreyes, G. Winroth, S. Brovelli, M. D. R. Yebra, F. Cacialli, Appl. Phys. Lett. 96 (2010).

[12] J. F. Fang, Y. L. Yang, L. Edman, Appl. Phys. Lett. 93 (2008) 063503.

[13] A. Sandstrom, P. Matyba, L. Edman, Appl. Phys. Lett. 96 (2010) 053303.

[14] Y. Shao, G. C. Bazan, A. J. Heeger, Adv. Mater. 20 (2008) 1191.

[15] J. F. Fang, P. Matyba, L. Edman, Adv. Funct. Mater. 19 (2009) 2671.

[16] S. Tang, L. Edman, J. Phys. Chem. Lett. 1 (2010) 2727.

[17] S. van Reenen, P. Matyba, A. Dzwilewski, R. A. J. Janssen, A. Edman, M. Kemerink, Adv. Funct. Mater. 21 (2011) 1795.

[18] N. D. Robinson, J. F. Fang, P. Matyba, L. Edman, Phys. Rev. B 78 (2008) 245202.

[19] J. Fang, P. Matyba, N. D. Robinson, L. Edman, J. Am. Chem. Soc. 130 (2008) 4562.

[20] D. M. de Leeuw, M. M. J. Simenon, A. R. Brown, R. E. F. Einerhand, Synth. Met. 87 (1997) 53.

[21] T. Wagberg, P. R. Hania, N. D. Robinson, J. H. Shin, P. Matyba, L. Edman, Adv. Mater. 20 (2008) 1744.

[22] P. G. Bruce, *Solid State Electrochemistry*. Cambridge University Press: 1995.

[23] M. Marzantowicz, J. R. Dygas, F. Krok, A. Tomaszewska, G. Z. Zukowska, Z. Florjanczyk, E. Zygadlo-Monikowska, Electrochim. Acta 55 (2010) 5446.

# **Chapter 4** Doping dynamics in light-emitting electrochemical cells

---

*A major drawback of light-emitting electrochemical cells (LECs) is the long time scale associated with switching, during which ions redistribute in the active layer. We present a numerical modeling study that gives fundamental insight in the dynamics during turn-on. The characteristic response of planar LECs to an applied bias is electrochemical doping of the active layer by doping fronts moving across the active layer. Formation and motion of such doping fronts are shown to be intimately related to both the electronic and ionic mobility and therefore provide useful information regarding these two quantities in LECs. In particular, it is shown that the switch-on time in LECs is directly related to the time an ion needs to cross approximately half the device, enabling the extraction of the ion mobility from the switch-on time.*

---

*Part of the work presented in this chapter has been published: S. van Reenen, R. A. J. Janssen, M. Kemerink, Org. Electron. 12 (2011) 1746.

## 4.1 Introduction

In the previous chapters mainly quasi steady-state operation in LECs was considered. Here the transient operation of LECs is studied. In wide-gap planar LECs, the transient operation can be visualized by monitoring the PL of the active layer under UV illumination (see Figure 3.1);[1] in the presence of doping, PL is quenched in the active layer.[2] Particularly interesting is the way in which this doping occurs. Starting from the electrodes, doped regions expand towards each other. During this expansion, doping fronts are visible as sharp transitions between the undoped region and the n- and p-type doped regions. These fronts have been observed to accelerate. Figure 4.1a (symbols) shows a typical measurement[3] of the front position versus time.

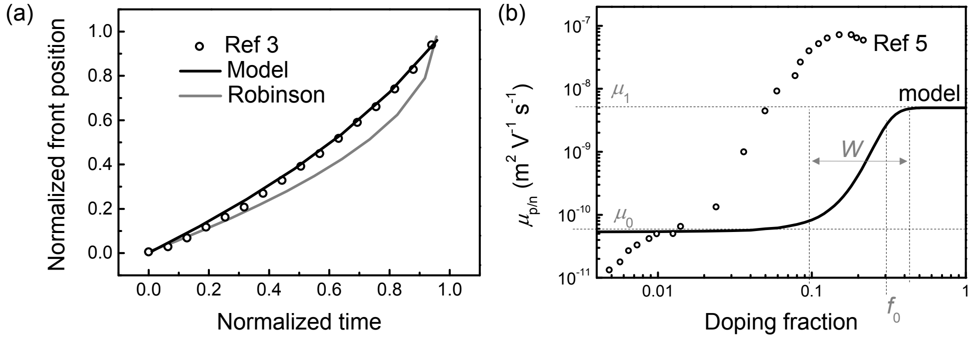

**Figure 4.1 (a) Front position during switch-on in an LEC as obtained experimentally (symbols)[3], analytically (gray line)[4] and by numerical modeling (black line). The model curve follows from modeling of a planar LEC with a doping dependent $\mu_{p/n}$ according to Eq. (4.1) for $\mu_0 = 5\cdot10^{-11}$ m$^2$ V$^{-1}$ s$^{-1}$, $\mu_1 = 5\cdot10^{-8}$ m$^2$ V$^{-1}$ s$^{-1}$, $f_0 = 0.13$ and $W = 0.015$. (b) The electron/hole mobility as a function of the doping fraction. The symbols were experimentally determined by Shimotani *et al.*[5] in regioregular P3HT (here the mobility values are divided by $10^2$) and the black line follows from Eq. (4.1) for $\mu_0 = 5\cdot10^{-11}$ m$^2$ V$^{-1}$ s$^{-1}$, $\mu_1 = 5\cdot10^{-9}$ m$^2$ V$^{-1}$ s$^{-1}$, $f_0 = 0.3$ and $W = 0.04$.**

Several experimental studies[6-8] have been performed on these fronts as well as analytical[4, 9] and numerical modeling.[10] Robinson and co-workers developed an analytical model that predicts the position of the doping fronts and the resultant switch-on time. They assumed that both the potential over the shrinking undoped region and the conductivity through this region remain equal. The first assumption is however not necessarily true in LECs. Measurements of the electrostatic potential in the previous chapter (Figure 3.3a) show that the potential does not strongly evolve during doping front progression.[11] Results presented in this chapter furthermore confirm these findings.

Here we demonstrate by numerical modeling[12] that a doping dependent mobility[5] is required to generate the accelerating doping fronts observed experimentally (Figure 4.1b, symbols). In addition the ion mobility with respect to the electron/hole mobility is critical for front formation as well as for other transient properties like the formation of electric double layers (EDLs)[13] and a light-emitting p-i-n junction. For formation of accelerating doping fronts, the ion mobility needs to be approximately equal to the electron/hole mobility in the undoped polymer. In simulations that obey these criteria, the doping front propagation shows an excellent agreement with experimentally observed doping fronts as shown in Figure 4.1a (black solid line).[3] As opposed to the $t^2$ dependency of the front position obtained by Robinson et al.[4] (Figure 4.1a, gray solid line) our model shows a less strong time dependence of the front position. Next to this fundamental understanding of the formation of doping fronts, also the transient behavior and the switch-on time in LECs are rationalized by means of numerical modeling. The simulations indicate that the switch-on time is mostly related to the time an ion needs to cross approximately half the device.

## 4.2 Material and methods

*Computational details*: The 1-dimensional model described in detail in Appendix A was used in which an active layer with a length of 2 µm was divided in discrete, equidistant grid points.[11-12] Devices with a bandgap $E_g$ = 2 eV were simulated during operation at a bias voltage $V_{bias}$ = 5 V. Simulations were run for devices with an initial homogeneous ion concentration $c_0$ = $1\cdot 10^{-1}$ nm$^{-3}$. No binding energy was assumed between anions and cations. The electrodes were ionically-blocking and electrons and holes were injected from the contacts according to a dedicated injection model that gives rise to field dependent injection.[12] The injection model (modified Boltzmann) is described in detail in Appendix A and has the advantage that injection is not affected by grid-point spacing. The hole and electron injection barriers were set at 0.5 and 1.5 eV respectively to simulate an asymmetric device. Such an asymmetry is realistic for actual planar LECs, in which both the anode and the cathode are made from a single material, e.g. Au. In addition, we set the relative dielectric constant $\varepsilon$ = 3 and the temperature $T$ = 300 K.

To implement a doping density dependency of the electron/hole mobility ($\mu_{p/n}$) the following expression was used:

$$\mu_{p/n}(f) = \frac{\mu_{p/n,1} - \mu_{p/n,0}}{1+\exp\left(\frac{f_0 - f}{W}\right)} + \mu_{p/n,0}. \qquad \textbf{(4.1)}$$

Here $f$ is the doping fraction which is equal to the carrier density divided by the density of states (= 0.3 nm$^{-3}$). Note that here the carrier density is assumed to represent the doping density. This approximation of the doping fraction is justified by the observation that the net ion density always equals the net electronic charge density in the doped regions. Regarding the other parameters, $\mu_{p/n,1}$ is the mobility at maximal doping ($f$ = 1), $\mu_{p/n,0}$ is the mobility in the absence of doping ($f$ = 0), and $f_0$ and $W$ are two parameters that set the transition from $\mu_0$ and $\mu_1$: $f_0$ determines at which doping fraction the mobility increases and $W$ determines the range of doping fractions over which this increase occurs. Figure

4.1b (line) shows a typical plot of the doping dependent mobility that follows from Eq. (4.1) for $f_0$ = 0.3, $W$ = 0.04, $\mu_0 = 5{\cdot}10^{-11}$ m$^2$ V$^{-1}$ s$^{-1}$ and $\mu_1 = 5{\cdot}10^{-9}$ m$^2$ V$^{-1}$ s$^{-1}$. The anion and cation mobilities were chosen to be equal to each other and doping independent. Ion mobilities ranged from $5{\cdot}10^{-12}$ to $5{\cdot}10^{-9}$ m$^2$ V$^{-1}$ s$^{-1}$.

Since our interest is the transient behavior of LECs, simulations started with the application of a bias voltage on a homogeneous device and were continued until steady-state was reached. At $t$ = 0 the electron and hole density equals zero and the anion and cation density equals $c_0$. It was checked that the inter-electrode gap and meshing did not affect the outcome of the simulations in any non-trivial manner.

## 4.3 Results and discussion

Multiple simulations were performed to analyze the effect of the electronic and ionic mobilities on the transient behavior in LECs and specifically on the formation of doping fronts. The time-evolution of the electron and hole density profiles that follow from these simulations are shown in Figure 4.2. The absence (Figure 4.2a-d) and presence (Figure 4.2e-f) of a doping dependent mobility was studied as well as the effect of the ion mobility. The doping dependent mobility that is shown in Figure 4.1b (model) was used in these simulations. It will be shown below that the qualitative behavior in these simulations only depends on the relative values of the mobilities of the electronic and ionic species.

Starting from $t$ = 0, the processes in these devices are similar: anions and cations move towards the anode and cathode respectively forming EDLs (see supplemental Figure 4.9 in paragraph 4.5). When the resultant potential drop at the interfaces has become similar in size to the injection barriers, charge carriers start being injected. During EDL formation, the anion and cation concentrations in the bulk remain equal to maintain charge neutrality. Only at the electrodes this neutrality is broken because of depletion of one type of ion and accumulation of the other. During the subsequent injection of either electrons or holes, a third type of charge carrier comes into play. To maintain charge neutrality in the bulk, the anion and cation densities start to differ. At this stage, where injection of carriers is initiated, differences in the transient processes arise when ion or carrier mobilities are altered.

When interpreting the results shown in Figure 4.2, the discussion focuses on two characteristics: (1) the collision of the p-type and n-type doped regions and (2) the saturation of doping at each grid-point after the doping front has passed. Here, doping is saturated when a doping fraction of approximately 0.2-0.3 is reached, i.e. at a charge density of $2\text{-}3{\cdot}10^{-1}{\cdot}0.3$ nm$^{-3}$ in Figure 4.2. Note that in experiments, strong PL quenching is observed when the doping density reaches a threshold level; PL quenching is not necessarily linear with doping fraction.[1]

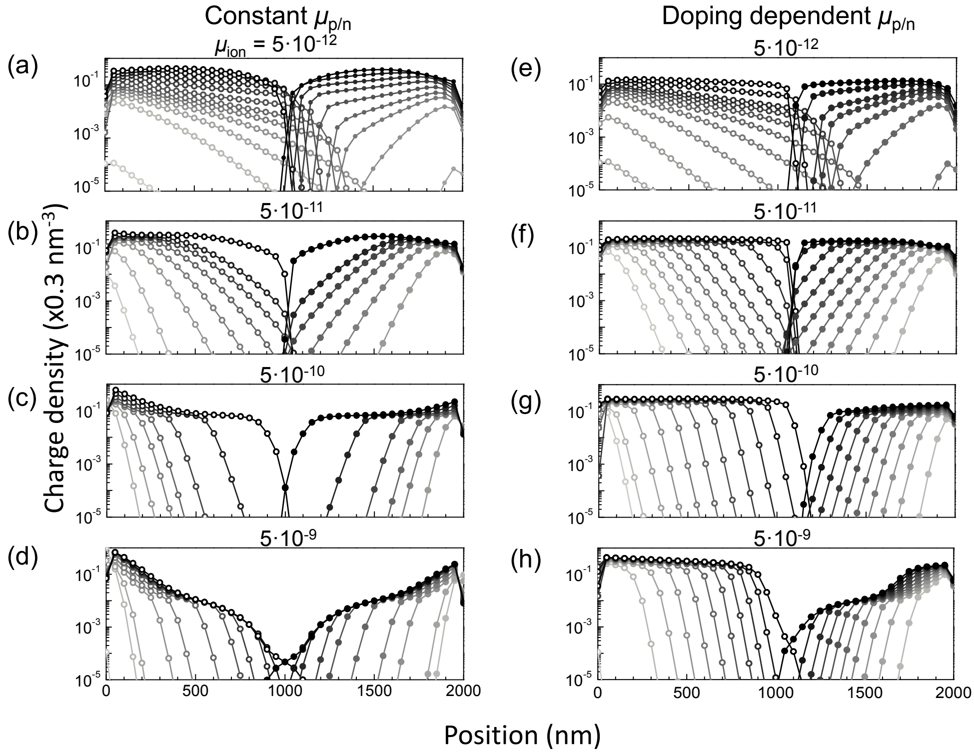

**Figure 4.2 Transient carrier concentration profiles in LECs for (a)-(d) a constant $\mu_{p/n}$ equal to $5\cdot10^{-11}$ $m^2$ $V^{-1}$ $s^{-1}$ and (e)-(h) a doping dependent $\mu_{p/n}$ (see Figure 4.1b, model). Holes (open circles) are injected from the left and electrons (closed circles) from the right. The corresponding values of $\mu_{ion}$ are shown at the top of each panel expressed in $m^2$ $V^{-1}$ $s^{-1}$. The movement in time is expressed by the color change of the graphs from light gray to black. The final black curves are not the steady-state distributions but represent the moment the fronts meet.**

As a first example, we show in Figure 4.2b, the time evolution of the doping of the active layer assuming a doping-independent mobility of $\mu_{ion} = \mu_{p/n} = 5\cdot10^{-11}$ $m^2$ $V^{-1}$ $s^{-1}$. No sharp transitions are observed from doped to undoped regions: the doped regions already connect to each other while the doping density in roughly half the cell is far from saturated. However, in case of a doping dependent mobility $\mu_{p/n}$ (Figure 4.2f), the transition between the doped and undoped regions is sharper; the increased mobility of electrons and holes injected behind the front results in a faster saturation of doping compared to the progression of the doped region through the intrinsic region. The enhanced mobility behind the front also ensures a sufficient supply of carriers towards the fronts to prevent a decrease of the doping rate at the front. In contrast to the situation for a doping-independent mobility (Figure 4.2b), the time needed to completely dope the active layer in Figure 4.2f is limited by the front progression and not by the process of saturating the doping behind the fronts.

When the ion mobility is decreased by a factor 10 ($\mu_{\text{ion}} = 5{\cdot}10^{-12}$ m$^2$ V$^{-1}$ s$^{-1}$, Figure 4.2a and e) both doping regions come into contact even before doping has saturated at any position in the cell. No sharp transitions are observed from doped to undoped regions. These observations are the result of the relative immobility of the ions compared to the electrons and holes, which mainly hampers the actual doping of the active layer. Since $\mu_{\text{p/n,0}} > \mu_{\text{ion}}$ progression of the electronic charges through the device is fast relative to the actual doping at any fixed position in the device. Consequently there is a small doping density difference between the front and the doped regions just behind it, which results in only a minor carrier mobility enhancement behind the front. Therefore, the carriers behind the front are not propelled towards the front as was observed in Figure 4.2f. For that reason, the two doping fronts have already moved across the active layer while the doping process is far from finished. After the doped regions have met, doping saturates more or less evenly throughout the LEC. This result indicates that if $\mu_{\text{ion}} < \mu_{\text{p/n,0}}$ homogeneous doping of the active layer is found rather than doping by doping fronts.

On the other hand, when the ion mobility is increased by a factor 10 ($\mu_{\text{ion}} = 5{\cdot}10^{-10}$ m$^2$ V$^{-1}$ s$^{-1}$, Figure 4.2c and g), sharp doping fronts are formed for both a density dependent and a density independent $\mu_{\text{p/n}}$. The origin of the formation of these sharp fronts is however different as compared to the fronts formed in Figure 4.2f. In case a constant $\mu_{\text{p/n}}$ is chosen (Figure 4.2c) anions and cations always move faster than the injected carriers. As a result, the available anions and cations are able to electrostatically compensate the injected carriers relatively fast. As shown in the previous chapter in Figure 3.3d,[12] in the absence of injected carriers, because of e.g. relatively poor carrier injection, the ions tend to screen the bulk from the electric field. Here this tendency is observed during doping of the active layer: the electric field $E_{\text{i}}$ in the intrinsic region, that drives the doping front, is reduced by ion screening (see e.g. the slope of the potential at $x$ = 1000 nm for the light gray graphs in supplemental Figure 4.7c at the last paragraph of this chapter). Accordingly the carriers at the fronts are slowed down, while newly injected carriers in the already doped regions are accelerated because of a locally enhanced field. (see the slope of the potential at $x$ = 300 for the dark gray graphs in supplemental Figure 4.7c). This combination results in a sharp doping front. For a doping dependent mobility (Figure 4.2g), the same behavior of the ions is observed; ions accumulate at the front to screen the intrinsic region from the applied field. In addition, in this case the doping-enhanced mobility of injected carriers is larger than the ion mobility. Hence, these carriers can more easily approach the carriers at the front, which further sharpens the doping front in Figure 4.2g as compared to Figure 4.2c. (see supplemental Figure 4.8 for an evaluation of the sharpness of the n-type doping front during propagation).

In case the ion mobility is increased even more, i.e. $5{\cdot}10^{-9}$ $m^2$ $V^{-1}$ $s^{-1}$, the effects of a reduction of $E_i$ become more pronounced, as shown by relatively large doping density close to the electrodes in Figure 4.2d and h. Furthermore, the strong depletion of ions from the intrinsic region becomes a limiting factor. The regions close to the electrodes absorb most of the ions and hence they are not directly available for electrochemical doping. Consequently, the doping fronts slow down as no more ions are available in the intrinsic region. After that, ions from the already doped regions are transported backwards to the front to complete the doping. (the ion density profiles are shown in supplemental Figure 4.9). This backward ion transport is driven by the inward movement of electrons and holes.

It is important to point out that the steady-state carrier distributions and potential profiles are the same for each ion mobility as the ion mobility only affects the transient characteristics in LECs, not the steady-state characteristics.[12] The graphs in Figure 4.2 are plotted until the p-i-n junction has formed, hence the black curves do not represent complete equilibrium.

The positions of the sharp doping fronts observed in Figure 4.2 are plotted vs. time in Figure 4.3a. For each doping profile in Figure 4.2 the position at which the doping density equaled a constant, arbitrarily chosen value of $3{\cdot}10^{-3}$ $nm^{-3}$ was taken to produce Figure 4.3a. A different choice of this value hardly affects the doping front propagation profiles in Figure 4.3a, because the shape of the doping density profile is more or less constant during doping front propagation (see e.g. Figure 4.2g). The observed acceleration (superlinear behavior in Figure 4.3a,c) or deceleration (sublinear behavior) of the sharp doping fronts can be related to the origins of sharp front formation as discussed above. A reduction of the electric field and/or ion density in the intrinsic region was found to underlay the fronts observed in panels c, d, g, and h of Figure 4.2. Both these effects directly lead to a deceleration of the doping front. Consequently, newly injected carriers have time enough to dope the region behind the front and thus maintain a constant doping density from the electrodes towards the fronts, which is perceived as a sharp doping front. In case sharp doping fronts are formed because the mobility of newly injected carriers is enhanced (Figure 4.2f), the doping front velocity is observed to slightly increase with time because of the large supply of injected carriers. These effects or combinations of these effects can be observed in the front position vs. time plots in Figure 4.3a. Consider the front position vs. time graphs for a doping-dependent mobility (circles). For $\mu_{ion} = 5{\cdot}10^{-9}$ $m^2$ $V^{-1}$ $s^{-1}$ (light gray circles) the front speed declines because of a reduction of both $E_i$ and ion density in the intrinsic region. For $\mu_{ion} = 5{\cdot}10^{-10}$ $m^2$ $V^{-1}$ $s^{-1}$ (dark gray circles) the front speed is constant, being the sum of opposite effects: a reduction of $E_i$ and an enhancement of $\mu_{p/n}$ in the doped regions. For $\mu_{ion} = \mu_{p/n,0} = 5{\cdot}10^{-11}$ $m^2$ $V^{-1}$ $s^{-1}$ (black circles), the front speed increases, because $\mu_{p/n}$ is enhanced. The latter, an increasing front speed, is in agreement with published experimental data, see Figure 4.1a.[4] In case $\mu_{p/n}$ is doping-independent (squares), the front speed mainly declines because of the reduction of $E_i$ and ion density in the intrinsic regions.

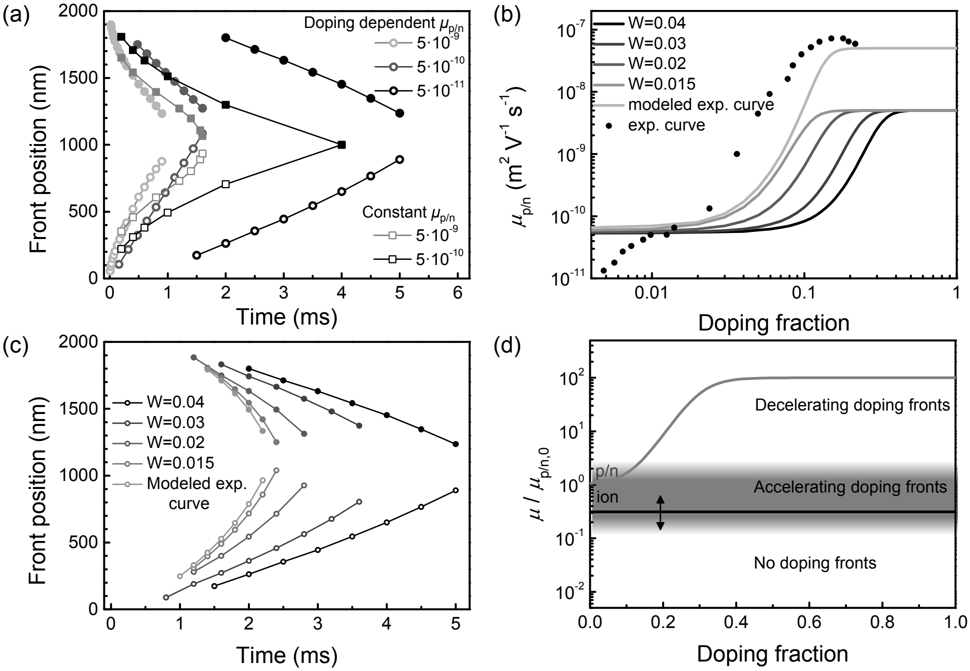

**Figure 4.3 Calculated doping front position vs. time plots in LECs for different carrier mobility functions. The p- and n-type doping fronts are denoted by the open and closed circles respectively. (a) The doping front propagation for different values of $\mu_{ion}$ as indicated in the legend in m$^2$ V$^{-1}$ s$^{-1}$. The circles and squares correspond to a density dependent and independent $\mu_{p/n}$ respectively. (b) Different doping dependent mobility functions for which $\mu_0$ = 5·10$^{-11}$ m$^2$ V$^{-1}$ s$^{-1}$, $\mu_1$ = 5·10$^{-9}$ m$^2$ V$^{-1}$ s$^{-1}$, $W$ = 0.04/0.03/0.02/0.015 and $f_0$ = 0.3/0.22/0.14/0.10. For the modeled experimental curve $W$ = 0.015, $f_0$ = 0.13 and $\mu_1$ = 5·10$^{-8}$ m$^2$ V$^{-1}$ s$^{-1}$ were taken. (c) The doping front propagation for the different doping dependent mobility functions shown in (b). (d) Schematic of the ion mobility criteria with respect to the doping dependent electron and hole mobility (gray line) that result in the formation of accelerating doping fronts in LECs during switch-on.**

To study the effect of a sharper mobility increase as a function of doping, simulations were performed in which parameters $W$ and $f_0$ in Equation (4.1) were decreased. The mobility curves are shown in Figure 4.3b. Simulations of the front propagation were performed for all these curves while $\mu_{ion}$ = 5·10$^{-11}$ m$^2$ V$^{-1}$ s$^{-1}$. The results are shown in Figure 4.3c. If the mobility increase becomes sharper with respect to an increased doping density, the time needed for both fronts to meet each other clearly decreases. Furthermore, also a larger acceleration of the fronts is observed. These observations are related to the enhanced carrier mobility at progressively lower doping levels: the higher carrier mobility behind the front results in an increased supply of carriers for doping at the fronts, enabling the front to move faster through the active layer. Also a simulation was performed with a doping dependency of the mobility that mimics the experimental mobility curve in Figure 4.1b (see 'modeled exp. Curve' in Figure 4.3b). The resultant front position vs. time curve is shown in Figure 4.3c. This result was normalized and plotted in Figure 4.1a to enable comparison with the experiment.[4] A striking similarity is observed, constituting the validity of the model. Furthermore, it shows that the chosen mobility dependency seems qualitatively correct in describing front propagation in LECs. Furthermore, it was checked by additional simulations that the results do not qualitatively depend on the ion concentration or the device length. Quantitatively, an increase of $c_0$ results in faster movement of the fronts through the device. This effect originates from the availability of more ions to dope the organic semiconductor, thereby increasing the rate of doping behind the fronts. The consequently increased doping density results in an increased supply rate of carriers towards the fronts that effectively increases the doping front propagation.

The phase diagram shown in Figure 4.3d summarizes the results shown in Figure 4.2 and Figure 4.3a-c. In the diagram the doping dependent $\mu_{p/n}$ is shown relative to $\mu_{p/n,0}$. Dependent on the ratio between $\mu_{ion}$ and $\mu_{p/n,0}$, three regions can be identified: (1) for $\mu_{ion} << \mu_{p/n,0}$ no doping fronts are formed; (2) for $\mu_{ion} \approx \mu_{p/n,0}$ accelerating doping fronts are formed; and (3) for $\mu_{ion} >> \mu_{p/n,0}$ decelerating doping fronts are formed. For a constant $\mu_{p/n}$ the central region disappears so either no or decelerating doping fronts are formed. As already mentioned, experiments on planar LECs have indicated the formation of doping fronts during turn-on that accelerate when closing in on each other.[3] Combination of these experimental results with our numerical modeling strongly indicates that $\mu_{p/n}$ depends similarly on doping and that $\mu_{ion}$ is of the same order as $\mu_{p/n,0}$.

From the simulations presented in Figure 4.2e-h current vs. time plots were made to study the transient behavior in LECs with a doping dependent mobility for varying ion mobility. A typical plot is shown in Figure 4.4. The ionic and electronic contributions to the current are plotted separately as well to make the total current transient more comprehensive. At $t$ = 0, the current is completely carried by the ions. These ions first form the EDLs at the electrodes, resulting in injection of holes (marked with arrow 1 in Figure 4.4) and electrons (arrow 2). Electron injection is delayed compared to hole injection because of the larger injection barrier that needs to be overcome by formation of a larger EDL. This injection results in an increased electronic current. Following this injection, the active layer is doped, during which the ionic current is observed to slowly decrease and the electronic current to increase. The initiation of recombination (diamond symbols in Figure 4.4) indicates that the doping fronts have met (arrow 3). After this, both recombination and the electronic current increase.[14] This indicates the further doping of the active layer until at some time the current as well as the recombination suddenly drop (arrow 4). This is related to a change in the electric field distribution after which the externally applied electric field becomes concentrated in the recombination region rather than being distributed over the entire active layer: The p-i-n junction has formed. Hence, meeting of the doping front does not coincide with but precedes the formation of a p-i-n junction. The appearance of a sharp potential drop in the p-i-n junction arises from the anions and cations being completely removed from the junction region.[12] These ions have been used to maximize doping in the surrounding regions. Because of the relatively small density of carriers in the recombination region, the conductivity is relatively low compared to the doped regions. Therefore, in order to fulfill current conservation, a larger field is required in the junction region rather than the doped regions.

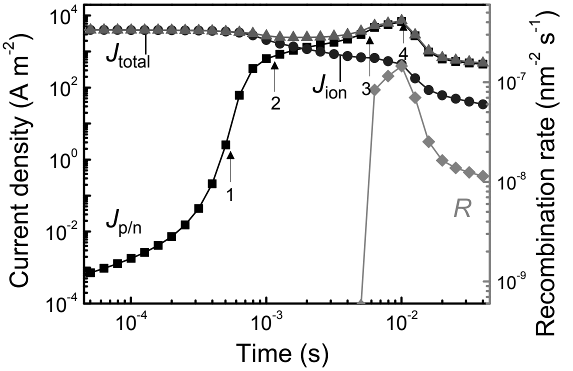

**Figure 4.4 Calculated *J*, *t* and *R*, *t* characteristics in an LEC for $\mu_{ion}$ = $5{\cdot}10^{-11}$ m$^2$ V$^{-1}$ s$^{-1}$ (c.f. Figure 4.2f) and a doping dependent $\mu_{p/n}$ (c.f. Figure 4.1b). The square, circle, triangle and diamond graphs represent the total current density $J_{total}$, the ion current density $J_{ion}$, the electron and hole current density $J_{p/n}$ and the recombination rate *R* respectively. 1, 2, 3, and 4 refer to initiation of hole injection, initiation of electron injection, front meeting and formation of a light-emitting p-i-n junction respectively.**

The time between the application of a bias and the injection of holes, the injection of electrons, the doping front meeting and the p-i-n junction formation is plotted in Figure 4.5 as a function of $\mu_{ion}$ relative to $\mu_{p/n,0}$. The results in Figure 4.5a and b correspond, respectively, to simulations with a constant and doping dependent $\mu_{p/n}$. The time is normalized by the time an ion needs to travel across the device in the presence of an (average) field equal to $(V_{bias} - E_g)/L$. A horizontal line in these graphs indicates that the time needed for the corresponding process depends linearly on $\mu_{ion}$ and bias. Accordingly, the graphs show that the time needed for the initiation of electron and hole injection linearly depends on $\mu_{ion}$. This can also be easily deduced from the fact that injection of carriers is directly related to the formation of EDLs, which results from a reorganization of the ion density across the device. The meeting of the doping fronts that follows after injection of carriers is however not linearly related to $\mu_{ion}$. Doping of the active layer is related to both $\mu_{p/n}$ and $\mu_{ion}$. This is unlike the conclusion drawn by Robinson *et al.* that mainly ionic movement in the intrinsic region determines the time needed to dope the active layer.[4] Rather, the doping front propagation is determined on one hand by the electron/hole transport in the doped regions and at the doping front, and on the other hand by the ion transport in the intrinsic region. Formation of a light-emitting p-i-n junction (process 4) is observed to be linearly dependent on $\mu_{ion}$ at small values of $\mu_{ion}$ / $\mu_{p/n,0}$. Dependent on the presence or absence of a doping dependence, this linear dependence exists in Figure 4.5a for $\mu_{ion}$ / $\mu_{p/n,0} < 1$ and in Figure 4.5b for $\mu_{ion}$ / $\mu_{p/n,0} < 10$. This process is namely related to ion depletion from the recombination zone, which causes the linear dependence in $\mu_{ion}$. This ion depletion can only occur when the transfer of mobile anions (cations) from the n-type (p-type) doped region to the p-type (n-type) doped region is completed. For this to complete, the largest distance ions need to travel in a mostly symmetric device is a bit more than half the device length. A value of $t_i \cdot \mu_{ion} \cdot (V-E_g) \cdot L^{-2} \sim 0.6$ is found in the modeling shown in Figure 4.5 (black graphs, numbered 4). For large $\mu_{ion}$ / $\mu_{p/n,0}$, corresponding to slow electronic carriers, the formation of a light-emitting p-i-n junction is no longer limited by ion depletion, but is limited by the meeting of the doping fronts. In this case, the ions are already depleted from the recombination region before the fronts have met, which is determined by the slow electronic charge carriers.

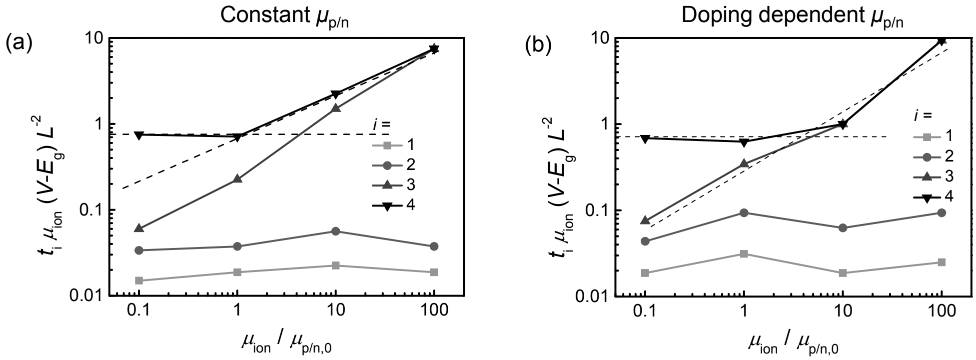

**Figure 4.5 Time scale comparison for four characteristic processes in LECs for different values of $\mu_{ion}$ / $\mu_{p/n,0}$ in case of (a) no doping dependent carrier mobility and (b) a doping dependent carrier mobility. 1, 2, 3, and 4 (c.f. Figure 4.4) refer to initiation of hole injection, initiation of electron injection, front meeting and formation of a light-emitting p-i-n junction, respectively. The dashed lines highlight the transition in behavior of the time needed for junction formation (4).**

The transition point (Figure 4.5a: $\mu_{ion}$ / $\mu_{p/n,0} \approx 1$; Figure 4.5b: $\mu_{ion}$ / $\mu_{p/n,0} \approx 5\text{-}10$) at which the switch-on time in LECs becomes dependent on the doping front propagation is related to the choice of the doping dependency of $\mu_{p/n}$. In the simulations from which Figure 4.5b is constructed, the doping fractions in case doping is nearly saturated lies in between 0.2

and 0.3, which can be translated to $\mu_{p/n} \approx 10 \cdot \mu_{p/n,0}$ following Eq. (4.1). This effective mobility in the doped regions determines the transition point. In case of a doping independent $\mu_{p/n}$, the effective mobility is equal to $\mu_{p/n}$ and the transition point is thus expected at $\mu_{ion} / \mu_{p/n,0} = 1$. This is indeed the case in our model (see Figure 4.5a).

In the previous chapter[11] results on a planar ion rich LEC were presented in which a significant amount of time was observed between initiation of light emission (at $t = 10$ s), i.e. meeting of the doping fronts, and the formation of a p-i-n junction (at $t = 20$ s). Comparison of those results (Figure 3.1) with the modeling presented here in Figure 4.5b indicates that $\mu_{ion} / \mu_{p/n,0} < 10$, as the 10 s time difference proves that p-i-n junction formation was not limited by doping front propagation. Therefore, the switch-on time of this LEC can be used to estimate the ion mobility, as $t_{switch-on}\mu_{ion}(V_{bias} - E_g)L^{-2} \approx 0.6$ must hold. For $L = 100$ µm and $V_{bias} = 8$ V and $E_g \approx 2$ eV, the ion mobility is then estimated to be $5 \cdot 10^{-11}$ m$^2$ V$^{-1}$ s$^{-1}$ at a temperature of 323 K. The conclusion that $\mu_{ion} / \mu_{p/n,0} < 10$ is also consistent with the discussion of Figure 4.3b since in these devices accelerating doping fronts are typically observed. More particularly, from the parameter window for accelerating doping fronts it can, with some caution, be estimated that the electronic charge carrier mobility in PPV-based LECs is also of the order of $5 \cdot 10^{-11}$ m$^2$ V$^{-1}$ s$^{-1}$, which is surprisingly close to typical values for pure PPV derivatives.[15-16] A further comparison can be done between the experimental results on the planar ion rich LEC in the previous chapter and the simulation results shown in Figure 4.2f, Figure 4.4 and supplemental Figure 4.7f. First of all the potential profile evolution is similar: The potential distribution (see supplemental Figure 4.7f) hardly changes during doping front propagation. Also the current response to an applied bias voltage (see Figure 4.4) is the same in both experiment and model. These results further prove that the experiment is adequately modeled.

One deviating experiment in literature is reported in which the doping fronts were found to have a constant speed.[17] Gao et al. did measurements on such an LEC, which has an inter-electrode distance of 2 mm and is biased at 200 V. Our modeling shows that in case a constant front speed is encountered, $\mu_{ion}$ must be large relative to $\mu_{p/n,0}$ (see Figure 4.2g and Figure 4.3a). Inspection of Figure 4.5b furthermore shows that the doping process in such an LEC is not limited by the ion redistribution, but by the electronic carrier mobility.

A side-note on the mobility discussion above is that rather than a single, constant ion mobility, a range of ion mobilities is expected in such LECs, which further may differ for anions and cations. The determined ion mobility therefore applies to the most mobile fraction of ions. This hypothesis is in agreement with the finding in Ref. 11 that the actual amount of *mobile* ions is far less than the amount of ions put into the active layer.

## 4.4 Conclusions

Numerical modeling has shown that the time needed for LECs to electrochemically dope the active layer and switch-on depends on a combination of the ion mobility, the electron/hole mobility, the applied bias voltage and the thickness of the active layer.

Regarding the doping process three regimes were identified, related to the mobilities of all present charge carriers. If $\mu_{\text{ion}} > \mu_{\text{p/n}}$, the active layer is doped by decelerating doping fronts sweeping the active layer, whereas if $\mu_{\text{ion}} < \mu_{\text{p/n}}$ the active layer is doped homogeneously across the complete device. Only in case a doping dependent $\mu_{\text{p/n}}$ is chosen in addition to $\mu_{\text{ion}}$ being approximately equal to $\mu_{\text{p/n}}$ in the undoped state ($\mu_{\text{p/n,0}}$), accelerating doping fronts are formed.

The switch-on time in LECs is shown to become independent of $\mu_{\text{p/n}}$ when the ratio between $\mu_{\text{ion}} / \mu_{\text{p/n}}$ becomes small enough. For a doping independent $\mu_{\text{p/n}}$ this critical ratio is unity, whereas in case of a doping dependent $\mu_{\text{p/n}}$, $\mu_{\text{ion}} < {\sim}10 \cdot \mu_{\text{p/n,0}}$. Generally the latter occurs in planar LECs where accelerating doping fronts are often observed. This enables the extraction of the ion mobility from the switch-on time of LECs.

# 4.5 Supplemental figures

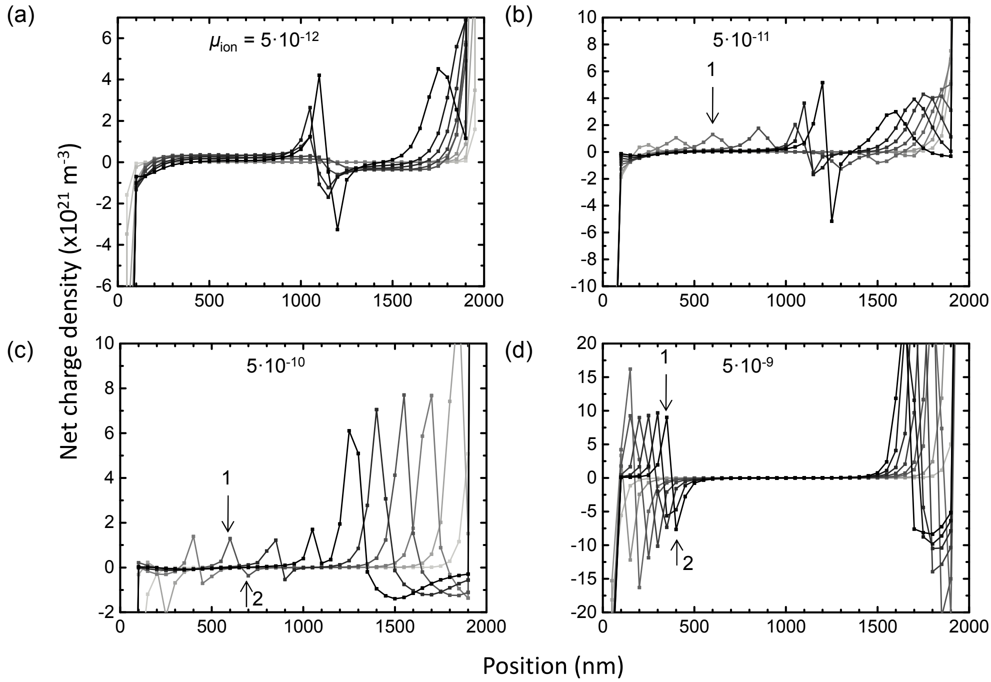

**Figure 4.6 Calculated transient net charge density profiles in LECs from start to end of the doping front propagation (c.f. Figure 4.2). Simulations were done with a doping dependent $\mu_{p/n}$. The corresponding values of $\mu_{ion}$ are shown at the top of each graph expressed in m$^2$ V$^{-1}$ s$^{-1}$. The movement in time is expressed by the color change of the graphs from light gray to black. The arrows indicate a surplus of electronic carriers (1) and ionic carriers (2).**

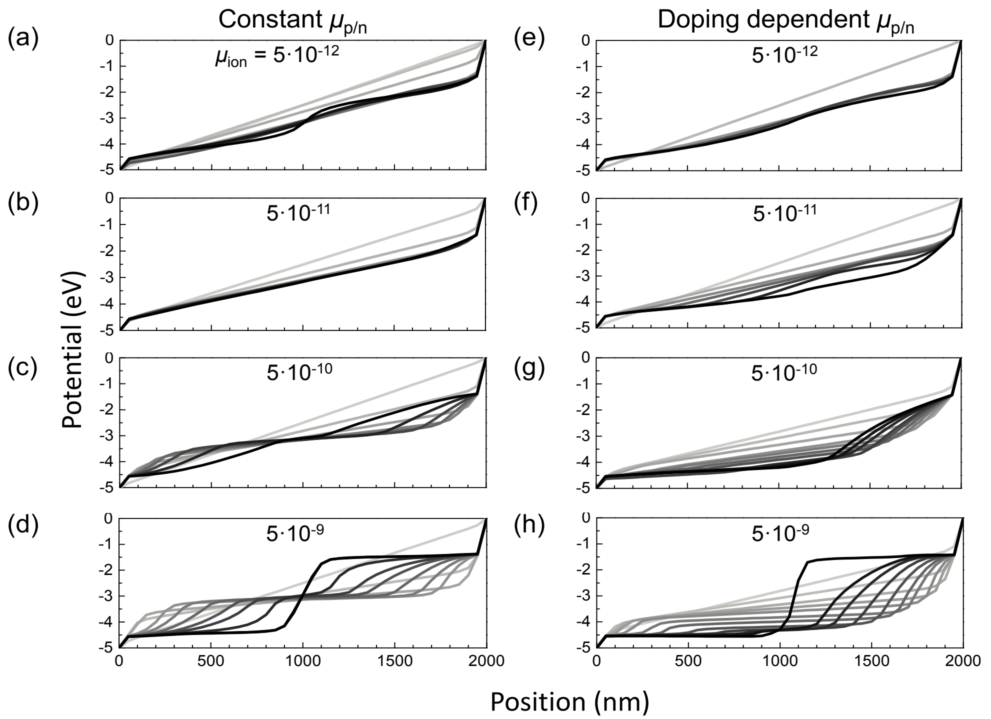

**Figure 4.7 Calculated transient potential profiles in LECs from start to end of the doping front propagation (c.f. Figure 4.2). Simulations were done with (a)-(d) a constant $\mu_{p/n}$ and with (e)-(h) a doping dependent $\mu_{p/n}$. The corresponding values of $\mu_{ion}$ are shown at the top of each graph expressed in $m^2 V^{-1} s^{-1}$. The movement in time is expressed by the color change of the graphs from light gray to black.**

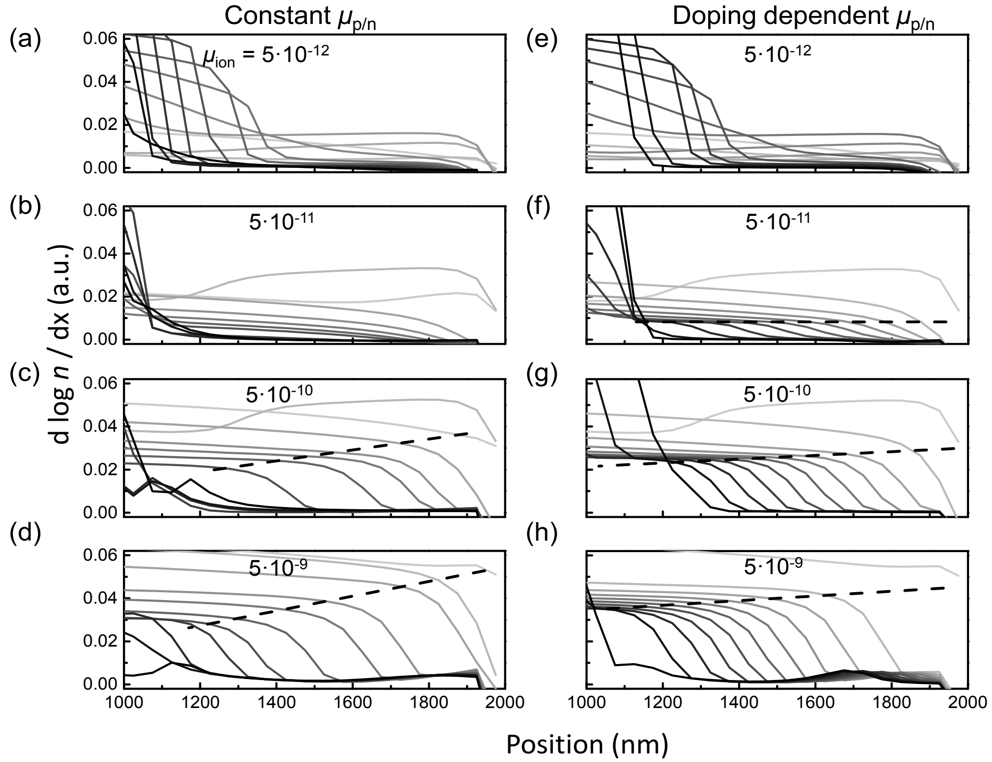

**Figure 4.8 Calculated sharpness of the n-type doping front during doping front propagation (c.f. Figure 4.2). Simulations were done with (a)-(d) a constant $\mu_{p/n}$ and with (e)-(h) a doping dependent $\mu_{p/n}$. The corresponding values of $\mu_{ion}$ are shown at the top of each graph expressed in $m^2 V^{-1} s^{-1}$. The movement in time is expressed by the color change of the graphs from light gray to black. The front sharpness is calculated by differentiating the logarithm of the electron density, *n*, as shown in Figure 4.2 with respect to the position. Dashed lines are added to graphs (c), (d), (f)-(h) to indicate the sharpness (magnitude) and position (where the line crosses the data) of the doping front during propagation.**

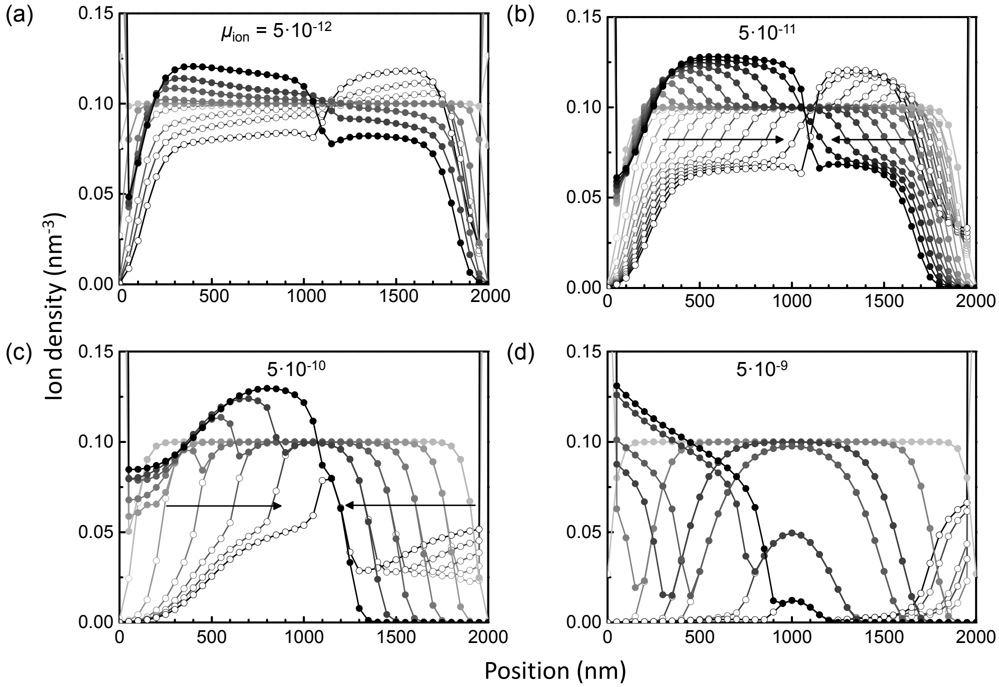

**Figure 4.9 Calculated transient ion density profiles in LECs during doping front propagation for a doping dependent $\mu_{p/n}$. The corresponding values of $\mu_{ion}$ are shown at the top of each graph expressed in $m^2V^{-1}s^{-1}$. The movement in time is expressed by the color change of the graphs from light gray to black. The closed and open circles represent the anion and cation density respectively. Arrows indicate the time progression as well.**

# References

[1] J. Gao, J. Dane, Appl. Phys. Lett. 84 (2004) 2778.

[2] A. L. Holt, J. M. Leger, S. A. Carter, J. Chem. Phys. 123 (2005) 044704.

[3] J. H. Shin, N. D. Robinson, S. Xiao, L. Edman, Adv. Funct. Mater. 17 (2007) 1807.

[4] N. D. Robinson, J. H. Shin, M. Berggren, L. Edman, Phys. Rev. B 74 (2006) 155210.

[5] H. Shimotani, G. Diguet, Y. Iwasa, Appl. Phys. Lett. 86 (2005) 022104.

[6] J. Gao, J. Dane, J. Appl. Phys. 98 (2005) 063513.

[7] D. Hohertz, J. Gao, Adv. Mater. 20 (2008) 3298.

[8] J. F. Fang, Y. L. Yang, L. Edman, Appl. Phys. Lett. 93 (2008) 063503.

[9] N. D. Robinson, J. F. Fang, P. Matyba, L. Edman, Phys. Rev. B 78 (2008) 245202.

[10] M. Modestov, V. Bychkov, G. Brodin, D. Valiev, M. Marklund, P. Matyba, L. Edman, Phys. Rev. B 81 (2010) 081203.

[11] S. van Reenen, P. Matyba, A. Dzwilewski, R. A. J. Janssen, A. Edman, M. Kemerink, Adv. Funct. Mater. 21 (2011) 1795.

[12] S. van Reenen, P. Matyba, A. Dzwilewski, R. A. J. Janssen, L. Edman, M. Kemerink, J. Am. Chem. Soc. 132 (2010) 13776.

[13] J. C. deMello, N. Tessler, S. C. Graham, R. H. Friend, Phys. Rev. B 57 (1998) 12951.

[14] J. Gao, Y. F. Hu, J. Am. Chem. Soc. 133 (2011) 2227.

[15] E. Lebedev, T. Dittrich, V. PetrovaKoch, S. Karg, W. Brutting, Appl. Phys. Lett. 71 (1997) 2686.

[16] E. Pinotti, A. Sassella, A. Borghesi, R. Tubino, Synth. Met. 122 (2001) 169.

[17] J. Dane, C. Tracy, J. Gao, Appl. Phys. Lett. 86 (2005) 153509.

# **Chapter 5** Dynamic processes in stacked polymer LECs

---

*The operational mechanism of polymer LECs in sandwich geometry is studied by admittance spectroscopy and numerical modeling. Capacitance and conductance at different frequencies and bias voltages indicate the conduction of ions, electric double layer formation and p-i-n junction formation which is all in line with the electrochemical doping model. Numerical modeling shows that impedance measurements cannot be used to determine the actual junction width. In addition, the long settling time of polymer LECs is shown to be due to a slow process of salt dissociation that continues after p-i-n junction formation, rather than ion conduction. This implies that in order to significantly decrease the response-time of LECs an electrolyte/salt combination with an as low as possible ion binding energy must be used.*

*Part of the work presented in this chapter has been published: S. van Reenen, R. A. J. Janssen, M. Kemerink, Adv. Funct. Mater. 22 (2012) 4547.

## 5.1 Introduction

The electrochemical doping model has been convincingly proved in the previous chapters for planar polymer LECs in which scanning Kelvin probe microscopy could be used to visualize the characteristic potential shape:[1-4] a p-i-n junction results in a high field in the intrinsic region and low field in the doped regions. LECs that are relevant for practical use have however a stacked structure, in which the active layer thickness is only a few hundreds of nanometers. This thickness difference forbids the direct translation of the electrochemical doping model from planar LECs to stacked LECs by simply reducing the thicknesses of the different regions. For instance, the recombination zone width found in planar LECs typically exceeds the layer thickness of stacked LECs.[3]

One method to study the operation mechanism in stacked LECs is impedance spectroscopy. As this method uses a time-dependent signal, it is possible to look separately at fast and slow processes in LECs. This makes impedance spectroscopy potentially an excellent technique to disentangle the various ongoing processes in operational LECs.[5-11] However, the data generated by this technique is generally rather complicated and difficult to interpret. The work done on impedance spectroscopy in LECs has so far mainly focused on the junction width during operation. In polymer LECs junction widths between 10% and 80% of the active layer have been reported.[6, 9] Furthermore, previous modeling studies to LECs were limited to steady-state.[4, 12-16] Recently a study on sandwich LECs was published by Munar *et al.* in which equivalent circuit modeling was used to shed light on the LEC impedance spectrum.[17] However, interpretation of such modeling results is complicated by the sometimes intransparent physical meaning of the components. In particular, (combinations of) space charge and transit time effects tend to give rise to 'inductive' responses that are hard to capture in equivalent RC networks.[6, 18]

Here impedance spectroscopy is combined with numerical drift-diffusion modeling of polymer light-emitting electrochemical cells in stacked or sandwich geometry. We demonstrate that the observations are fully consistent with the electrochemical doping model. Information regarding the electric double layers (EDLs), ion conduction and the junction region is obtained. Furthermore, our results show that the width of the recombination region cannot be simply extracted from the intermediate- or high-frequency capacitance: there is no abrupt transition from the doped regions to the intrinsic recombination region. The doping close to the junction region is not as dense as it is near the contacts. This can lead to a conductivity difference of a factor >10 throughout the doped regions. Moreover, we identify the dissociation of salt molecules into anions and cations as the slow process that is responsible for the characteristic long settling time of LECs.

## 5.2 Material and methods

*Device preparation*: For the conjugated polymer in the active layer of our sandwich LECs either poly[2-methoxy-5-(3’,7’-dimethyloctyloxy)-p-phenylene vinylene] (MDMO-PPV, $M_w > 1\cdot10^6$ g mol$^{-1}$, American Dye Source) or a phenyl-substituted poly(p-phenylene vinylene) copolymer (SY-PPV, Merck, catalogue number PDY-132), commonly termed “Super Yellow” was used. Poly(ethylene oxide) (PEO, $M_w = 5\cdot10^5$ g mol$^{-1}$, Aldrich) was used as received. The salt potassium trifluoromethanesulfonate ($KCF_3SO_3$, 98 %, Aldrich) was dried at 473 K under vacuum before use. MDMO-PPV (10 mg ml$^{-1}$) and SY-PPV (5 mg ml$^{-1}$) were dissolved in chloroform (> 99 %, anhydrous, Aldrich). PEO and $KCF_3SO_3$ were dissolved separately (10 mg ml$^{-1}$) in cyclohexanone (> 99 %, anhydrous, Aldrich). These solutions were mixed together in a weight ratio of PPV:PEO:$KCF_3SO_3$ = 1:1.35:0.25. These blend solutions were thereafter stirred on a magnetic hot plate at a temperature $T$ = 323 K for 5 h.

ITO patterned substrates were spin-coated with the blend solution at 800 rpm for 60 s, followed by 1000 rpm for 10 s after which they were dried on a hot plate at $T$ = 323 K for at least 1 h. The resulting active layer thickness was 200-250 nm for MDMO-PPV LECs and 100 nm for SY-PPV LECs, as determined by profilometry. Al electrodes were deposited by thermal evaporation under high vacuum on top of the spin-coated films. The final device area was 0.091 cm$^2$. All the above procedures, except for the cleaning of the substrates, were done in a glove box under $N_2$ atmosphere ([$O_2$] < 1 ppm and [$H_2O$] < 1 ppm) or in an integrated thermal evaporator.

*Electrical characterization*: A Keithley 2636a sourcemeter was used to drive the devices and measure the current. The brightness was measured with a luminance meter (LS-110 Konica-Minolta). A Solartron 1260 was used to perform complex admittance measurements on the LECs in the glove box at room temperature. After applying a bias, cells were allowed to settle for 1 minute before the admittance spectrum was measured. Each point (from 30 MHz to 1Hz) was measured during an integration time of 1 s. The rms-value of the AC voltage was 0.01 V.

*Computational details*: For the numerical simulations, the 1-dimensional model was used which is described in detail in Appendix A. An active layer of length $L$ = 200 nm was divided in $N$ = 99 discrete points. Devices with a bandgap $E_g$ = 2.4 eV were simulated during operation at a given bias voltage $V_{bias}$ until steady-state had been reached, recognized by a zero ion current. Simulations were run for devices with initial ion concentrations $c_0$ = 0.1 nm$^{-3}$. Unless stated otherwise, no binding energy was assumed between anions and cations. The electrodes were ionically-blocking and electrons and holes were injected from the contacts according to an empirical injection model that gives rise to field-dependent injection: the ‘modified Boltzmann model’ described in Appendix A.2. This model has the advantage that injection is not affected by grid-point spacing. The hole and electron injection barriers were set at 0.5 and 1.4 eV respectively to simulate an asymmetric device. Similar injection barriers are expected for PPV-type materials sandwiched between ITO and Al electrodes. Bimolecular electron-hole recombination was described as a Langevin process. In addition, we set the relative dielectric constant $\varepsilon$ = 4.5 and the temperature $T$ = 300 K. Energetic and spatial disorder in the system were implemented via the hole and electron mobilities that were described by a field- (see Appendix A.3) and density-dependent (see Appendix A.3, Eq. A.22) mobility model.[19] The field dependence is assumed to follow Poole-Frenkel behavior with exponential factor $\gamma = 2 \cdot 10^{-4}$ $\mathrm{m^{0.5}\,V^{-0.5}}$.[20-21] The parameters for the density dependence of the mobility were $f_0$ = 0.8, $W$ = 0.09, $\mu_0 = 1 \cdot 10^{-12}$ $\mathrm{m^2\,V^{-1}\,s^{-1}}$ and $\mu_1 = 1 \cdot 10^{-9}$ $\mathrm{m^2\,V^{-1}\,s^{-1}}$. The carrier mobility in the absence of field and doping was $\mu_{p/n} = 1 \cdot 10^{-12}$ $\mathrm{m^2\,V^{-1}\,s^{-1}}$. The anion and cation mobilities were chosen to be $\mu_{ion} = 1 \cdot 10^{-13}$ $\mathrm{m^2\,V^{-1}\,s^{-1}}$. To model the admittance spectrum (see also Appendix A.6), the LEC was first allowed to reach steady-state. After this, a voltage step of 0.01 V was applied and the resulting step response of the current was calculated. The complex admittance spectra were then derived by a Fast Fourier Transform of the derivative of the conductance. All simulations were started from a pristine device which only contained a homogeneously distributed amount of ions. After setting a specified bias voltage over the electrodes, the device was allowed to evolve in time, as determined by the processes described above. The parameters given above were used for all simulations presented in this chapter, unless stated otherwise.

## 5.3 Results and discussion

Complex admittance measurements were performed on sandwiched polymer LECs. The complex admittance $\hat{Y}$ can be decomposed in a real part, the conductance $G$, and an imaginary part, which is proportional to the capacitance $C$. Both $C$ and $G$ typically depend on the angular frequency $\omega$:

$$\hat{Y} = \frac{I_{ac}}{V_{ac}} = G(\omega) + i\omega C(\omega). \tag{5.1}$$

Here $I_{ac}$ and $V_{ac}$ are the AC current and voltage signal respectively. In the next paragraphs impedance measurements at a below-bandgap dc biases are discussed, which gives information on ion dynamics in pristine devices. Subsequently, measurements at above-bandgap dc biases are discussed, which gives information on the operational mechanism of stacked LECs.

### 5.3.1 Below-bandgap biases

Figure 5.1 shows the experimental and modeling results for LECs biased at 0 V. Figure 5.1a shows the conductance and capacitance in LECs biased at 0 V as a function of frequency.

The device under test is a pristine device, i.e. it has not been biased before. Therefore, only ions are present in the active layer and the presence of a significant amount of electronic carriers can be excluded. At high frequencies (>1 MHz) the conductance shows $f^2$ dependence which results from the displacement current.[6] At longer timescales a conductivity plateau (~10 kHz) is observed which is related to ion transport. At these frequencies the geometric capacitance, $C_{geo}$, is observed, being approximately 2 nF. Moving towards lower frequencies, an increase in capacitance is observed. This increase is related to the formation of electric double layers (EDLs). At these low frequencies (~10 Hz) the ions apparently have enough time to move towards the electrode interfaces where they are blocked. This results in the formation of EDLs, which resultantly remove the field in the bulk region. Consequently, the conductance starts to decrease at the same time scale at which EDLs start to form. The second conductance plateau (~1 Hz) is related to leakage current. A modeling result of the conductance and capacitance spectra is shown in Figure 5.1a as well, showing good agreement with the experiments. A total of 0.5 V drops over the active layer because of the built-in voltage. The latter results from the choice of electrode work functions. After EDL formation the potential drops only at the electrode interfaces leaving the bulk field-free.

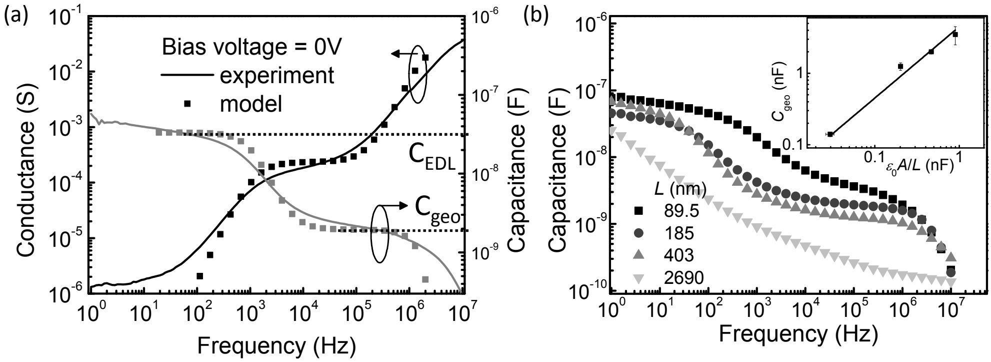

**Figure 5.1 (a) Conductance (black) and capacitance (gray) spectra of an MDMO-PPV at 0 V determined experimentally and by the numerical model. (b) Measured capacitance spectra of MDMO-PPV LECs with different thicknesses. The inset shows the geometric capacitance (taken as $C_{geo}$ at 0.1 MHz) as a function of device length to determine the dielectric constant: $\varepsilon_r = 4.5 \pm 0.3$.**

To obtain information about the EDLs in these devices, first the dielectric constant must be determined. This was done by measurement of the capacitance spectrum of LECs with different active layer thicknesses, $L$, as shown in Figure 5.1b. Here it is clear that at high frequency (~0.1 MHz) the geometric capacitance decreases with increasing thickness. Furthermore it is observed that the low frequency (~10 Hz) capacitance is not highly affected by a change of $L$. The inset of Figure 5.1b shows $C_{geo}$ as a function of $\varepsilon_0 A/L$, such that the slope of the fitted line equals the relative dielectric constant, $\varepsilon_r$, of the layer. Here it is assumed that the LEC behaves like a parallel plate capacitor at high frequencies. $\varepsilon_r$ is then determined to be 4.5±0.3. This value was used for the modeling results shown in Figure 5.1a.

**Table 5.1 Electric double layer properties from model and experiment. Underlined values are determined by calculations from the measured values (not underlined values).**

| | model | experiment |
|---|---|---|
| **$C_{EDL}$ (nF)** | 66.1 | 70±8 |
| **$C_{geo}$ (nF)** | 1.94 | 1.9±0.2 |
| **$L$ (nm)** | 200 | 200±10 |
| **$\underline{L_{EDL}\text{ (nm)}}$** | $\underline{5.87}$ | $\underline{5.4\pm1.7}$ |
| **Figure 5.1b: $L_{EDL}$ (nm)** | 6.00 | - |
| **$\underline{n/V\text{ (nm}^{-3})}$** | $\underline{0.0070}$ | $\underline{0.0089\pm0.001}$ |
| **Figure 5.1b: $n/V$ (nm$^{-3}$)** | 0.0050 | -- |

Now $\varepsilon_r$ is known it is possible to obtain information about the EDLs shown in Table 5.1. It is assumed that the capacitance of both EDLs, $C_{EDL}$, is more or less similar. Both capacitances are connected in series such that the EDL with the smallest capacitance, i.e. the thickest EDL, is dominant. The thickness of the EDLs $L_{EDL}$ can then be approximated as $L_{EDL} \cdot C_{EDL} = L \cdot C_{geo}$ must hold. The layer in between the sheet of ions and the electrodes is assumed to have the same dielectric constant as the rest of the film. From the experiment this procedure yields an EDL thickness of 5.4±1.7 nm and from the model 5.87 nm. Note that over this width the EDL potential drops. From $C_{EDL}$ also the charge density $n$ per unit voltage can be calculated that drops over the EDL: $n/V=C/(q \cdot A \cdot L)$, where $q$ is the elementary charge. A value of 0.007 and 0.009 nm$^{-3}$ V$^{-1}$ is determined for the model and experiment respectively. In the simulations, this value can also independently be determined from the anion and cation density difference near the electrodes. The potential drop over the electrodes is expected to become no more than 2 V during operation. Such a potential drop corresponds to a density of uncompensated ions of ~$14 \cdot 10^{-3}$ nm$^{-3}$. Such a density is only a small fraction of the average ion density, i.e. 0.1 nm$^{-3}$. This means that EDL formation to overcome injection barriers of even 2 V should not be problematic as sufficient ions are present in the active layer and that the thickness of the EDL is hardly affected by the actual potential drop over the EDLs. In general the model and experiment are in good agreement with each other (see Figure 5.1a and Table 5.1), suggesting that the described methods to determine both the ion density in the EDLs and the EDL thickness are valid.

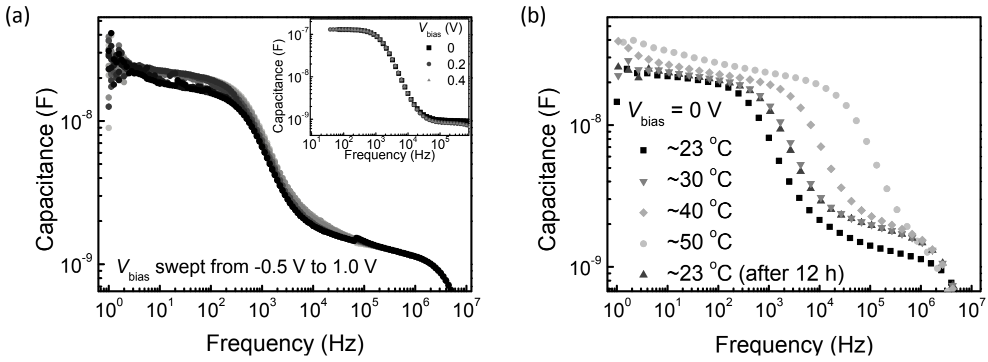

**Figure 5.2 Electric double layer capacitance at (a) different bias voltages below the bandgap and (b) different temperatures. The inset in (a) shows the modeling of the EDL capacitance at different voltages.**

The effect of a larger potential drop over the EDLs was studied by measurement of the capacitance spectra at different bias voltages below the bandgap of the polymer. These results are shown in Figure 5.2a. Clearly $C_{\mathrm{EDL}}$ is not affected by a different $V_{\mathrm{dc}}$, which corroborates the conclusion above that the density of ions in the EDL is small compared to the average ion density in the film. In the model the same result is obtained as shown in the inset. The effect of an elevated temperature was determined as well in Figure 5.2b. Here it is observed that $C_{\mathrm{EDL}}$ remains approximately constant when the temperature remains below the melting point (~60 °C) of the PEO. Close to this melting point the capacitance increases by a small fraction, indicating a decrease of the EDL thickness. This can be rationalized by assuming that ions can move more easily through the 'molten' PEO towards the electrode. After this the temperature was reduced and the former $C_{\mathrm{EDL}}$ was retrieved. The higher temperature clearly did not result in an irreversible change in the formation of EDLs. The frequency at which $C_{\mathrm{EDL}}$ transfers into $C_{\mathrm{geo}}$ will be discussed below.

The results shown in Figure 5.1a also give information about the ion conductivity, next to the already discussed dielectric constant and EDLs. First of all the presence of a conductance plateau (at ~10 kHz) indicates that at least a part of the salt is dissociated in the active layer, most likely in the PEO phase. The plateau value of the conductance can be used to determine the total conductivity of the ions, $\sigma$, in the active layer by

$$\sigma = q \cdot (\mu_a + \mu_c) \cdot c_0 = \frac{G \cdot L}{A}, \tag{5.2}$$

where $\mu_{\mathrm{a}}$ and $\mu_{\mathrm{c}}$ are the anion and cation mobility respectively and $c_0$ is the ion density. Extracted values for $(\mu_a + \mu_c) \cdot c_0$, which in turn can be used to make an estimate of the sum of the anion and cation mobilities, are shown in Table 5.2. This is done by a simple division by the ion density. For the model a similar value for the ion mobility is retrieved as was initially put into the simulation. For the experiment only a lower limit of the summed mobility can be determined as the amount of mobile ions has not been determined. From this follows a summed mobility of $10^{-13}$ $m^2$ $V^{-1}$ $s^{-1}$. Unfortunately, admittance measurements cannot be used for independent determination of the ion density and ion mobility. Aggregation of anions and cations as well as a difference in anion and cation density has furthermore not been taken into account and is subject of further study.

**Table 5.2 Ion conductivity properties extracted from model and experiment. Underlined values are determined by calculations from measured values (not underlined values).**

| | **model** | **experiment** |
|---|---|---|
| ***G* (S)** | $2.36 \cdot 10^{-4}$ | $(2.2 \pm 1.0) \cdot 10^{-4}$ |
| ***L* (nm)** | 200 | 200±10 |
| ***A* ($cm^2$)** | 0.091 | 0.091 |
| $\underline{q \cdot (\mu_a + \mu_c) \cdot c_0\ (V^{-1}\,s^{-1}\,m^{-1})}$ | $\underline{5.2 \cdot 10^{-6}}$ | $\underline{(4.8 \pm 2.0) \cdot 10^{-6}}$ |
| **$c_0$ ($nm^{-3}$)** | 0.1 | 0.3 |
| $\underline{\mu_a + \mu_c\ (m^2\,V^{-1}\,s^{-1})}$ | $\underline{3.04 \cdot 10^{-13}}$ | $\underline{(1.0 \pm 0.6) \cdot 10^{-13}}$ |
| **$\mu_a + \mu_c$ ($m^2\,V^{-1}\,s^{-1}$)** | $2.92 \cdot 10^{-13}$ | ? |

Temperature dependent measurements of the conductivity are shown in Figure 5.3, represented as loss-frequency plots. The loss is determined by of the ratio of the conductance and the frequency of the AC signal at which it was measured. A strong dependence on temperature is found. The first measurement at room temperature shows a clear peak at $10^3$ Hz. Subsequent measurements show a strong increase at low frequency which is attributed to leakage (c.f. Figure 5.1a). Therefore the other peaks become shoulders on the larger leakage peak; the effect of the temperature on the conductance is nevertheless still clear. The loss peak moves towards higher frequencies for higher temperatures whereas the peak height remains constant. At ~50 $^{o}$C the ion conductance has increased by 2 decades as compared to RT. Similar temperature effects on the conductivity have been reported by Torell et al.[22] on PEO-based NaTf polymer electrolytes. In particular, they showed that mainly the mobility is affected by a change in temperature, whereas the ion density even slightly decreases at higher temperatures. Combined with the results in Figure 5.3a this indicates that the ion mobility in LECs is strongly temperature dependent. In Figure 5.3b modeling results are shown to study the effect of the ion mobility and mobile ion density on the loss spectrum of the LEC. In line with the preceding discussion, the calculated loss spectrum moves to higher frequencies without substantial changes in peak height for increasing ion mobility. Reduction or increase of the mobile ion density has a less pronounced effect on the peak position, and does strongly affect the loss peak height. In the experiment the peak height is observed to be constant.

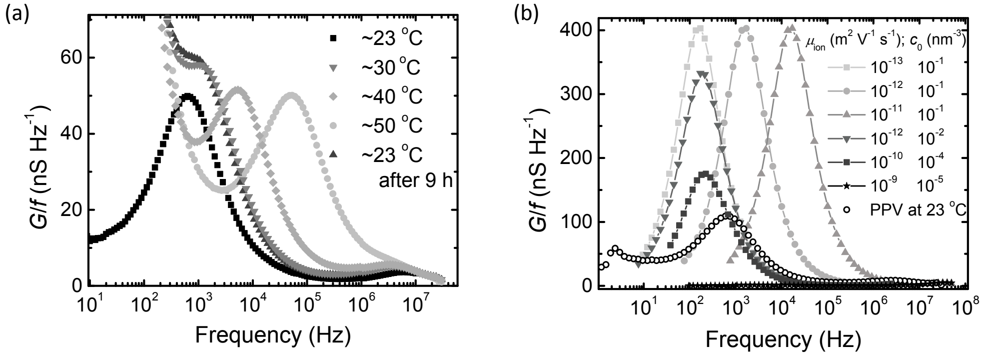

**Figure 5.3 (a) The loss (i.e. conductance/frequency) in MDMO-PPV LECs at different temperatures. (b) Modeled effect of ion mobility and ion density on the loss spectrum in LECs.**

### 5.3.2 Above-bandgap biases

Complex admittance spectra of a typical MDMO-PPV:PEO:$KCF_3SO_3$ LEC at multiple bias voltages are shown in Figure 5.4. Already at $V_{\text{bias}}$ = 2 V the admittance spectra start to differ from the 0 V measurement, indicating the onset of charge injection and doping. At larger bias voltages ($V_{\text{bias}}$ > 2 V) the high frequency capacitance increases, which below will be related to the formation of highly conductive doped regions. Towards lower frequencies a change of sign is observed in the capacitance.[6] The cross-over to this negative capacitance (NC) moves to higher frequencies for increasing bias voltage. Its position stabilizes near 1 kHz. The NC dominates the rest of the low frequency capacitance.

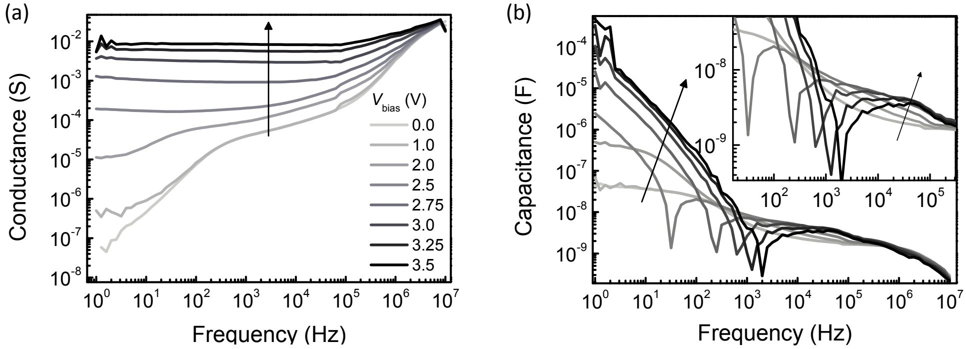

**Figure 5.4 The (a) conductance and (b) capacitance spectra of an MDMO-PPV:PEO:$KCF_3SO_3$ LEC at different bias voltages. The inset in (b) shows the high-frequency part of the capacitance in more detail. Measurements were taken upward in voltage.**

In the conductance spectrum a relatively high conductance is observed at high frequencies (~1 MHz). This conductance decreases when the frequency of the driving signal is decreased and is accompanied by an increase in the capacitance. This behavior can be explained by the presence of highly conductive regions near the electrodes that sandwich a less conductive region: At the highest frequencies the distance the electronic charge carriers can travel is short in comparison to all other length scales in the device, hence all carriers can contribute to the conductance. Upon reducing the frequency, this distance increases and consequently carriers will start to enter regions of lower density/conductance, causing (a) a reduction in conductivity and (b) a pile-up of charges which is reflected in an increasing capacitance. In reality the density and conductivity vary gradually throughout the doped regions, causing also the changes in $C$ (ω) and $G$ (ω) to be gradual. The maximum capacitance (at ~10 kHz) is then related to the capacitance of the junction region. From this maximum capacitance the junction width was determined by the same procedure as shown e.g. in Ref. 6-7, 9. Below however we show that the width determined from this capacitance is not a correct estimate of the width of the light-emitting p-i-n junction. Concomitantly, the corresponding conductance at these intermediate frequencies is related to the conductance in the low-conductive region of the cell, i.e. the p-i-n junction. Moving towards lower frequencies, the conductance is observed to increase again. This increase coincides with the NC observed in the capacitance plots.

Further admittance measurements were taken on nominally identical pristine LECs at 10 kHz to study the time- and voltage-dependence of the low-conductivity region. In Figure 5.5 typical results are shown for MDMO-PPV LECs and SY-PPV LECs. The junction width was estimated from the measured capacitance by approximating the junction region by a parallel plate capacitor with area $A$ = 0.091 cm$^2$. First the settling time of the capacitance was measured after application of 3.5 V (see Figure 5.5a and b). For the MDMO-PPV device the capacitance increases to a maximum within a few seconds. Initially the geometric capacitance was obtained, i.e. 3.6 nF, after which it peaks at 6.3 nF in 5 s. After that the capacitance slowly decreases. Simultaneously, the current, and hence the conductance, increase monotonously. The combination of capacitance and conductance in time show that junction formation is relatively fast <2 s, and is followed by a relatively slow doping process that takes approximately a minute to come close to settling. For the SY-PPV LEC a similar result is observed. Differences are a faster settling time for SY-PPV and a decreasing junction width during doping maximization.

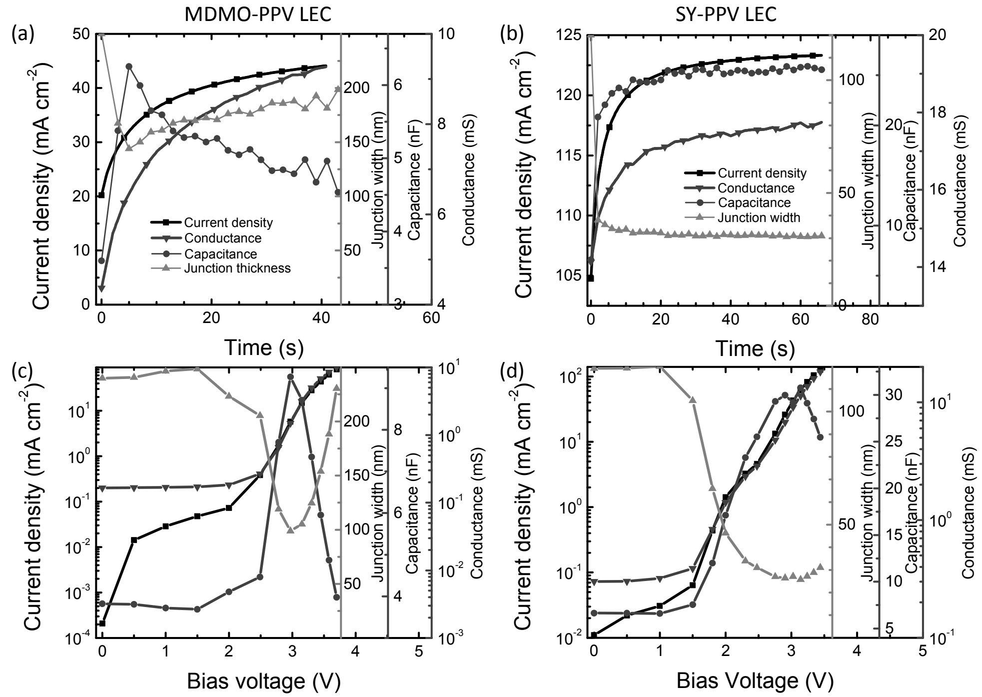

**Figure 5.5 Electrical characterization as a function of (a,b) time and (c,d) voltage for (a, c) MDMO-PPV LECs and (b, d) SY-PPV LECs.**

Measurements of the 10 kHz capacitance and conductance were also performed at different bias voltages as shown in Figure 5.5c and d for MDMO-PPV and SY-PPV LECs, respectively. Pristine LECs were used. At each bias voltage the device was allowed to settle for at least 3 minutes. The capacitance of the MDMO-PPV LEC (see Figure 5.5c) increases sharply between 2.5 and 3 V, reaching a maximum value of ~9 nF at 3 V. The increase of the capacitance can be explained by the progressive formation of doped regions starting at the electrodes. Consequently, a central low-conductivity region remains which leads to an increase in the capacitance above the geometric capacitance of the device. Apparently the increase of voltage between 2.5 V and 3.0 V leads to a strong enhancement of the doping. This is also visible in the strongly increasing conductance and current. Above 3.0 V the capacitance decreases again, indicating that the doped regions shrink. This can be explained by current conservation and exhaustion of paired mobile ions, i.e. salt. The increase in voltage leads to an increase in field in the junction region. This field would significantly increase the current density through the junction region if its width remained constant. However, since the conductivity of the doped regions cannot be increased further because of the exhaustion of salt, the current is limited and the junction region needs to become wider again. Concomitantly the doped regions become more compact, creating a larger doping density in a smaller region. Note that in the same voltage range, current and conductance do show a net increase. Qualitatively similar behavior is observed for the SY-PPV LEC in Figure 5.5d. Differences between SY-PPV LECs and MDMO-PPV LECs are likely related to differences in the doping- and field-dependence of the carrier mobility. Also the salt binding may be affected by the use of different (batches of) polymers. All these effects will be discussed below.

Next to electrical characterization of the LECs, also optical measurements were performed. The results hereof are presented in the Supplementary Information of Ref. 23 and are in line with the results presented in this chapter and in full agreement with previously reported results by Lenes *et al.*[10] However, the trends of the luminance and efficacy measured as a function of time and voltage showed no relevant correlation with the trends in the junction width as determined from the high frequency capacitance.

An interesting comparison between the different device configurations used in this and the previous chapters can be made. The width of the recombination zone in a planar polymer LEC (interelectrode distance of 35 µm) was found to be between 3 to 6 µm: a junction width to active layer thickness ratio of ~0.1.[3] In sandwich LECs this ratio can vary between 0.3 and 0.8. Clearly scaling down the interelectrode distance of the LEC increases the relative width of the recombination zone although the absolute width decreases significantly.

To further understand the admittance results shown in Figure 5.4 and Figure 5.5, the 1D drift-diffusion model was used to calculate both transient and steady-state properties of LECs. In Figure 5.6a modeled current transients are shown using the parameters given in the Materials and methods section. The bias voltage that is applied to the 200 nm LEC is 3.5 V. The ion mobility was set at $10^{-13}$ m$^2$ V$^{-1}$ s$^{-1}$ to speed up calculations. The ion mobility is at least a factor 10 smaller than the slowest electron or hole in the device. Simulations were done with and without a binding energy between the paired anions and cations, i.e. the neutral salt, to study its effect on the current transients. A detailed description of ion binding and salt dissociation is given in Appendix A.4. Here, a binding energy of 0.15 eV and an ion capture coefficient of $10^{-25}$ m$^3$ s$^{-1}$ were taken.[15] The capture coefficient was chosen such that the current transient in Figure 5.6a resembled the experimental results in Figure 5.5a and b.

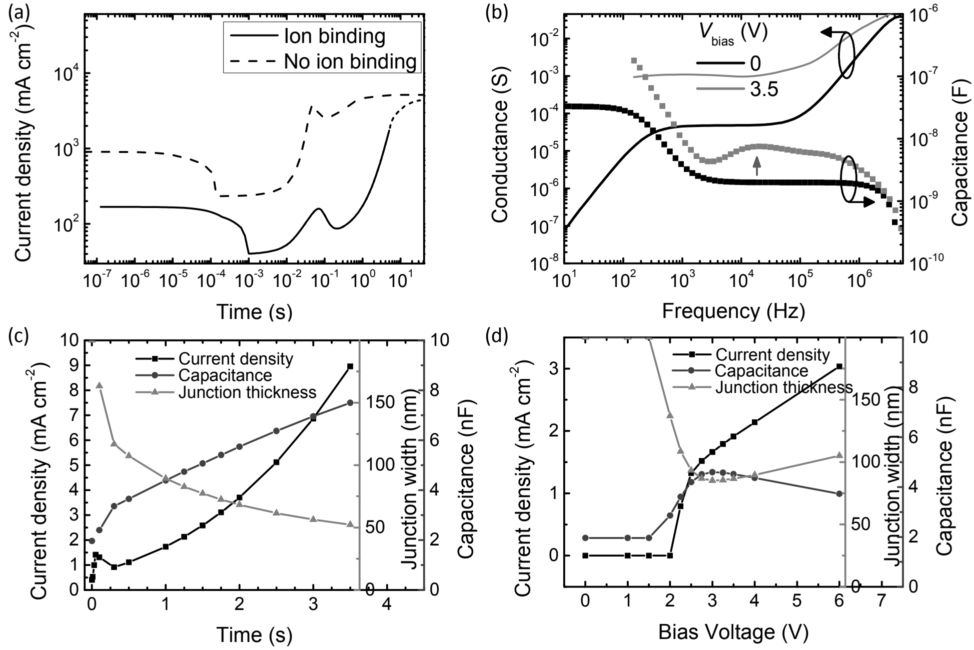

**Figure 5.6 Modeling results of a 200 nm LEC with a surface area of 0.1 cm$^2$. (a) Current transients for an LEC with and without binding energy between the cations and anions at $V_{bias}$ = 3.5 V. The dotted line indicates the continuing trend. (b) Typical high frequency impedance spectra. The vertical arrow denotes the peak position used for junction width determination. (c) Electric characterization as a function of time at 3.5 V. (d) Electric characterization as a function of voltage after 1.0 s.**

At the shortest times in Figure 5.6a ($t < 10^{-3}$ s) the current is solely carried by ions, forming EDLs. During EDL formation the current drops ($10^{-4} < t < 10^{-3}$) due to screening of the electric field by the EDLs. At the same time injection and doping are initiated. The results both show junction formation at around $10^{-1}$ s, highlighted by a peak in the current. The junction formation time is not related to the ion conductivity, but seems solely related to the mobility of the ions, which is the same for both current transients in Figure 5.6a. The mobile ion density differs by a factor 10 as does the ion conductivity. After junction formation both simulations start to qualitatively differ. In case no binding energy is present, the current relaxes towards a steady-state value. This behavior was also observed and modeled in wide inter-electrode gap LECs shown in Figure 3.6b.[4] In case a salt binding energy is present, a large fraction of the ions cannot immediately be used for doping. The salt however slowly dissociates over time because of the depletion of free anions and cations from the n- and p-type doped regions, respectively. As a result, the current increases over a long time span. The same was observed in Figure 5.6a and b, where relatively fast junction formation was followed by a slow increase of the current. Because of long calculation times, it is not feasible to calculate the complete transient for a time span of 50 s and only the first few seconds have been modeled. In either case, the long turn-on time in LECs can now be directly related to the binding energy between the anions and the cations; junction formation itself is a relatively fast process that occurs within a second. The experimental time resolution was insufficient to observe sub-second transient features.

Typical admittance spectra of modeled LECs are shown in Figure 5.6b. The increased capacitance at high frequencies (>1 kHz) as well as the behavior of the conductance are qualitatively similar in the experiment and the model. One major difference however is the strong positive capacitance at low frequencies (<1 kHz) encountered in the modeling result, whereas a negative capacitance is observed in the experiment (see Figure 5.6b). We will come back to this discrepancy at the end of this section. To show that the intermediate- and high-frequency part of the spectrum is correctly modeled and interpreted, similar experiments were done in the model as were done in the experiments (Figure 5.5). In Figure 5.6c the time evolution of the capacitance at 10 kHz is shown. Initially, at $t$ = 0 s the geometric capacitance is obtained. After that the junction forms within 0.1 s, as shown in Figure 5.6a. Necessarily doping of the active layer has then also started, but complete doping is delayed by the dissociation-limiting binding energy. The timescale of the process modeled here is mostly related to the binding-debinding of the salt and the related doping process; the mobility of the carriers is not limiting the evolution of the LEC as follows from the fast (<0.1 s) junction formation. Like for panel a, the modeling results in panel c are qualitatively similar to the experiments in Figure 5.5a and b. The high capacitance due to the low-conductivity region forms within 2 s and is then nearly saturated. The current density however has not and will continue to increase for a much longer time: dissociation of the salt is on-going. The voltage dependence of the capacitance is plotted in Figure 5.6d. Again a qualitatively similar result is obtained as in the experiment (Figure 5.5c and d). For above-bandgap (2.4 eV) voltages the junction has formed; its width decreases until 2.8 V and starts to increase again for larger bias voltages. The current however increases monotonously with increasing voltage. The doped regions were furthermore observed to become narrower, resulting in an increase of conductance in the doped regions.

Figure 5.7a shows the potential profile of the modeled LEC after different times following the application of 3.5 V. In Figure 5.6c the junction width is plotted as well, determined by assuming the low-conductivity region can be described as a parallel plate capacitor. In Figure 5.7a this junction width, ranging between ~60 and ~100 nm, is compared to the potential drop over the recombination zone. They are not at all identical: there is a large mismatch, e.g. ~60 nm vs. ~20 nm for times longer than ~1 s. In Figure 5.7b the electronic conductivity is plotted as a function of position. The conductivity is determined by multiplication of the carrier density, the (local field and doping dependent) mobility and the elementary charge *q*. The conductivity is largest close to the electrodes and gradually decreases towards the recombination region in the center. The conductivity in the recombination zone ($90 < x < 110$ nm) is a factor $10^2$ smaller compared to the average conductivity in the doped regions. Interestingly, the junction width as determined from the capacitance seems to be more related to the width of the low-conductivity region then to the width of the recombination region as estimated from the potential drop. The latter is also equal to the width of the recombination profile.

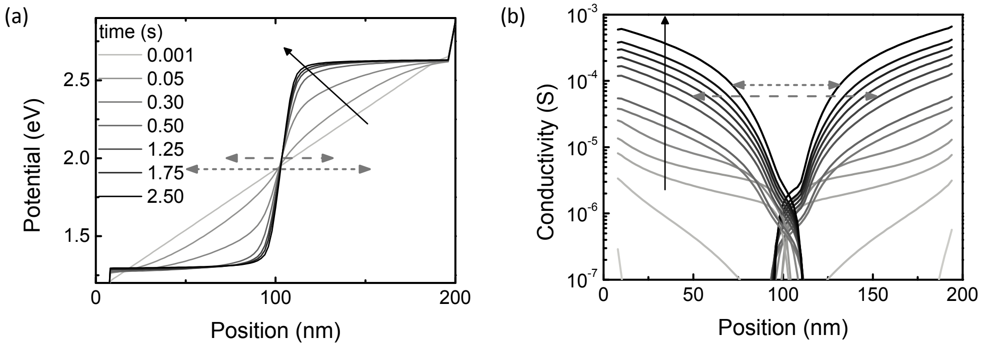

**Figure 5.7 Modeling results of a 200 nm thick LEC with a surface area of 0.1 cm$^2$. (a) Potential and (b) carrier conductivity profile evolution corresponding to results shown in Figure 5.6c.**

These findings indicate that the junction width as obtained from impedance measurements is determined by the mobility and density of electrons and holes throughout the device. The mobility is density[24] and field dependent, complicating things further. Also the recombination process has a large influence on the conductivity in the intrinsic region: a low recombination probability results in larger space charge compensation, leading to larger carrier densities, hence a larger carrier conductivity. The high frequency capacitance is therefore only a measure for the conductance difference between the highly doped regions near the contacts and the less conductive central region. Examples of LECs in which the doping and field dependencies of the mobility were altered are shown in Figure 5.8. By determining the high frequency capacitance at $10^7$ Hz, a junction thickness is calculated similarly as done for Figure 5.5. In Figure 5.8b these values are indicated by the arrows. Note that the horizontal axis indicates the position in the symmetric device where 0 is positioned in the centre. A large spread in junction widths is obtained as indicated by the arrows ranging from 10-70 nm. The calculated potential profile throughout the active layer does however not show such large variation for the various mobility functionalities in Figure 5.8b, which indicates that the calculated 'junction width' is not the actual junction width. More likely it is somewhat related to the conductivity throughout the active layer as shown in Figure 5.8b. The large variation in calculated 'junction thickness' due to different mobility functionalities may explain the wide range of reported junction widths obtained by admittance measurements.[6-7, 9]

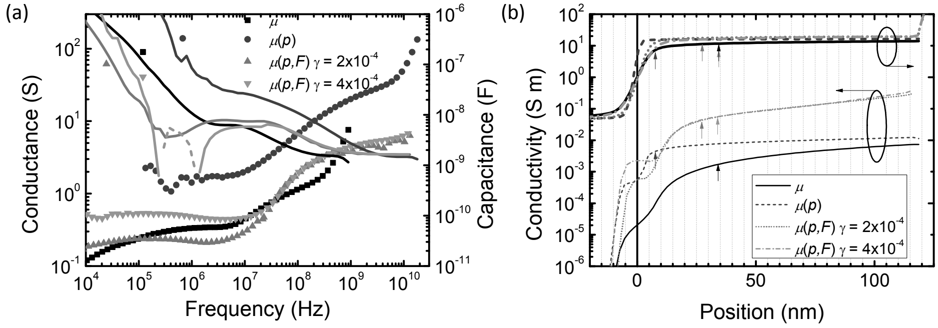

**Figure 5.8 Modeled (a) capacitance (symbols) and conductance (lines) spectra and (b) carrier conductivity plots for different mobility functionalities in LECs as indicated in the legends. The arrows in (b) denote the boundary of the junction thickness as determined from the high frequency capacitance at *f* = $10^7$ Hz in (a).**

The only part of the admittance measurements that is presently not understood is the negative capacitance (NC) at $V_{\text{bias}} > E_{\text{g}}$ below 1 kHz (Figure 5.4b). A similar NC was reported before in Ref. 6. The measurements show that the process related to this negative capacitance is reversible and continuous below 1 kHz. Carrier traps in the doped or intrinsic region were introduced in the model but did not result in an NC. Alternatively, one might associate the NC with space charge compensation effects as known in conventional bipolar diodes,[25] especially since space charge limited behavior has been observed in LECs.[10] Also this scenario seems unlikely as the model does reproduce the pronounced NC behavior for bipolar diodes without ions/salt. The fact that the model cannot reproduce the low-frequency NC indicates that the numerical model, and our understanding of LECs, is not yet complete.

## 5.4 Conclusions

Admittance spectroscopy proves valuable to gain more information on the operational mechanism of polymer LECs in stacked or sandwich geometry. The obtained results were successfully modeled and can be interpreted according to the electrochemical doping model.[26] Measurements where the bias voltage does not exceed the bandgap enabled determination of the electric double layer thickness and of the conductivity of the mobile ions. Measurements in which the bias voltage exceeds the bandgap, enabled the identification of a low-conductivity junction region sandwiched by high-conductivity doped regions. Modeling of LECs has, counter intuitively, shown that the low-conductivity region is not similar in width as the recombination zone. Finally, the relatively large turn-on time in LECs, typically in the order of seconds, was found to be unrelated to the low ion mobility, but rather to be due to the binding energy between anions and cations.

# References

[1] P. Matyba, K. Maturova, M. Kemerink, N. D. Robinson, L. Edman, Nat. Mater. 8 (2009) 672.

[2] J. D. Slinker, J. A. DeFranco, M. J. Jaquith, W. R. Silveira, Y. W. Zhong, J. M. Moran-Mirabal, H. G. Craighead, H. D. Abruna, J. A. Marohn, et al., Nat. Mater. 6 (2007) 894.

[3] D. B. Rodovsky, O. G. Reid, L. S. C. Pingree, D. S. Ginger, ACS Nano 4 (2010) 2673.

[4] S. van Reenen, P. Matyba, A. Dzwilewski, R. A. J. Janssen, L. Edman, M. Kemerink, J. Am. Chem. Soc. 132 (2010) 13776.

[5] J. Gao, A. J. Heeger, I. H. Campbell, D. L. Smith, Phys. Rev. B 59 (1999) R2482.

[6] G. Yu, Y. Cao, C. Zhang, Y. F. Li, J. Gao, A. J. Heeger, Appl. Phys. Lett. 73 (1998) 111.

[7] Y. F. Li, J. Gao, G. Yu, Y. Cao, A. J. Heeger, Chem. Phys. Lett. 287 (1998) 83.

[8] Y. F. Li, J. Gao, D. L. Wang, G. Yu, Y. Cao, A. J. Heeger, Synth. Met. 97 (1998) 191.

[9] I. H. Campbell, D. L. Smith, C. J. Neef, J. P. Ferraris, Appl. Phys. Lett. 72 (1998) 2565.

[10] M. Lenes, G. Garcia-Belmonte, D. Tordera, A. Pertegas, J. Bisquert, H. J. Bolink, Adv. Funct. Mater. 21 (2011) 1581.

[11] M. Buda, G. Kalyuzhny, A. J. Bard, J. Am. Chem. Soc. 124 (2002) 6090.

[12] J. C. deMello, N. Tessler, S. C. Graham, R. H. Friend, Phys. Rev. B 57 (1998) 12951.

[13] J. C. deMello, J. J. M. Halls, S. C. Graham, N. Tessler, R. H. Friend, Phys. Rev. Lett. 85 (2000) 421.

[14] J. C. deMello, Phys. Rev. B 66 (2002) 235210.

[15] D. L. Smith, J. Appl. Phys. 81 (1997) 2869.

[16] S. van Reenen, P. Matyba, A. Dzwilewski, R. A. J. Janssen, A. Edman, M. Kemerink, Adv. Funct. Mater. 21 (2011) 1795.

[17] A. Munar, A. Sandstrom, S. Tang, L. Edman, Adv. Funct. Mater. 22 (2012) 1511.

[18] H. H. P. Gommans, M. Kemerink, W. H. A. Schilders, Phys. Rev. B 72 (2005) 165110.

[19] S. van Reenen, R. A. J. Janssen, M. Kemerink, Org. Electron. 12 (2011) 1746.

[20] A. R. Buckley, Synth. Met. 160 (2010) 540.

[21] J. Frenkel, Phys. Rev. 54 (1938) 647.

[22] M. Kakihana, S. Schantz, L. M. Torell, J. Chem. Phys. 92 (1990) 6271.

[23] S. van Reenen, R. A. J. Janssen, M. Kemerink, Adv. Funct. Mater. 22 (2012) 4547.

[24] H. Shimotani, G. Diguet, Y. Iwasa, Appl. Phys. Lett. 86 (2005) 022104.

[25] H. H. P. Gommans, M. Kemerink, R. A. J. Janssen, Phys. Rev. B 72 (2005) 235204.

[26] Q. B. Pei, Y. Yang, G. Yu, C. Zhang, A. J. Heeger, J. Am. Chem. Soc. 118 (1996) 3922.

# **Chapter 6** Dynamic doping in planar iTMC-LECs

---

*Using a planar electrode geometry, the operational mechanism of iridium(III) ionic transition metal complex (iTMC)-based light-emitting electrochemical cells (LECs) is studied by a combination of fluorescence microscopy and scanning Kelvin probe microscopy (SKPM). Applying a bias to the LECs leads to the quenching of the photoluminescence (PL) in between the electrodes and to a sharp drop of the electrostatic potential in the middle of the device, far away from the contacts. The results shed light on the operational mechanism of iTMC-LECs and demonstrate that these devices work essentially the same as LECs based on conjugated polymers do, i.e. according to an electrochemical doping mechanism. Moreover, with proceeding operation time the potential drop shifts towards the cathode coincident with the onset of light emission. During prolonged operation the emission zone and the potential drop both migrate towards the anode. This event is accompanied by a continuous quenching of the PL in two distinct regions separated by the emission line.*

*Part of the work presented in this chapter has been published: S. B. Meier, S. van Reenen, B. Lefevre, D. Hartmann, H. J. Bolink, A. Winnacker, W. Sarfert, M. Kemerink, Adv. Funct. Mater. 23 (2013) 3531.

## 6.1 Introduction

Despite the broad variety of experimental evidence of electrochemical doping in polymer LECs, the operational mechanism of iTMC-LECs has so far remained unclear. Until now planar iTMC-LECs were only reported to operate according to the ED.[1] Additionally, few works exist describing experimental results in sandwiched configuration which support the ECD.[2-6] Hence, there still remains doubt concerning the operational mechanism of iTMC-LECs which is hindering its further progress.

Here, we report the results of transient experiments carried out on planar iTMC-LECs using as active material the ionic iridium(III) complex bis(2-phenylpyridine)(6-phenyl-2,2'-bipyridine)iridium(III) hexafluorophosphate $[Ir(ppy)_2(pbpy)][PF_6]$ admixed with the ionic liquid 1-butyl-3-methylimidazolium hexafluorophosphate $[BMIM][PF_6]$. A combination of fluorescence and optical microscopy was used to probe the photoluminescent behavior of the iTMC in between the planar electrodes during operation and after switch-off and to identify the location of the emission zone. SKPM was performed to record the evolution of the electrostatic potential. The outcomes of both studies, PL quenching during operation and a sharp potential drop far away from the electrodes, are in line with each other and confirm that iTMC-based LEC devices, just as their polymer counterparts, work according to an electrochemical doping mechanism.

## 6.2 Material and methods

*Device preparation:* bis(2-phenylpyridine)(6-phenyl-2,2'-bipyridine)iridium(III) hexafluorophosphate $[Ir(ppy)_2(pbpy)][PF_6]$ was synthesized similarly according to methods described in Ref. 7-8. Acetonitrile (anhydrous, 99.8 %) and the ionic liquid (IL) 1-butyl-3-methylimidazolium hexafluorophosphate $[BMIM][PF_6]$ (purum, ≥ 97.0 %) were obtained from Sigma Aldrich and used as-received. Indium tin oxide (ITO)-coated glass substrates (ShinAn SNP) were photolitographically structured to yield ITO interdigitated electrodes (IDEs) with spacings of 5 µm and 10 µm. The ITO electrodes had a height of 100 nm and were contacted via evaporated chromium supplies. Before use the substrates were extensively cleaned using sonication in detergent bath and distilled water as well as subsequent oxygen plasma treatment. The latter improved the wettability of the emitter solution on the substrate and additionally resulted in an increase of the ITO work function[9] giving rise to better alignment to the HOMO level of the iridium complex. A stock solution was prepared, dissolving five percent by weight of the iridium complex and the IL in a molar ratio of 3:1 in acetonitrile. IL was used to decrease the turn-on time of the devices.[10] The stock solution was filtered using a 0.1 µm PTFE-filter and spin-coated on top of the IDE substrates (750 rpm, 60 s) under ambient conditions. Afterwards the substrate was transferred to an argon-filled glovebox ($[O_2]$ and $[H_2O]$ < 1 ppm) and annealed on a hotplate at 100 °C for 1 h to give a final active layer thickness of 100 nm as determined by a KLA Tencor P–15 profilometer. To test the devices under ambient conditions they were encapsulated under inert atmosphere by a cavity glass capping (Shanghai Amerina Optoelectronic) equipped with a silica getter to protect the active layer against penetrating oxygen and water. The capping was directly glued to the substrate without prior removal of the organic layers using a self-made, two-component, Bisphenol A-based, UV-curable epoxy adhesive which was coated locally onto the margin of the capping. To test the functionality of the encapsulation, control devices were processed using a calcium layer as a sensor. As the calcium sensor stayed metallic during the long-term study of several hundreds of hours, a possible reaction with water and oxygen to CaO or $Ca(OH)_2$ which would have changed the optical appearance and the resistivity of the transparent film, could be excluded.

*Fluorescence microscopy*: Images of the optically excited photoluminescence of the iTMC-LECs were recorded with an Olympus BX61 microscope equipped with a fluorescence unit which consists of a high pressure mercury vapor arc discharge lamp and a super wide band mirror (SWBM). The SWBM comprises an excitation filter, a dichromatic mirror and an emission filter. Emitted light from the mercury lamp is reduced to the spectral range in between 380 nm and 400 nm via the excitation filter and is then reflected by the dichromatic mirror to impinge on the planar LEC device. The photoexcited light of the LEC passes through the dichromatic mirror and the emission filter and is collected by the microscopy optics. To decrease the intensity of the incident light on the sample in order to avoid photoinduced degradation and to be able to observe the weak electroluminescence, two additional neutral density filters were used. Images of the device without photoexcitation were taken as well to identify the location of the emission zone. Interdigitated electrodes (IDEs) with a gap size of 10 µm were used and a voltage of 210 V was applied to the device to study the transient evolution of the photoluminescence and electroluminescence during a period of roughly 18 hours. Images were recorded every 60 seconds with an exposure time of 7 seconds. In parallel with the optical probing, the current was measured with a computer-controlled sourcemeasure unit (Keithley 2400). The measurements were performed at room temperature.

*Image processing*: To calculate the proportions of the p- and n-type doped region as well as of the emission zone of the entire interelectrode area, image processing was performed on every single picture recorded during the fluorescence microscopy study. As the emission line served as the border for the determination of both regions the first calculations could not be run before the onset of clearly visible light emission. In brief, the images were initially converted to grayscale and then transferred to binary values (bright regions = 1 and dark regions = 0). The bright (emissive) and two dark (doped) regions are purged from background noise and finally the proportions of each region are calculated by relating the number of pixels in each region to the total amount of pixels in the image.

*Fluorescence recovery after photobleaching (FRAP)*: The FRAP experiment was carried out by using the emitted and spectrally reduced light of the mercury lamp of the Olympus BX61 microscope (see fluorescence microscopy paragraph). To allow for maximum near-UV light intensity on the LEC in order to effectively photobleach the iTMCs no grey filters were used. Bleaching was performed for 24 hours with a subsequent recovery period of 39 hours. Images were recorded every 60 seconds with an exposure time of 7 seconds. The measurements were performed at room temperature.

*Scanning Kelvin probe microscopy (SKPM)*: SKPM images were recorded in a glove box under $N_2$ atmosphere ($[O_2] < 1$ ppm and $[H_2O] < 1$ ppm) with a Veeco Instruments MultiMode AFM with Nanoscope IV controller, operating in lift mode with a lift height of 50 nm. Ti-Pt coated silicon tips (MikroMasch NSC36/Ti-Pt, $k \sim 1.75$ N m$^{-1}$) were employed. IDEs with a gap size of 5 µm were used and a voltage of 100 V was applied to the device to study the transient evolution of the electrostatic potential during a period of roughly 4.5 hours. The measurements were carried out at room temperature.

*Computational details*: For the numerical simulations, the 2-dimensional model was used which is described in detail in Appendix A. To model the SKPM experiments a lateral device with buried contacts was simulated. The grid-point spacing was not constant but varied between 20 and 40 nm to reduce the calculation time. The carrier mobility was chosen to be field and doping *in*dependent and set to $\mu_{p/n} = 5 \cdot 10^{-11}$ m$^2$ V$^{-1}$ s$^{-1}$. The anion and cation mobility was chosen to be $\mu_{ion} = 5 \cdot 10^{-11}$ m$^2$ V$^{-1}$ s$^{-1}$. The ion mobility at the interface layer at the contacts was set to zero to prevent accumulation at the electrodes: If not, a large amount of ions piles up next to the electrodes and is resultantly being screened. This is a crude way of introducing a maximum doping density due to finite ion size effects. The temperature is set at 300 K, the dielectric constant at 4.5 and the initial homogeneous salt density at $5 \cdot 10^{25}$ nm$^{-3}$. The simulations were allowed to reach a quasi steady-state indicated by a constant electronic current and an ionic current approaching zero. Injection barriers were set at 0.7 eV for both electron and hole injection and the bandgap of the semiconductor at 2.2 eV to model a symmetric device. The size of the bandgap only determines the voltage needed to start injection. For the rest it has no effects on the final result. The applied bias voltage was 100 V.

## 6.3 Results and discussion

The chemical structures of the compounds used and a sketch of the investigated planar device architecture are depicted in Figure 6.1a. Two sets of indium tin oxide (ITO) interdigitated electrodes (IDEs) with different electrode spacings of 5 µm and 10 µm were used. A section of a bright field optical microscopy picture of the 10 µm gap electrode structure is depicted in Figure 6.1b. The energy level diagram of the device is shown in Figure 6.1c.

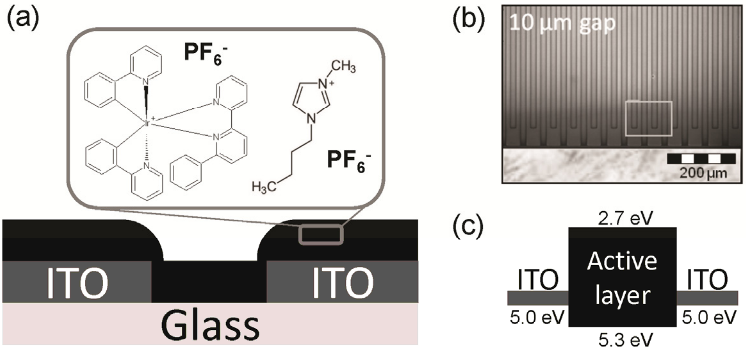

**Figure 6.1 (a) Schematic device layout and structural formulae of the organic constituents. (b) Optical microscopy image of a 10 µm interdigitated electrode structure. The white frame reflects the picture section of the images in Figure 6.2. (c) Energy level diagram of the planar LEC device.**

### 6.3.1 Fluorescence microscopy

First analyses were performed using an IDE device with an interelectrode spacing of 10 µm. Even though ionic liquid (IL) was admixed to the iTMC to accelerate the device response,[10] a high voltage of 210 V was used to operate the LEC. This will be commented on in the second section of this chapter but we note that also without additional IL added the iTMC-LEC does work at 210 V. As expected the time scales are, however, dramatically slowed down by roughly two orders of magnitude. To study the photoluminescent behavior of iTMC-LECs during device operation, fluorescence microscopy was carried out under near-UV illumination of the active layer. Additionally images of the plain electroluminescence without photo-excitation were recorded to be able to identify the location of the emission zone within the interelectrode spacing. Microscopy images were taken of a section of the cell, highlighted in Figure 6.1b, at different time intervals during operation of the LEC both with and without UV illumination (Figure 6.2). To facilitate the evaluation we superimposed the fluorescence image with the plain EL image so that both the fluorescence and the electroluminescence can be observed. As pre-patterned IDE substrates were used, the active layer covered also the finger-like electrodes, referred to as bottom or buried electrode configuration, for which reason the whole device area revealed UV excited PL. Moreover, the dark spots that appear in the image of the pristine (undriven) device (Figure 6.2a) are due to particles in the UV light source. With a new lamp the spots did not appear any longer (Figure 6.2f).

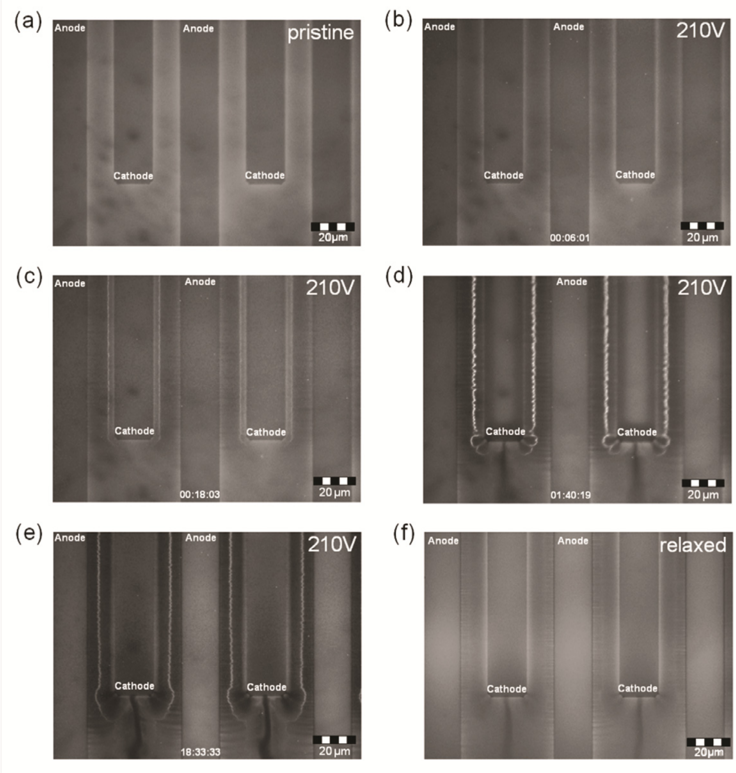

**Figure 6.2 Fluorescence microscopy investigation of a planar iTMC-LEC with an interelectrode spacing of 10 µm at various points in time during operation. A driving voltage of 210 V was applied. (a) UV image of the pristine device. (b)-(e) Superimposed UV illuminated and optical images at various points in time during operation. (f) UV image of a driven device after relaxation for 1000 h.**

The current flowing through the entire interdigitated electrode device was also monitored during the operation of the LEC. From the logarithmic presentation (Figure 6.3) three different regimes can be easily identified. Initially, during the first 15 minutes of operation, the current increases linearly which is associated with quenching of the PL in the interelectrode gap (Figure 6.2a and b). Intuitively one would relate this decrease in PL to the degradation of the iTMC. However, as we will demonstrate below, this is not what is predominantly happening during device operation. After 15 minutes of driving a positive change in the current slope is observed. This change coincides with the onset of weak light emission, visible as the white line in Figure 6.2c. For clarity, the image in Figure 6.2c does not exactly correspond to the beginning of the light emission but to a marginally later point in time (18 minutes). This is due to the fact that the light intensity immediately after the onset of emission is very weak and cannot be distinguished in the recorded image. However, by using image processing software to adjust the brightness and contrast settings of the image, light emission can be visualized and identified to be located very close to the cathode interface after 15 minutes of operation. Moreover, the emission line clearly separates two distinct regions within the interelectrode spacing of which the major region adjacent to the anode shows more pronounced PL quenching compared to the thinner region adjacent to the cathode. During the second regime, up to 100 minutes, the emission line moves towards the middle of the interelectrode gap and becomes brighter (Figure 6.2c and d). Furthermore, the PL quenching in the two regions next to the emission line becomes more intense, still being more pronounced in the region adjacent to the anode. In the third regime, after 100 minutes of operation, the current density reaches a plateau until the end of the measurement after 1000 minutes. During this time interval the emission line migrates slowly further towards the anode and the light intensity decreases (Figure 6.2d and e). The PL quenching in both the anodic and cathodic region is strong and is approximately equal in magnitude. The fact that quenching is also observed on top of the cathode (Figure 6.2c and e) will be discussed later on. After turning off the bias and allowing the device to relax for nearly 1000 hours it was studied again under UV illumination (Figure 6.2f). Compared to the condition immediately before switch-off (Figure 6.2e) an almost entire recovery of the PL intensity in between the electrodes and atop the cathode is observed. This relaxation process occurred slowly over the duration of several hours.

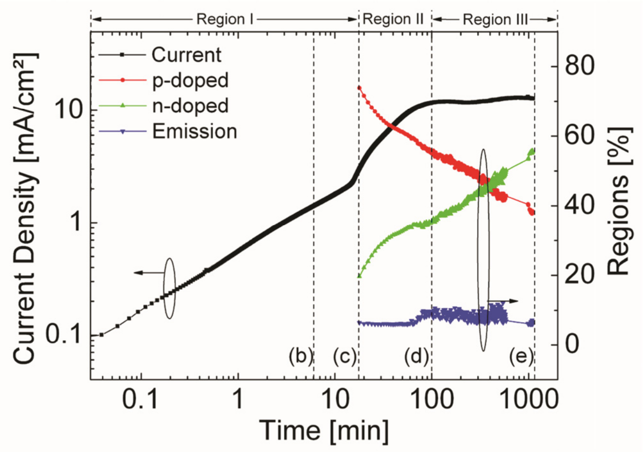

**Figure 6.3 Transient current and evolution of the dimensions of the p-type doped region, the n-type doped region and the emission zone of a planar iTMC-LEC with an interelectrode spacing of 10 µm at a driving voltage of 210 V. The percentaged fractions of the doped regions and the emission zone refer to the total interelectrode area.**

In view of the previous observations, planar iTMC-LECs possess clear features in accordance with the ECD.[11-15] As both p- and n-type doping quench the photo-excited PL, doped regions appear darker than undoped regions.[14-18] The quenching of the PL during operation can therefore be attributed to electrochemical doping of the iTMC layer in between the electrodes, p-type at the anode and n-type at the cathode, which finally gives rise to a light emitting p-i-n junction. The p-type doping process can be envisioned as the trapping of injected holes on the iridium iTMC cation stabilized by uncompensated $PF_6^-$ anions. In case of n-type doping the iTMC cation itself acts as the counter charge for the injected electrons. The quenching almost entirely disappears after turning off the bias which may be related to either dedoping of the iTMCs or to diffusion of electrochemically damaged iTMC cations out of the imaging zone. The latter might be possible as the active material was not only restricted to the interelectrode spacing but instead covered the whole device area.

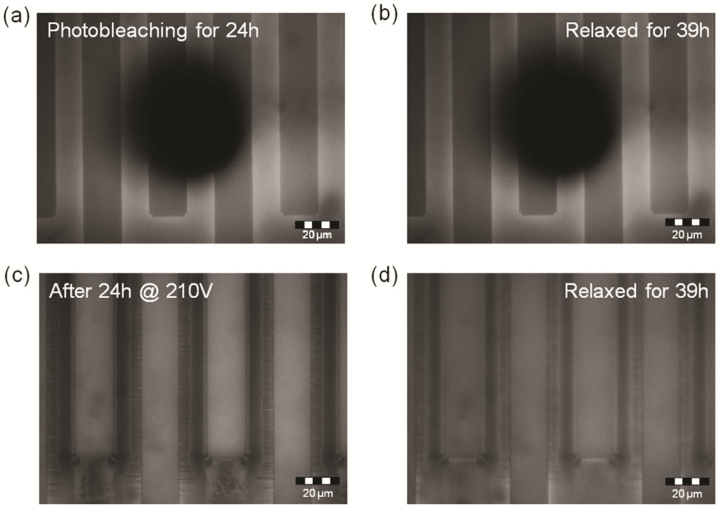

**Figure 6.4 (a) Planar iTMC-LEC after 24 hours of local photobleaching with near-UV light. (b) Same device as in (a) after a recovery period of 39 hours after the photobleaching was stopped. (c) Planar iTMC-LEC after 24 hours of operation at 210 V. (d) Same device as in (c) after a recovery period of 39 hours after bias switch-off.**

To probe a possible diffusivity of the bulky iridium cations we performed a fluorescence recovery after photobleaching (FRAP) experiment. The outcomes of the study are illustrated in Figure 6.4. Figure 6.4a and b reveal a pristine iTMC-LEC photobleached for 24 hours and the same device 39 hours after the bleaching was stopped, respectively. During the chosen recovery period neither significant changes in the dimensions of the bleaching spot nor differences in its coloring could be observed. In contrast, as depicted in Figure 6.4c and d, respectively, an LEC electrically driven for 24 hours at 210 V shows a clearly diminished quenching intensity in the interelectrode area after a recovery period of 39 hours, in conjunction with the results demonstrated before (Figure 6.2e and f). From the experiment we can conclude that on the one hand the iTMC cation is not or only marginally mobile and on the other hand that the PL recovery of the electrically operated LEC is due to the dedoping of the iTMCs. The PL quenching is nearly completely reversible after an extended recovery period (Figure 6.2f) indicating that virtually no permanent degradation occurred during the time frame of these analyses.

As the position of the narrow electroluminescent zone within the interelectrode spacing is related to the dimensions of the p- and n-type doped regions, their fractions with respect to the total interelectrode area were calculated as a function of operation time by means of image processing and the results are included in Figure 6.3. Note that the first calculations could not be run before the onset of clearly visible light emission after 18 minutes, as the emission line served as the border for the determination of the doped regions. Moreover, due to its jagged shape, the emission line captures a quite large fraction of the interelectrode spacing of 5-10 %. The outcomes of the calculations in Figure 6.3 clearly demonstrate a large extent of p-type doping (> 70 %) during the early stages of operation and only a small fraction of n-type doping (< 20 %). During the subsequent operation the p-type doped region is gradually consumed by the n-type doped region. A description of this process can be found in the literature.[19] N-type doping becomes dominant after around 400 minutes and covers more than 55 % of the entire interelectrode area in the end of operation after 1000 minutes. The results are in accord with the emission line forming at the cathode and moving towards the anode and highlight the prerequisite for a migration of the emission zone in LECs: the consumption of one kind of doping by the other.

### 6.3.2 Scanning Kelvin probe microscopy

In addition to the PL experiments we performed scanning Kelvin probe microscopy (SKPM) to study the transient behavior of the electrostatic potential in the planar iTMC-LEC. The outcomes are plotted in Figure 6.5. Due to restrictions in the measurement setup the maximum voltage that could be applied to the LEC was limited to 100 V. As this voltage was not sufficient to observe light emission in a device with 10 µm interelectrode spacing, we used IDEs with a smaller gap size of 5 µm for these investigations. This electrode spacing can also be clearly deduced from the height profile which is depicted in Figure 6.5a. For clarity the anode and cathode edges are labeled correspondingly. The height scan was recorded along the horizontal dashed blue line denoted in the AFM topography image which is displayed as the top inset in Figure 6.5a. This line also corresponds to the scan direction for the measurement of the potential profiles during operation which are also included in Figure 6.5a. The arrow denotes the temporal evolution of the electrostatic potential within a time interval of roughly 4.5 hours. The reason not to use a 5 µm device as well for the fluorescence microscopy investigations in the previous section is that this would have led to substantial losses in the image resolution due to the smaller dimensions of the device structure.

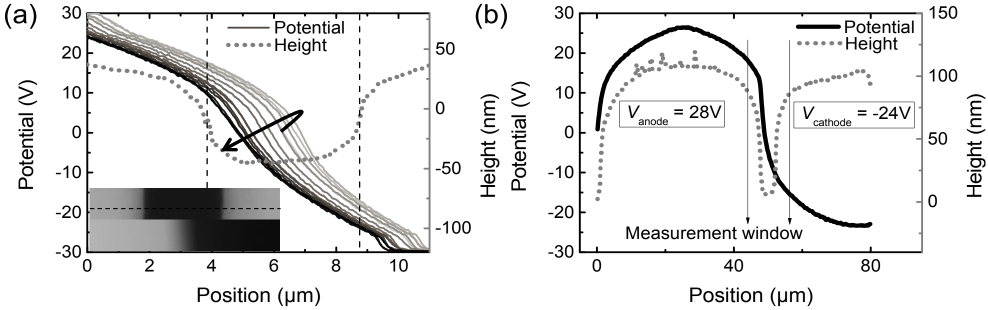

**Figure 6.5 (a) Height and transient potential profiles during operation of an iTMC-LEC. The inset shows AFM images of the topography (top) and the potential map (bottom). The dashed lines indicate the orientation of the profiles with respect to the electrodes and the arrow denotes the temporal evolution of the potential. (b) Complete potential profile across the LEC biased at 52 V. The arrows indicate the measurement window of the profiles shown in (a).**

The first SKPM measurement was performed immediately after applying a bias of 100 V to the iTMC-LEC at which a sharp potential drop is registered in the middle of the interelectrode gap. During the subsequent 30 minutes of operation the potential drop shifts towards the cathodic interface whereas with prolonged operation it moves in the opposite direction and is displaced towards the anode by the end of the device operation. For visualization purposes a topography and potential map recorded during the later stages of operation are shown in the bottom part of the inset in Figure 6.5a. The present findings are in full agreement with the ECD[11-15] especially with regard to recent SKPM studies on planar pLECs[13, 20-21] and provide clear evidence for the formation of a p-i-n junction in iTMC-LECs. The ED which predicts potential drops to occur only at the electrode interfaces,[1, 22-24] can be ruled out. Our results demonstrate that during the entire SKPM analysis the potential drop occurs within the interelectrode gap far away from the contacts. This implies the existence of a high-ohmic intrinsic region where the large electric field has to compensate for the low conductivity. Moreover, the intrinsic area is not fixed to a specific position in between the electrodes but migrates with time as visualized by the shift of the potential drop.

Even though devices with two different interelectrode spacings have been used, the results of the SKPM and fluorescence microscopy study are in excellent agreement. The initially centered drop of the electrostatic potential implies that p- and n-type doping set in immediately. Note that in the fluorescence microscopy experiments no EL could be detected in the first 15 minutes. This is probably related to a relatively low doping density. As the doping density continuously increases, the EL increases until at some moment it is large enough to be observed. The shift of the potential drop in the SKPM experiments is in accordance with the fluorescence investigations. Such shifts may be related to imbalances in carrier injection, conductivity, doping speed or a combination of these. We note that even though a voltage of 100 V has been applied to operate the planar iTMC-LEC, a large portion of the potential is screened from the interelectrode spacing and drops on top of the electrodes (see Figure 6.5a). This screening as well as the PL quenching observed on top of the cathode (see Figure 6.2d and e) indicates that doping also takes place atop the electrodes. The absence of quenching on top of the anode may be due to a difference in quenching cross-sections or doping density.

As the length of the previous potential scans was limited and did not involve the entire electrodes' width, we performed a larger-area scan in a separate SKPM measurement to record the complete potential profile across the LEC. To allow for a stable SKPM measurement with reliable results, the maximum voltage that could be applied to the LEC was limited to below 60 V and we chose a voltage of 52 V. The outcome of the experiment is illustrated in Figure 6.5b which, for comparison, also shows the measurement window for the recording of the potential profiles in the initial study. Again a large drop of the electrostatic potential is observed in the interelectrode gap and also atop both electrodes. Moreover, the full applied potential is visible which separates into 28 V in the anodic region and -24 V in the cathodic region. A rough estimate of the potential drop in the interelectrode gap yields a value of 25 V which implicates large potential drops of more than 10 V atop each electrode. The large potential screening from the gap may be related to the presence of EDLs that consume more potential than one would expect from the size of the injection barriers: 0.3 and 2.3 eV (see Figure 6.1c).

To check this, numerical simulations were performed of a 2D representation of the LEC with buried contacts as shown in Figure 6.6a. The potential map of the simulation in steady-state is shown in Figure 6.6b. In Figure 6.6c a side view of Figure 6.6b is shown for clarity. A clear p-i-n junction is visible in between the electrodes, where the slope of the potential is steepest. Similar to the experiments shown in Figure 6.5 a large part of the potential drops over the doped regions. Also electric double layers are observed in the channel and on top of the electrodes, indicated by the large potential drop surrounding the contacts (see black line in Figure 6.6c). The potential drop over the EDLs is much larger than the injection barriers of 0.7 eV. In the simulations, the enhanced carrier injection on top of the electrodes also results in electrochemical doping. Experimentally this is observed as quenching of the PL on top of the cathode (see Figure 6.2d and e). This indicates that the geometry of the device may play a role in carrier transport and, related to this, in the positions of the doped regions as well as of the p-i-n junction. The dashed line in Figure 6.6c represents the potential profile at the interface between the vacuum and the iTMC layer. This is the interface that would be probed by SKPM. Here the potential drop over the EDLs (black line) is not observed which is in agreement with Figure

6.5 where buried electrodes were used. Using top electrodes instead, the existence of EDLs has already been experimentally confirmed in pLECs.[20-21]

To summarize the numerical modeling, we prove that it is possible to have a p-i-n junction in combination with large, i.e. exceeding the bandgap, EDLs, provided injection is partially frustrated. The resultant operation can be viewed as a combination of the ED and ECD model. This means that in this specific device, device operation is not independent on electrode material. We should stress that non-frustrated injection gives rise to purely ECD behavior.[20]

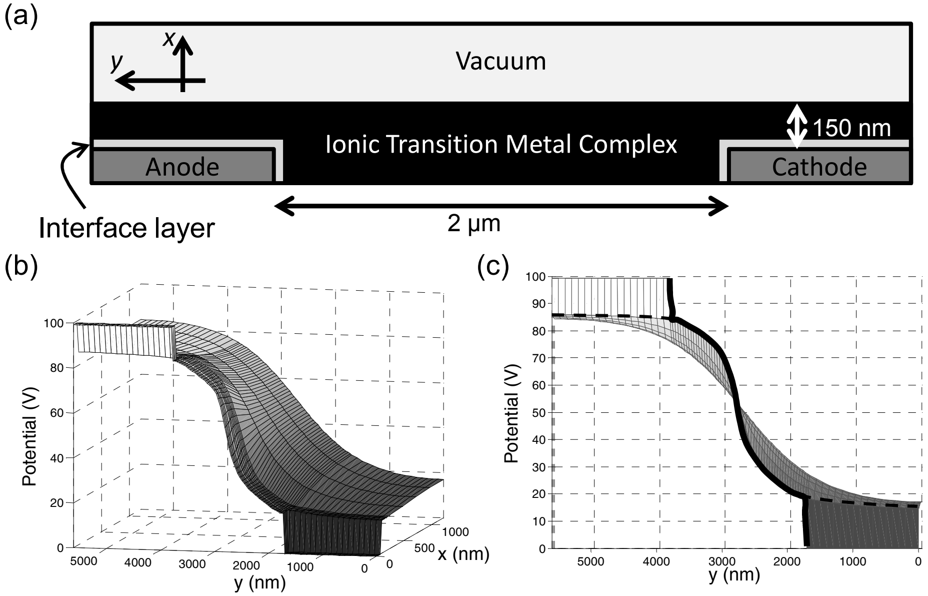

**Figure 6.6 (a) Schematic of the simulated planar LEC device. (b,c) Steady state result of the simulation of a planar iTMC-LEC. The dashed line in (c) is taken at the vacuum-iTMC interface shown in (a) and the thick line in (c) is taken at *x* = 0, i.e. at the bottom of (a).**

A remaining issue is the extremely large bias voltage of ~ 100 V needed to operate the iTMC-LECs. Similar bias voltages have been used in pLECs with millimeter-sized gaps.[14] Later the voltage was reduced by operation above the melting temperature of the electrolyte[25] or by a different choice of electrolyte.[26] The device physics was, however, not affected. In all cases a thin recombination zone positioned in between two oppositely doped regions was observed. Here, the use of relatively large bias voltages was necessary to reduce the turn-on time as well as to obtain detectable light emission. The generally low turn-on time of iTMC-LECs in comparison to pLECs seems to be related to pronounced differences in the ionic conductivities, a topic which is addressed in a very recent publication.[27]

Finally, based on the present findings and the literature results, a few differences can be distinguished between planar polymer and iTMC-LECs. First of all relatively large potential drops over the EDLs seem to be present in the Ir-iTMC LEC in contrast to pLECs where these drops equal the injection barriers.[20-21] This may be related to the sensitivity of LEC operation on the electrode contacts as previously addressed. For example injection limitation was demonstrated to result in a device behavior according to the ED whereas the ECD holds when charge injection is non-limited.[20] In general the electrode work function was shown to affect charge carrier injection and doping in LECs.[16, 28] Moreover, in the doped regions of iTMC-LECs large potential drops are identified (Figure 6.5), whereas in pLECs based on MDMO-PPV this is typically not the case.[20] However, in LECs based on MEH-PPV relatively large electric fields are detected in the n-doped region.[13, 17] This indicates a compensation of dissimilarities between the carrier conductivity in the doped and undoped regions by the electric field distribution. A similarly large field seems to be needed in both doped regions in the iTMC-LEC (Figure 6.4a), which spans a gap of 5 µm. Hence, these devices still deviate from the idealized LEC in that they are still sensitive to the interelectrode distance and, related to that, are too resistive to be operated at relatively low bias voltages. The operational mechanism, however, remains the same: electrochemical doping enables enhanced carrier injection and transport, while the applied field redistributes to maximize the overall current passing through.

## 6.4 Conclusions

By a combination of fluorescence and scanning Kelvin probe microscopy insight is gained in the operational mechanism of planar ionic transition metal complex-based light-emitting electrochemical cells. Quenching of the photoluminescence in the interelectrode gap and a sharp drop in the electrostatic potential far away from the electrodes confirm an electrochemical doping mechanism which results in the formation of a light-emitting p-i-n junction. The intrinsic region, where light emission occurs, is not fixed but migrates with time which might be related to a change in the conductivity of electrons and holes. The results provide a fundamental basis for a better understanding of iTMC-based LEC devices and additionally demonstrate an important challenge: an emission zone centered and fixated in the middle of the interelectrode spacing immediately at the beginning of operation to allow for stable and efficient light-emission.

# References

[1] J. D. Slinker, J. A. DeFranco, M. J. Jaquith, W. R. Silveira, Y. W. Zhong, J. M. Moran-Mirabal, H. G. Craighead, H. D. Abruna, J. A. Marohn, et al., Nat. Mater. 6 (2007) 894.

[2] D. Tordera, S. Meier, M. Lenes, R. D. Costa, E. Orti, W. Sarfert, H. J. Bolink, Adv. Mater. 24 (2012) 897.

[3] M. Buda, G. Kalyuzhny, A. J. Bard, J. Am. Chem. Soc. 124 (2002) 6090.

[4] H. Rudmann, S. Shimada, M. F. Rubner, J. Appl. Phys. 94 (2003) 115.

[5] M. Lenes, G. Garcia-Belmonte, D. Tordera, A. Pertegas, J. Bisquert, H. J. Bolink, Adv. Funct. Mater. 21 (2011) 1581.

[6] S. B. Meier, D. Hartmann, D. Tordera, H. J. Bolink, A. Winnacker, W. Sarfert, Phys. Chem. Chem. Phys. 14 (2012) 10886.

[7] H. J. Bolink, E. Coronado, R. D. Costa, E. Orti, M. Sessolo, S. Graber, K. Doyle, M. Neuburger, C. E. Housecroft, et al., Adv. Mater. 20 (2008) 3910.

[8] F. Gartner, D. Cozzula, S. Losse, A. Boddien, G. Anilkumar, H. Junge, T. Schulz, N. Marquet, A. Spannenberg, et al., Chem. Eur. J. 17 (2011) 6998.

[9] D. J. Milliron, I. G. Hill, C. Shen, A. Kahn, J. Schwartz, J. Appl. Phys. 87 (2000) 572.

[10] S. T. Parker, J. D. Slinker, M. S. Lowry, M. P. Cox, S. Bernhard, G. G. Malliaras, Chem. Mater. 17 (2005) 3187.

[11] Q. B. Pei, G. Yu, C. Zhang, Y. Yang, A. J. Heeger, Science 269 (1995) 1086.

[12] Q. B. Pei, Y. Yang, G. Yu, C. Zhang, A. J. Heeger, J. Am. Chem. Soc. 118 (1996) 3922.

[13] P. Matyba, K. Maturova, M. Kemerink, N. D. Robinson, L. Edman, Nat. Mater. 8 (2009) 672.

[14] J. Gao, J. Dane, Appl. Phys. Lett. 83 (2003) 3027.

[15] J. Gao, J. Dane, Appl. Phys. Lett. 84 (2004) 2778.

[16] D. B. Rodovsky, O. G. Reid, L. S. C. Pingree, D. S. Ginger, ACS Nano 4 (2010) 2673.

[17] Y. F. Hu, J. Gao, J. Am. Chem. Soc. 133 (2011) 2227.

[18] Y. F. Hu, C. Tracy, J. Gao, Appl. Phys. Lett. 88 (2006) 123507.

[19] N. D. Robinson, J. F. Fang, P. Matyba, L. Edman, Phys. Rev. B 78 (2008) 245202.

[20] S. van Reenen, P. Matyba, A. Dzwilewski, R. A. J. Janssen, L. Edman, M. Kemerink, J. Am. Chem. Soc. 132 (2010) 13776.

[21] S. van Reenen, P. Matyba, A. Dzwilewski, R. A. J. Janssen, A. Edman, M. Kemerink, Adv. Funct. Mater. 21 (2011) 1795.

[22] J. C. deMello, N. Tessler, S. C. Graham, R. H. Friend, Phys. Rev. B 57 (1998) 12951.

[23] J. C. deMello, J. J. M. Halls, S. C. Graham, N. Tessler, R. H. Friend, Phys. Rev. Lett. 85 (2000) 421.

[24] J. C. deMello, Phys. Rev. B 66 (2002) 235210.

[25] J. H. Shin, A. Dzwilewski, A. Iwasiewicz, S. Xiao, A. Fransson, G. N. Ankah, L. Edman, Appl. Phys. Lett. 89 (2006) 013509.

[26] J. H. Shin, L. Edman, J. Am. Chem. Soc. 128 (2006) 15568.

[27] S. van Reenen, T. Akatsuka, D. Tordera, M. Kemerink, H. J. Bolink, J. Am. Chem. Soc. 135 (2013) 886.

[28] D. Hohertz, J. Gao, Adv. Mater. 20 (2008) 3298.

# Chapter 7 Universal transients in polymer- and iTMC-LECs

---

*Two types of light-emitting electrochemical cells (LECs) are commonly distinguished, the polymer-based LEC (pLEC) and the ionic transition metal complex-based LEC (iTMC-LEC). Apart from marked differences in the active layer constituents these LEC types typically show operational time scales that can differ by many orders of magnitude at room temperature. Here, we demonstrate that despite these differences pLECs and iTMC-LECs show current, light output and efficacy transients that follow a universal shape. Moreover, we conclude that the turn-on time of both LEC types is dominated by the ion conductivity since the turn-on time exhibits the same activation energy as the ion conductivity in the off-state. These results demonstrate that both types of LECs are really two extremes of one class of electroluminescent devices. They also implicate that no fundamental difference exists between charge transport in small molecular weight or polymeric mixed ionic and electronic conductive materials. Additionally, it follows that the ionic conductivity is responsible for the dynamic properties of devices and systems using them. This likely extends to mixed ionic and electronic conductive materials used in organic solar cells and in a variety of biological systems.*

*Part of the work presented in this chapter has been published: S. van Reenen, T. Akatsuka, D. Tordera, M. Kemerink, H. J. Bolink, J. Am. Chem. Soc. 135 (2013) 886.

## 7.1 Introduction

Despite the similarity in steady-state operation between polymer- and iTMC-LECs as shown in the previous chapters,[1-9] large differences exist in key properties such as lifetime, turn-on time, brightness and efficiency. For comparison, state-of-the-art pLECs exhibit lifetimes of ~5600 h at a brightness of >100 cd $m^{-2}$.[10-14] iTMC-LECs have similar lifetimes at higher brightness (>600 cd $m^{-2}$).[15-16] Furthermore iTMC-LECs consist of triplet emitters that intrinsically allow for higher quantum efficiencies. Of all the key properties the turn-on time shows the largest difference between both types of devices. Biased at 3-4 V at room temperature, pLECs typically turn-on within a second, whereas iridium-based iTMC-LECs frequently need hours.[2, 17-21] These dynamic differences are the main reason that these two type of LECs are considered as different classes.

Here we report on a comparative study on the transient behavior of stacked LECs based on either the polymer MDMO-PPV or the ionic iridium complex bis(2-phenylpyridine)(2,2-bipyridine)iridium(III) hexafluorophosphate, $[Ir(ppy)_2(bpy)]^+$ $[PF_6]^-$. These were studied by determining the current and luminance transients at different cell temperatures. The shape of the transients is found to be independent of operating temperature and more importantly independent of the type of semiconductor used. The turn-on time however varied over several orders of magnitude with temperature and could be described by an Arrhenius-type activation energy. The same activation energy was found in the thermal activation of the ion conductivity in the unbiased state: the turn-on time is inversely proportional to the ion conductivity. Together these results prove that next to the steady-state operation, also the transient behavior of iTMC and polymer LECs are qualitatively the same. Hence, pLECs and iTMC-LECs are really one class of electroluminescent devices. These results also demonstrate that the ionic conductivity is responsible for the dynamic properties of devices and systems using mixed electronic and ionic materials.

## 7.2 Material and methods

*Device preparation*: For the conjugated polymer in the active layer of our sandwich LECs poly[2-methoxy-5-(3′,7′-dimethyloctyloxy)-p-phenylene vinylene] (MDMO-PPV, $M_w > 10^6$ g $mol^{-1}$, American Dye Source) was used. Poly(ethylene oxide) (PEO, $M_w = 5 \cdot 10^5$ g $mol^{-1}$, Aldrich) was used as received. The salt potassium trifluoromethanesulfonate ($KCF_3SO_3$, 98 %, Aldrich) was dried at a temperature $T$ = 473 K under vacuum before use. MDMO-PPV (10 mg $ml^{-1}$) was dissolved in chloroform (> 99 %, anhydrous, Aldrich). PEO and $KCF_3SO_3$ were dissolved separately (10 mg $ml^{-1}$) in cyclohexanone (> 99 %, anhydrous, Aldrich). These solutions were mixed together in a weight ratio of PPV:PEO:$KCF_3SO_3$ = 1:1.35:0.25. This stock solution was thereafter stirred on a magnetic hot plate at $T$ = 323 K for 5 h.

Cleaned glass/ITO substrates were spin-coated with the stock solution (at 800 RPM for 60 s, followed by 1000 RPM for 10 s) after which they were dried at $T$ = 323 K for at least 1 h on a hot plate. The thickness of the active layer was ~230 nm as determined by profilometry. Al electrodes were deposited by thermal evaporation under high vacuum ($p \sim 10^{-6}$ mbar) on top of the spin-coated films. All of the above mentioned procedures, save for the cleaning of the substrates, were done in a glove box under $N_2$ atmosphere ($[O_2] < 1$ ppm and $[H_2O] < 1$ ppm) or in an integrated thermal evaporator.

For the iTMCs-LECs the devices were made as follows. The emitting complex, $[Ir(ppy)_2 (bpy)]^+ [PF_6]^-$, was synthesized according to methods described previously.[22] Indium tin oxide ITO-coated glass plates were patterned by conventional photolithography (www.narajosubstrates.com). The substrates were cleaned by sonication in successively water-soap, water, and 2-propanol baths. After drying, the substrates were placed in an UV-ozone cleaner (Jelight 42-220) for 20 min. An 80 nm layer of PEDOT:PSS (CLEVIOS P VP AI 4083, aqueous dispersion, 1.3–1.7 % solid content, Heraeus) was spin-coated on the ITO glass substrate to improve the reproducibility of the devices and to prevent the formation of pinholes. Then a 100 nm transparent film of the emitting complex $[Ir(ppy)_2 (bpy)]^+ [PF_6]^-$ was spin-coated from 30 mg mL$^{-1}$ acetonitrile solution at 1000 RPM for 20 s. Unless stated otherwise, the ionic liquid (IL) 1-butyl-3-methylimidazolium hexafluorophosphate, $[BMIM]^+ [PF_6]^-$, (> 98.5%, Sigma-Aldrich) was added in a 4 to 1 molar ratio (iTMC:IL). The thickness of the films was determined with an Ambios XP-1 profilometer. After coating the films the substrates were transferred to an inert atmosphere glovebox (< 1 ppm $[O_2]$ and $[H_2O]$, M. Braun). The Al electrode (70 nm) was thermally vacuum-evaporated using a shadow mask ($< 3{\cdot}10^{-6}$ mbar) with an Edwards Auto500 evaporator integrated in the glovebox. The area of the device was 6.5 mm$^2$. The devices were characterized inside the glovebox.

*Electrical characterization*: For characterization of the pLECs a Keithley 2636a sourcemeter was used to drive the devices and measure the current. The brightness was measured with a luminance meter (LS-110 Konica-Minolta). A Solartron 1260 was used to perform complex admittance measurements on the LECs in the glovebox. Each point (from 10 MHz to 1 Hz) was measured during an integration time of 1 s. The rms-value of the AC voltage was 0.01 V. The temperature of the device was controlled by use of a Peltier element and the temperature was measured by a thermocouple.

For characterization of the iTMC-LECs, transients were measured by applying constant voltages and monitoring the current and luminance by a True Colour Sensor MAZeT (MTCSiCT Sensor) using a Botest OLT OLED Lifetime-Test System. The conductance spectrum was determined by using a fast Fourier transform of the derivative of the transient current after setting a small step in the voltage (from 0 V to -0.5 V to prevent carrier injection) by monitoring the current flow using a Keithley 2400 sourcemeter via a Labview controlled custom-made protocol. The temperature of the device was controlled by use of a Peltier element and the temperature was measured by a thermocouple.

## 7.3 Results and discussion

The layouts of the iTMC- and polymer-based LECs as well as the structural formulae of the active layer constituents are shown in Figure 7.1a and b. Figure 7.2 shows the typical transient behaviors of the luminance, current and efficacy in pristine iTMC-LECs and pLECs after application of 3.5 V at two different temperatures. In all measurements the same is observed: current, luminance and efficacy start to increase after which first the efficacy rolls off followed by the luminance. These typical transients can be rationalized by electrochemical doping of the active layer assisted by the mobile ions. Initially, upon application of a bias voltage, ions start moving and form EDLs at the electrode interfaces. This initiates injection of electrons and holes. Consequently an electron-hole current arises that overtakes the ion current in magnitude. These electrons and holes recombine radiatively before reaching the other electrode. This explains the initial increase of current and luminance. The initial increase in efficacy results from the decreasing relative contribution of the ionic current with respect to the electronic current. Additionally it may be related to a transition from unipolar to bipolar current due to more balanced carrier injection. After some time the efficacy is observed to reach a maximum. The following decrease can be related to exciton quenching. This exciton quenching sets in after EDL formation when the semiconductor is being electrochemically doped: the carrier density in the doped regions increases and the n- and p-type doped regions grow towards each other. The high polaron density in the doped regions close to the recombination region can cause significant exciton-polaron quenching.[23] Furthermore the enhanced recombination leads to an enhanced triplet exciton density in the iTMC-LEC. This is likely accompanied by triplet-triplet exciton annihilation.[23] After extended operation times the current density reaches a maximum (not shown) followed by a decrease attributed to irreversible degeneration.[10]

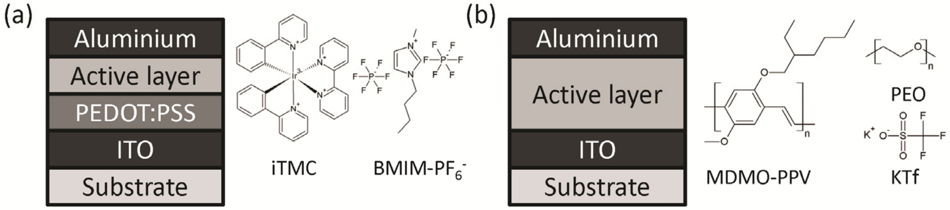

**Figure 7.1 Device layout and the structural formulae of the active layer constituents of (a) the iTMC-LEC and (b) the polymer LEC.**

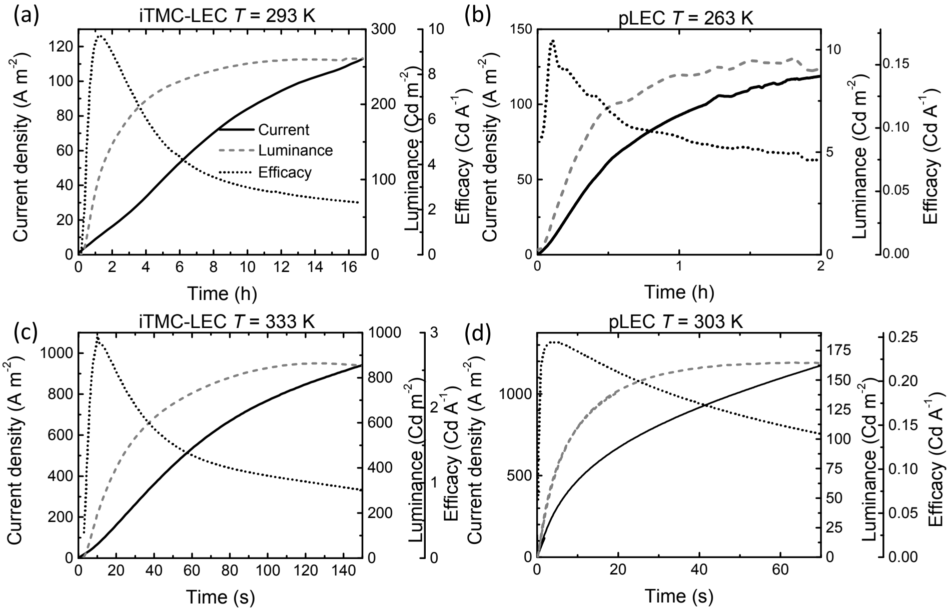

**Figure 7.2 Current, luminance and efficacy transients of (a,c) pristine Ir-iTMC-LECs and (b,d) pristine MDMO-PPV pLECs biased at 3.5 V. The temperature during operation is shown at the top of each graph.**

For comparison the transients in Figure 7.2a-d were all normalized and plotted in one graph, shown in Figure 7.3. Normalization of the transients was performed by division of the efficacy and luminance with their respective peak values. The time and current at which the luminance peaked was used to normalize these quantities respectively. The good overlap of the transients in Figure 7.3 indicates that all four devices behave qualitatively the same, despite differences in semiconductor, ion-type, operational temperature, turn-on time and magnitude of current, luminance and efficacy. The invariance of the shape by temperature in particular indicates that a single process or property determines the turn-on behavior of these cells in this temperature range: most likely thermal activation of the 'slow' ions. The fact that the use of different semiconductors and ions only leads to minor qualitative differences in the transients further proves that both types of devices operate according to the same operational model.[1-2, 7, 9] Processes such as ion dissociation and transport, exciton quenching and electrochemical doping are (anticipated to be) active in both types of LECs. The large differences in the magnitude of the current, luminance and efficacy can be related to differences in the type of emitting material and salt used as well as to the ratio in which they are mixed. For example, the Ir-iTMC is a phosphorescent emitter, whereas the PPV is a fluorescent emitter. Furthermore, the doping dependence of the carrier mobility is likely different which may lead to differences in the thicknesses of the doped and intrinsic regions and as a consequence in the current density. The maximum efficacy of both types of LECs was however found to be independent of the operating temperature (see e.g. supporting information Figures A.2 and A.3 of Ref. 24).

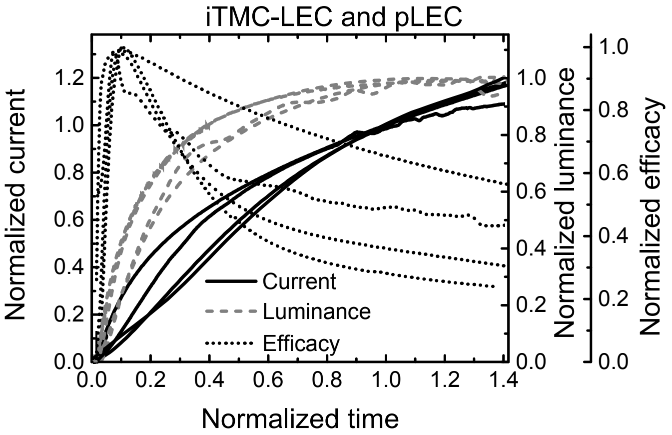

**Figure 7.3 Normalized current, luminance and efficacy transients of polymer and iTMC-LECs at two temperatures each and biased at 3.5 V.**

Comparison of Figure 7.2a and b with respectively Figure 7.2c and d shows a strong temperature dependence of the turn-on time in both types of LECs: for the iTMC-LEC the turn-on time changes from hours to tens of seconds by an increase of the temperature from 27 to 60 °C (see Figure 7.2a and c). For the pLEC similar turn-on times are obtained in a different temperature range, namely -10 to 30 °C (see Figure 7.2b and d).

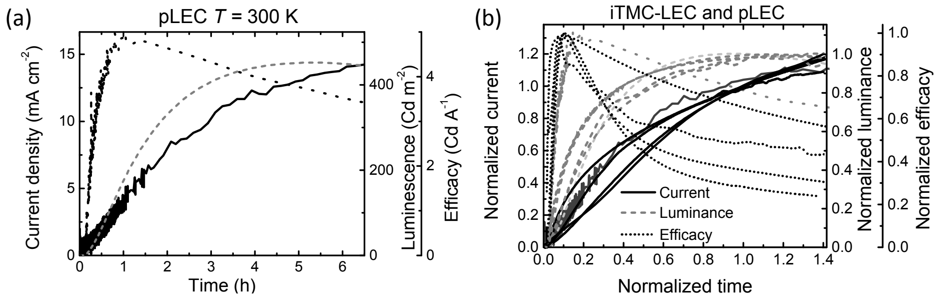

**Figure 7.4 (a) current, luminance and efficacy transients of a Super Yellow/tetrahexylammonium hexafluorophosphate (1:0.1 in weight) LEC biased at 5 V. The normalized characteristics are plotted together with the results from Figure 7.3 in (b).**

Similarly shaped turn-on transients were reported in other LECs. For example in iTMC-LECs based on ruthenium with[25] and without[26] the addition of PEO. Literature on polymer LECs without PEO is also available. However, no constant voltage turn-on transients were reported.[17-18] Therefore we prepared similar LECs comprising Super Yellow PPV admixed with the salt tetrahexylammonium hexafluorophosphate in a 10% weight ratio. The (normalized) characteristics are shown in Figure 7.4 and can be identified in Figure 7.4b by the lighter tone. Again similarly shaped turn-on transients are observed despite a relatively large turn-on time in the order of hours, supporting our claim that the qualitative operation of semiconductor-electrolyte systems is universal despite potentially large differences in performance and response times.

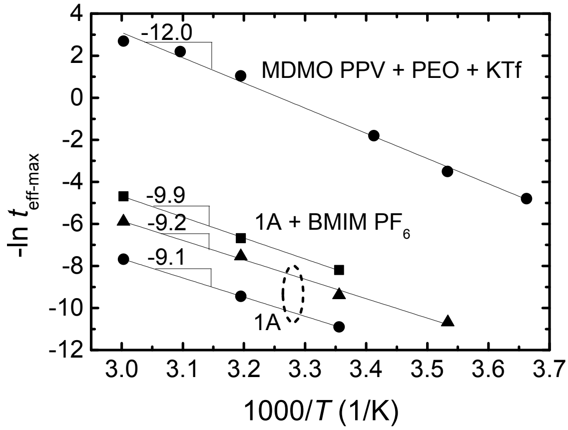

**Figure 7.5 Arrhenius plots of the inverse maximum efficacy time iTMC-LECs with and without the ionic liquid BMIM PF$_6$ and an MDMO-PPV based LEC. The activation energy determined from the fits is 1.03 and 0.78-0.85 eV for the pLECs and iTMC-LECs respectively.**

The transients shown in Figure 7.2 originate from four different cells, which do show a variation in performance that is typical for LECs. To study the temperature dependence more carefully, more measurements were done on a single pLEC and iTMC-LEC. Again the temperature had no effect on the shape of the current, luminance and efficacy transients. When normalized the transients at different temperatures collapse on top of each other. Therefore the turn-on time can be quantified by an arbitrary point on the transients. Here we take the time at which the efficacy reaches a maximum value. The invariance of the shape of the transients, the temperature independent peak efficacy as well as additional PL quantum yield experiments on iTMC-LECs[24] indicate that the EL efficacy is roughly temperature independent. In Figure 7.5 the natural logarithm of the inverse turn-on time was plotted against 1000/*T*. A linear decrease could be observed in both types of devices hinting at an Arrhenius type activation in this temperature range. The activation energy was determined to be ~0.8 eV for the iTMC-LEC and ~1.0 eV for the pLEC. Arrhenius plots for iTMC-LECs without ionic liquid gave similar values for the activation energy (~0.8 eV) despite an order-of-magnitude slower response.

The transient behavior during turn-on is determined by the slowest charge carriers in the LECs: the ions. A way to study the transport of the ions is by looking at the ion conductivity at sub-bandgap voltages. For the pLECs the temperature dependence of the ion conductivity was measured by impedance spectroscopy.[9] For the iTMC-LECs step response experiments were performed because of the relatively slow ionic response.[27] Here the voltage was stepped from 0.0 V to -0.5 V. The relatively large size of the step was necessary to obtain a reasonable signal-to-noise ratio. The negative polarity of the voltage prevents any carrier injection from the electrodes at the used sub-bandgap voltages. The Fourier transform of the time derivative of the step response of the conductance *S* equals the complex admittance. The real part of the admittance gives the conductance as a function of frequency.

Typical ion conductivity spectra at different temperatures of the iTMC- and pLEC are shown in Figure 7.6a and b respectively. All spectra contain a conductivity plateau that spans roughly 2 decades in the frequency range.[9] At higher frequencies an increasing conductivity is observed that can be related to the response of the dielectric. At lower frequencies a decreasing conductivity is observed related to EDL formation that effectively decreases the electric field in the bulk. The minimal value of the measured conductance is $\sim 10^{-10}$ S m$^{-1}$ below which leakage current starts to dominate the experiment. From the conductivity plateau an estimate of the ion conductivity could be extracted as indicated by the arrows. These values are plotted in Figure 7.6c against 1000/*T*. The linear decrease of the two semi-log plots hints again at an Arrhenius type activation. Note that the ion conductivity in the iTMC-LEC (see Figure 7.6a) at room temperature or below could not be determined because of the leakage current. Therefore this data point was ignored in the fitting. The curves were fitted with the same activation energies as extracted from the activation in turn-on time in Figure 7.5. This shows that the ion conductivity and turn-on time have the same activation energy and thus are likely related. This strongly suggests that the turn-on time in both pLECs and iTMC-LECs is determined by the ionic conductivity, i.e. the product of ion density and mobility. This process can be accelerated by e.g. i) increasing the temperature, ii) use of other (smaller) ions, iii) addition of ion-solvating materials like PEO[17, 25, 28] or iv) increasing the applied bias voltage.

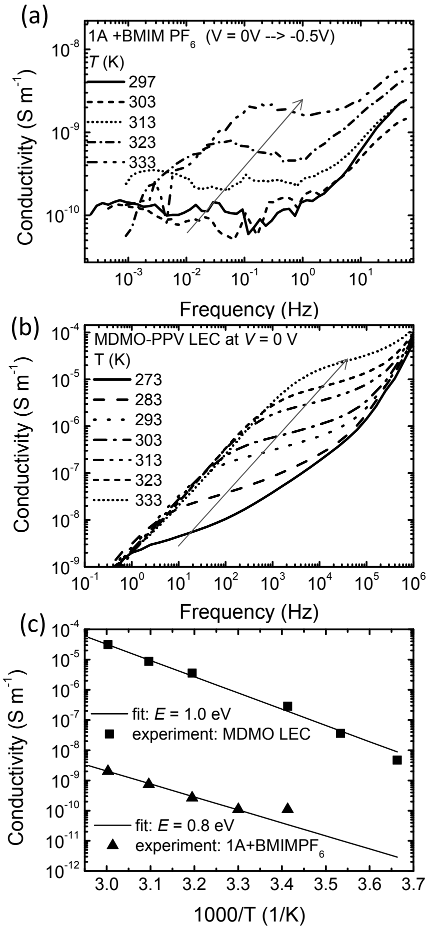

**Figure 7.6 Conductivity spectra for (a) an iTMC-LEC as determined by step response measurements from 0 V to -0.5 V and for (b) a pLEC as determined by impedance spectroscopy. (c) Fits of the ion conductivity by $\sigma(T) = \sigma_0 e^{-E/kT}$ where the activation energy, $E$, was chosen equal to the activation energy determined in Figure 7.5. To fit the data the following values of $\sigma_0$ were used: $1.6 \cdot 10^4$ S m$^{-1}$ and $4.3 \cdot 10^{11}$ S m$^{-1}$ for the iTMC-LEC and pLEC respectively.**

So far the actual value of the determined activation energy has not been discussed. As ion conductivity is the product of ion density and mobility, its activation may also be split up in these two components. The activation in ion density is then related to salt dissociation into ions, the activation in ion mobility can be regarded as activation of viscosity. In polymer LECs the equilibrium between the ion density $n_i$ and salt density $n_s$ can be described by the following expression:[9, 29]

$$n_i^2 = n_s K e^{-\frac{E_S}{kT}}. \tag{7.1}$$

Here $K$ is the mass action law constant. $E_s$ is the binding energy that is generally estimated to lie between 0.2 to 0.6 eV.[9, 29] For this range of binding energies at the used temperature range, $n_s$ can be estimated to be much larger than $n_i$. As the sum of associated and dissociated salt is constant, the thermal activation of the ion density can be roughly described by $n_i \sim \exp(E_s/2kT)$. So effectively 0.1 to 0.3 eV of the 1.0 eV obtained in Figure 7.5 arises from the activation in mobile ion density. That means that the ion mobility has an activation energy of roughly 0.8 eV. The Arrhenius type activation indicates that the ion conduction can be described by a simple ion hopping model. A barrier of ~0.8 eV must be overcome by the ion to reach an adjacent site. This hopping is then facilitated by the motion of PEO chains.[30] In literature activation energies of ~0.9 eV are reported in high molecular weight PEO admixed with $LiCF_3SO_3$.[31] These values are comparable with the energies found in this work. In the iTMC-LECs the salts are of a different nature as they consist of the large iTMC cation and a rather small anion. These ions are not very tightly bound and therefore the dissociation energy is expected to be low. The activation energy observed for the iTMC-LECs may therefore be only related to the activation energy of the ionic mobility. The addition of ionic liquid only decreased the turn-on time as shown in Figure 7.5, whereas the activation energy remained more or less the same. This effect could originate from an increase in the prefactors of the mobility and carrier density. These prefactors may also explain why a higher activation energy is found in the polymer LEC, despite having a smaller turn-on time.

Mixed electronic and ionic conductive materials are used in a variety of systems and devices, such as organic photovoltaics,[32-33] electrochemical,[34] biological and organic bioelectronic,[35-36] systems and devices. Therefore, the results obtained here can be of use to establish the dynamic operation of these devices.

## 7.4 Conclusions

Despite large quantitative differences, the transient behavior of iTMC-LECs and pLECs after switch-on is shown to be qualitatively equal. This further confirms the identical operational behavior in both types of LECs. The qualitative transients are independent on semiconductor- and ion-type and also on the temperature. The thermal activation of both the turn-on time and the ion conductivity in the unbiased state were found to be proportional and could be described by Arrhenius-type activation with an activation energy of ~0.8-1.0 eV. These results clearly demonstrate that pLECs and iTMC-LECs are really behaving as one class of device.

# References

[1] P. Matyba, K. Maturova, M. Kemerink, N. D. Robinson, L. Edman, Nat. Mater. 8 (2009) 672.

[2] M. Lenes, G. Garcia-Belmonte, D. Tordera, A. Pertegas, J. Bisquert, H. J. Bolink, Adv. Funct. Mater. 21 (2011) 1581.

[3] S. van Reenen, P. Matyba, A. Dzwilewski, R. A. J. Janssen, L. Edman, M. Kemerink, J. Am. Chem. Soc. 132 (2010) 13776.

[4] S. B. Meier, D. Hartmann, D. Tordera, H. J. Bolink, A. Winnacker, W. Sarfert, Phys. Chem. Chem. Phys. 14 (2012) 10886.

[5] A. Munar, A. Sandstrom, S. Tang, L. Edman, Adv. Funct. Mater. 22 (2012) 1511.

[6] T. J. Mills, M. C. Lonergan, Phys. Rev. B 85 (2012) 035203.

[7] S. B. Meier, S. Van Reenen, B. Lefevre, D. Hartmann, H. J. Bolink, A. Winnacker, W. Sarfert, M. Kemerink, Adv. Funct. Mater. 23 (2013) 3531.

[8] D. B. Rodovsky, O. G. Reid, L. S. C. Pingree, D. S. Ginger, ACS Nano 4 (2010) 2673.

[9] S. van Reenen, R. A. J. Janssen, M. Kemerink, Adv. Funct. Mater. 22 (2012) 4547.

[10] A. Asadpoordarvish, A. Sandstrom, S. Tang, J. Granstrom, L. Edman, Appl. Phys. Lett. 100 (2012) 193508.

[11] J. F. Fang, P. Matyba, L. Edman, Adv. Funct. Mater. 19 (2009) 2671.

[12] L. Edman, S. Tang, J. Phys. Chem. Lett. 1 (2010) 2727.

[13] A. Sandstrom, P. Matyba, L. Edman, Appl. Phys. Lett. 96 (2010) 053303.

[14] Z. Yu, M. Wang, G. Lei, J. Liu, L. Li, Q. Pei, J. Phys. Chem. Lett. 2 (2011) 6.

[15] D. Tordera, S. Meier, M. Lenes, R. D. Costa, E. Orti, W. Sarfert, H. J. Bolink, Adv. Mater. 24 (2012) 897.

[16] D. Tordera, M. Delgado, E. Orti, H. J. Bolink, J. Frey, M. K. Nazeeruddin, E. Baranoff, Chem. Mater. 24 (2012) 1896.

[17] Y. Shao, G. C. Bazan, A. J. Heeger, Adv. Mater. 19 (2007) 365.

[18] B. Gautier, J. Gao, Appl. Phys. Lett. 101 (2012) 093302.

[19] R. D. Costa, E. Orti, H. J. Bolink, F. Monti, G. Accorsi, N. Armaroli, Angew. Chem. Int. Ed. 51 (2012) 8178.

[20] C. V. Hoven, H. P. Wang, M. Elbing, L. Garner, D. Winkelhaus, G. C. Bazan, Nat. Mater. 9 (2010) 249.

[21] I. V. Kosilkin, M. S. Martens, M. P. Murphy, J. M. Leger, Chem. Mater. 22 (2010) 4838.

[22] R. D. Costa, E. Orti, H. J. Bolink, S. Graber, S. Schaffner, M. Neuburger, C. E. Housecroft, E. C. Constable, Adv. Funct. Mater. 19 (2009) 3456.

[23] M. A. Baldo, R. J. Holmes, S. R. Forrest, Phys. Rev. B 66 (2002) 035321.

[24] S. van Reenen, T. Akatsuka, D. Tordera, M. Kemerink, H. J. Bolink, J. Am. Chem. Soc. 135 (2013) 886.

[25] C. H. Lyons, E. D. Abbas, J. K. Lee, M. F. Rubner, J. Am. Chem. Soc. 120 (1998) 12100.

[26] H. J. Bolink, L. Cappelli, E. Coronado, M. Gratzel, E. Orti, R. D. Costa, P. M. Viruela, M. K. Nazeeruddin, J. Am. Chem. Soc. 128 (2006) 14786.

[27] D. D. Macdonald, Electrochim. Acta 51 (2006) 1376.

[28] Q. B. Pei, G. Yu, C. Zhang, Y. Yang, A. J. Heeger, Science 269 (1995) 1086.

[29] D. L. Smith, J. Appl. Phys. 81 (1997) 2869.

[30] M. S. Mendolia, G. C. Farrington, Chem. Mater. 5 (1993) 174.

[31] C. J. Leo, G. V. S. Rao, B. V. R. Chowdari, Solid State Ionics 148 (2002) 159.

[32] R. Hany, B. Fan, F. A. de Castro, J. Heier, W. Kylberg, F. Nuesch, Progress in Photovoltaics 19 (2011) 851.

[33] M. S. Su, H. C. Su, C. Y. Kuo, Y. R. Zhou, K. H. Wei, J. Mater. Chem. 21 (2011) 6217.
[34] S. Kim, S. Yamaguchi, J. A. Elliot, MRS Bull. 34 (2009) 900.
[35] R. M. Owens, G. G. Malliaras, MRS Bull. 35 (2010) 449.
[36] M. Berggren, A. Richter-Dahlfors, Adv. Mater. 19 (2007) 3201.

# **Chapter 8** Photoluminescence quenching by electrochemical doping

---

*An important loss mechanism in organic electroluminescent devices is exciton quenching by polarons. Gradual electrochemical doping of various conjugated polymer films was studied here to determine the doping density dependence of photoluminescence quenching. Electrochemical doping was achieved by contacting the film with a solid electrochemical gate and an injecting contact. A sharp reduction in photoluminescence was observed for doping densities between* $1\cdot10^{24}$ *and* $2\cdot10^{25}$ $m^{-3}$*. The doping density dependence is quantitatively modeled by exciton diffusion in a homogeneous density of polarons followed by either Förster resonance energy transfer or charge transfer. Both mechanisms need to be considered to describe polaron-induced exciton quenching. Thus, to reduce exciton-polaron quenching in organic optoelectronic devices, both mechanisms must be prevented by reducing the exciton diffusion, the spectral overlap, the doping density, or a combination thereof.*

*Part of the work presented in this chapter has been published: S. van Reenen, M. V. Vitorino, S. C. J. Meskers, R. A. J. Janssen, M. Kemerink, Phys. Rev. B 89 (2014) 205206.

## 8.1 Introduction

Optimization of the external quantum efficiency (EQE) for charge to emitted photon conversion is presently one of the major challenges in improving organic light-emitting devices. At high luminance levels the efficiency typically rolls off due to exciton quenching.[1] Excitons are electron-hole pairs with a luminescent lifetime dependent on the type of semiconductor and spin state that can be either a singlet or triplet. They are either formed by the absorption of a photon or by the meeting of injected electrons and holes. Excitons can be quenched in the presence of sufficiently large electric fields,[2] by other excitons[3] or by polarons[4]. Which of these is dominant depends on the device and the emitter used.

Exciton quenching by polarons typically occurs in devices in which high carrier densities are present close to the region where excitons are formed. Devices with such high carrier densities are not only light-emitting electrochemical cells (LECs),[5] but also light-emitting field-effect transistors (LEFETs)[6] or organic electrochemical light-emitting transistors (OECTs).[7] In organic light-emitting diodes (OLEDs), exciton-polaron quenching becomes significant at high brightness, necessary for lighting and display applications.[1] Also in organic photovoltaic cells (OPV) exciton quenching is found to be an important loss process.[4] To address this loss process efficiently, it is necessary that the underlying mechanism is known. In literature attention is mainly given to Förster resonance energy transfer (FRET) as the main loss mechanism.[4, 8-10] This however does not exclude other competing loss processes like charge transfer (CT).[10-11]

Here we present an experimental study of quenching of optically induced excitons by polarons introduced by controlled electrochemical doping.[12-13] The doping density was determined by the integration of the current and confirmed by bleaching of the light-emitting polymer. By this method the doping dependence of exciton quenching was determined for several prototypical conjugated polymers. The doping dependence was then analytically described by two alternative processes: 1) exciton diffusion followed by FRET to the polaron associated with the dopant or 2) exciton diffusion followed by CT between the polaron and the exciton. As both models successfully fit the data, both processes can account for the observed exciton-polaron quenching. Doping densities at which quenching occurs range between $1 \cdot 10^{24}$ and $2 \cdot 10^{25}$ $m^{-3}$, setting an upper limit for the doping, or charge density at or near the recombination zone in organic optoelectronic devices.

## 8.2 Materials and methods

*Device preparation:* The devices in this study consist of a bilayer of a conjugated polymer and an electrolyte sandwiched between an indium tin oxide (ITO) and a Au electrode. A schematic of the device is shown in Figure 8.1a. The conjugated polymers are either i) phenyl-substituted poly(p-phenylene vinylene) copolymer (SY-PPV, Merck, catalogue number PDY-132), commonly termed "Super Yellow", ii) poly[2-methoxy-5-(3',7'-dimethyloctyloxy)-1,4-phenylenevinylene] (MDMO-PPV, $M_w > 1\times10^6$ g mol$^{-1}$, American Dye Source) or iii) poly(3-hexylthiophene) (P3HT, > 98% head to tail, $M_n$ = 54,000–75,000 g mol$^{-1}$, Plextronics, purchased from Aldrich). The PPV variants and P3HT were deposited by first dissolving them in chloroform or chlorobenzene, respectively, to obtain 10 mg ml$^{-1}$ solutions, followed by spin coating to yield ~100 nm films on top of cleaned ITO substrates. The electrolyte is a mixture of poly(ethylene oxide) (PEO, $M_w = 5\text{x}10^5$ g mol$^{-1}$, Aldrich) and potassium triflate ($KCF_3SO_3$, 98 %, Aldrich) at a weight ratio of 5:1. The electrolyte was drop coated from acetone on top of the polymer film, which was placed on a hotplate at $T$ = 45 $^{o}$C. The thickness of the solid electrolyte droplet was 2-3 µm. Gold electrodes were subsequently thermally deposited in a deposition chamber in a glovebox under a vacuum of ~$10^{-6}$ mbar. The thickness of the gold layer was 100 nm. Alternatively, to enable absorption measurements by transmission, a 30 nm semi-transparent gold electrode was used. The active area of the device, defined by a shadow mask, was 0.161 cm$^2$. All device manufacturing was done under nitrogen atmosphere.

*Electrical characterization:* Current-voltage characteristics were measured by a Keithley 2400 sourcemeter. For the detection of photoluminescence during electrochemical doping an Edinburgh time-resolved fluorescence spectrometer FLS920 was used. For these measurements the device was put in a closed nitrogen-filled box with a glass window. For the detection of the absorption during electrochemical doping, a Shimadzu UV-1601PC UV/visible scanning spectrophotometer was used. For these measurements the device was put in a closed nitrogen-filled box with two windows to allow for measurements in transmission. Absorption measurements were also performed by measurement of the reflection. In this case, a device with a 100 nm gold top electrode was used.

## 8.3 Experimental results

To investigate the polaron density dependence of luminescence quenching in conjugated polymers, a solid-state electrochemical cell was fabricated as described above. A schematic of the device layout is shown in Figure 8.1a. The device contains a 100 nm film of conjugated polymer. On the bottom side this film is contacted by a transparent ITO electrode to allow for electronic charge carrier injection. The top side of the film is electrochemically gated to allow ionic charge carrier injection. Dependent on the sign of the applied bias voltage, the cell was electrochemically n-type or p-type doped. Schematic illustrations of both types of doping are drawn in Figure 8.1b and c. This doping can be viewed as electrostatic stabilization of injected electronic charges in the conjugated polymer by injected anions or cations. Note, in this context, the strong similarity to the dynamic doping process occurring in LECs. [14-15]

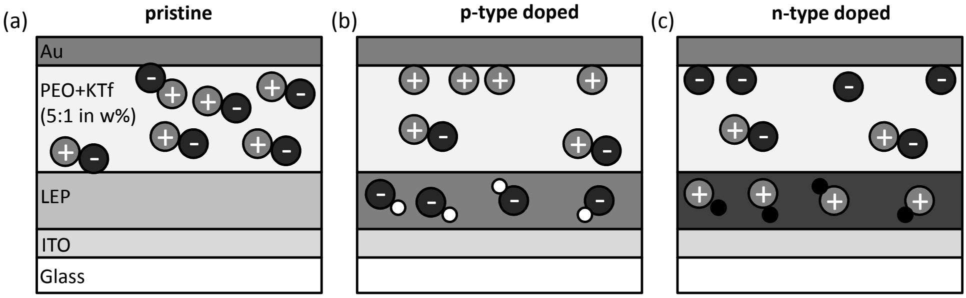

**Figure 8.1 (a) Schematic device layout for electrochemical doping of light-emitting polymers (LEP). The same schematic after p-type and n-type electrochemical doping is shown in (b) and (c) respectively. Dark gray, light gray, white, and black dots represent anions, cations, holes, and electrons, respectively.**

To determine the doping density dependence of the exciton quenching in the conjugated polymer films, two experiments were performed simultaneously: i) the change in the photoluminescence of the illuminated film was measured and ii) the polymer film was gradually, electrochemically doped. To confirm that doping of the conjugated polymer indeed took place, the optical absorption was monitored in an additional experiment.

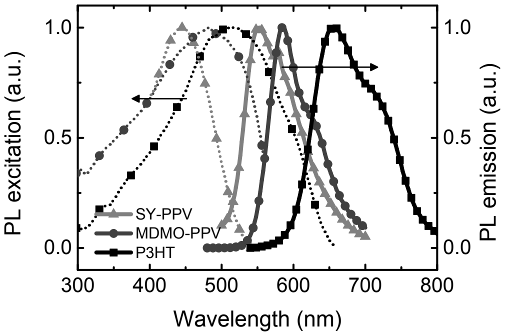

**Figure 8.2 PL-excitation and PL-emission spectra of SY-PPV, MDMO-PPV, and P3HT. For the PL excitation measurements a detection wavelength of 550 nm was used. For the PL emission measurements an excitation wavelength of 440 nm was used.**

Prior to the experiment photoluminescence (PL) excitation and emission spectra were determined for the different polymer films (Figure 8.2). The wavelengths at which the spectra show a peak were used as the excitation and emission wavelength during the transient quenching experiment. To compensate for the background emission an ITO-electrolyte-Au device was prepared and characterized at the same emission and excitation wavelengths. During the doping experiments, that are explained below, the normalized change in PL was determined as well. In Figure 8.3, it is indicated by the solid line. As the doping progresses in time, the PL is found to decrease.

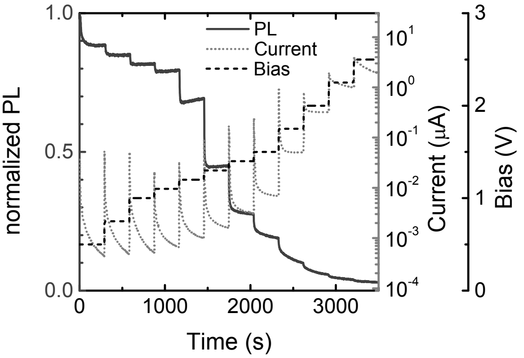

**Figure 8.3 PL (solid line), applied bias voltage (dashed line), and current (dotted line) transients during p-type doping of SY-PPV. The device was excited at *λ* = 440 nm. PL was detected at *λ* = 550 nm.**

Regarding the doping experiments, a stepwise increasing bias voltage was applied to the contacts as shown by the dashed line in Figure 8.3. Each bias level was maintained for approximately 300 s to allow doping to saturate. A typical trace of the current passing through the cell is indicated on a logarithmic scale by the dotted line in Figure 8.3. After each bias voltage step, the current is observed to quickly increase, followed by a slow decrease towards a constant value. This constant value is attributed to leakage and cannot be related to ongoing electrochemical doping: ions are blocked by the ITO electrode, and electronic carriers are blocked by the electrolyte, so the electronic current should ultimately vanish when maintaining a constant bias voltage. This interpretation is substantiated by the stabilization of the PL quenching signal (light gray line) after each voltage step on the same time scale as on which the current stabilizes. The fact that the PL signal does not completely stabilize indicates either a slow redistribution of doping or ongoing, slow injection of ions into the semiconductor. Leakage currents may be related to Au diffused into the electrolyte, forming conducting pathways. However, for example in Ref. 16 we have observed a penetration of Cs into a soft polymer layer by only ~15 nm. The much lower reactivity of Au may, however, increase the penetration depth. By subtracting the leakage current from the overall current at each bias voltage, the doping current is determined. Integration of this current with respect to time then gives the amount of doping put into the 100 nm film. By dividing by the volume of the film the doping density is obtained. As the leakage current can only be estimated, an error in the doping density arises which may approximately be a factor 2, as deduced from repetitive measurements (see supplemental Figure 8.9a in paragraph 8.6).

During doping of the conjugated polymer, the same amount of ions, oppositely charged, is transported towards the electrolyte-electrode interface and must be electrostatically compensated. We assume electric double layer formation of 1 nm at a completely flat interface would give rise to a significant voltage drop of ~3 V,[17] which is equal to the maximum applied potential. Clearly this assumption is not correct as a bias voltage of 3 V is found to be sufficient to dope the organic semiconductor so that a significant bleaching peak in the absorbance occurs, as is discussed below. The absence of large voltage drops at the electrolyte-electrode interface may be related to a large irregular surface area induced by diffusion of Au into the electrolyte during deposition.[16] Furthermore diffusion of ions through Au during the experiment is also possible, and has been reported before by Matyba et al.[14]

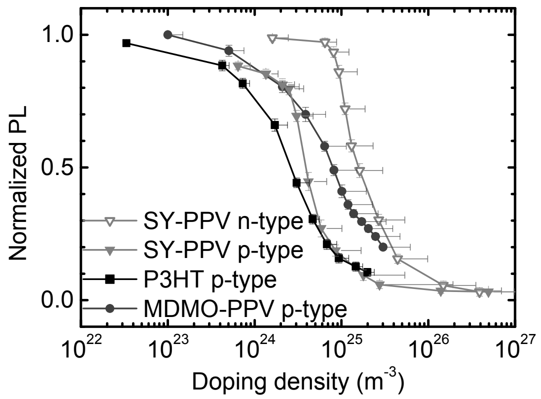

**Figure 8.4 PL quenching as a function of doping density for SY-PPV, MDMO PPV, and P3HT.**

Combination of the results in Figure 8.3 allowed characterization of the doping density dependence of the PL quenching process. This was done similarly for n- and p-type doping of SY-PPV as well as for p-type doping of MDMO-PPV and P3HT. The results are shown in Figure 8.4. The vertical error bars are related to the PL signal not being stable yet. In each case a relatively strong decrease in PL emission occurs at doping densities between $1{\cdot}10^{24}$ and $2{\cdot}10^{25}$ $m^{-3}$, which corresponds to doping levels of approximately 0.1 % and 1.0 % when assuming a density of states of $10^{27}$ $m^{-3}$.[18] The doping density is determined by integrating the current after correction for the leakage current. The magnitude of the leakage current is however uncertain. Therefore the doping density was also calculated without accounting for the leakage current. The relative contribution of leakage and doping current (as shown in supplemental Figure 8.9b in paragraph 8.6) shows that the doping and leakage current increase roughly in parallel. This limits the relative error in the extracted doping concentration, which is the important quantity in the present discussion. To quantify the effects of the leakage current, we added corresponding error margins in Figure 8.4. The indicated upper limit is given by the absolute maximum of possible doping density in case we correct for no or an underestimated (for P3HT) leakage current. The data point itself is based on the (over)estimated leakage current and forms therefore a lower limit. A reference measurement on a cell without organic semiconductor is included in supplemental Figure 8.10. Neither indications of side-reactions were observed in the measured current nor any change in color. More importantly, the leakage currents found here are approximately an order of magnitude below the currents observed in the full device, i.e. with the semiconductor present, indicating that the latter is dominated by doping and not by leakage, in line with our arguments above. In more detail, in supplemental Figure 8.10 we calculated the associated charge densities by integration of the leakage currents. The integrated carrier density in the devices with organic semiconductor is at least larger by an order of magnitude than without the semiconductor, demonstrating that the extracted doping densities are maximally overestimated by 10 %.

For accurate determination of the doping density a homogeneous doping distribution is required. The incomplete stabilization of the PL signal observed in Figure 8.3 indicates that doping redistributes. Likely, ions are injected in the film in a filamentary or otherwise inhomogeneous manner, causing strong quenching in those regions. However, the corresponding density gradients are unstable and a redistribution of ions will follow, lowering the maximum concentrations and reducing the quenching. The tendency of ions to redistribute is related to drift and diffusion, both in favor of a homogeneous distribution. Another, indirect, indication that the doping is relatively homogeneous is the abrupt reduction of PL versus doping density as shown in Figure 8.4 for SY-PPV. Inhomogeneity, i.e. the formation of doped and undoped domains would correspond to a more gradual reduction of the PL signal. The absence of substantial inhomogeneity is finally substantiated by optical inspection of the device darkening during doping, which was found to be homogeneous within the experimental resolution of $\sim 10^2$ µm.

Comparison between p- and n-type doping in SY-PPV demonstrates that p-type doping quenches at lower carrier densities. This is in line with observations in planar LECs. In such cells both types of doping are present simultaneously. The n-type doped regions of PPV are typically observed to quench less than the p-type doping regions.[15] Here, we show that this behavior can at least partially be explained by stronger PL quenching by p-type doping. A comparison between P3HT and MDMO-PPV shows only small differences in shape and critical doping density of PL quenching by p-type doping. N-type doping in MDMO-PPV and P3HT occurred at relatively large bias voltages at which electrochemical reactions with the electrolyte distort the measurements. Therefore, these measurements were not included. The functional shape of the quenching curve of P3HT and MDMO-PPV seems to be different from that of SY-PPV. We return to this at the end of the discussion section.

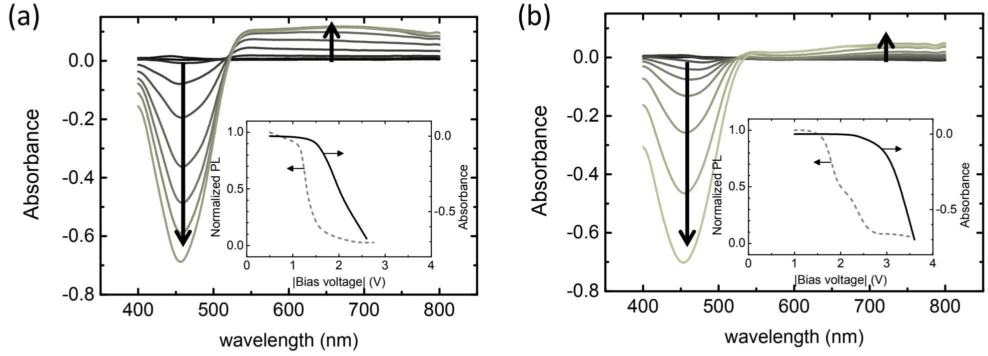

**Figure 8.5 Absorbance of (a) p- and (b) n-type doping in SY-PPV at different doping levels. The absorbance by doping is determined by subtracting the absorbance at any bias voltage by the absorbance of the unbiased cell: $A_{\text{doping}} = A(V_{\text{bias}}) - A(V_{\text{bias}} = 0)$. A semi-transparent Au top electrode was used with a thickness of 30 nm. The black arrows indicate the change in absorbance for larger doping densities, starting at zero doping. The insets show the normalized PL (gray dashed) and the absorbance (black solid) by doping as a function of applied bias.**

Next to the effect of PL quenching induced by doping, the absorption spectrum of the dopants was also measured in SY-PPV. The change in absorbance by doping of SY-PPV is plotted in Figure 8.5(a) and (b) for p- and n-type doping, respectively. The negative differential absorbance at $\lambda = 460$ nm is at the same position as the absorption spectrum of SY-PPV (dotted light gray line in Figure 8.2). The effect is therefore related to bleaching: doping fills the density of states, reducing the number of sites available for the formation of excitons.[12] This bleaching is an important observation as it indicates filling of the density of states of the light-emitting polymer. The enhanced transmission due to ground state bleaching of $\Delta T/T \approx 2.1$ (see Figure 8.5(a); the trace where a bleaching peak at $\lambda = 460$ nm is observed of A = -0.5, where $\Delta T/T = 10^{-A}-1$) was measured at an electrically determined charge density between $5{\cdot}10^{26}$ and $3{\cdot}10^{27}$ $\text{m}^{-3}$. To estimate whether these values are reasonable, we made a comparison with values obtained from Ref. 19-20, where a relative enhancement in transmission by $6{\cdot}10^{-4}$ was observed at a (photoexcited) charge density of $1{\cdot}10^{24}$ $\text{m}^{-3}$. Making the reasonable assumption that bleaching is linear in density, densities of $5{\cdot}10^{26}$ and $3{\cdot}10^{27}$ $\text{m}^{-3}$ would then lead to $\Delta T/T$ between 0.3 and 1.8, respectively. This value is in more than reasonable agreement with the $\Delta T/T \approx 2.1$ we measure, especially since we ignore differences, for example in site density, between the materials. This confirms that electrochemical doping of the conjugated polymer indeed takes place and that the calculated doping density by the integration of the current is reliable.

To determine whether the PL quenching in Figure 8.4 originates from the reduced optical density as observed in Figure 8.5, the relative absorbance and the normalized PL are plotted in the same graph in the insets in Figure 8.5a and b. For both p- and n-type doping of SY-PPV, bleaching sets in clearly after the majority of PL has already been quenched. Hence PL quenching and absorption bleaching are independent processes in this respect. At larger wavelengths in Figure 8.5a and b absorption bands appear for both n- and p-type doping. These bands sit partially at the same wavelength as the PL spectrum of SY-PPV (solid light gray line in Figure 8.2) and are attributed to polaron absorption.[12]

## 8.4 Discussion

To interpret the results shown in Figure 8.4, first the effect of applying a bias voltage to the device (see Figure 8.1a) needs to be understood. Initially, the PEO is filled with ions whereas the PPV is considered empty. The difference in chemical potential of the ions in both layers is expected to be strongly in favor of the PEO film due to its chemical structure. This difference forms an ion injection barrier which impedes ion injection into the PPV film. This difference across the PEO-PPV interface is however opposed by i) a difference in ion density resulting in an ion diffusion current and ii) a difference in electrostatic potential due to the bias voltage applied to the contacts. Increasing the applied bias voltage results in an increased ion density at the interface, enlarging both the potential drop and the density gradient at the interface. This, in turn, drives ions into the semiconductor. In the experiment the bias voltage is increased stepwise and ion injection is observed at sufficiently large voltages. $K^+$ or $CF_3SO_3^-$ injection in SY-PPV are observed to start at $|V_{\text{bias}}| \approx 1.6$ V and 1.2 V for n- and p-type doping, respectively, see insets in Figure 8.5a and b.

The exciton quenching process in Figure 8.4 is the result of an interaction between a polaron, stabilized by an ionic dopant, and an exciton. No significant external electric field, which could also contribute to exciton quenching, is expected within the SY-PPV layer: the boundary conditions induced by the electrode and the electrolyte result in a homogeneous pile-up of ionic and electronic carriers in the SY-PPV film. Once injected by, respectively, the electrolyte or the electrode, the carrier cannot leave the film through the other contact. This means that ultimately the net electronic and ionic current must be zero. The net current is determined by drift and diffusion, which should thus cancel or both be equal to zero. As the doping mechanism leads to electronic and ionic carriers having the same density profile, diffusion is in the same direction for both types of carriers. Drift, however, is in opposite directions for both types of carriers due to the difference in charge. Hence, to obtain a zero net electronic and ionic current the drift and diffusion components of the ionic dopants and the polarons must both be zero. The zero diffusion current implies that constant concentrations for electronic and ionic carriers are present. These qualitative arguments are confirmed by numerical drift-diffusion simulations shown in supplemental Figure 8.11.

Regarding exciton quenching by polarons, two alternative processes shall be considered: Förster resonance energy transfer and charge transfer. Other alternatives like multipolar interactions[21] were not considered. Diffusion of the exciton through the film prior to quenching must, however, be accounted for. Polaron diffusion was found to be negligible compared to exciton diffusion, as will be justified below in section C. In Figure 8.6 a schematic representation is given of both models. In the next two paragraphs these models are discussed in detail and will be related to our experimental findings.

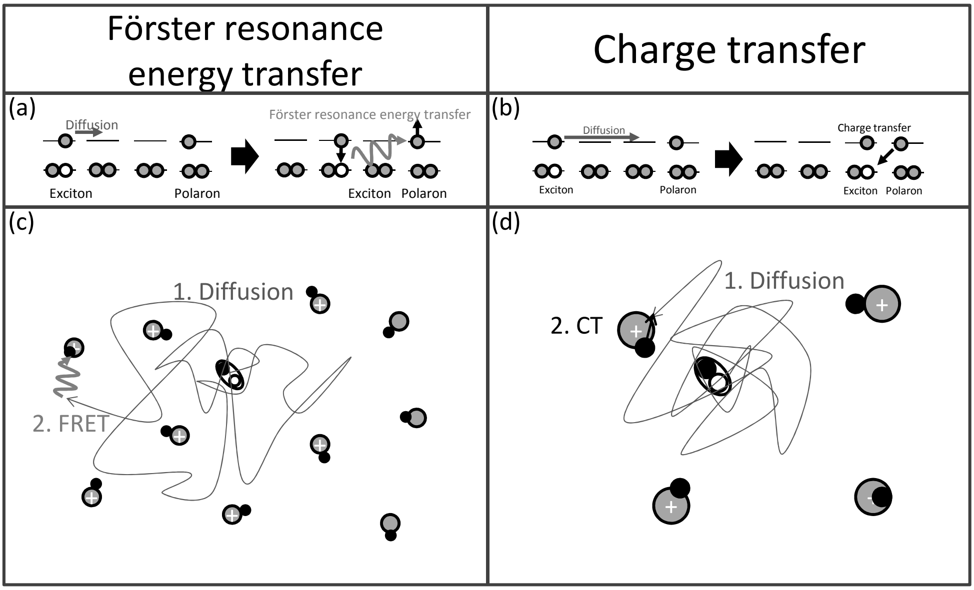

**Figure 8.6 Schematic representation of the considered exciton quenching mechanisms in a random distribution of doping sites: (a,c) Förster resonance energy transfer and (b,d) charge transfer. Both mechanisms are preceded by exciton diffusion.**

### 8.4.1 Förster resonance energy transfer (FRET)

Resonance energy transfer is an energy transfer between a donor and an acceptor.[22] In our case the acceptor is an electron- or hole-polaron that is excited to a higher state, as illustrated in Figure 8.6a. Since the donor loses its excitation by to the acceptor by the coupling of transition dipoles it is a non-radiative loss process. Spectral overlap, however, is required between the emission spectrum of the donor and the excitation spectrum of the acceptor to make the process efficient. The spectra in, respectively, Figure 8.2 and Figure 8.5 show that this is indeed the case in SY-PPV for exciton emission and polaron excitation. In the next subsections two possible scenarios for FRET are explained.

### 8.4.1.1 Single pair of fixed dipoles

The most basic description of FRET is between a donor and an acceptor that are two dipoles, fixed in their relative orientation and position. The transfer rate constant derived by Förster is expressed as

$$k_T = \frac{1}{\tau_D^0}\left[\frac{R_0}{r}\right]^6, \tag{8.1}$$

where $\tau_D^0$ is the lifetime of the donor in absence of energy transfer, *r* is the distance between donor and acceptor, and $R_0$ is the critical distance at which the probability of transfer and decay of the donor is equal. The Förster radius $R_0$ can be determined experimentally and is expressed as

$$R_0^6 = \frac{9000(ln\,10)\kappa^2\Phi_D^0}{128\pi^5 N_A n^4}\int_0^\infty I_D(\lambda)\varepsilon_A(\lambda)\lambda^4 d\lambda, \tag{8.2}$$

where $\kappa^2$ is the orientational factor, $\Phi_D^0$ is the fluorescence quantum yield of the donor without transfer, *n* is the average refractive index of the medium, $I_D(\lambda)$ is the normalized fluorescence spectrum of the donor, and $\varepsilon_A(\lambda)$ is the molar absorption coefficient of the acceptor.

In our case, this description of FRET does not apply as the formed exciton is likely to be mobile and is excited in a film filled with multiple acceptors. Therefore, exciton diffusion and multiple acceptors need to be taken into account for a correct description.

### 8.4.1.2 Exciton diffusion with multiple acceptors

The exciton quenching process can be described by diffusion with a sink term, $k(r) = a/r^6$, with the correct distance dependence between the donor and acceptor, *r*.[22-23] The donor and acceptor are approximated as point dipoles, i.e. excluding delocalization of the polaron and exciton. For excitons a delocalization over several monomer subunits may be expected (e.g. ~1 nm[24]). Polarons compensated by ions at relatively low doping levels of ~1% are more localized due to the ionic Coulomb trap (i.e. < 1 nm).[13] The diffusion equation then becomes

$$\frac{\partial C_E(r,t)}{\partial t} = D_{exc}\nabla^2 C_E(r,t) - k(r)C_E(r,t), \tag{8.3}$$

where $C_E$ is the exciton density and $D_{exc}$ the exciton diffusion coefficient. Gösele *et al.* found the following approximate solution to this problem:[23]

$$k_T(t) = 4\pi R_{eff} D_{exc}\left[1 + \frac{R_{eff}}{(\pi D_{exc} t)^{1/2}}\right], \tag{8.4}$$

where

$$R_{eff} = 0.676\left(\frac{R_0^6}{\tau_D^0 D_{exc}}\right)^{1/4}. \tag{8.5}$$

The fluorescence decay after excitation can then be described by

$$\frac{i(t)}{i(0)} = \exp\left\{\frac{1}{\tau_D^0} + C_A\int_0^t k_T(t')dt'\right\} = \exp\left(-\frac{1}{\tau_D^0}t\right. \tag{8.6}$$

$$\left.-4\pi R_{eff} D_{exc} C_A t - 2\cdot 4\sqrt{\pi D_{exc}} R_{eff}^2 C_A \sqrt{t}\right),$$

where $C_A$ is the density of the absorbing species. The ratio in fluorescence quantum yield with ($\Phi_D$) and without ($\Phi_D^0$) the presence of a quencher then becomes:

$$\frac{\Phi_D}{\Phi_D^0} = \frac{\int_0^\infty\left[\exp\left(-\frac{1}{\tau_D^0}t - 4\pi R_{eff} D_{exc} C_A t - 2\cdot 4\sqrt{\pi D_{exc}} R_{eff}^2 C_A \sqrt{t}\right)\right]dt}{\int_0^\infty\left[\exp\left(-\frac{1}{\tau_D^0}t\right)\right]dt}. \tag{8.7}$$

To fit Eq. (8.7) to the experimental data, the following values were taken from literature: $k_{\text{decay}} = 1/\tau_D^0 = 1.54\ \text{ns}^{-1}$ found in SY-PPV and $D_{\text{exc}} = 3\cdot 10^{-8}\ \text{m}^2\,\text{s}^{-1}$ found in the related NRS-PPV.[25-26] These fits are shown in Figure 8.7a (solid black lines) for different values of $R_0$ ranging from 1 to 4 nm. The dashed gray lines indicate similar fits with the only difference that $D_{\text{exc}} = 0\ \text{m}^2\text{s}^{-1}$ to illustrate the effect of resonance energy transfer quenching of immobile excitons excited in a semiconductor that is homogeneously filled with polarons. As expected, diffusion significantly enhances the likelihood of quenching. As quenching occurs at distances (~2.5 nm) larger than the size of an exciton delocalized over several monomer subunits (~1 nm), the point dipole approximation gives a valid estimation of the polaron-induced exciton quenching with an error margin of 1 nm.

### 8.4.2 Charge transfer (CT)

To derive an expression of the fluorescence quantum yield of the donor as a function of the doping density, the following simple model was used. An exciton diffuses step-wise through the semiconductor. After each step the exciton has a probability to decay radiatively, $P_{\text{decay}}$, or a probability, $P_{\text{quench}}$, to arrive next to a polaron, which results in quenching of the exciton when the polaron recombines with the charge of opposite polarity in the exciton, as illustrated in Figure 8.6b and d. Here we assume that polarons and excitons can only occupy one site and that quenching always takes place when the exciton is next to a polaron as CT is a relatively fast process.[27] By comparison of these probabilities, the probability of exciton quenching can be determined as a function of doping density.

The exciton quenching probability after one diffusion step can be related to the ratio of doped site density $n_{\mathrm{doping}}$ and the density of states $n_{\mathrm{DOS}}$:

$$P_{quench} = A\frac{n_{doping}}{n_{DOS}}, \tag{8.8}$$

where $A$ is the average number of new neighboring sites that can quench the exciton. The value of $A$ depends on the coordination of the excitons and polarons. In the first instance, a one-dimensional system is assumed for the polymer system. To determine the quenching probability as a function of doping density, $n_{\mathrm{DOS}} = 6\cdot10^{26}$ m$^{-3}$ and $A = 2$ were taken.[18] Furthermore we assumed 'physical' contact between exciton and charge is required for quenching and $n_{\mathrm{DOS}}^{-1}$ equals the mean volume of a site –we assume excitons and polarons sit on sites of equal volume. Clearly, this is a gross simplification as some tunneling is likely to be relevant to quenching, implying the presence of a spatial gap and thus a reduced site volume. Here, $n_{\mathrm{DOS}}^{-1}$ is thus a coarse upper limit to the 'real' exciton and polaron volumes. The used value for $n_{\mathrm{DOS}}$, $6\cdot10^{26}$ m$^{-3}$, puts an upper limit just above 1 nm$^3$, consistent with the length scales of a delocalized exciton.[24]

The radiative decay rate of a single exciton was set to a fixed rate $k_{\mathrm{rad,decay}}$. For an ensemble of excitons this gives rise to an exponential radiative decay with a radiative decay rate $k_{\mathrm{rad,decay}}$ when exciton-exciton interactions are ignored. The time of a single diffusion step is set equal to the time needed to overcome the distance of one neighboring site $r = n_{DOS}^{-1/3}$ by diffusion. The diffusion length $r$ is, in turn, related to the exciton diffusion constant $D_{\mathrm{exc}}$ as $r = \sqrt{2D_{exc}t_{step}}$. The radiative decay probability during this single diffusion step can then be described by

$$P_{rad,decay} = 1 - exp\left(-\frac{k_{rad,decay}}{2D_{exc}\cdot n_{DOS}^{2/3}}\right). \tag{8.9}$$

To determine the radiative decay probability, the following values were taken from literature: $k_{\mathrm{rad,decay}} = 1.54$ ns$^{-1}$ and $D_{\mathrm{exc}} = 3\cdot10^{-8}$ m$^2$ s$^{-1}$.[25-26]

Under the assumption that initial and final sites are independent the fluorescence quantum yield can then be determined by:

$$\frac{\Phi_D}{\Phi_D^0} = \frac{P_{rad,decay}}{P_{quench}+P_{rad,decay}}, \tag{8.10}$$

A fit of this function for the given parameters is shown in Figure 8.7b by the solid black lines for $A$ = 6, 4, 3, 2 neighbors. The dashed gray lines indicate similar fits with the only difference that $D_{\mathrm{exc}} = 0$ m$^2$ s$^{-1}$ to illustrate the effect of CT quenching of immobile excitons excited in a semiconductor that is homogeneously filled with polarons. An alternative approach to determine the effect of CT on the fluorescence quantum yield is by using Eq. (8.3) with a sink term $k \sim \exp(-r/b)$,[10, 28] which must be solved numerically. An analytical expression can however be found when solving Eq. 3 for $k$ = 0 and the boundary condition that the probability of exciton quenching equals 1 when the exciton is inside a sphere with radius $R_c$ around the acceptor.[22] A fit based on this model for $R_c = \frac{1}{2} n_{DOS}^{-1/3}$, $k_{rad,decay}$ = 1.54 ns$^{-1}$ and $D_{exc}$ = 3·10$^{-8}$ m$^2$ s$^{-1}$ gives fits qualitatively similar to the fits based on Eq. (8.10).[25-26]

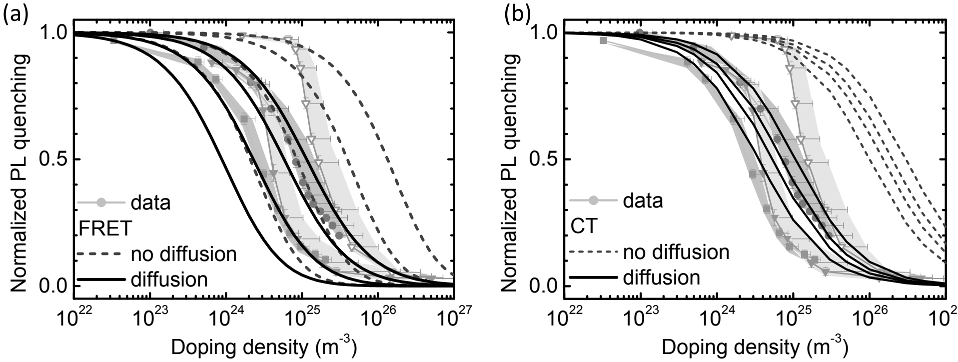

**Figure 8.7 Fits (lines) of the PL quenching data (symbols + shaded region) of n-type doping of SY-PPV (down triangles) and p-type doping of SY-PPV (up triangles), MDMO-PPV (squares) and P3HT (dots). (a) Fits following the resonance energy transfer model without diffusion are dashed gray (see Eq. (8.7); $D_{exc}$ = 0 m$^2$ s$^{-1}$; $R_0$ = 4, 2.5, 1.5, 1.0 nm from left to right) and with diffusion solid black (see Eq. (8.7); $D_{exc}$ = 3·10$^{-8}$ m$^2$ s$^{-1}$; $R_0$ = 4, 2.5, 1.5, 1.0 nm from left to right). (b) Fits following the charge transfer model without diffusion dashed gray (see Eq. (8.10); $D_{exc}$ = 0 m$^2$ s$^{-1}$; A = 2, 3, 4, 6 neighbors from left to right) and with diffusion solid black (see Eq. (8.10); $D_{exc}$ = 3·10$^{-8}$ m$^2$ s$^{-1}$; A = 2, 3, 4, 6 neighbors from left to right).**

### 8.4.3 Comparison of FRET and CT

Comparison between the fits related to FRET and CT in Figure 8.7 shows that there is little qualitative difference in the doping dependence between the two quenching mechanisms. This demonstrates that instead of the actual quenching model, FRET or CT, the homogeneous density of quenchers determines the qualitative doping density dependence of the exciton quenching. In fact it is not at all unlikely that both processes, CT and FRET, take place simultaneously. Given the fact that the doping density dependence is slightly different for both models, the relative contributions of both processes would also be dependent on the doping density. Regarding diffusion, also polaron diffusion may play a role in exciton quenching. This is however only the case for high mobility semiconductors like P3HT. The exciton diffusion itself can also be expected to be doping density dependent. An indication for this is discussed below.

The data that is qualitatively fit by both models is that of the p-type doping in MDMO-PPV and P3HT. The shift towards a lower doping density observed for P3HT can be related to the larger exciton diffusion coefficient in P3HT:[29] $1.8{\cdot}10^{-7}$ $m^2 s^{-1}$ compared to $3.2{\cdot}10^{-8}$ $m^2 s^{-1}$ in MDMO-PPV.[30] The exciton lifetime in both materials is similar.[31-32] It should be noted that given the exciton lifetime and the exciton diffusion coefficients of P3HT and MDMO-PPV, a relatively small value of $R_0$ of ~1-1.5 nm is needed to quantitatively fit FRET in Figure 8.7a. The error in experimentally determined doping density of roughly a factor 2 results in an uncertainty in $R_0$ of 0.5 nm. By measurement of the absorption spectrum in reflectance of p-type doping in MDMO-PPV (see supplemental Figure 8.12a), $R_0$ could be calculated from Eq. (8.2). To this purpose the emission spectrum as shown in Figure 8.2 was used. The orientation factor $\kappa^2$ was taken to be 0.655[33] and the refractive index $n$ is estimated to be 2.[34] Note that $\kappa^2$ can possibly range between 0 and 4. In case the donor and emitter dipole lie in a plane $\kappa^2$ equals 0.655.[22, 33] A fluorescence quantum yield of 8% was taken from Ref. 35. The resultant $R_0$ for p-type doping in MDMO-PPV was found to be approximately 3.0±0.3 nm. This value is larger than the fitted value of ~1.5 nm in Figure 8.7b. However, the factor ~2 difference is well within the margins induced by the uncertainties in the assumed exciton lifetime and diffusion coefficient, in the orientation factor and in the measured doping density.

The data for SY-PPV are, on the other hand, not nicely fit by either of the two models, see Figure 8.7: the PL declines steeply at relatively large doping densities. The onset of PL quenching at these large doping densities can only be reconciled with the models when exciton diffusion is excluded (see Figure 8.7a and b for $D_{exc} = 0$). Regarding FRET, a $R_0$ of maximally ~2.5 and ~1.5 nm would then be required for exciton quenching by p- and n-type doping, respectively. To address the consistency of this hypothesis, $R_0$ was calculated from Eq. (8.2), using the emission spectrum of SY-PPV in Figure 8.2. The molar absorption coefficients of the n- and p-type polarons were determined by either the absorption spectra in Figure 8.5 or the absorption spectra measured in reflectance in supplemental Figure 8.12a. These absorption spectra were taken at known doping densities. The orientation factor $\kappa^2$ was again taken to be 0.655[33] and the refractive index $n$ to be 2.[34] A fluorescence quantum yield of 17% was taken from Ref. 25. The resultant values of $R_0$ for p- and n-type doping were 2.8±0.6 nm and 2.3±0.4, respectively. This means that the rather large p-type doping density threshold at which PL in SY-PPV is quenched can indeed be explained by both the FRET and the CT modeling in case exciton diffusion is somehow blocked. For n-type doping an $R_0$ value of 2.3±0.4 nm would suggest a stronger quenching by FRET than observed in Figure 8.7a, even when diffusion is excluded. However, the sources of possible errors discussed above for MDMO-PPV can also in this case very well lead to this discrepancy.

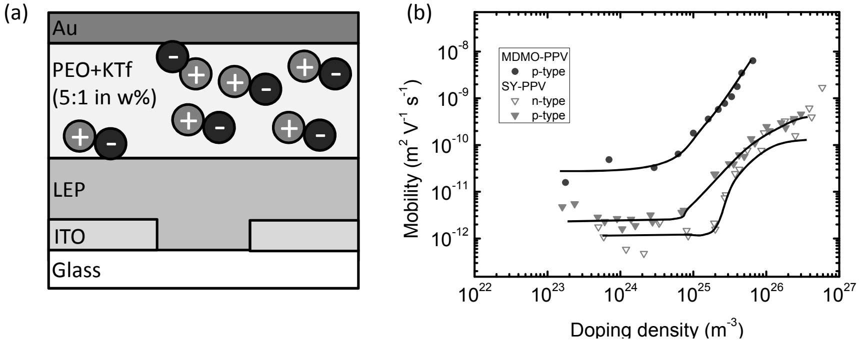

**Figure 8.8 (a) Schematic device layout of the electrochemical transistor. (b) Electronic carrier mobility as a function of doping density. Lines were added that serve as guides to the eye to visualize the density threshold after which the mobility is observed to increase significantly.**

The sudden drop in PL intensity beyond the onset of quenching may then be related to an enhancement of the exciton diffusion: in case exciton diffusion in SY-PPV rapidly increases around a p-type doping density of $2 \cdot 10^{24}$ m$^{-3}$, a rapid transition between the dashed gray line and the solid black line for, as an example, $R_0$ = 2.5 nm is expected in Figure 8.7a. This would then be in line with the experimentally obtained PL quenching profile for p-type doping in SY-PPV. To substantiate the suggestion of an abrupt increase in exciton diffusion and to provide a possible physical reason, mobility measurements in n- and p-type doped SY-PPV in an electrochemical transistor structure (see Figure 8.8a) were performed. The results show a threshold for the doping density dependence of the mobility, as plotted in Fig. 8b. Interestingly, the thresholds for n- and p-type doping in Figure 8.8b coincide quite well with the densities at which the sudden transitions in Figure 8.7 occur. Note that the error in experimentally determined doping density is relatively small at these low doping densities. Also note the coincidence of doping density at which PL quenching is initiated and at which the mobility is enhanced. This suggests a direct connection between on the one hand charge mobility and trapping, and on the other hand exciton diffusion.[36] Within the lifetime of the exciton, diffusion by polarons is, however, not significant in SY-PPV. From the mobilities in Figure 8.8b and the Einstein relation, a polaron diffusion constant $D_{\mathrm{pol}}$ between $10^{-14}$ m$^2$ s$^{-1}$ and $10^{-11}$ m$^2$ s$^{-1}$ can be estimated. These numbers are small compared to the exciton diffusion constant that is in the range $10^{-8}$ m$^2$ s$^{-1}$. Nevertheless, the relatively weak quenching in SY PPV found here (again) confirms the finding that electroluminescence from copolymers is relatively strong compared to their homopolymer counterparts, e.g. MDMO-PPV.[37-38]

In principle the abrupt PL quenching in SY-PPV could also be related to an erroneous determination of the doping density. Due to the chemical potential difference at the PEO:LEP interface, an electric double layer (EDL) is formed by a small (fraction of the) charging current before actual doping sets in. A difference in chemical potential for the ions in SY-PPV, MDMO-PPV and P3HT might then result in the different quenching profiles as shown in Figure 8.4. A ~1 nm sheet electric double layer with a potential drop of 1 V would then correspond to a surface charge density of $3 \cdot 10^{21}$ $m^{-2}$. Such a charge density residing in a ~1 nm sheet at the interface would correspond to a doping concentration in the entire film (~100 nm) of a factor 100/1 = 100 times lower. Since the biases used in the experiment are in the 0 V to 3 V range, the amount of doping lost to EDL formation is negligible in comparison to the total doping concentration. Hence, the anomalous behavior in SY-PPV compared to MDMO-PPV or P3HT cannot be attributed to a difference in chemical potentials between these materials.

The qualitative behavior of the doping dependence of PL quenching in the experiment and the models (see Figure 8.7) confirms on hindsight that the experiment is characterized by homogeneous doping. Successive doping of phase separated regions would lead to a two-step reduction of the PL. In case such an effect is more gradual, then quenching would still be expected to be distributed over a larger total injected charge density (horizontal axis of Figure 8.7) than in the case of homogeneous doping. The models assume a homogeneous doping density and are able to model the qualitative behavior relatively well (for P3HT and MDMO-PPV). It is in this context important that, for both models, changes in parameter values have little or no effect on the steepness of the slope; hence, an inhomogeneity-induced broadening cannot easily be mapped on (a change in) any of the fitting parameters. A steeper doping density dependence (for SY-PPV) is furthermore not in line with the doping over phase-separated regions as indicated above. Therefore, combined with the discussion in the Experimental results section, we do not see any indication that significant inhomogeneous doping of the conjugated polymer takes place.

The doping densities at which polaron-induced exciton quenching occurs are relevant densities for various types of devices. In efficient polymer LECs, salt densities of ~$6 \cdot 10^{25}$ $m^{-3}$ are present in the active layer.[39] In case all salt dissociates into ions, such salt densities lead to highly doped regions that can quench all excitons in case they sit close to the recombination zone. Organic light-emitting diodes operating in the space charge limited regime on the other hand generally do not reach the carrier densities found here for exciton quenching. Only when relatively large bias voltages are used to obtain high brightness may the polaron density result in significant exciton quenching.[1] In light-emitting field effect transistors carrier densities in the range $10^{24}$-$10^{26}$ $m^{-3}$ pile up near the recombination zone. As a result exciton-polaron quenching may significantly reduce the efficiency if not prevented by, for example, the introduction of multiple layers to separate carrier transport from carrier recombination.[40] In bulk heterojunction solar cells, polaron densities around $10^{22}$ $m^{-3}$ are typically reached under illumination.[41] Therefore, in these cells, polaron-induced exciton quenching is unlikely to lead to a significant reduction in efficiency.

## 8.5 Conclusions

The effect of polaron-induced exciton quenching in conjugated polymers has been studied in a solid-state polymer film. By controlled electrochemical doping the polaron density dependence of the exciton quenching could be determined in several polymers. The density was furthermore confirmed by the occurrence of a bleaching peak in the optical absorption. The critical doping density at which exciton quenching occurs ranges between $1\cdot10^{24}$-$2\cdot10^{25}$ $m^{-3}$ , including the experimental uncertainty, setting an upper limit for the carrier density near and at the recombination zone of efficient emissive devices. The density dependence itself could be modeled by considering exciton diffusion followed by either charge transfer or Förster resonance energy transfer in a homogeneous density of polarons. Both FRET and CT qualitatively fit the data. Fitting with parameters obtained from literature resulted in reasonable quantitative fits with PL quenching occurring at similar polaron densities. It shows that for interpreting experimental data related to polaron-induced exciton quenching, i) exciton diffusion, ii) charge transfer and iii) resonance energy transfer should be considered. Thus, to reduce exciton quenching in devices which convert electrical current in light, the exciton diffusion, the spectral overlap between the emitting exciton and the absorbing polaron, and/or the polaron density need to be reduced.

## 8.6 Supplemental figures

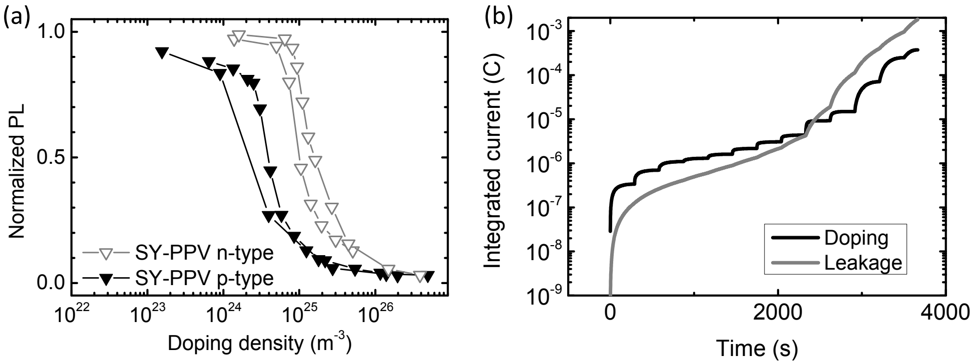

**Figure 8.9 (a) PL quenching as a function of doping density for SY-PPV. (b) Integrated leakage and doping current, c.f. Figure 8.3. To calculate the integrated leakage and doping current in (b) the last current value at each voltage-step in Figure 8.3 was assumed to be equal to the leakage current during the whole voltage-step. As this is likely an overestimation, the plotted integrated leakage current should be regarded as an absolute upper limit. The error margins indicated in Figure 8.4 are based on these upper limits.**

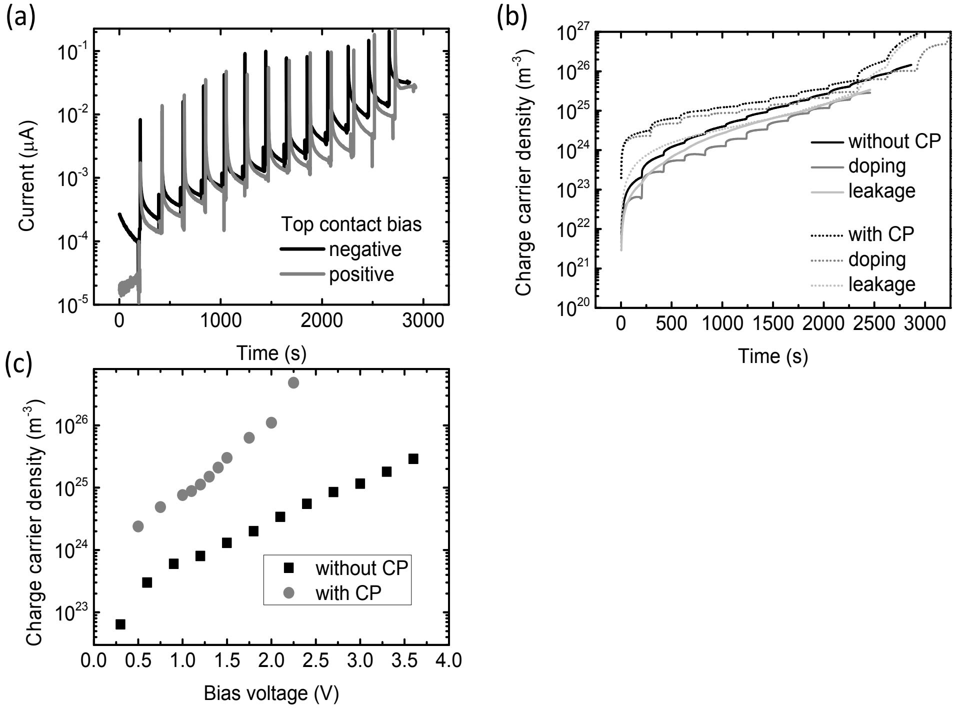

**Figure 8.10 (a) Doping experiment without an organic semiconductor (see Figure 8.1(a)). The observed current presumably originates from leakage and ion migration through the electrolyte. The bias voltage of the top electrode was stepped from 0 to ±3.9 V in steps of ±0.3 V. No color changes or other indications of side reactions related to the electrolyte or the ITO were observed. Note also that the leakage currents here are approximately an order of magnitude below the currents observed in the full device, i.e. with an organic semiconductor contacting the electrolyte, indicating that the latter is dominated by doping and not by leakage. (b) The integrated carrier density for negatively biased top contact for the device without conjugated polymer (CP) (see Figure 8.10(a)) and with CP, i.e. SY-PPV (see Figure 8.9(b)). Integrated leakage and doping current of both series were included as well. To enable comparison, we assumed that the integrated current (charge) in the device without CP is distributed over the same volume as for the device with CP, i.e. SY-PPV: $10^{-5}\cdot 0.091$ $cm^{-3}$, being the volume of the CP film. The integrated current density related to doping is plotted versus bias voltage in (c) for comparison. Importantly the carrier density in the device with CP is at least one order of magnitude above the integrated carrier density in the reference cell without CP.**

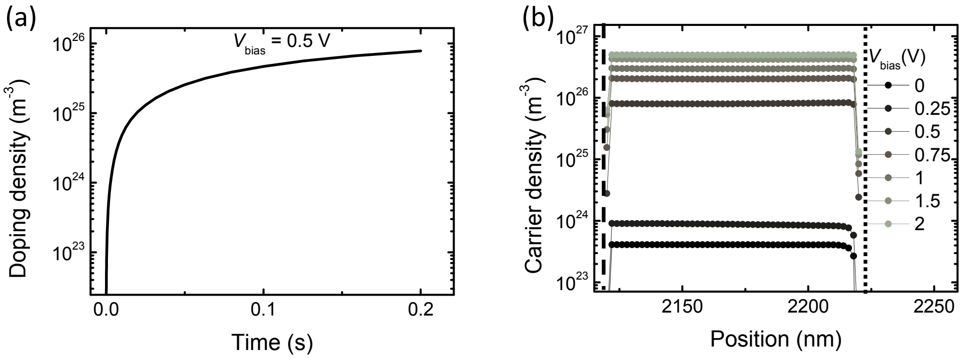

**Figure 8.11 (a) Modeled transient doping density after switching the bias voltage from 0 V to 0.5 V. Note that the ionic and electronic mobility determine the time-dependence of the doping density. The doping density throughout the modeled semiconductor in the device biased at $V_{bias}$ for 0.2 s is shown in (b). The dashed black line indicates the interface between the ionic and electronic conductor. The dotted black line indicates the interface between the electronic conductor and the injecting electrode.**

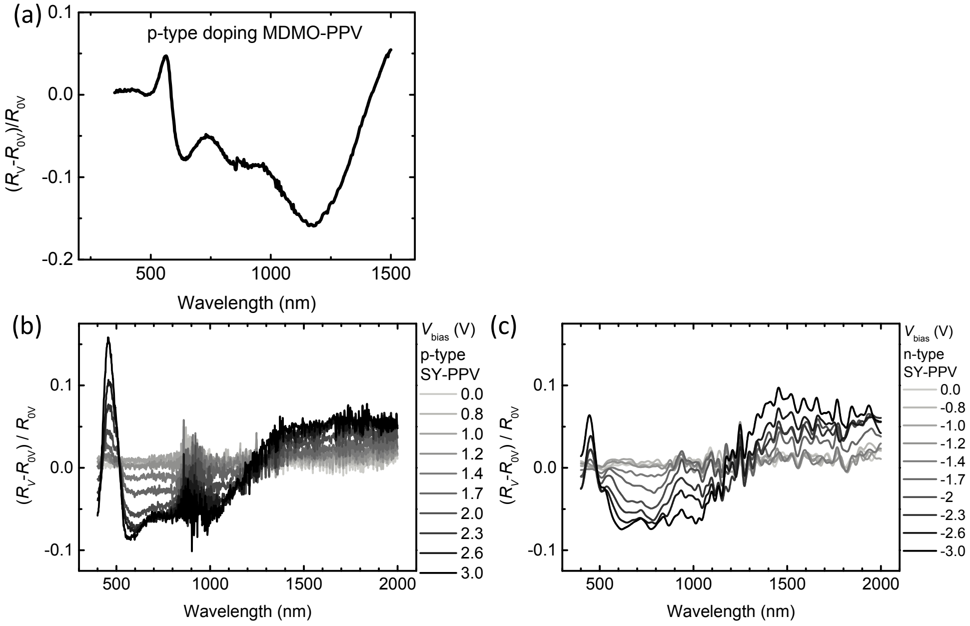

**Figure 8.12 Relative measurement of the absorption, measured in reflectance at various doping densities for a) p-type doped MDMO-PPV, b) p-type doped SY-PPV and c) n-type doped SY-PPV. $R_{0V}$ and $R_V$ represent the reflectance at $V_{bias}$ = 0 V and at $V_{bias}$, respectively.**

# References

[1] N. C. Giebink, S. R. Forrest, Phys. Rev. B 77 (2008) 235215.

[2] J. Kalinowski, W. Stampor, J. Szmytkowski, D. Virgili, M. Cocchi, V. Fattori, C. Sabatini, Phys. Rev. B 74 (2006) 085316.

[3] S. M. King, D. Dai, C. Rothe, A. P. Monkman, Phys. Rev. B 76 (2007) 085204.

[4] J. M. Hodgkiss, S. Albert-Seifried, A. Rao, A. J. Barker, A. R. Campbell, R. A. Marsh, R. H. Friend, Adv. Funct. Mater. 22 (2012) 1567.

[5] S. van Reenen, T. Akatsuka, D. Tordera, M. Kemerink, H. J. Bolink, J. Am. Chem. Soc. 135 (2013) 886.

[6] M. C. Gwinner, D. Kabra, M. Roberts, T. J. K. Brenner, B. H. Wallikewitz, C. R. McNeill, R. H. Friend, H. Sirringhaus, Adv. Mater. 24 (2012) 2728.

[7] J. Liu, I. Engquist, X. Crispin, M. Berggren, J. Am. Chem. Soc. 134 (2012) 901.

[8] R. H. Young, C. W. Tang, A. P. Marchetti, Appl. Phys. Lett. 80 (2002) 874.

[9] H. Z. Lin, S. R. Tabaei, D. Thomsson, O. Mirzov, P. O. Larsson, I. G. Scheblykin, J. Am. Chem. Soc. 130 (2008) 7042.

[10] G. Li, J. Shinar, G. E. Jabbour, Phys. Rev. B 71 (2005) 235211.

[11] A. Salleo, R. A. Street, J. Appl. Phys. 94 (2003) 471.

[12] A. L. Holt, J. M. Leger, S. A. Carter, J. Chem. Phys. 123 (2005) 044704.

[13] H. Shimotani, G. Diguet, Y. Iwasa, Appl. Phys. Lett. 86 (2005) 022104.

[14] P. Matyba, K. Maturova, M. Kemerink, N. D. Robinson, L. Edman, Nat. Mater. 8 (2009) 672.

[15] S. van Reenen, P. Matyba, A. Dzwilewski, R. A. J. Janssen, A. Edman, M. Kemerink, Adv. Funct. Mater. 21 (2011) 1795.

[16] H. H. P. Gommans, M. Kemerink, G. G. Andersson, R. M. T. Pijper, Phys. Rev. B 69 (2004) 155216.

[17] Using Gauss' law, the electric field $E$ equals the ratio of surface charge $\sigma$ and the dielectric constant $\varepsilon_r\varepsilon_0$: $E = \sigma/\varepsilon_r\varepsilon_0$. The surface charge for $1\cdot10^{25}$ m$^{-3}$ doping in the light-emitting polymer film then corresponds to an electric field $E = q\cdot[1\cdot10^{25}\text{ m}^{-3}]\cdot[100\text{ nm}]/\varepsilon_r\varepsilon_0$, where $\varepsilon_r$ in the bulk of the electrolyte equals 6 (or maybe even be higher at an undefined metal interface). In that case an electric field of $3\cdot10^{9}$ V m$^{-1}$ is obtained, leading to an EDL of 3 V for a Debye screening length of 1 nm.

[18] W. C. Germs, J. J. M. van der Holst, S. L. M. van Mensfoort, P. A. Bobbert, R. Coehoorn, Phys. Rev. B 84 (2011) 165210.

[19] F. Etzold, I. A. Howard, R. Mauer, M. Meister, T. D. Kim, K. S. Lee, N. S. Baek, F. Laquai, J. Am. Chem. Soc. 133 (2011) 9469.

[20] I. A. Howard, F. Etzold, F. Laquai, M. Kemerink, Adv. Energy Mater. (2014).

[21] R. Paulini, K. Muller, F. Diederich, Angew. Chem. Int. Ed. 44 (2005) 1788.

[22] B. Valeur, *Molecular Fluorescence: Principles and Applications*. WILEY-VCH: Weinheim, 2001.

[23] U. Gosele, M. Hauser, U. K. A. Klein, R. Frey, Chem. Phys. Lett. 34 (1975) 519.

[24] M. C. Heiber, A. Dhinojwala, J. Phys. Chem. C 117 (2013) 21627.

[25] E. W. Snedden, L. A. Cury, K. N. Bourdakos, A. P. Monkman, Chem. Phys. Lett. 490 (2010) 76.

[26] D. E. Markov, J. C. Hummelen, P. W. M. Blom, A. B. Sieval, Phys. Rev. B 72 (2005) 045216.

[27] A. J. Gesquiere, S. J. Park, P. F. Barbara, J. Am. Chem. Soc. 127 (2005) 9556.

[28] G. Wilemski, M. Fixman, J. Chem. Phys. 58 (1973) 4009.

[29] P. E. Shaw, A. Ruseckas, I. D. W. Samuel, Adv. Mater. 20 (2008) 3516.

[30] O. V. Mikhnenko, F. Cordella, A. B. Sieval, J. C. Hummelen, P. W. M. Blom, M. A. Loi, J. Phys. Chem. B 112 (2008) 11601.

[31] J. Piris, T. E. Dykstra, A. A. Bakulin, P. H. M. van Loosdrecht, W. Knulst, M. T. Trinh, J. M. Schins, L. D. A. Siebbeles, J. Phys. Chem. C 113 (2009) 14500.
[32] K. M. Gaab, C. J. Bardeen, J. Phys. Chem. A 108 (2004) 10801.
[33] M. A. Stevens, C. Silva, D. M. Russell, R. H. Friend, Phys. Rev. B 63 (2001) 165213.
[34] J. M. Ziebarth, M. D. McGehee, Appl. Phys. Lett. 83 (2003) 5092.
[35] F. Marchioni, R. Chiechi, S. Patil, F. Wudl, Y. Chen, J. Shinar, Appl. Phys. Lett. 89 (2006) 061101.
[36] Z. Q. Liang, B. A. Gregg, Adv. Mater. 24 (2012) 3258.
[37] H. Spreitzer, H. Becker, E. Kluge, W. Kreuder, H. Schenk, R. Demandt, H. Schoo, Adv. Mater. 10 (1998) 1340.
[38] S. Gambino, A. K. Bansal, I. D. W. Samuel, Org. Electron. 14 (2013) 1980.
[39] S. Tang, J. Pan, H. A. Buchholz, L. Edman, J. Am. Chem. Soc. 135 (2013) 3647.
[40] R. Capelli, S. Toffanin, G. Generali, H. Usta, A. Facchetti, M. Muccini, Nat. Mater. 9 (2010) 496.
[41] T. G. J. van der Hofstad, D. Di Nuzzo, S. van Reenen, R. A. J. Janssen, M. Kemerink, S. C. J. Meskers, J. Phys. Chem. C 117 (2013) 3210.

# Chapter 9 Understanding the efficiency in LECs

---

*The admixed ions in LECs cause a trade-off between electrical transport and luminescent efficiency. Experiments and numerical modeling on thin film LECs prove that on the one hand carrier injection and transport benefit from electrochemical doping by mobile ions, whereas on the other hand the electroluminescent efficiency is reduced by exciton quenching by polarons involved in the doping. As a consequence the quasi-steady-state luminescent efficiency is found to decrease with increasing ion concentration. The transient of the luminescent efficiency furthermore shows a characteristic roll-off while the current still increases, attributed to ongoing electrochemical doping and the associated quenching. Both effects can be modeled by exciton polaron-quenching described by diffusion-assisted Förster resonance energy transfer. These results indicate that the tradeoff between efficiency and charge transport is fundamental in nature, suggesting that the application realm of future LECs should likely be sought in high-brightness, low-production cost devices, rather than in high-efficiency devices.*

## 9.1 Introduction

Despite significant efforts aimed at improving the performance and the understanding of light-emitting electrochemical cells (LECs), their efficiency has remained low (20 lm $W^{-1}$ for best reported white LEC[1-2]) compared to multilayer organic light emitting diodes (OLEDs) (114 lm $W^{-1}$ for best reported white OLED[3]). To determine the origin of the seemingly limited performance of LECs, the conversion from electrical current into radiatively decaying excitons must be fully understood. This conversion occurs through multiple steps, starting from recombination of carriers into excitons followed by exciton decay and the outcoupling of the generated light. As light outcoupling in LECs is expected to be similar to that in OLEDs, the relatively low performance of LECs seems related to the recombination and/or radiative efficiency.

The recombination efficiency of electrical carriers into excitons depends on the balance between the injected electron and hole currents. In case of imbalanced currents part of the injected charges do not recombine but leave the device via the oppositely charged electrode.[4] In well-functioning LECs the high density of n- and p-type doping (see e.g. Figure 2.3a) make transport of free carriers through oppositely doped regions without recombination unlikely.[5] Therefore the conversion of electrical carriers into excitons is regarded to be extremely efficient in LECs.[6] Consequently no blocking layers, as typically encountered in multilayer OLEDs, are required in LECs.[7]

Radiative decay of excitons into photons depends on several processes. First of all, depending on the type of emitter only part of the formed excitons can decay radiatively. Most polymers for example are singlet emitters, leaving only a quarter of the formed excitons available for immediate radiative decay, assuming that singlet and triplet excitons are formed with equal probability. Like in OLEDs, triplets can be harvested in LECs by the use of triplet emitters[8] or the addition of dyes.[9] Despite the fine PL efficiency of the materials used in LECs, e.g. polymers[10] or ionic transition metal complexes (iTMCs)[6], the radiative efficiency of the operational device remains relatively low. To explain this, non-radiative decay processes should be considered. Quenching of excitons may be induced by the large density of polarons in the doped regions, which was investigated for homogeneous layers in Chapter 8. Additionally, exciton-exciton interactions may also be expected as excitons are predominantly formed in the relatively narrow intrinsic zone in the dynamic p-i-n junction. Also impurities in the active layer related to the inclusion of an electrolyte, may give rise to further reduction of the radiative exciton fraction.

A strong indication that excitons are quenched by polarons in LECs is the typical roll-off in efficiency that was described for polymer-based LECs and iTMC-LECs in Chapter 7. This roll-off occurs while the current density continues to increase, which indicates continuous electrochemical doping. In Chapter 5 this slow doping process was attributed to slow dissociation of salt into mobile ions that subsequently can be used in doping. In fact, in a number of recent papers doping-related quenching was proposed as cause for the efficiency roll-off.[11-14] A formal justification of this assignment is however lacking.

Here we investigated the difference in efficiency in LECs compared to OLEDs based on the same organic semiconductor. The origin of the efficiency roll-off in LECs was studied in detail as well as the influence of the admixed salt concentration $c_0$ in the active layer on the quasi-steady-state electroluminescent efficiency. To this purpose different series of polymer LECs were prepared with varying active layer constituents to determine the effect of the doping concentration on electrical transport and light emission. Experiments on LECs with varying salt densities showed a strong reduction in quasi-steady-state efficiency for increasing $c_0$. Additionally, transient characterization of these devices displayed the typical roll-off in efficiency during electrochemical doping. The data was reproduced by numerical modeling to constitute that, compared to OLEDs, the efficiency in LECs is limited by doping-induced exciton quenching. These results point towards a fundamental tradeoff between charge transport and radiative decay by electrochemical doping in LECs.

## 9.2 Materials and methods

*Device preparation:* The conjugated polymer used in the active layer of the sandwich LECs is a phenyl-substituted poly(p-phenylene vinylene) copolymer (SY-PPV, Merck, catalogue number PDY-132), commonly termed “Super Yellow”. Poly(ethylene oxide) (PEO, $M_w$ = $5 \cdot 10^5$ g mol$^{-1}$, Aldrich) was used as received. The salt potassium trifluoromethanesulfonate ($KCF_3SO_3$, 98 %, Aldrich) was dried at a temperature $T$ = 373 K under vacuum before use. SY-PPV (5 mg ml$^{-1}$), PEO (10 mg ml$^{-1}$), and $KCF_3SO_3$ (20 mg ml$^{-1}$) were dissolved in cyclohexanone (> 99 %, anhydrous, Aldrich). These solutions were mixed together in varying weight ratios. The resultant stock solutions were thereafter stirred on a magnetic hot plate at $T$ = 323 K for at least 5 h.

Cleaned glass/ITO substrates were optionally first spin-coated with poly(3,4-ethylenedioxythiophene)-poly(styrenesulfonate) (PEDOT:PSS, Clevios P VP AI 4083) from Heraeus (at 2000 RPM for 60 s) and subsequently transferred to a glove box under $N_2$ atmosphere ([$O_2$] < 1 ppm and [$H_2O$] < 1 ppm) where the substrates were annealed for 10 minutes at 120 $^oC$. All the next steps were done in a glove box. Subsequently the stock solution was spin coated (in general at 1000 RPM for 60 s) after which the samples were dried at $T$ = 323 K for at least 2 h on a hot plate. Then the substrates were transferred to a thermal evaporator where LiF/Al or Al electrodes were deposited by thermal evaporation under high vacuum ($p \sim 10^{-6}$ mbar) on top of the spin-coated films. The active areas of the devices, defined by a shadow mask, were either 0.091 or 0.161 cm$^2$. The thickness of the active layers was measured after complete electrical characterization by profilometry in air.

*Electrical characterization:* Current-luminance-voltage characteristics were measured by a Keithley 2636a sourcemeter and a silicon photodiode. The brightness was calibrated with a luminance meter (LS-110 Konica-Minolta). In general two types of measurements were performed. Current and luminance were measured while sweeping the bias voltage $V_{\mathrm{bias}}$. To achieve reproducible *I-V* curves, 3 subsequent voltage sweeps were performed typically from 0 V to 8 V to 0 V in ~20 s. In addition, the current and luminance were also measured as a function of time at a constant bias voltage of 6 V.

*Computational details*: For the numerical simulations, the 2-dimensional model was used which is described in detail in Appendix A. Here follows a general description of the used parameters. Deviating parameters are mentioned in the discussion. The model was used to describe a 1D device with constant grid-point spacing of 2 nm and a total active layer thickness of 100 nm. The carrier mobility was chosen to be field and doping *in*dependent and set to $\mu_{\mathrm{p/n}} = 10^{-11}$ m$^2$ V$^{-1}$ s$^{-1}$ unless stated otherwise. The anion and cation mobilities were chosen to be $\mu_{\mathrm{ion}} = 10^{-12}$ m$^2$ V$^{-1}$ s$^{-1}$. The ion mobility at the interface layer at the contacts was set to zero to prevent accumulation at the electrodes. If not, an unphysically large amount of ions would pile up next to the electrodes and is completely screened by the metal electrode. This is a crude but sufficient way of introducing a limit to doping density due to finite ion size effects. The temperature is set at 300 K and the relative dielectric constant at 4. A semiconductor band gap of 2.4 eV was chosen and ohmic and non-ohmic injection was modeled by setting the electron and hole injection barriers to 0.1 and 1.2 eV, respectively. Carrier injection was described by the 'modified Boltzmann' method as described by Eq. A.21 in appendix A.2. The applied bias voltage is 3.5 V. The initial homogeneous salt density was set at varying values ranging from $10^{22}$ to $3\cdot10^{26}$ nm$^{-3}$. Optionally a binding energy between the ions was introduced as explained in Appendix A.4 with varying values for the binding energy $E_{\mathrm{s}}$ and the capture coefficient $\gamma_c$ (m$^3$ s$^{-1}$). Optionally a doping dependent mobility described by A.23 in Appendix A.3 was used with the parameters $A = -1\cdot10^{-11}$, $B = 7.2\cdot10^{-10}$ and $C = 0.167$ which were obtained by fitting the doping dependent mobility measured in SY-PPV shown in Figure 8.8b.

Exciton quenching by polarons is described in the model by diffusion-mediated Förster resonance energy transfer (see Chapter 8.4.1.2). Implementation of this model is as follows. For each time step an exciton quenching rate is calculated at each grid-point for a given polaron density on the same grid-point. Diffusion of excitons between grid points is included. Diffusion within a grid-point is taken into account via the implemented exciton quenching rate. The polaron density dependent singlet exciton quenching rate $k_{\mathrm{PQ}}$ (m$^{-3}$ s$^{-1}$) is based on Eq. 8.5 and Eq. 8.6:

$$k_{PQ} = \frac{\left[1 - \exp\left(4\pi R_{eff} D_{exc} C_A t_0 - 2\cdot 4\sqrt{\pi D_{exc}} R_{eff}^2 C_A \sqrt{t_0}\right)\right]}{t_{step}}, \tag{9.1}$$

where $R_{\mathrm{eff}}$ is an effective quenching radius based on the Förster critical radius for quenching and exciton diffusion with diffusion constant $D_{\mathrm{exc}}$ as described by Eq. 8.5. $C_A$ is the acceptor concentration, which is set equal to the sum of the electron and hole densities, and $t_0$ is the time step taken in the simulation. Note that polarons on neighboring grid-points do not contribute to exciton quenching, which will give rise to some error in the quenching rate.

The computational time to reach quasi-steady-state depends on the number of time steps taken. In simulating LEC transients, the transient length is determined by the slowest process, ion redistribution, whereas the maximum time step is determined by the fastest process, related to exciton diffusion and decay. To obtain a reasonable computational time, which is proportional to the ratio of the transient length and the time step, we needed to slow down the fastest processes. The inverse lifetime of the excitons, $k_{FL}$, and $D_{\mathrm{exc}}$ were reduced by a factor $10^{-5}$. The resultant delay can, however, give errors in the simulation of the transient behavior of the exciton decay processes. To minimize this effect for transients which are limited by the movement of ions, care is taken that the ion diffusion coefficient $D_{\mathrm{ion}} = \mu_{\mathrm{ion}} kT/q$ remains smaller than $D_{\mathrm{exc}}$ by at least a factor 10.

## 9.3 Results and discussion

The luminescent efficiency of polymer LECs is experimentally investigated by measurement of the transient luminescent efficiency and quasi-steady-state luminescent efficiency in devices with varying doping concentrations. The doping concentration is altered by variation of the admixed salt density $c_0$. Simulations to complement the experiments were performed by the numerical model.

### 9.3.1 Steady-state operation

To avoid studying injection limited devices, LECs were prepared with low work function cathodes, LiF-Al, and high work function anodes, ITO-PEDOT:PSS, to enable ohmic injection in the semiconductor, SY-PPV. The active layer consisted of PPV:PEO in a fixed weight ratio of 5:1 and a variable amount of salt, $KCF_3SO_3$, resulting in an average salt density between ~$10^{24}$ and ~$10^{27}$ $m^{-3}$. Several series of LECs were studied with varying active layer thickness $L$ of 100±10, 250±25 and ~600±40 nm. The latter two series of LECs were prepared by spin-coating subsequent layers on top of each other. Before spin-coating, care was taken that the previous layers on the substrate were dry. These devices were electrically characterized by subsequent voltage sweeps up to 8 V. During these sweeps, the current density was found to converge to a single quasi-steady-state value at

8 V. The current density and luminance at 8 V are plotted for all three series in Figure 9.1a and b.

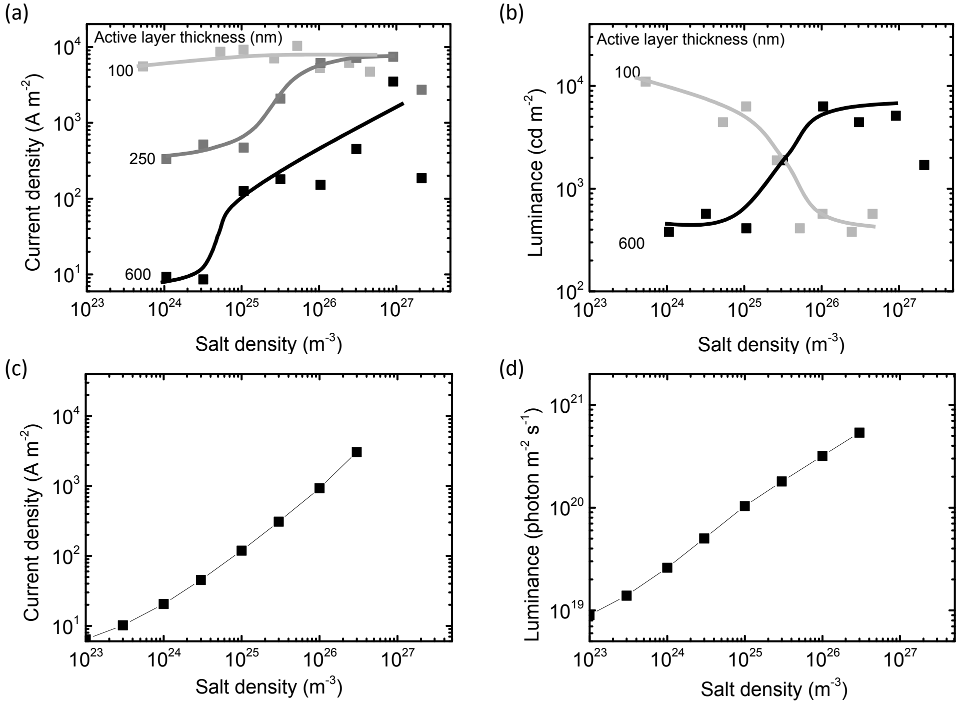

**Figure 9.1 (a,b) Experimentally ($V_{\text{bias}}$ = 8 V) and (c,d) numerically ($V_{\text{bias}}$ = 3.5 V) determined quasi-steady-state current density and luminance of LECs. In (a,b) the active layer thicknesses of the ITO-PEDOT-PPV:PEO:Salt=5:1:x-LiF-Al devices is indicated. No luminance measurements were performed on the 250 nm cells. The thickness of the modeled LEC was 100 nm. Heavy lines guide the eye.**

To enable qualitative comparison with the experiments, the results of simulations are shown in Figure 9.1c and d of the steady-state current density and luminance of an LEC biased at 3.5 V. Here *L* is 100 nm and a constant electronic carrier mobility is assumed. Due to long calculation times, only a single device thickness (*L*) was used in the modeling. Given the constant electronic carrier mobility, variation of *L* between 100 and 600 nm would mainly result in enlargement of the doped regions. Consequently, the supply of carriers towards the recombination zone would remain similar. Therefore, when varying *L,* only minor quantitative differences are expected. A diffusion-assisted polaron-induced exciton-quenching model was implemented in the model as described in the methods section. The following parameters related to the excitons were set to values obtained from literature: the radiative decay rate $k_{\text{decay}} = 1/\tau_D^0 = 1.54$ ns$^{-1}$ found in SY-PPV and the exciton diffusion coefficient $D_{\text{exc}} = 3\cdot10^{-8}$ m$^2$ s$^{-1}$ found in the related NRS-PPV.[15-16] The

Förster critical radius $R_0$ was set at 3 nm. This value is similar to the values obtained in Chapter 8 for p- and n-type doping of SY-PPV of 2.8±0.6 and 2.3±0.4 nm, respectively. These were determined from the polaron absorption and excitation spectra.

The modeling results show that an enhancement of the salt density results in an enhancement of the current density. This is related to the ability of the device to prevent space charge formation while accumulating a larger density of mobile charge carriers in the active layer through electrochemical doping.[17] The luminance increases accordingly.

Comparison between the simulations and the experiments reveals that especially for the thicker LECs ($L$ = 250 and 600 nm) an enhancement of the current density is observed for increasing salt density. For the 600 nm device the luminance is also observed to be enhanced. No luminance measurements were performed for the 250 nm devices. For the series with $L$ = 100 nm, surprisingly a current density is observed that is nearly independent of the admixed salt density. Apparently carrier transport cannot be further enhanced in these 100 nm thick LECs, probably due to a cancelation of various factors. The luminance is however reduced, which is rationalized below.

The efficiency of the experimental and simulated LECs (see Figure 9.1) is plotted in Figure 9.2. The dashed lines indicate the experimentally determined efficiency of OLEDs with layer stacks ITO-PEDOT-PPV-LiF-Al and ITO-PEDOT-PPV:PEO (5:1 in w%)-LiF-Al. The efficiency of these OLEDs is highly similar compared to each other, indicating that the inclusion of PEO hardly affects the efficiency. Additionally it is also similar to the efficiencies measured in the LECs at low $c_0$. The efficiency of the 100 and 600 nm thick LECs in Figure 9.2 (symbols) is reduced by an order of magnitude by increasing the salt density from $\sim 10^{24}$ to $\sim 10^{27}$ $m^{-3}$.

In the numerical modeling, excitons can either decay radiatively or be quenched by electrons or holes. The efficiency of the modeled LEC is plotted in Figure 9.2 for varying exciton diffusion coefficients (note that $D_{exc} = 3 \cdot 10^{-8}$ $m^2$ $s^{-1}$ was experimentally determined in NRS-PPV, which is structurally and electro-optically comparable to SY-PPV).[16] The modeled results lie more or less in between the experimentally obtained efficiency values (symbols in Figure 9.2). The maximal efficiency of the model (0.25 photon/electron) is set at the same position on the vertical axis as the experimentally determined efficiency of the salt-free OLEDs (dashed lines). This procedure is used to effectively account for the absence of other non-radiative loss channels in our simulations. Importantly, the same y-axis scale on left and right assures that *relative* salt-induced changes can be one-on-one compared.

The qualitative and quantitative agreement between model and experiment strongly suggests that polaron-induced exciton quenching indeed causes the efficiency reduction in

LECs. Note that all relevant parameters in the model have been independently determined or were taken from literature, so that the agreement does not rely on any fitting.

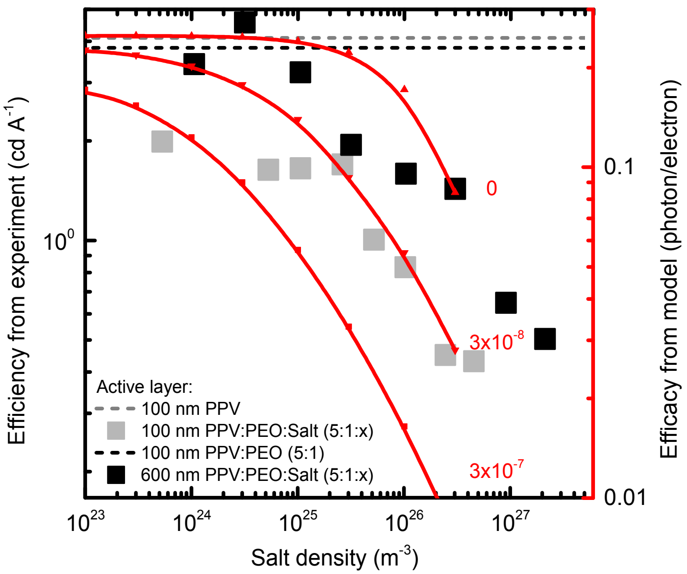

**Figure 9.2 Experimentally (squares) and numerically (red lines + small symbols) determined efficiency in LECs for varying admixed salt densities. The dashed lines indicate the efficiency in absence of salt. The legend indicates the active layer composition for the experiments, which is sandwiched between ITO-PEDOT and LiF-Al electrodes. The exciton diffusion coefficients in $m^2$ $s^{-1}$ are indicated for each numerical simulation.**

### 9.3.2 Transient operation

Another route to determine the origin of the reduced luminescent efficiency in LECs is by study of its transient behavior. As already shown in Chapter 7 for different types of LECs, after application of a constant, above-band gap bias voltage the transient of LECs shows a characteristic roll-off of the efficiency while the current density continues to increase. In the LECs studied here this characteristic is also observed as shown in Figure 9.3. The current, luminance and efficiency were characterized in three subsequent measurements on different timescales as shown in Figure 9.3b. Due to the disabling of the bias voltage in between, the transients do not connect perfectly, but they do show the general behavior of the LEC over eight orders in time. Transients below ~$10^0$ seconds were observed to be qualitatively reproducible with the same LEC, as deduced from repetitive measurements. Quantitatively minor differences occur nevertheless as visible in Figure 9.3b. Prolonged operation for $t > 10^1$ s however typically changes the LECs irreversibly, presumably due to remnant doping which does not relax within at least several hours.

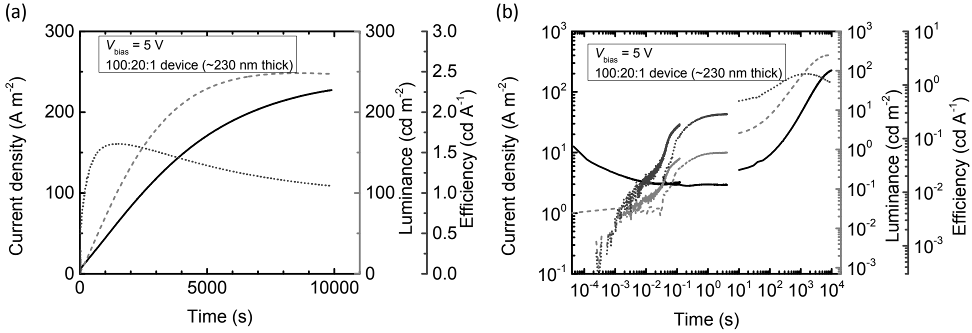

**Figure 9.3 Experimentally determined transients of the current density (solid line), luminance (dashed lines) and efficiency (dotted lines) in an ITO-PEDOT-PPV:PEO:KTf(=100:20:1)-LiF-Al LEC with $L$ = 230 nm and $V_{bias}$ = 5 V. (a) and (b) show the same results on linear and logarithmic scales respectively.**

Also in transient experiments, enhancement of $c_0$ results in enhanced quenching as shown in Figure 9.4. For increasing $c_0$ the current density is observed to be increased, at the cost of efficiency. Roll-off in the efficiency transients is observed to appear for $c_0 > 10^{25}$ m$^{-3}$, towards lower efficiency values for larger $c_0$. The relatively low efficiency reached in case $c_0$ is relatively low, i.e $< 3{\cdot}10^{24}$ m$^{-3}$, may be related to imbalanced transport or to the insufficient bias voltage of 6 V, c.f. 8 V used in the steady-state experiments shown in Figure 9.2.

To complement the experiments, the numerical model was used to calculate current, luminance and efficiency transients in LECs. In case only free ions are considered in the model the transients represented by the dashed lines in Figure 9.5b,d and f are obtained. Neither a large enhancement in current density nor a roll-off in efficiency is observed. Clearly a key ingredient is missing in this description of the LECs. This transient however does resemble the transients typically observed in planar LECs as shown in Figure 2.6 in Chapter 2.

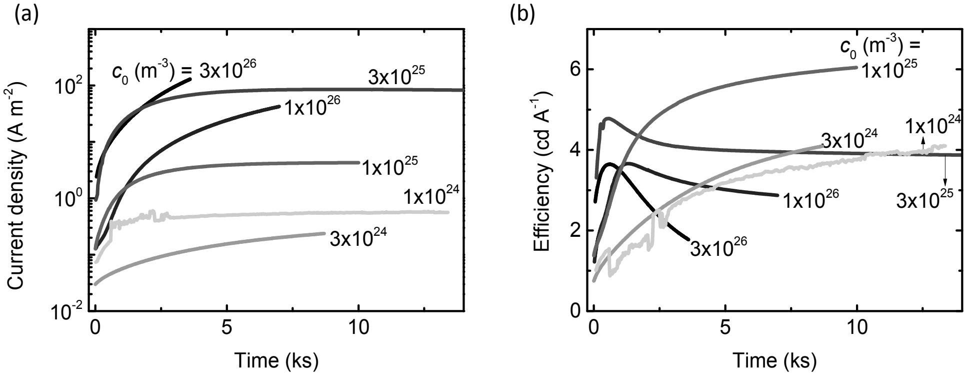

**Figure 9.4 Experimentally determined transients of (a) the current density and (b) the efficiency of a ITO-PEDOT-PPV:PEO(5:1)+KTf-LiF-Al LEC with $L \approx 600$ nm and $V_{\text{bias}} = 6$ V. The admixed salt density $c_0$ is indicated at each graph.**

In Chapter 5 we found that the inclusion of anion-cation pairs, i.e. salt, with a binding energy $E_s$ enables a good description of the transient behavior of the electronic current density in thin film LECs. Next to the binding energy, also the capture coefficient $\gamma_c$ of anions and cations is a free parameter as described in Appendix A.4. Introduction of bound anion-cation pairs in the model used here significantly changes the transients as demonstrated in Figure 9.5 for varying $E_s$ and $\gamma_c$. The transients in Figure 9.5 are from LECs which at $t = 0$ are in equilibrium regarding salt association and dissociation. $E_s$ therefore determines the initial fraction of mobile ions of the total salt density $c_0$. The turn-on transients of LECs with varied $E_s$ ($\gamma_c$ was changed so as to keep the salt dissociation coefficient $\gamma_d = \gamma_c \cdot \exp(E_s/kT)$ constant) is shown in Figure 9.5a,c, and e. They show, as expected, that for a large initial mobile ion fraction, the initial current at $t \sim 10^{-4}$ s is relatively large. Turn-on of light emission is observed around $t \sim 10^{-4}$ s which indicates that the first electrons and holes have traversed the device towards each other. This time is related to the carrier mobility and the externally applied electric field. Simultaneously electrochemical doping takes place by association of free charges with mobile ions. Dissociation of bound anion-cation pairs takes place as well, enabling further electrochemical doping. As salt dissociation is the slowest process, it limits the evolution of the turn-on transient. Simulations for different capture coefficients $\gamma_c$ and a fixed $E_s$ = 0.54 eV are shown in Figure 9.5b,d, and f. Reduction of $\gamma_c$ mainly slows down the doping process and enhances the time needed to reach steady-state accordingly. Due to long calculation times steady-state was not reached in these simulations, but the transients should converge to the same final state. The reason is that at steady-state all ions are completely separated from each other and have a fixed density profile due to the contacts which block ion transport. As a consequence not the mobility, the binding energy or the capture coefficient, but only the density of the ions is of importance for steady-state operation of the modeled LEC.[5]

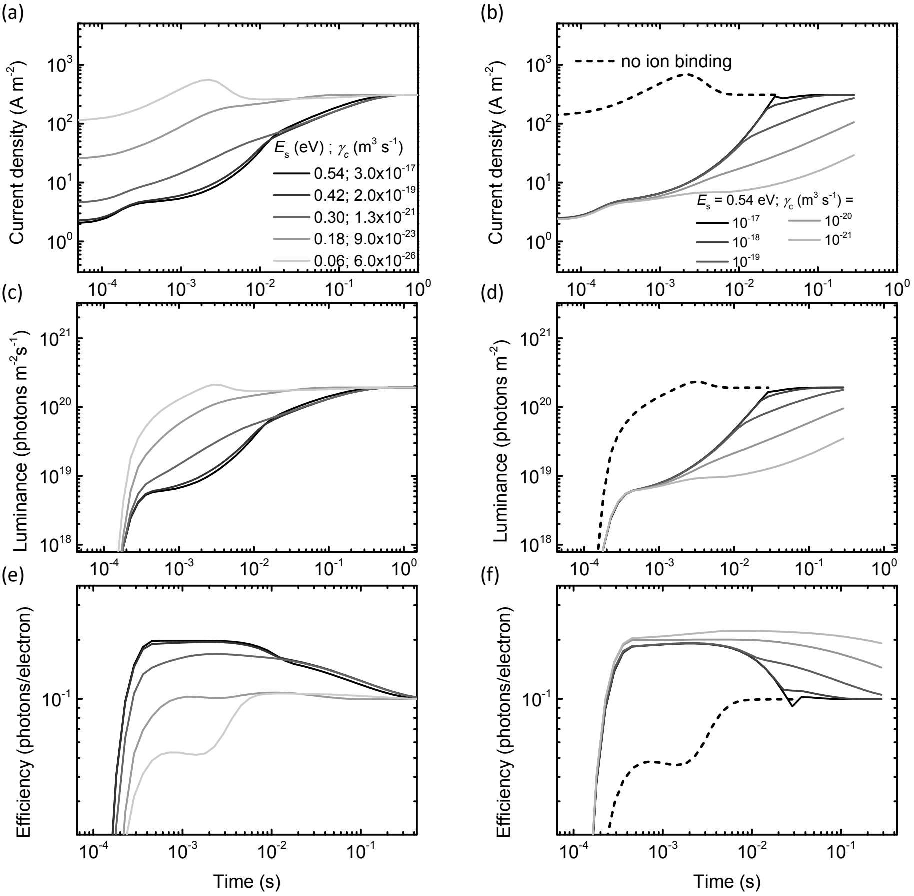

**Figure 9.5 Calculated current density, luminance and efficiency transients for varying salt binding parameters (a), (c), (e) $E_s$ and $\gamma_c$ ($\gamma_c$ was varied in such a way to maintain a constant salt dissociation coefficient, $\gamma_d = \gamma_c \cdot \exp(E_s/kT)$, which essentially results in the majority of salt dissociation to occur between $10^{-3} < t < 10^{-1}$) and (b), (d), (f) $\gamma_c$ as indicated in the legend. The dashed lines represent a simulation where no associated salt complex can be formed. The salt density is $3 \cdot 10^{25}$ m$^{-3}$ and the applied bias voltage 3.5 V.**

Looking at the transient efficiency of the calculated LECs in Figure 9.5e and f, a slow roll-off is observed on the same timescale as the current increase –both result from the slow ion dissociation enabling the ongoing doping process. In Figure 9.6 the simulation for $E_s$ = 0.42 eV and $\gamma_c = 3 \cdot 10^{-17}$ m$^3$ s$^{-1}$ is plotted on a linear and logarithmic scale. Qualitatively the experimental and calculated transients in Figure 9.3 and Figure 9.6 display the same features. In the modeling (experimental) results, an initial onset of luminance is observed at $10^{-4}$ s ($10^{-3}$ s) followed by a relatively constant current density until $10^{-3}$ s ($10^1$ s).

Current density and luminance subsequently continue to increase, whereas the efficiency reaches its peak-value and rolls off.

In the experiment several additional steps in the efficiency (and luminance) are observed between $10^{-3}$ s < $t$ < $10^{3}$ s before the maximal efficiency is reached, which is not reproduced by the numerical model. The first step at ~$10^{-1}$ s may be related to initial imbalanced charge transport due to a difference in electron and hole mobility, resulting in recombination near one of the contacts followed by exciton quenching due to the contact. In the model equal carrier mobilities were chosen. Note that after significant electrochemical doping the recombination efficiency is expected to be ~100 % and recombination is expected to take place further away from the contacts. The increase in efficiency at ~$10^{2}$ s is possibly related to a reduced importance of non-radiative trap-assisted recombination.[18] At relatively high current densities, these traps are saturated so their relative effect on recombination is reduced. Consequently the efficiency is raised at higher current densities, similar as is observed in the transient experiments reported here in Figure 9.3. This may also explain why the efficiency is reduced for the lowest ion densities in Figure 9.4b. Such non-radiative exciton decay processes were not taken into account by the model to not obscure the calculated trends due to polaron-induced exciton quenching.

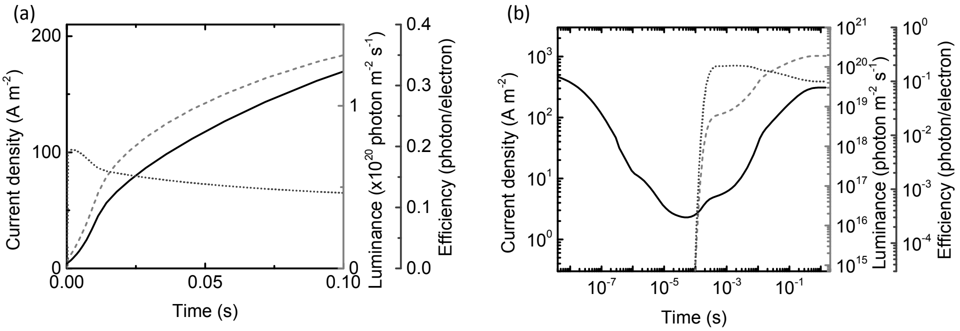

**Figure 9.6 Calculated transients of the current density (solid), luminance (dashed) and efficiency (dotted) in a modeled LEC with ohmic contacts, $L$ = 100 nm, $c_0 = 3\cdot10^{25}$ m$^{-3}$, $V_{\mathrm{bias}}$ = 3.5 V, $\mu_{\mathrm{ion}} = 10^{-12}$ m$^2$V$^{-1}$s$^{-1}$, $\mu_{\mathrm{p/n}} = 10^{-11}$ m$^2$V$^{-1}$s$^{-1}$, $E_s$ = 0.42 eV and $\gamma_c = 3\cdot10^{-17}$ m$^3$ s$^{-1}$. (a) and (b) show the same results on linear and logarithmic scales respectively.**

The transients in Figure 9.6 are qualitatively similar to the transients in Figure 9.3. For a better quantitative fit some additional parameters can be modified which only slightly influence the qualitative shape of the simulation. The mobility of the electrons and holes in absence of electrochemical doping is linearly related to the time at which electrochemical doping and luminance is initiated (at $t$ = $10^{-4}$ s in Figure 9.6). In the previous chapter (see Figure 8.8b) it was shown that this mobility is roughly $10^{-12}$ m$^2$ V$^{-1}$ s$^{-1}$.

Here, such a mobility would result in an initiation of luminance at $t = 10^{-3}$ s, which is in line with the experimental data shown in Figure 9.3. Then, to achieve the correct steady-state current density (see Figure 9.3), a doping dependent mobility needs to be included, as well as a salt density of $5 \cdot 10^{25}$ m$^{-3}$, similar as was used in the experiments in Figure 9.3. Finally the parameters affecting the ions should be altered to move the transient doping process from $10^{-3} < t(\mathrm{s}) < 10^{0}$, i.e. from start to finish, in Figure 9.6 to $10^{1} < t(\mathrm{s}) < 10^{4}$ in Figure 9.3. To do so the ion mobility and the ion capture coefficient ($\gamma_c$) need to be reduced. Now assume that anion-cation recombination is similar to electron-hole recombination and can be described by a Langevin process with a recombination coefficient equal to $2q\mu_{ion}/\varepsilon_0\varepsilon_r = \gamma_c$. Then the time at which electrochemical doping takes place is linearly related to $\mu_{\mathrm{ion}}$ for $\mu_{\mathrm{ion}} < 10\ \mu_{\mathrm{p/n}}$. In Chapter 4 we showed that for $\mu_{\mathrm{ion}} > 10\ \mu_{\mathrm{p/n}}$, the electrochemical doping process is constrained by the less mobile electronic charge carriers (see Figure 4.5b). An ion mobility of $10^{-16}$ m$^2$ V$^{-1}$ s$^{-1}$ and a corresponding $\gamma_c = 9 \cdot 10^{-25}$ m$^3$ s$^{-1}$ likely result in the best fit of the data shown in Figure 9.3. This mobility value is lower than found in previous chapters by impedance spectroscopy ($10^{-13}$ m$^2$ V$^{-1}$ s$^{-1}$ in Chapter 4) or modeling of transient operation of LECs in planar device configuration at $T = 323$ K ($5 \cdot 10^{-11}$ m$^2$ V$^{-1}$ s$^{-1}$). In these experiments a PPV:PEO ratio of 1:1.35 was used as opposed to the 1:0.2 used in the experiments in this chapter. This reduction in PEO concentration is likely to result in a strong reduction of the ion mobility, possibly to $10^{-16}$ m$^2$ V$^{-1}$ s$^{-1}$ which is needed here to fit the experimental data.

Due to extremely long calculation times a simulation with these low ion mobilities could not be performed. However, for $\mu_{\mathrm{ion}} = 10^{-12}$ m$^2$ V$^{-1}$ s$^{-1}$ and the discussed parameters, a simulation was carried out, shown in Figure 9.7 (narrow lines). Also the experimental results from Figure 9.3 are included (see Figure 9.7 wide lines). The vertical axes of Figure 9.7 correspond to the calculated data; the experimental data was scaled to these axes by the factors included in the caption. Determination of these factors is based on the relative positions of the vertical axes in the steady-state results shown in Figure 9.2. To enable comparison of the transients during electrochemical doping in model and experiment, the horizontal axis was shifted to compensate for the enhanced ion mobility used in the model. Electrochemical doping in Figure 9.7 takes place at $10^{-2} < t < 10^{1}$. During this time, the current, luminance and efficiency transients show quantitative agreement between model and experiment within an order of magnitude.

The qualitative and (partially) quantitative agreement between modeled and experimental transients of current, luminance and efficiency suggests that the main processes governing charge transport and radiative decay in LECs are included in the model. This furthermore confirms that the efficiency in LECs is reduced by polaron-induced exciton quenching. Note again that all relevant parameters in the model have been independently determined or were taken from literature, so that the agreement does not rely on any fitting.

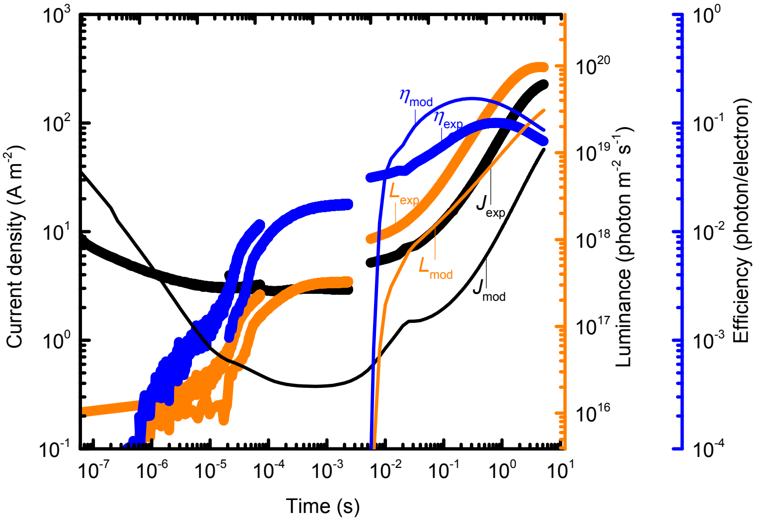

**Figure 9.7 Calculated (narrow lines) and experimental (wide lines) transients of current (black), luminance (orange), and efficiency (blue) of 200 and 230 nm thick LECs biased at 5 V. The axis labels correspond to the calculated data. For the experimentally determined data, $t_{exp}$ / $t_{model}$ = $2 \cdot 10^3$, $\eta_{exp}$ / $\eta_{model}$ = 16 (cd/A)/(photon/electron), $L_{exp}$ / $L_{model}$ = $3.9 \cdot 10^{17}$ (cd)/(photon/s), and $J_{exp}$ / $J_{model}$ = 1.**

## 9.4 Conclusions

The efficiency reduction in LECs due to electrochemical doping has been studied systematically in experiments by investigation of the transient and quasi-steady-state performances. Enhancement of the salt density in LECs is found to reduce the efficiency for admixed salt densities >$10^{25}$ m$^{-3}$. This reduction in efficiency was successfully reproduced by numerical modeling of LECs in which the only non-radiative loss channel of excitons was quenching by doping. Also the transient efficiency roll-off, typical for many types of LECs, was reproduced by the model. The roll-off is caused by ongoing doping that is facilitated by the slow dissociation of salt into mobile ions that subsequently are used to further dope the semiconductor. Hence, the current continues to increase while the efficiency rolls off.

The results show that the ions which enable electrochemical doping therefore improve electrical transport in LECs at the cost of the luminescent efficiency. This tradeoff seems fundamental in nature, suggesting that the application realm of future LECs should likely be sought in high-brightness, low-production cost devices, rather than in high-efficiency devices.

Given the complexity of the device and the fact that all relevant parameters in the model have been independently determined or were taken from literature, the qualitative and even quasi-quantitative agreement between the model and the experiments may be considered as quite good. This strongly suggests that all major processes in operational PPV-based LECs are known and taken into account in the model, highlighting the current understanding of LEC operation.

# References

[1] T. Hu, L. He, L. Duan, Y. Qiu, J. Mater. Chem. 22 (2012) 4206.

[2] Y. P. Jhang, H. F. Chen, H. B. Wu, Y. S. Yeh, H. C. Su, K. T. Wong, Org. Electron. 14 (2013) 2424.

[3] http://panasonic.co.jp/corp/news/official.data/data.dir/2013/05/en130524-6/en130524-6.html

[4] M. J. Tsai, H. F. Meng, J. Appl. Phys. 97 (2005) 114502.

[5] S. van Reenen, P. Matyba, A. Dzwilewski, R. A. J. Janssen, L. Edman, M. Kemerink, J. Am. Chem. Soc. 132 (2010) 13776.

[6] H. J. Bolink, E. Coronado, R. D. Costa, N. Lardies, E. Orti, Inorg. Chem. 47 (2008) 9149.

[7] K. Narayan, S. Varadharajaperumal, G. M. Rao, M. M. Varma, T. Srinivas, Curr. Appl. Phys. 13 (2013) 18.

[8] D. Tordera, S. Meier, M. Lenes, R. D. Costa, E. Orti, W. Sarfert, H. J. Bolink, Adv. Mater. 24 (2012) 897.

[9] F. C. Chen, Y. Yang, Q. Pei, Appl. Phys. Lett. 81 (2002) 4278.

[10] F. Marchioni, R. Chiechi, S. Patil, F. Wudl, Y. Chen, J. Shinar, Appl. Phys. Lett. 89 (2006) 061101.

[11] S. B. Meier, D. Hartmann, D. Tordera, H. J. Bolink, A. Winnacker, W. Sarfert, Phys. Chem. Chem. Phys. 14 (2012) 10886.

[12] J. F. Fang, Y. L. Yang, L. Edman, Appl. Phys. Lett. 93 (2008) 063503.

[13] J. Fang, P. Matyba, N. D. Robinson, L. Edman, J. Am. Chem. Soc. 130 (2008) 4562.

[14] X. Y. Li, J. Gao, G. J. Liu, Appl. Phys. Lett. 102 (2013) 223303.

[15] E. W. Snedden, L. A. Cury, K. N. Bourdakos, A. P. Monkman, Chem. Phys. Lett. 490 (2010) 76.

[16] D. E. Markov, J. C. Hummelen, P. W. M. Blom, A. B. Sieval, Phys. Rev. B 72 (2005) 045216.

[17] S. van Reenen, P. Matyba, A. Dzwilewski, R. A. J. Janssen, A. Edman, M. Kemerink, Adv. Funct. Mater. 21 (2011) 1795.

[18] M. Kuik, L. J. A. Koster, A. G. Dijkstra, G. A. H. Wetzelaer, P. W. M. Blom, Org. Electron. 13 (2012) 969.

# **Chapter 10** Large magnetic field effects in electrochemically doped polymer LECs

---

*Magnetic field effects in conductance and electroluminescence give insight in spin-dependent processes. Besides other effects a large negative magneto-conductance (MC) of 12 % is observed in electrochemically doped LECs at sub-bandgap bias voltages. These effects indicate processes like delayed fluorescence from triplet-triplet annihilation and spin-mixing prior to exciton formation. The latter is found to result in a reduction in triplet exciton density which is argued to reduce detrapping of polarons in the recombination zone at low bias voltages, explaining the observed negative MC. Regarding organic magneto-resistance this study provides novel experimental data to verify existing models describing magnetic field effects in organic semiconductors which contribute to better understanding hereof. Furthermore we present indications of strong magnetic field effects related to interactions between trapped carriers and excitons, which can be specifically studied in electrochemically doped OLEDs. Regarding LECs, this work shows that delayed fluorescence from triplet-triplet annihilation substantially contributes to the electroluminescence and the device efficiency.*

*Part of the work presented in this chapter has been published: S. van Reenen, S. P. Kersten, S. H. W. Wouters, M. Cox, P. Janssen, B. Koopmans, P. A. Bobbert, M. Kemerink, Phys. Rev. B 88 (2013) 125203.

## 10.1 Introduction

In the field of organic magnetoresistance (OMAR), LECs have only scarcely been studied as opposed to OLEDs. In OLEDs transport typically takes place by hops through a percolating pathway. Typically this pathway is the optimal transport channel, which as a result is least influenced by charge traps. In LECs on the other hand, charge trapping is dominant in the form of electrochemical doping. Ions electrostatically compensate electrons or holes, resulting in effective Coulomb traps. In this chapter this charge trapping is shown to be especially dominant at low bias voltages equal to or smaller than the bandgap of the semiconductor. Therefore LECs can be regarded as an ideal test bed to study OMAR effects on trapped charges.

OMAR in LECs biased above the semiconductor bandgap has been reported by Vardeny *et al.*[1] They observed a positive magneto-conductance (MC) of ~0.4 % and magneto-electroluminescence (MEL) of ~5 %. The results were explained by the polaron pair model.[2] The difference in MC and MEL was attributed to imbalanced device characteristics regarding carrier injection and/or transport. As a result, a relatively large part of the current does not contribute to electroluminescence, leading to MC being smaller than MEL.

Here we report on OMAR in Poly[2-methoxy-5-(3’,7’-dimethyloctyloxy)-1,4-phenylenevinylene (MDMO-PPV) LECs. Large negative MC effects (-12 %) are observed at $V_{\text{bias}} < E_{\text{gap}}$ after prolonged biasing at $V_{\text{bias}} = 4.0$ V. Simultaneously, a positive effect in the magneto-efficiency (Mη), determined by MEL – MC, is observed when electroluminescence (EL) is detectable. Both effects are low magnetic field effects (LFE) that are best described by a “non-Lorentzian”[3] lineshape with a width of $B_0 = 2.2$ mT. The magnetic field effect (MFE) in efficiency is described by the two-site model previously reported by Kersten *et al.*[4], which models the competition between hyperfine field induced spin mixing and exciton formation. The MFE in current is rationalized as an indirect effect of the enhanced singlet:triplet ratio: long-living triplet excitons can detrap carriers from doping sites and hence indirectly enhance the current. Especially after conditioning and in the low voltage regime the number of trapped polarons is expected to be large. Next to both low field effects, also a negative high field effect (HFE) in the EL was observed at relatively large bias voltages. This effect is attributed to field dependent triplet-triplet annihilation that is found to have a significant contribution to the electroluminescence in LECs.

## 10.2 Materials and methods

*Device preparation:* The LECs in this study consist of an active layer of ~200 nm sandwiched between an indium tin oxide (ITO) and an aluminum electrode. The active layer is a blend of materials spin-coated from solution. This blend was prepared by mixing of the following 10 mg ml$^{-1}$ stock solutions in a mass ratio of 1 : 1.35 : 0.25: poly[2-methoxy-5-(3′,7′-dimethyloctyloxy)-1,4-phenylenevinylene] (MDMO-PPV) in chloroform, poly(ethylene oxide) (PEO) in cyclohexanone and potassium triflate ($KCF_3SO_3$) in cyclohexanon. The aluminum electrodes were thermally deposited in a deposition chamber in a glovebox under a vacuum of ~10$^{-6}$ mbar. All device manufacturing and characterization was done under nitrogen atmosphere. The active area of the device, defined by a shadow mask, was 0.091 cm$^2$.

*Device characterization:* The current-voltage characteristics were measured by a Keithley 2400 sourcemeter. For MC and MEL measurements a magnetic field perpendicular to the device was used. Current and electroluminescence (EL) were simultaneously measured at a constant bias voltage ranging between 0 and 4 V while the magnetic field was swept from 0 to 500 mT. The MC and MEL were determined by the relative change in current and EL: $\mathrm{MC} = (I_B - I_{B=0})/I_{B=0}$ and $\mathrm{MEL} = (\mathrm{EL}_B - \mathrm{EL}_{B=0})/\mathrm{EL}_{B=0}$. Mη was determined by the difference between MEL and MC: $\mathrm{M}\eta = (\eta_B - \eta_{B=0})/\eta_{B=0} \equiv \mathrm{MEL} - \mathrm{MC}$. Three magnetic field sweeps were performed at each bias voltage to account for temporal drift in the current and electroluminescence. Electroluminescence was measured by a Hamamatsu Si photodiode S1337-33BQ connected to a Keithley 6430 sub-Femtoamp remote sourcemeter.

*Computational details:* The 1D numerical LEC model as described in Appendix A was used. A grid of 52 points was chosen with a gridpoint spacing of 2 nm. The first and last grid points were the contacts with equal work functions of 4.6 eV. HOMO and LUMO levels of the semiconductor in between the contacts were 5.1 and 2.9 eV, respectively. A dielectric constant of 3.4 was chosen and a temperature of 300 K. The carrier mobility was chosen to be field and doping independent and set to $\mu_{p/n}$ = 1·10$^{-10}$ m$^2$ V$^{-1}$ s$^{-1}$. The anion and cation mobilities were chosen to be $\mu_{ion}$ = 1·10$^{-11}$ m$^2$ V$^{-1}$ s$^{-1}$ and could be set to 0 to mimic trapped ions. The ion mobility at the interface layer at the contacts was set to zero to prevent accumulation at the electrodes: If not, all ions pile up next to the electrodes and are consequently being screened by the contacts. This is a crude way of introducing a maximum doping density due to finite ion size effects. An initial homogeneous cation and anion density of 5·10$^{25}$ nm$^{-3}$ was chosen. The simulations were allowed to reach a quasi steady-state indicated by a constant electronic current and an ionic current approaching zero. The applied bias voltage ranged from 0 to 4 V.

Magnetic field effects in the device operation were modeled by changing the summed carrier mobility in Eq. A.24 by introduction of a prefactor $R_{pre}$ in the recombination rate. To model the MC each time two simulations were performed for $R_{pre}$ = 1 and $R_{pre} \neq 1$. MC then equals $(I_{Rpre\neq1} - I_{Rpre=1})/I_{Rpre=1}$.

## 10.3 Experimental results

Initially pristine LECs were studied by measurement of current-voltage and luminance-voltage characteristics (IVL) in combination with MC-voltage measurements at magnetic field strengths $B$ = 0 and 83 mT.[5] The results are displayed in Figure 10.1a and b (open symbols) and show typical LEC behavior: turn-on of electroluminescence for $V_{bias} \approx E_{gap}$ (i.e. ~2.4 eV for MDMO-PPV). No MC effects were observed in the studied voltage range. As doping in LECs is typically a slow process, the device was then operated for ~20 minutes at $V_{bias}$ = 4 V. After this so-called conditioning,[6] the device was set back to $V_{bias}$ = 0 V followed by another measurement of an IVL characteristic shown in Figure 10.1a (closed symbols). An enhancement of the current is mainly observed at bias voltages at and below $E_g$. Furthermore, electroluminescence was observed already at voltages lower than 2.4 V: for 2.1 V < $V_{bias}$ < 2.4 V. The current is also observed to change sign at $V_{bias} \approx$ 0.3 V instead of 0.0 V. This can be related to slow discharging of the LEC after conditioning.

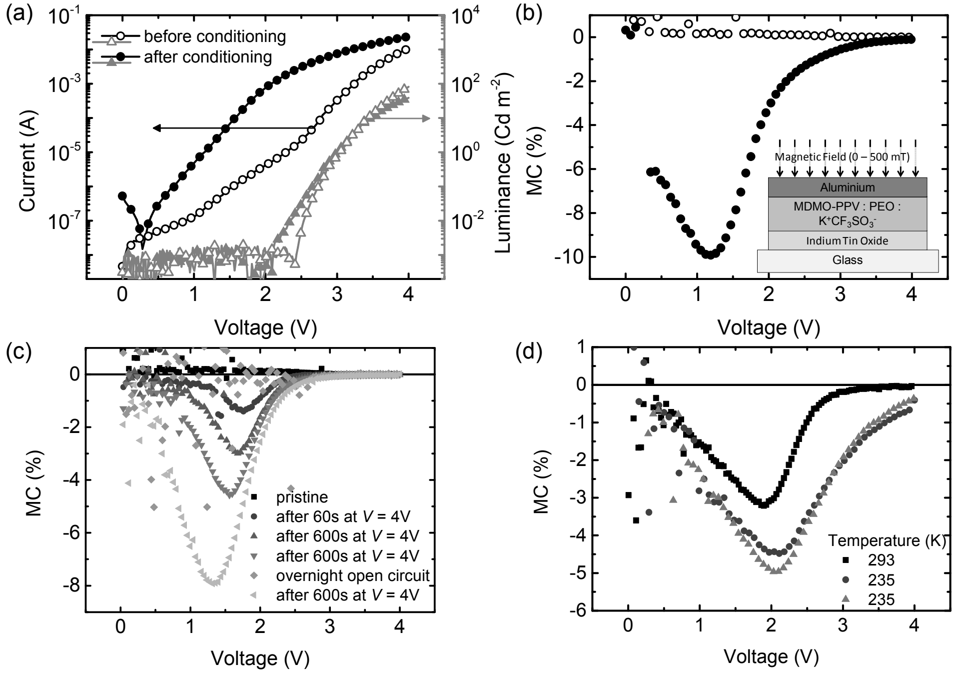

**Figure 10.1 (a) Current-voltage and luminance-voltage characteristics of a PPV-based LEC (layer stack shown in inset of (b)) before and after conditioning at $V_{bias}$ = 4 V in the absence of a magnetic field. (b) Magneto-conductance of the LEC at a magnetic field of 83 mT. (c) Effect of conditioning time and relaxation time at open circuit on the magneto-conductance in a similar device. (d) Magneto-conductance in a similar device measured in the following sequence: (squares) conditioning and measurement at $T$ = 293 K; (dots) conditioning started at $T$ = 293 K while cooling until $T$ = 235 K and measurement at $T$ = 235 K; (triangles) conditioning and measurement at $T$ = 235 K.**

An MC measurement on the conditioned device is shown in Figure 10.1b (closed symbols). A negative MC has appeared for bias voltages below the semiconductor band gap with a minimum value of roughly -10 %. The strongest effect observed was -12 % when replicating the measurements on similar devices. This large effect is by itself quite a spectacular observation. First of all, in ordinary OLEDs OMAR is typically relatively small when biased below the bandgap. Furthermore the LEC is not optimized with respect to OMAR. In addition, the here reported value is among the largest MC reported in OLEDs.

The appearance of negative MC after conditioning is a temporal effect that persists for at least 1 hour after conditioning. After leaving the device unbiased for 12 hours the effect has vanished. Conditioning again at 4.0 V for 30 minutes makes it reappear. The effect of conditioning can therefore be considered reversible (see Figure 10.1c). To freeze the dopants the temperature of a fresh, similar sample was reduced during conditioning at 4 V. The MC was observed to increase slightly in magnitude and move towards higher bias voltages as shown in Figure 10.1d.

MC and MEL measurements as a function of magnetic field strength are shown in Figure 10.2a and b respectively. The MC curves were fitted using the modified Lorentzian expression[3] $f(B,B_0){\sim}B^2/(|B|+B_0)^2$ with a linewidth $B_0$ = 2.2 mT. The MEL curves were fitted with two modified Lorentzians with linewidths of $B_0$ = 2.3 and 220 mT, accounting for a low- and high-field effect, respectively. By subtracting the MC from the MEL, Mη was determined and plotted in Figure 10.2c. In Figure 10.2d values of MC, MEL and Mη in the limit of $B \rightarrow \infty$ are plotted together as a function of voltage. Additional experiments on LECs based on another type of PPV (Super Yellow) gave qualitatively similar results.

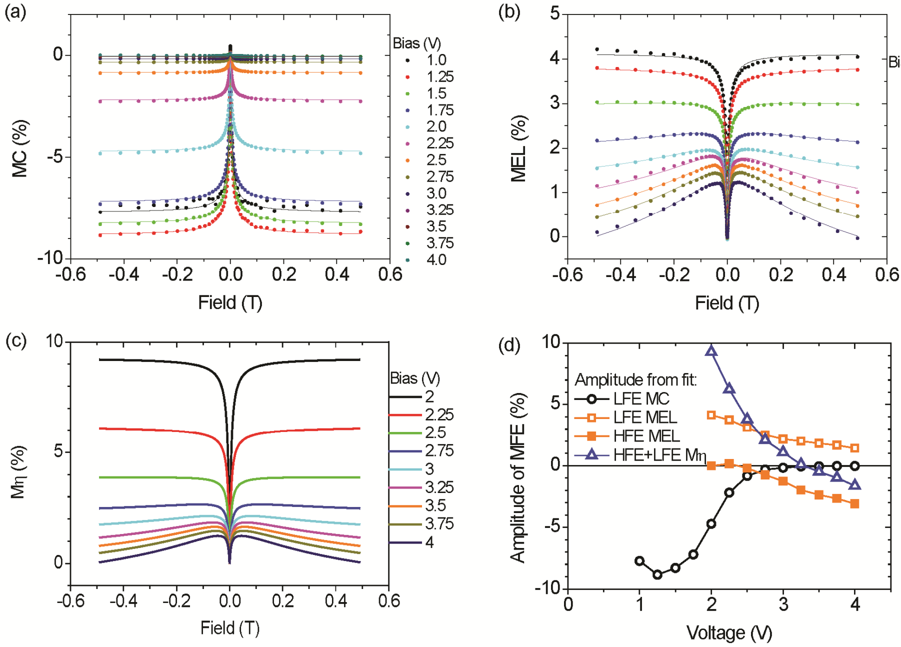

**Figure 10.2 (a) MC($B$) and (b) MEL($B$) measurements on a conditioned PPV-based LEC at different bias voltages (symbols). (a) The MC($B$) was fitted (lines) with one non-Lorentzian ($B_0$ = 2.2 mT). (b) The MEL($B$) was fitted (lines) with two non-Lorentzians accounting for a low field effect ($B_0$ = 2.3 mT) and a high field effect ($B_0$ = 220 mT). (c) Mη($B$) as derived from the ratio of the fits shown in (b) and (a). (d) Values of the fitted MC($B$), MEL($B$) and Mη($B$) curves in the limit of $B \rightarrow \infty$ vs. applied bias voltage. The amplitude of the low (LFE) and high (HFE) field effects in the MEL are split up in two graphs.**

## 10.4 Discussion

### 10.4.1 Device physics

To facilitate discussion of the observed magnetic field effects we will first briefly review the device operation of an LEC.[7-10] In Figure 10.3 schematics are shown of the carrier distributions and potential profiles in the LEC before, during and after conditioning at $V_{\text{bias}}$ = 4 V.[7] In a pristine device only ionic charges related to the salt are present as shown in Figure 10.3a. The binding energy of this salt is a few tenths of an eV,[7] resulting in a fraction of the salt that is thermally dissociated and thus susceptible to external fields. At the contacts the ions form thin electric double-layers (EDLs) to compensate for the built in-voltage induced by the difference in electrode work functions.

If now a bias voltage is applied that exceeds the polymer bandgap, larger EDLs are formed resulting in the formation of Ohmic contacts. Consequently carriers are injected and form space charge in the bulk. This space charge attracts mobile ions of opposite charge, leading to the formation of doped regions as is shown in Figure 10.3b. In between the doped regions the electrons and holes recombine, forming an intrinsic region. In the intrinsic region the carrier density and mobility are low compared to the doped regions. Therefore a relatively large fraction of the applied potential drops over the intrinsic region to maintain current conservation as is shown in Figure 10.3b. The corresponding relatively large field results in depletion of mobile ions from this junction region.[8] This initial doping due to carrier injection is a fast process that occurs within a second, and is determined by the mobility and density of mobile ions.[7] Part of the salt, however, remains undissociated.

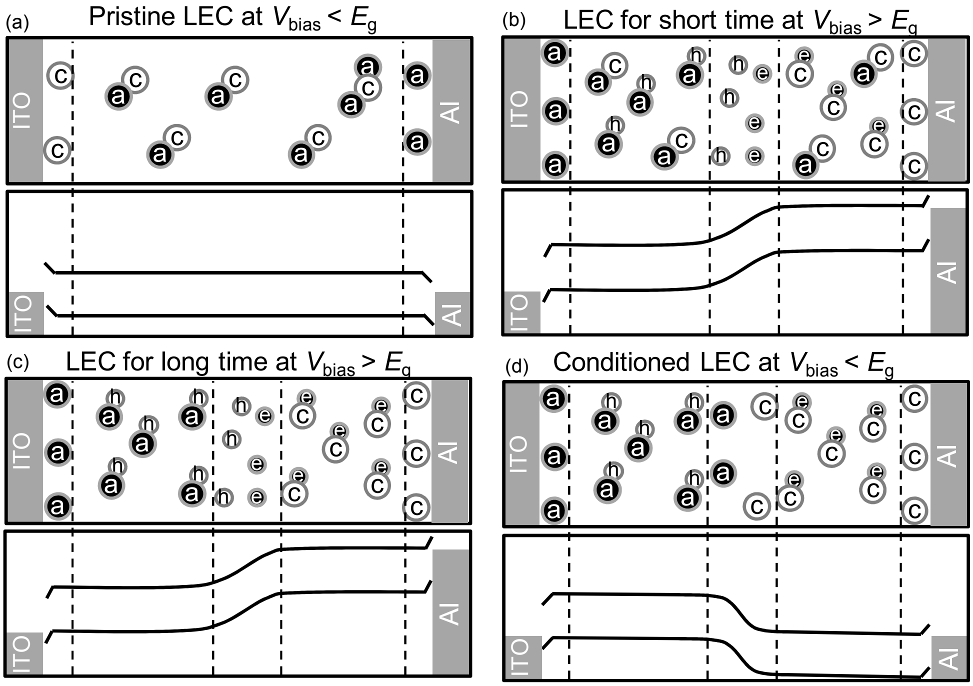

**Figure 10.3 Schematic of carrier distribution and potential profile in an LEC (a) before, (b, c) during and (d) after operation. The carrier distributions for relatively short and long times of operation are shown in (b) and (c), respectively. The different types of carriers are indicated with their initials: a (anion), c (cation), e (electron) and h (hole).**

If the bias voltage is switched off at this point, the device returns to more or less the pristine state: the injected charges either recombine or move back towards the electrodes whereas the ions redistribute to compensate each other electrostatically. If, alternatively, the bias is maintained, the remaining salt complexes have time to dissociate into mobile anions and cations. These are then as well separated from each other by moving into the p- and n-type doped regions, respectively, as shown in Figure 10.3c. This slow doping process is dominated by the dissociation of salt complexes into ions rather than by the ion mobility. As a result the doping process saturates in the order of minutes instead of within a second.[7] Experimentally this slow saturation is demonstrated by a continuous increase of current while the efficiency decreases. The efficiency decrease is related to exciton quenching at doping sites.[9] This quenching is an interaction between singlet excitons and trapped charges. It is typically a strong effect in LECs, as p-i-n junction formation allows for relatively large numbers of carriers close to a narrow recombination zone. As triplet excitons typically live longer than singlet excitons, interactions between triplet excitons and trapped charges are likely present as well, although they cannot be directly observed in the efficiency. Such interactions will, however, prove to be important for the OMAR effects described later in this chapter.

When removing the bias voltage after such a long transient, again the excess electronic carriers will recombine or be collected by the electrodes. However, as the doping density is maximized in this case, a larger amount of doping is expected to remain trapped inside the device as illustrated in Figure 10.3d. The difference in quasi-Fermi levels of the p- and n-type doped regions then leads to a compensating electric field in the junction region. In planar cells it has been observed that the sign of the electric field in the junction region changes after removal of the bias voltage.[10] This is drawn in Figure 10.3d. During operation the electrons and holes cause uncompensated space charge in the junction region. After switch-off the electrons and holes recombine, leaving anions and cations to form space charge in this region. The anions and cations in the junction region either originate from ions that were already trapped in this region or ions that entered the junction region by drift and/or diffusion. In either case, the removal of the bias voltage leads to a switch in sign of the polarity of the electric field in the p-i-n junction. In this state the electronic transport is strongly influenced by the Coulomb traps formed by the ions in the p-i-n junction. This is an interesting case for studying OMAR as charge traps are known to enhance the magnitude of OMAR in general.[11]

The magnetic field effects reported in this chapter are rationalized in the next sections in the light of the device physics explained above. In short, conditioning changes the device operation in the voltage regime at and below the semiconductor bandgap. In a conditioned device the active layer contains ions that trap electronic charges as well as uncompensated ions acting as Coulomb traps.

### 10.4.2 Magnetic field effects

The magnetic field effects observed in Figure 10.1b and Figure 10.2 can be separated by their respective linewidths: an MC and MEL effect with $B_0 \approx 2.2$ mT and an MEL effect with $B_0 \approx 220$ mT. The low-field effects arise at magnetic fields that are similar in size as that of the hyperfine fields, which are mainly caused by the surrounding hydrogen nuclei. In the absence of an external magnetic field, these hyperfine fields are randomly oriented, enabling spin mixing of nearby carriers. Sufficiently large external fields on the other hand reduce spin mixing. In literature, several models have been proposed in which hyperfine interactions are relevant for electron-hole interactions[4, 12-13] or electron-electron and hole-hole interactions.[14-15]

To first give an overview of all for this case relevant processes regarding electronic charge transport and recombination, a schematic was drawn in Figure 10.4. The schematic starts from free electrons and holes. When a free charge comes in the vicinity of another charge of equal polarity, a polaron pair is formed with either singlet or triplet character. As both carriers are on different sites, hopping through the semiconductor can lead to spin mixing, which is induced by the presence of random hyperfine fields. Both charges can, however, only arrive at the same site if the polaron pair has a singlet spin-state. In that case a bipolaron is formed. Polaron pairs and bipolarons also dissociate, leading again to free electrons or holes.

Free electrons and holes can also meet each other and form electron-hole pairs with either singlet or triplet character. This process is favored by Coulomb attraction, which is rather strong in organic semiconductors due to the relatively low dielectric constant. The spin-state of the electron-hole pairs can again be mixed by hopping through the semiconductor having random hyperfine fields. In case when the electron and hole arrive on the same site an exciton is formed with a fixed spin-state. In case when the exciton does not interact with any surrounding particles, the exciton will ultimately decay to the ground state.

In this work only the following interactions involving excitons are considered: triplet-triplet annihilation, which is not shown in Figure 10.4, and triplet-polaron interaction. In the latter case, the triplet exciton and polaron form a doublet or a quartet spin state. The doublet and quartet manifold show a zero field splitting and these spin states can be mixed. Ultimately, either the exciton-polaron complex dissociates in a triplet exciton and a polaron, or the complex decays by energy or charge transfer resulting in the loss of the exciton, whereas the polaron remains. Singlet exciton quenching on polarons is not considered in this work because of the orders of magnitude shorter singlet lifetime in PPV.

In Figure 10.4 gray arrows are drawn to indicate the magnetic field dependent transitions between polaron pairs of equal and opposite charges and between a combination of a triplet exciton and a trapped charge. In the next sections these interactions are discussed in relation to the experimentally obtained magnetic field effects in conditioned LECs.

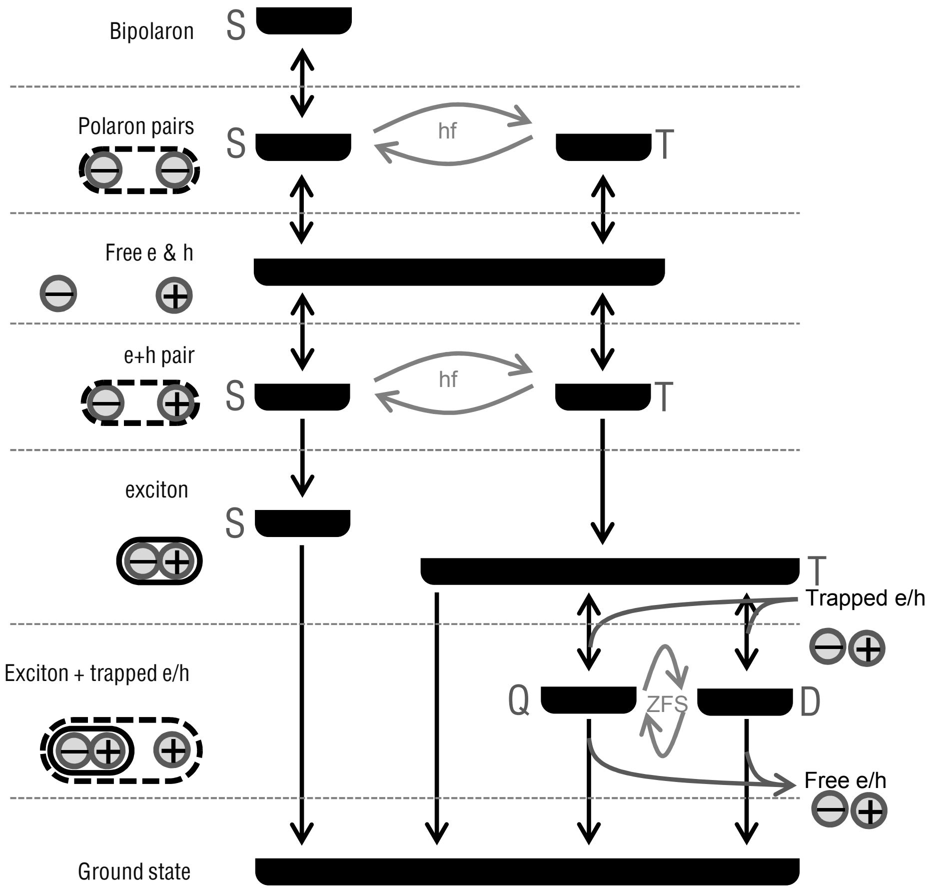

**Figure 10.4 Schematic representation of all particles and processes that can lead to magnetic field effects in current and electroluminescence. Note that this is not a strict energy diagram.**

### 10.4.3 Low-field effects in efficiency

The non-zero Mη shown in Figure 10.2c and d indicates that, by application of a magnetic field, a change in singlet:triplet ratio has been established. Such a magnetic field effect originates from magnetic-field dependent singlet-triplet interconversion within the electron-hole pair prior to exciton formation. To describe this effect we used the two-site model that was recently introduced by Kersten *et al.*[4] This model describes the exciton formation process by considering the final hop of an electron from the site where it resides to a site where a hole is residing, or vice versa. As electron and hole are on different sites, the spins of both carriers can change due to hyperfine mixing because the exchange coupling is relatively small. The rate of spin mixing is proportional to the hyperfine precession frequency: $\omega_{hf} = g\mu_B B_{hf}\hbar^{-1}$, where $g$ is the $g$-factor; $g \approx 2$ is taken in this case for both electrons and holes, $\mu_B$ is the Bohr magneton and $B_{hf}$ is the strength of the hyperfine field. The exciton formation itself can be described by the hopping rates $k_T$

and $k_S$ that are slightly different for triplet (T) and singlet (S) exciton formation due to a difference in energy and wave function. Further details on this model can be found in Ref. 4.

The model is used to determine the parameters needed to obtain similar values of MC and Mη as in the experiment. The maximal experimental value of MC, -0.09, was taken from Figure 10.2 at $V_{\text{bias}}$ = 1.25 V. The corresponding value for Mη at the same bias voltage could not be determined, as the electroluminescence was below the detection limit in the experiment. Therefore a value of Mη = 0.15 is assumed, which can be deduced by extrapolation to $V_{\text{bias}}$ = 1.25 V.[16] The model was used to calculate the Mη for different ratios i) of the singlet and triplet exciton formation rates, $k_S/k_T$, and ii) of the triplet exciton formation rate and spin mixing rate, $k_T/\omega_{\text{hf}}$. Mη is plotted in a contour plot in Figure 10.5a. From the contour plot a set of parameters can be deduced for which Mη ≈ 0.15. This set is indicated by the white dashed line in Figure 10.5a. As a check whether this set comprises realistic values of these parameters, we compared the obtained results with parameters reported earlier in pure MDMO-PPV: $k_S/k_T$ = 0.7 and $k_T/\omega_{\text{hf}}$ = 1.1.[4] These parameters are close to the parameters obtained in the modeling here (see white arrow in Figure 10.5a), proving that the model description for the Mη effect is possible.

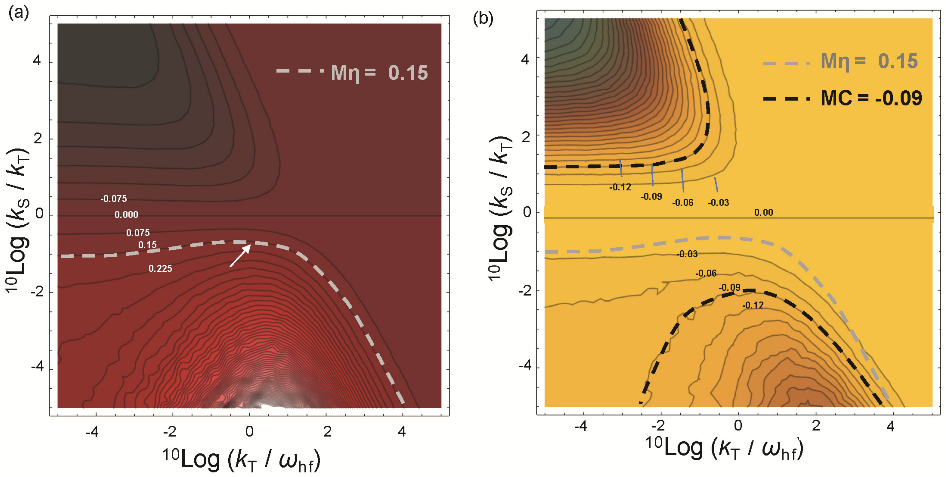

**Figure 10.5 Contourplots of (a) Mη and (b) MC as a function of $k_S$ / $k_T$ and $k_T$ / $\omega_{\text{hf}}$ for the two-site model. The dashed lines in (a) and (b) indicate the contours of the experimentally obtained values of Mη and MC (see Figure 10.2d).**

What is left to explain is the diminishing of the low-field effect in the efficiency at higher bias voltages as observed in Figure 10.2d: both the negative low-field MFE in current and the positive low-field MFE in electroluminescence decrease, resulting in a lowering of the low-field MFE in efficiency. This can be explained by a shift in the contour plot towards larger values of $k_T/\omega_{hf}$ starting at ${}^{10}\log k_T/\omega_{hf} = 0$. In that case, Mη is observed to be reduced. An increase of the parameter $k_T/\omega_{hf}$ is likely, as at low bias voltages the carrier density is low in the LEC, favoring localization of polarons and increasing the contribution of traps to transport. Especially at sub-bandgap voltages, ions in the junction region are expected to act as traps (see Figure 10.3d) as their space charge is dominant in the junction region. This means that the mobility, which is related to the hopping rate $k_T$, is relatively low at sub-bandgap bias voltages. When increasing the bias voltage, the trap states fill up so that free polarons cannot relax into these states. This as well as the larger carrier densities leads to an enhanced carrier mobility, hence a larger hopping rate.[17-18] As the hopping rate of polarons is related to the exciton formation rate; also the latter is enhanced by the larger bias voltage. Such an enhancement means a shift towards the right-hand side in the contour plot shown in Figure 10.5a, which implies a reduction in Mη as well.

In summary, the two-site model shows that the observed low-field effect in Mη at bias voltages around the bandgap originates from an interplay between i) a magnetic field dependent spin mixing rate, ii) a singlet exciton formation rate and iii) a triplet exciton formation rate of an electron-hole pair. Suppression of spin mixing effectively favors exciton formation with the lowest rate, i.e. the singlet exciton formation, leading to an enhanced efficiency. The roll-off of Mη at higher voltages is arguably due to an enhanced hopping rate, leading to an enhancement of both the singlet and triplet exciton formation rate whereas the spin mixing rate remains the same. As a consequence the effects of spin mixing and the external magnetic field are reduced, leading to smaller values of Mη.

### 10.4.4 Low-field effects in current

For the rationalization of the negative MC in conditioned LECs biased below the bandgap, the following magnetic field dependent interactions were considered (see also Figure 10.4): polaron pair interactions between equal carrier types, polaron pair interactions between unequal carrier types, the interaction between excitons and trapped charges and the influence of the triplet exciton density on the dielectric constant.

#### 10.4.4.1 Polaron pair with equal carriers

To determine whether magnetic field dependent polaron pair interactions between equal carrier types in the doped regions play a role in the observed MC, an electrochemical transistor as described in Figure 8.8 and similar to Ref. 19 was fabricated. In this transistor either n- or p-type doping is established, excluding any excitonic or recombination effects. No MC effects were observed at any doping level. Also during and after de-doping no MC was observed. This strongly suggests that spin-related interactions between electrons and electrons or holes and holes in electrochemically doped and partially de-doped MDMO-

PPV do not play a significant role in transport. Moreover, it excludes magnetic field dependent interactions between electronic and ionic species.

### 10.4.4.2 Polaron pair with unequal carriers

Another option to explain the MC is polaron pair interaction between unequal carrier types during exciton formation. This interaction can only occur if both electrons and holes are injected. Despite biasing the LEC with a bias voltage below the bandgap, both types of carriers can still be injected.[20] A sign that this is indeed the case is the *L*-*V* characteristic of the conditioned device as opposed to the unconditioned device in Figure 10.1a. For 2.1 V < $V_{\mathrm{bias}}$ < 2.4 V the appearance of electroluminescence is observed in the conditioned device. For lower bias voltages electroluminescence may still be present but lies below the detection limit of the diode. To further substantiate this statement the 1D numerical drift-diffusion model was used to calculate carrier density, recombination and potential profiles in an LEC before ($V_{\mathrm{bias}}$ = 1 V), during ($V_{\mathrm{bias}}$ = 4 V) and after ($V_{\mathrm{bias}}$ = 1 V) conditioning. These profiles are plotted in Figure 10.6a-c. The trapping by dopants was simulated by first biasing the device at 4 V, followed by a short relaxation at $V_{\mathrm{bias}}$ = 0 V after which the ions were artificially immobilized in the model. The short time span at which the device has been biased at 0 V determines the trapped doping density. The profiles in Figure 10.6a-c show that due to the fixed doping (Figure 10.6a) and the formation of Ohmic contacts by p- or n-type doping (Figure 10.6c), recombination still takes place even though the device is biased ($V_{\mathrm{bias}}$ = 1 V) below the bandgap ($E_{\mathrm{gap}}$ = 2.2 eV). In the case shown here, the recombination has been lowered by a factor ~$10^6$ compared to the case of $V_{\mathrm{bias}}$ = 4 V. This is in line with the luminance being below the detection limit of the experimental setup.

The profiles in Figure 10.6a-c furthermore show that the vast majority of the injected carriers form excitons instead of being extracted by the contacts: electron and hole densities only overlap in the central region of the device. This means that exciton formation limits the current passing through the cell. This knowledge can be used to determine the magneto-conductance by considering the sum of singlet and triplet exciton formation. Therefore it is possible to determine the magneto-conductance related to spin mixing and singlet/triplet exciton formation by using the two-site model presented in the previous section. As shown in Figure 10.5a, the absence of spin mixing induced by a magnetic field enhances the singlet:triplet ratio, as evidenced by a positive Mη. Reasonable values of Mη were found for $k_{\mathrm{S}}/k_{\mathrm{T}}$ < 1, see Figure 10.5a. Hence, the total exciton formation rate decreases with magnetic field. This decrease leads to a reduced current, as the current is proportional to the exciton formation rate. In Figure 10.5b a contour plot of the MC is shown. Here, the MC is calculated from the sum of the exciton formation rates weighted by the calculated singlet:triplet ratio. The black, dashed lines indicate the parameters at which MC = -0.09 is obtained. The gray dashed line is copied from Figure 10.5a to indicate the parameters at which Mη = 0.15. The mismatch between the gray and black lines indicate that no solution exists for which MC = -0.09 and Mη = 0.15. The corresponding values of the MC on the gray dashed line lie between 0.00 and -0.03, i.e. 0 % to -3 %. This is not in line with the experimentally determined -10 % (see Figure 10.1b). Therefore this mechanism cannot be the main cause of the observed MC effects.

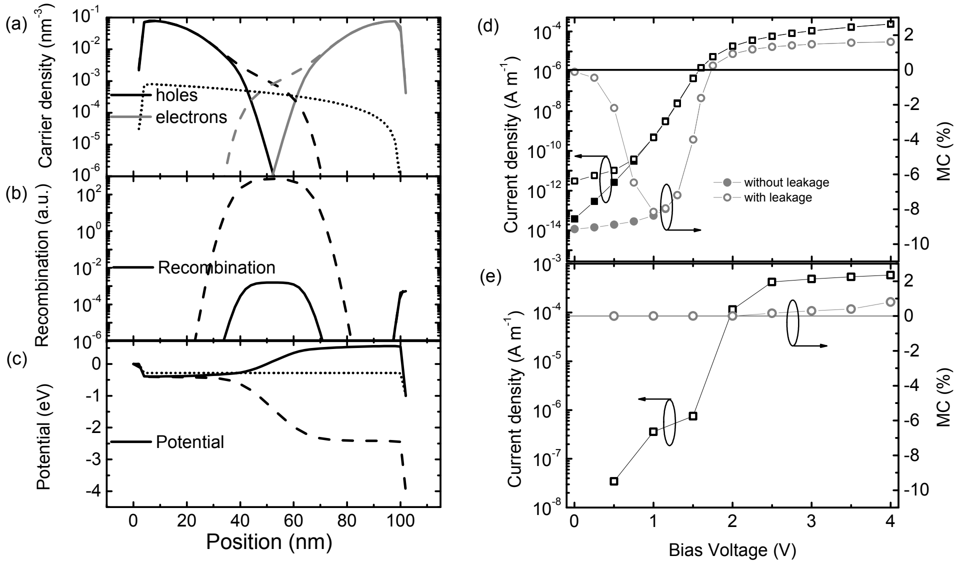

**Figure 10.6 Calculated profiles of (a) electron and hole density, (b) recombination and (c) potential in an unconditioned LEC at $V_{bias}$ = 1 V (dotted lines), the same LEC at $V_{bias}$ = 4 V (dashed lines) and at $V_{bias}$ = 1 V (solid lines) after conditioning. Conditioning is modeled by allowing the device to reach steady-state at $V_{bias}$ = 4 V, followed by a short time relaxation to allow part of the doping to deplete. After that the ion mobility was set to zero to artificially trap electronic charges with immobile ions. (d, e) Calculated current density and MC(*V*) according to the numerical drift-diffusion model (d) with and (e) without zero ion mobility. In (d), leakage current is included: ($J_{leakage} = 10^{-11} \cdot V_{bias}$).**

### 10.4.4.3 Magnetic field dependent triplet density: effect on triplet exciton-polarons interactions

So far, polaron pair interactions were studied by means of an electrochemical transistor and the two-site model. The results of these studies prove that the negative MC in LECs is not related to polaron pair interactions in the doped regions (electron-electron, hole-hole) or in the junction region (electron-hole). Therefore, excitonic interactions may need to be included. To obtain an effect on the current density, the excitons need to interact with polarons either in the doped regions or in the recombination zone. As excitons are only formed in the recombination zone, the interaction is most likely to take place in or just next to this region. Due to the relatively large lifetime of triplet excitons, most likely their interaction with polarons is dominant.[21-24] The triplet exciton density itself is magnetic field dependent, which followed from the change in singlet:triplet ratio as calculated in Figure 10.5a. Polarons in the intrinsic region are expectedly trapped in deep states because of their relatively low density for $V_{\text{bias}} < E_{\text{gap}}$ (Figure 10.6a) and due to uncompensated immobile ions that lead to the space charge in the junction region (Figure 10.6c). The interaction relevant here is then recombination of a trapped polaron and a triplet exciton producing a molecule in the ground state and a polaron, as shown in the bottom right in Figure 10.4. The recombination process can then lead to detrapping of the polaron either due to energy or charge transfer from the triplet exciton. Hence the triplet exciton density, which itself is magnetic field dependent, can effectively change the mobility of polarons and concurrently the current passing through the cell. Note that this effect would be absent in a non-conditioned device, as then no excitons are formed for $V_{\text{bias}} < E_{\text{gap}}$, and because of the lesser importance of trapping, see paragraph 10.4.1. For $V_{\text{bias}} > E_{\text{gap}}$ the trap states will be filled, resulting in trap-free carrier transport. This reduces the effect of detrapping on the total current density. Hence the MC rolls off at higher bias voltages, which is indeed observed in Figure 10.1b. Note that OMAR experiments on LECs by Vardeny *et al.*[1] did not show the negative MC as observed here. They found that during operation electron and hole transport was asymmetric, leading to pinning of the recombination zone to one of the electrodes. Therefore, bipolar injection can in that work argued to be absent for $V_{\text{bias}} < E_{\text{gap}}$, as either one of the doped regions has not developed properly during operation.

A remark is in place regarding a possible magnetic field dependence of triplet-polaron (T-P) interactions (see Figure 10.4). If interactions between triplet excitons and trapped polarons indeed play a role, a high-field MFE is expected related to the zero-field splitting of the resultant doublet and quartet manifold.[25] In anthracene, for example, the rate of triplet quenching by polarons was found to be magnetic field dependent.[26-27] As MDMO-PPV is a singlet emitter, this effect cannot be observed in the electroluminescence. The reason why no high-field MFE in the current is observed is unknown to us.

To attempt to explain the absence of a high-field MFE, the following processes need to be considered: a triplet exciton can either decay to the ground state or form a triplet polaron pair if a (trapped) polaron is near. The triplet-polaron pair either dissociates again in a triplet exciton and a polaron or the triplet exciton is quenched, leading to a molecule in the ground state and an energetically excited polaron. The quenching process is likely dependent on the spin state, which can be altered by spin mixing related to the zero-field splitting. In case quenching is not possible due to the spin configuration, the pair has to dissociate. The resultant polaron then remains trapped, whereas the triplet exciton can either decay or form a new triplet-polaron pair. In case the decay rate of triplet excitons is relatively small, it is most likely that triplet excitons sequentially form pairs with different trapped polarons until the right spin-configuration for quenching is obtained. In such a case no high-field MFE in the current is expected. In the conditioned LEC discussed here the latter seems to be the case. One argument is the fact that singlet exciton quenching is already highly efficient in the doped regions, whereas the lifetime of singlets is typically a factor $10^3$ smaller in MDMO-PPV than the lifetime of triplets. Furthermore, in a recent paper, Friend *et al.* characterized both triplet-triplet annihilation as well as triplet-charge quenching as the dominant triplet decay mechanisms in polymer LEDs.[28] Therefore it is most likely that in the conditioned LEC no high-field MFE is observed. Another possible explanation for the absence of a high-field MFE is that the presence of ions favors spin mixing, suppressing effectively any magnetic field dependence of the transition between quartet and doublet states.

### 10.4.4.4 Magnetic field dependent triplet density: effect on dielectric constant

An alternative explanation of MC in OLEDs was given in terms of a magnetic field dependent change in the dielectric constant $\varepsilon$.[29] The recombination current is proportional to $\varepsilon$ via the Langevin factor $\gamma = q(\mu_n + \mu_p)/\varepsilon$. A change of 10 % of $\varepsilon$ would then be necessary to explain the observed MC of -10 %. The change in $\varepsilon$ can originate from an altered triplet exciton density. The small dipoles formed by the triplet excitons are then expected to enhance the dielectric constant. If this would be the case here, then, in a hypothetical situation, a dramatic change of $\varepsilon$ far beyond 10 % would be expected when comparing an unbiased device and a device biased at e.g. 4 V. The difference in triplet density would be significantly larger than at $V < E_g$ with and without a magnetic field. Large changes in the dielectric constant in similar LECs biased at 0 V and 4 V have, however, not been observed in impedance measurements.[7] Hence, we do not think that this alternative explanation is applicable to our results. On the contrary, we suggest that the effects observed in the air-treated MEH-PPV diodes in Ref. 29 can also be described by a triplet exciton dependent detrapping of polarons.

### 10.4.4.5 Device simulations

To check whether the proposed mechanism of triplet exciton assisted detrapping of polarons can explain the observed bias voltage dependence of the MC (see Figure 10.2d), numerical drift-diffusion simulations were performed (see paragraph 10.3 and appendix A for more details). The model does not explicitly describe spin states or magnetic field effects. Nonetheless, these effects can be mimicked by altering parameters that are supposed to be magnetic field dependent.[30] In paragraph 10.4.4.3, the MC was attributed to an effective change in polaron mobility in the junction region. To model the effect of such a mobility change on the device current, the modeling results of the conditioned LEC shown in Figure 10.6a-c (straight lines) were used as starting points. Changing the polaron mobility in the complete device gives the trivial result of a proportional change in current. It was argued above, however, that only the mobility in the junction region is affected by interaction with triplet excitons. The carrier mobility in the junction region affects carrier transport as well as carrier recombination. Recombination is described by the Langevin description in the model and is proportional to the sum of the electron and hole mobilities: $R = \gamma np$, where the Langevin factor is $\gamma = q(\mu_n + \mu_p)/\varepsilon$. Here, $n$ and $p$ are the respective electron and hole densities, $q$ is the elementary charge, $\mu_n$ and $\mu_p$ are the electron and hole mobilities, respectively, and $\varepsilon$ is the dielectric constant. To model the effect of an altered recombination rate due to a reduced carrier mobility, a prefactor $R_{pre}$ was introduced in the Langevin formula for the recombination rate: $R = R_{pre}\gamma np$. A prefactor of 0.9 was used, mimicking a reduction of 10 % of the carrier mobility in the junction region. The magneto-conductance was then determined by comparing the current for simulations with $R_{pre} = 0.9$ and 1.0. Similar modeling results were obtained when instead of changing $R_{pre}$, the electronic charge carrier mobility in the recombination zone was altered by 10 %.[31]

In Figure 10.6d and e modeled *J*-*V* and MC-*V* characteristics are shown in, respectively, a conditioned and a pristine device operating in steady-state at different bias levels. In the conditioned device the ions are artificially frozen at their positions after conditioning by setting the ion mobility to zero; in the pristine device the ion mobility is nonzero, as this corresponds to a non-conditioned device. In the pristine device no MFE in current is observed, whereas in the conditioned device the decrease of the carrier mobility with magnetic field has resulted in a MFE in the current, denoted as MC = $(I_{\mathrm{Rpre=0.9}}-I_{\mathrm{Rpre=1}})/I_{\mathrm{Rpre=1}}$ for $V_{bias} < E_{gap}$. Here $I_{\mathrm{Rpe=0.9}}$ and $I_{\mathrm{Rpre=1}}$ represent the current for the cases when $R_{pre} = 0.9$ or 1.0. To make the modeling results resemble the experimental results at bias voltages around 0 V (e.g. Figure 10.1b), a small, linear leakage current was added to the simulated current density. The leakage current dominates the total current at these relatively small bias voltages, leading to an effective reduction of MC. The small MC values around $V_{bias} = 0$ V may furthermore also be related to the relatively low generation rate of triplet excitons due to the low current density here.

For $V_{bias} > E_{gap}$ a positive MC is observed in Figure 10.6d due to two artificial problems in the modeling. First of all, in reality the high bias voltage would enable the ions to move. The results in Figure 10.6e show what the effect of mobile ions on the MC would be: MC ≈ 0. Secondly, polaron detrapping in the junction region becomes less dominant: trap states are completely filled resulting in polarons to be in energetically higher-lying states, leading to a higher mobility. The current is therefore not dominated by traps anymore. As a result, the T-P effect is not likely to enhance the carrier mobility in this bias range: a change of 10 % in electronic carrier mobility is most likely an overestimate. Therefore, the part of the modeling for $V_{bias} > E_{gap}$ can be ignored.

The modeling results can be summarized as follows: a reduction of the carrier mobility in the recombination region can only reduce the total current through the device in the specific case that a fixed p-i-n junction structure is present. This was achieved in the model by reducing the ion mobility to 0 during steady-state operation at $V_{\text{bias}}$ = 4 V. For this, the applied bias voltage must be below the bandgap of the semiconductor. In case $V_{\text{bias}} > E_{\text{gap}}$ the effect of the frozen p-i-n junction is reduced due to the formation of electronic space charge. Experimentally, the negative MC is measured at the same conditions as described here: A fixed p-i-n junction is present and electronic space charge is absent due to first conditioning the device at $V_{\text{bias}}$ = 4 V followed by operation at $V_{\text{bias}} < E_{\text{gap}}$.

Considering all results together we attribute the negative MC in conditioned LECs to polaron-triplet exciton interactions that lead to an enhanced carrier mobility in the trap-dominated intrinsic region. This effect is unique in LECs as opposed to OLEDs. In OLEDs, transport occurs by percolation through optimal pathways, which typically are not dominated by traps. In conditioned LECs biased at low bias voltages, the trap density is large relative to the carrier density so that transport occurs from trap to trap. Interaction with triplet excitons can help to release carriers from these traps by transfer of energy from the triplet exciton to the trapped polaron. The observed magnetic field dependence itself does not originate from T-P interactions, but from the change in triplet exciton density. The triplet exciton density changes due to a change in singlet:triplet exciton formation ratio discussed in the previous section.

### 10.4.5 High-field MFE in efficiency

The last observed MFE that has not been discussed yet is the effect in the efficiency that arises at $B_0$ = 220 mT and $V_{\text{bias}} > E_{\text{gap}}$ as shown in Figure 10.2d. The relatively large size of the characteristic magnetic field $B_0$ indicates a mechanism related to zero-field splitting. Furthermore, the effect only changes the electroluminescence, whereas it has no effect on the current. Species that may be involved because of their presence in the recombination zone are polarons and singlet and triplet excitons. Singlet excitons can interact with polarons leading to quenching. This quenching is, however, not magnetic field dependent. A possible MFE in the electroluminescence can originate from delayed fluorescence (DF) arising from triplet-triplet annihilation (TTA).[25, 32-33]

A pair of triplets can produce nine possible spin states with equal probability: a quintet, a triplet and a singlet state. Due to spin conservation, only the latter can annihilate forming an excited and a ground-state singlet state. The excited singlet state can then relax by emitting a photon. This process is called delayed fluorescence (DF) and was recently shown to be of importance in OLEDs.[34] Mixing between all nine spin states is possible when the Zeeman splitting is equal to or smaller than the zero-field splitting. If on the other hand a relatively large magnetic field is applied, then the Zeeman splitting suppresses spin mixing, leading to a reduced fluorescence. The high-field effect shown in Figure 10.2d is negative, which is in line with the previous discussion. The zero-field splitting parameter of MDMO-PPV is $D \approx 60$ mT,[35-36] which corresponds with the experimental results presented in Figure 10.2b and d: the high-field effect appears roughly at 50 mT. The observed voltage dependence can be explained by the enhancement of the current, leading to a larger triplet exciton density. Accordingly, the probability of triplet-triplet encounters grows, leading to an enhanced contribution of DF from TTA to fluorescence. Additionally, it is likely that the triplet-triplet interactions are in competition with the triplet-polaron encounters, which were argued in the previous section to result in a negative MC. The enhanced probability for TTA at larger bias voltages may therefore result in an effective reduction of triplet-polaron encounters leading to a reduced MC effect as is experimentally observed in Figure 10.2d (for $V_{\text{bias}} > 1.2$V). These results indicate that part of the luminance in LECs is comes from DF by TTA. The maximal contribution of this process to the total electroluminescence can be determined under the following assumptions: i) all triplets form pairs; ii) the singlet:triplet ratio is close to 25:75 and iii) the magnetic field is large enough to prevent any spin mixing. In that case a fraction of 1/18 of the triplets is converted in singlets, resulting in roughly 14 %[37] of the total fluorescence originating from DF. Removal of the magnetic field then enhances this contribution at $V_{\text{bias}}$ = 4 V to ~17 %. This means that a significant fraction of the electroluminescence in PPV-based LECs originates from DF by TTA.

## 10.5 Conclusions

In summary, we have shown that light-emitting electrochemical cells can show large magnetic field effects because of trap-dominated transport and recombination in a relatively narrow region due to electrochemical doping. Large negative magneto-conductance values of around -12 % are observed in conditioned LECs simultaneously with a positive magneto-efficiency. Both effects originate from the competition between magnetic field dependent spin mixing and the formation rates of singlet and triplet excitons. The change in singlet:triplet ratio leads to the enhanced efficiency. The reduced triplet exciton density is suggested to lead to a reduction in polaron detrapping in the recombination zone, resulting in a reduced current density. At bias voltages that significantly exceed the semiconductor bandgap, a negative magneto-electroluminescence effect is observed arising at relatively large magnetic fields of 220 mT. This effect is attributed to delayed fluorescence which originates from magnetic field dependent triplet-triplet annihilation. The contribution of delayed fluorescence to the total light output of the LEC is estimated to be at most 17 %.

# References

[1] G. Ni, T. D. Nguyen, Z. V. Vardeny, Appl. Phys. Lett. 98 (2011) 263302.

[2] T. D. Nguyen, G. Hukic-Markosian, F. J. Wang, L. Wojcik, X. G. Li, E. Ehrenfreund, Z. V. Vardeny, Nat. Mater. 9 (2010) 345.

[3] Ö. Mermer, G. Veeraraghavan, T. L. Francis, Y. Sheng, D. T. Nguyen, M. Wohlgenannt, A. Köhler, M. K. Al-Suti, M. S. Khan, Phys. Rev. B 72 (2005) 205202.

[4] S. P. Kersten, A. J. Schellekens, B. Koopmans, P. A. Bobbert, Phys. Rev. Lett. 106 (2011) 197402.

[5] W. Wagemans, W. J. Engelen, F. L. Bloom, B. Koopmans, Synth. Met. 160 (2010) 266.

[6] U. Niedermeier, M. Vieth, R. Patzold, W. Sarfert, H. von Seggern, Appl. Phys. Lett. 92 (2008) 193309.

[7] S. van Reenen, R. A. J. Janssen, M. Kemerink, Adv. Funct. Mater. 22 (2012) 4547.

[8] S. van Reenen, P. Matyba, A. Dzwilewski, R. A. J. Janssen, L. Edman, M. Kemerink, J. Am. Chem. Soc. 132 (2010) 13776.

[9] S. van Reenen, T. Akatsuka, D. Tordera, M. Kemerink, H. J. Bolink, J. Am. Chem. Soc. 135 (2013) 886.

[10] P. Matyba, K. Maturova, M. Kemerink, N. D. Robinson, L. Edman, Nat. Mater. 8 (2009) 672.

[11] J. Rybicki, R. Lin, F. Wang, M. Wohlgenannt, C. He, T. Sanders, Y. Suzuki, Phys. Rev. Lett. 109 (2012) 076603.

[12] V. N. Prigodin, J. D. Bergeson, D. M. Lincoln, A. J. Epstein, Synth. Met. 156 (2006) 757.

[13] P. Desai, P. Shakya, T. Kreouzis, W. P. Gillin, Phys. Rev. B 76 (2007) 235202.

[14] P. A. Bobbert, T. D. Nguyen, F. W. A. van Oost, B. Koopmans, M. Wohlgenannt, Phys. Rev. Lett. 99 (2007) 216801.

[15] S. P. Kersten, S. C. J. Meskers, P. A. Bobbert, Phys. Rev. B 86 (2012) 045210.

[16] 0.15 is obtained by taking the measured value of the LFE MC at 1.25 V (= -0.09) and by extrapolating the LFE MEL to 1.25 V (~ +0.06). The corresponding value of Mη results from 0.06 - 0.09 = 0.15.

[17] H. Shimotani, G. Diguet, Y. Iwasa, Appl. Phys. Lett. 86 (2005) 022104.

[18] S. van Reenen, R. A. J. Janssen, M. Kemerink, Org. Electron. 12 (2011) 1746.

[19] M. J. Panzer, C. D. Frisbie, J. Am. Chem. Soc. 129 (2007) 6599.

[20] P. Santhanam, D. J. Gray, R. J. Ram, Phys. Rev. Lett. 108 (2012) 097403.

[21] B. Koopmans, W. Wagemans, F. L. Bloom, P. A. Bobbert, M. Kemerink, M. Wohlgenannt, Philos. Trans. R. Soc. London, Ser. A 369 (2011) 3602.

[22] J. Yu, R. Lammi, A. J. Gesquiere, P. F. Barbara, J. Phys. Chem. B 109 (2005) 10025.

[23] M. Wittmer, I. Zschokkegranacher, J. Chem. Phys. 63 (1975) 4187.

[24] S. Reineke, K. Walzer, K. Leo, Phys. Rev. B 75 (2007) 125328.

[25] A. J. Schellekens, W. Wagemans, S. P. Kersten, P. A. Bobbert, B. Koopmans, Phys. Rev. B 84 (2011) 075204.

[26] V. Ern, Merrifie.Re, Phys. Rev. Lett. 21 (1968) 609.

[27] V. Ern, Bouchrih.H, J. Fourny, G. Delacote, Solid State Commun. 9 (1971) 1201.

[28] B. H. Wallikewitz, D. Kabra, S. Gelinas, R. H. Friend, Phys. Rev. B 85 (2012) 15.

[29] K. Kanemoto, H. Matsuoka, Y. Ueda, K. Takemoto, K. Kimura, H. Hashimoto, Phys. Rev. B 86 (2012) 125201.

[30] M. Cox, P. Janssen, S. H. W. Wouters, E. H. M. van der Heijden, M. Kemerink, B. Koopmans, Synth. Met. 173 (2013) 6.

[31] S. van Reenen, S. P. Kersten, S. H. W. Wouters, M. Cox, P. Janssen, B. Koopmans, P. A. Bobbert, M. Kemerink, Phys. Rev. B 88 (2013) 125203.

[32] Y. Zhang, R. Liu, Y. L. Lei, Z. H. Xiong, Appl. Phys. Lett. 94 (2009) 083307.

[33] R. C. Johnson, Merrifie.Re, P. Avakian, R. B. Flippen, Phys. Rev. Lett. 19 (1967) 285.

[34] Y. F. Zhang, S. R. Forrest, Phys. Rev. Lett. 108 (2012) 267404.

[35] L. S. Swanson, P. A. Lane, J. Shinar, K. Yoshino, F. Wudl, Synth. Met. 50 (1992) 473.

[36] L. S. Swanson, J. Shinar, P. A. Lane, B. C. Hess, F. Wudl, Synth. Met. 50 (1992) 481.

[37] 1 of 9 possible spin states formed by two triplet excitons can generate one singlet exciton: 1/2 x 1/9 = 1/18. A singlet:triplet ratio of 25:75 then means that 75x1/18 ≈ 4 % of delayed singlet excitons are formed. This means that 4/(25+4) ≈ 14 % of the singlet exciton density is due to DF from TTA in case a magnetic field is present.

In the absence of a magnetic field spin mixing takes place between the spin states formed by two triplet excitons. The high magnetic field effect improves the efficiency by 3 % at $V_{\text{bias}}$ = 4 V (see Figure 10.2d). As a result the percentage of delayed singlet excitons increases from 4 % to [(25+4)x1.03]-25 ≈ 5 %. This means that 5/(25+5) ≈ 17 % of the singlet exciton density is due to DF from TTA in case no magnetic field is present.

# Chapter 11 Origin of work function modification by electrolytes

*An alternative use of electrolytes besides in the active layer of LECs is as thin injection layers in organic electronics. The microscopic origin behind work function modification by such polyelectrolytes and tertiary aliphatic amines used as interlayers is however unclear. Scanning Kelvin probe microscopy is used to determine the work function modification by thin layers of such materials on different substrates. Both reductions and increases in work function were found to follow a general mechanism. Such modifications are found to only take place when the work function modification layer (WML) is deposited on conductors or semiconductors. On insulators no effect is observed. Additionally, the work function modification is independent of the WML thickness or the substrate work function in the range of 3 to 5 eV. This data supports work function modification by dipole formation at the electrode interface, induced by interaction with its image dipole. Differences in size and side groups of the ionic constituents lead to differences in approach distance towards the surface. These differences determine magnitude and direction of the resulting dipole. This understanding facilitates design and synthesis of new air-stable and solution-processable WMLs for organic electronics.*

*Part of the work presented in this chapter has been published: S. van Reenen, S. Kouijzer, R. A. J. Janssen, M. M. Wienk, M. Kemerink, accepted for publication in Adv. Mater. Interfaces (2014).

## 11.1 Introduction

The remarkable efficiency leap from less than 5% to over 10% in the past 7 years makes it plausible that organic solar cells can evolve into a successful thin film photovoltaic technology. To this end, further improvements in the sunlight-to-electricity conversion efficiency are still needed. To do so, not only the optoelectronic, active layer should be considered, but also the connection between this layer and the electrodes. This connection is facilitated by so-called work function modification layers (WMLs) that serve to align the transport levels in the organic semiconductor and the conductor by modification of the work function. Materials that are often used are poly(3,4-ethylenedioxythiophene) poly(styrenesulfonate) (PEDOT:PSS) for improving hole collection and injection in combination with an indium tin oxide (ITO) electrode and LiF for the electron contact in combination with an Al metal electrode. A new generation of WMLs first introduced by Cao et al. is based on polyelectrolytes or tertiary aliphatic amines, such as poly[(9,9-bis(3'-(N,N-dimethylamino)propyl)-2,7-fluorene)-*alt*-2,7-(9,9-dioctylfluorene)] (PFN) and the corresponding ethyl ammonium bromide.[1] Although these materials improve carrier injection or extraction in different organic diode devices,[1-7] the mechanism behind this improvement is not completely clear. This ambiguity hinders synthesis, selection and optimization of new WMLs.

Mechanisms that are generally considered to result in electric fields and concomitant work function shifts at metal-organic interfaces are doping, charge transfer, and dipole formation.[8-10] Regarding the work function modification of amine side-groups, Lindell et al.[11] found by photoelectron spectroscopy and density functional calculations that the electron donor para-phenylenediamine chemisorbs onto atomically clean Ni in vacuum.[12] Due to partial electron transfer from the amine unit, a work function reduction of 1.55 eV is achieved, resulting in a less deep Fermi level. This explanation is not likely to hold for the technologically more relevant procedure on which we shall focus, being the deposition of WMLs from solution on a metal at atmospheric pressure: the metal is not atomically clean, which likely inhibits chemisorption. In other work by Zhou et al.[13] it is shown that the work function reduction, at atmospheric pressure, by the amine groups in poly(ethylenimine ethoxylated) (PEIE), is generally the same on different conductors. They attributed the effect both to i) orientation of the internal molecular dipole, induced by the lone pair of the nitrogen atom, and ii) an interfacial dipole due to partial charge transfer from the amine group after the physisorption on the conductor. Important for determining the origin of the effect is also the thickness dependence of the amine-containing layer.[13-17] In this respect different observations have been made. Xia et al.[15] reported an optimum of the work function modification at 8 nm thickness and above, while Zhou et al.[13] and Zhang et al.[16] did not observe any thickness dependence. Kim et al.[17] reported a thickness dependence where thicker films resulted in a reduced work function modification.

Next to PFN, also cationic polyelectrolytes can be used to lower the work function of the electrode.[1, 5-6] A recent study on conjugated polymer zwitterions revealed a similar lowering in work function, attributed to electrostatic realignment of the dipolar zwitterionic side-chains near the metal interface.[18] The formation of interfacial dipoles and electric field-induced reorientation of molecules has also been reported.[19] Other work has shown that in the specific case that cationic polyelectrolytes are brought into contact with fullerenes, doping of fullerenes is observed. [20] This however does not explain the work function modification of conductors in absence of fullerenes.[6]

The anionic polyelectrolyte Nafion, which is also an acid, is found to give the opposite effect compared to cationic polyelectrolytes. A thin film of Nafion on ITO is found to increase the work function by 0.5 eV,[21-23] which indicates that Nafion can modify the metal work function. Another anionic polyelectrolyte is poly(4-styrenesulfonic acid) (H-PSS), a component of PEDOT:PSS formulations. In literature evidence exists that a thin layer of H-PSS forms on top of PEDOT:PSS.[24] Processing of PEDOT:PSS from aqueous dispersions with different amounts of added sorbitol was found to lead to a reduction in the work function, which has been interpreted as being the result of removal of the H-PSS top layer.[25]

In this chapter we present results which indicate that work function modification by anionic or cationic (poly)electrolytes and by tertiary aliphatic amines originates from a single mechanism: the formation of a dipole at the interface. This dipole formation is driven by the energetic stabilization by its image charges in the contacting (semi)conductor. On metals coated with a ~10 nm thin insulator no dipole orientation or formation is observed when an additional WML is applied: the work function is not modified. Equal work function modification is observed by scanning Kelvin probe microscopy for different thicknesses of PFN or H-PSS deposited on conductors with different work functions, ranging from Au to Ca. This excludes charge transfer or doping as a possible origin of the work function modification. The net direction of the dipole is furthermore determined by the ability of the positive and negative part of the dipole to get in the proximity of the (semi-)conductor. The ability to do so is found to depend on the geometric properties of the positive and negative part. This behavior is confirmed by series of tetrabutylammonium halides and H-PSS, Li-PSS, and Na-PSS. The magnitude of the net dipole can be related to both the ability to orient as well as the density of dipoles at the interface.

## 11.2 Materials and methods

*Device preparation:* Devices that were measured consisted of a substrate covered with an electrode as shown schematically in Figure 11.1.

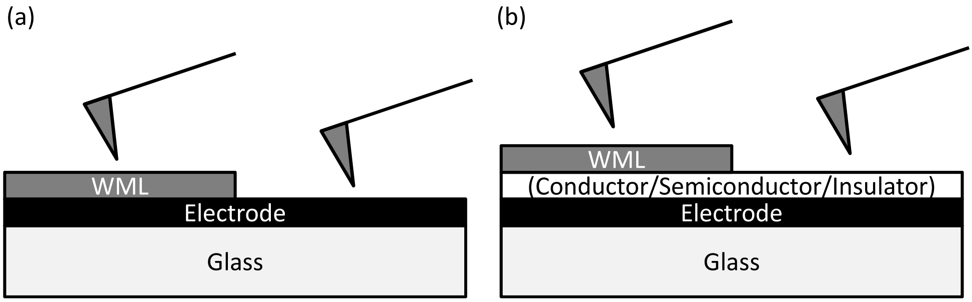

**Figure 11.1 Schematic of the general device layout. SKPM measurements were performed on (a) metal electrodes with and without a work function modification layer (WML) on top and on (b) metal electrodes covered with a ~10 nm layer of conductor/semiconductor/insulator with and without a work function modification layer on top.**

The conductor was either sputtered, e.g. indium tin oxide (ITO), vacuum evaporated (Au, Ag, Al, Ca) or spin coated (poly(3,4-ethylenedioxythiophene)-poly(styrenesulfonate) (PEDOT:PSS, Clevios P VP AI 4083) from Heraeus). Deposition of $V_2O_5$ was performed similarly as described in Ref. [26]. Approximately 10 nm thick organic semiconductor or insulator films were deposited on top by spin coating from solution: [6,6]-phenyl $C_{70}$-phenylbutyric acid methyl ester ($PC_{70}BM$, Solenne BV), poly(3-hexylthiophene) (P3HT, Aldrich, $M_n$ = 54000-75000 g $mol^{-1}$) and a blend of $PC_{70}BM$ and poly[2,6-(4,4-bis-(2-ethylhexyl)-4H-cyclopenta[2,1-b;3,4-b0]-dithiophene)-*alt*-4,7-(2,1,3-benzothiadiazole)] (PCPDTBT, $M_w$ = 27700 g $mol^{-1}$) from *o*-DCB, poly[(9,9-dioctylfluorenyl-2,7-diyl) (PFO), and a poly(*p*-phenylene vinylene) copolymer (Super Yellow PPV, Merck, catalogue number PDY-132) from toluene, polystyrene (PS, Aldrich, $M_w$ = 35000 g $mol^{-1}$), and poly(methylmethacrylate) (PMMA, Aldrich, $M_w$ = $10^5$ g $mol^{-1}$) from toluene. On top of these conductors, organic semiconductors and insulators, a ~10 nm thick film of poly[(9,9-bis(3'-(N,N-dimethylamino)propyl)-2,7-fluorene)-*alt*-2,7-(9,9-dioctylfluorene)] (PFN) was deposited from either 2 mg $ml^{-1}$ methanol (MeOH) + acetic acid (AcOH) (200:1 volume ratio) or 2 mg $ml^{-1}$ toluene. Synthesis of PFN is described elsewhere.[1] Alternatively, poly(4-styrenesulfonic acid) (H-PSS, Aldrich, $M_w$ = 75000 g $mol^{-1}$), poly(lithium 4-styrenesulfonate) (Li-PSS, Aldrich, $M_w$ = 75000 g $mol^{-1}$) and poly(sodium 4-styrenesulfonate) (Na-PSS, Aldrich, $M_w$ = 70000 g $mol^{-1}$) dissolved in ultrapure water (4 mg $ml^{-1}$); tetrabutylammonium (TBA, Aldrich) tetramethylammonium (TMA, Aldrich), and tetrahexylammonium (THA, Aldrich) salts dissolved in tetrahydrofuran (4 mg $ml^{-1}$), or Nafion (Aldrich, perfluorinated ion exchange resin 5 wt% in mixture of lower aliphatic and $H_2O$, including 45% water) diluted in ethanol with a 1:200 volume ratio were deposited on top of the mentioned conductors, organic semiconductors, and insulators. Structural formulae of the above-mentioned materials are shown in Figure 11.2. The thickness of the layers ranged between 5 and 10 nm. The thicknesses of the different layers were measured by a Veeco Dektak profilometer. Device preparation was performed in a $N_2$ filled glovebox in case air-sensitive materials like Ca, Al or Ag were used.

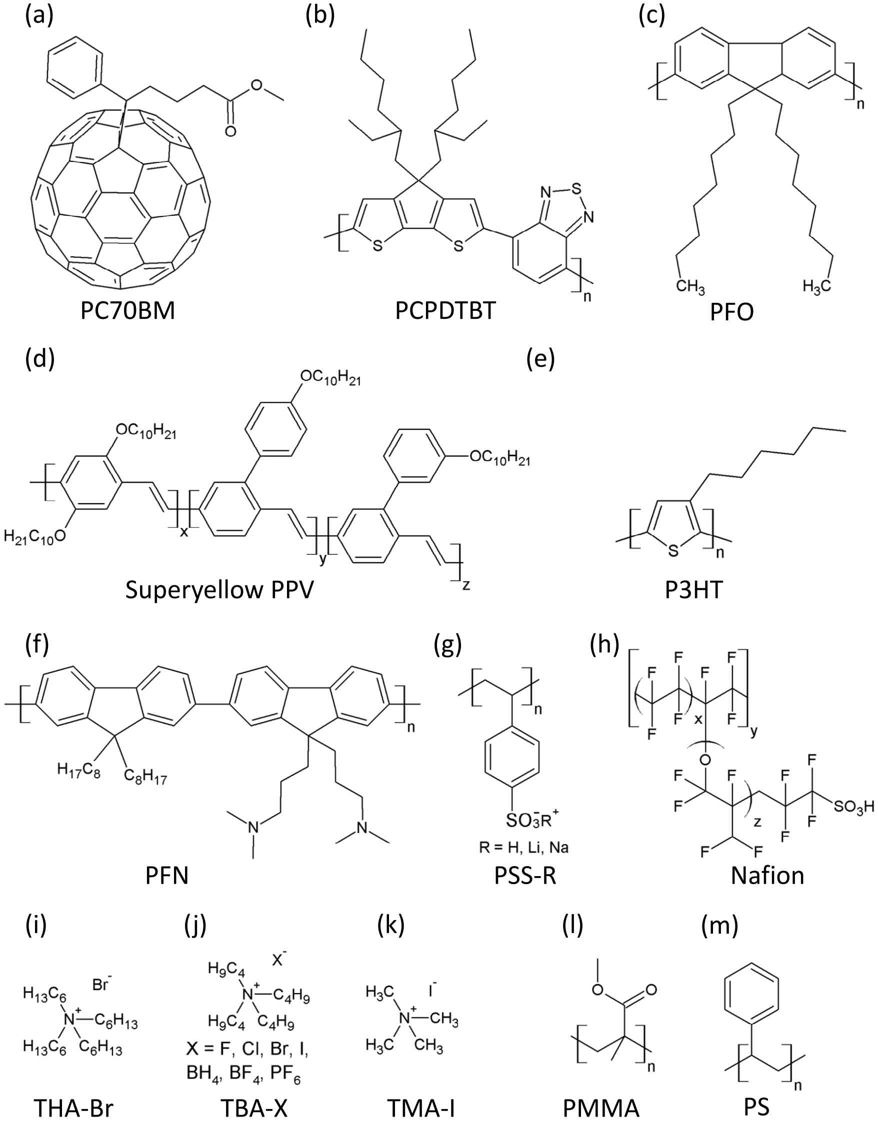

**Figure 11.2 Structural formulae of the organic compounds.**

*Device characterization:* SKPM images were recorded in a glove box under $N_2$ atmosphere ($[O_2] < 1$ ppm and $[H_2O] < 1$ ppm) with a Veeco Instruments MultiMode AFM with

Nanoscope IV controller, operating in lift mode with a lift height of 50 nm. Au-coated silicon tips from MikroMasch were employed. During surface potential measurements the sample was grounded. An Au substrate was used as reference to monitor any tip wear after multiple measurements. The measurements were carried out at room temperature. As SKPM is based on nullification of the electric field between tip and sample, no driving force for ion displacement during characterization exists. The discussed ion work function shifts and ion displacements therefore have taken place upon or immediately after layer deposition and not during SKPM probing.

## 11.3 Results and discussion

To study the mechanism behind the work function modification by several types of WMLs, samples as depicted in Figure 11.1 were used. The parameter of interest is the work function of a conducting, semiconducting, or insulating layer with and without coverage of the WML. Insulators and intrinsic organic semiconductors, however, do not have a well-defined work function as the Fermi level resides in the bandgap. Therefore thin insulating or semiconducting layers were deposited on top of a metal electrode as illustrated in Figure 11.1b. The electrostatic potential at the surface is measured by scanning Kelvin probe microscopy (SKPM) with respect to an Au-coated tip. The structural formulae of the materials used as WML or semiconducting/insulating substrate are shown in Figure 11.2.

### 11.3.1 Work function reduction by PFN

The effect of the WML PFN on substrates of conducting (also highly doped semiconductors like p-type Si, p-type doped PEDOT:PSS and n-type doped $V_2O_5$,[27] prepared following the procedure reported in Ref. [26]), semiconducting (intrinsic), or insulating nature was measured as shown in Figure 11.3 and Table 11.1. The qualitative criterium for the classification of these substrate materials is based on the ability to provide charges which is proportional to the dielectric response of the substrate material to the WML. Conductors have a significant amount of mobile charges, which is why we share highly doped semiconductors in this paper under the same denominator. Intrinsic semiconductors only provide few charges which are relatively mobile. Insulators do not contain mobile charges. In Figure 11.3, the horizontal axis represents the work function of each sample without coverage of the WML: the work function of the substrate. The vertical axis represents the work function shift of the sample after coverage with the WML. A negative work function modification corresponds to a reduction of the work function, i.e. improved electron injection from the substrate.

**Table 11.1 Work function modification by PFN.**

| Work function (eV) | Pristine | With PFN |
|---|---|---|
| **ITO** | 4.4 | 3.65 |
| **Au** | 4.6 | 4.0 |
| **Ag** | 4.3 | 4.0 |
| **Al** | 3.07 | 2.76 |
| **$V_2O_5$** | 5.0 | 4.2 |
| **PEDOT** | 4.92 | 4.48 |
| **p-type Si** | 4.22 | 3.5 |
| **Ca** | 2.85 | 1.85 |
| **ITO-PC$_{70}$BM:PCPDTBT** | 4.5 | 4.04 |
| **ITO-PPV** | 4.55 | 4.21 |
| **ITO-P3HT** | 4.24 | 4.24 |
| **Au-PFO** | 4.42 | 4.03 |
| **Au-PC70BM** | 4.62 | 4.02 |
| **Au-PS** | 4.44 | 4.35 |
| **Au-PMMA** | 4.59 | 4.49 |

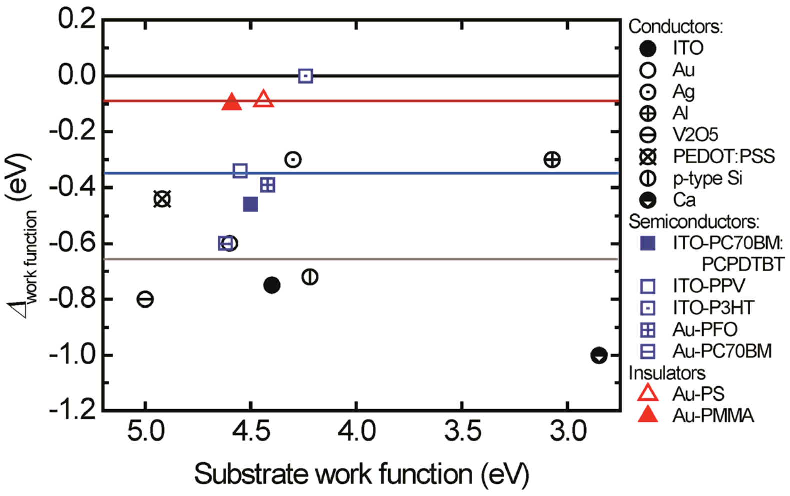

**Figure 11.3 Work function as measured by SKPM for substrates covered by ~10 nm PFN. Substrates are categorized in clean conductors (black circles) and metals coated with a 5 – 10 nm thick film of semiconductor (blue squares) or insulator (red triangles). The symbol filling indicates the specific substrate material as shown in the legend. The horizontal lines indicate the average change in work function for each substrate category. The data is also presented in Table 11.1.**

In case PFN was used as WML the work function of the substrate is either reduced or constant as shown in Figure 11.3. In case the substrate is a conductor (black dots), an average work function reduction of 0.7 eV (gray line) is obtained. This value is independent of the substrate work function in the range measured here: from PEDOT with $\Phi \approx 5$ eV to Ca with $\Phi \approx 3$ eV. Regarding Ca and Al, PFN was spin coated from dry toluene rather than from methanol to prevent reaction of the solvent with the metal. The solvent from which PFN was deposited, either methanol with acetic acid, or toluene, did not affect the work function change by PFN for other metallic substrates. In case PFN is deposited on top of an organic semiconductor (blue squares), the work function is reduced as well, albeit slightly less compared to conductors: approximately 0.4 eV (blue line). The work function modification by PFN was furthermore found to not depend on the thickness of the intrinsic, organic semiconductor, as verified for SY-PPV films with varying thickness between 7±3 and 180±10 nm. On insulators (red triangles) PFN did not result in any significant change in the work function (red line).

Another experiment to resolve the origin of the work function modification of conductors by PFN is the determination of the layer thickness dependence of the work function change. We deposited PFN with varying layer thickness on Au and on a thin film of SY-PPV on PEDOT:PSS and studied the thickness dependence of the work function by SKPM. Different layer thicknesses were obtained by spin coating solutions with two different concentrations at a series of spin speeds ranging from 1000 to 4000 RPM. The work function modification of Au or SY-PPV by PFN was found to be constant for all these layers as shown in Figure 11.4: 0.7±0.1 eV and 0.22±0.1 eV, respectively. It was verified that spin coating with solely the solvent did not modify the Au or PEDOT/SY-PPV work function.

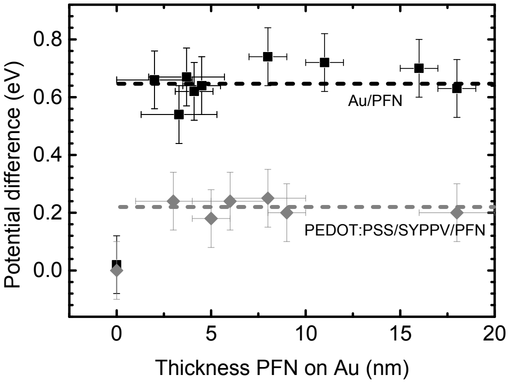

**Figure 11.4 Potential difference as determined by SKPM between a Au tip and Au covered by PFN (black symbols) and between a Au tip and SY-PPV on PEDOT:PSS covered by PFN (gray symbols). The dashed lines are to guide the eye.**

In literature qualitatively different results have been reported regarding the dependence of the work function modification on the thickness of interlayers like PFN. [13-17, 28] Increasing[15], constant[13, 16] and decreasing[17] work function shifts have all been reported.

Part of these works comprises the characterization of complete devices, which complicates the interpretation as charge transport is involved as well.[14, 16-17] Use of thicker layers of insulating materials will reduce the performance due to additional series resistance. Characterization of the open-circuit voltage circumvents this issue, although also the open-circuit voltage depends on many factors. Characterization of WMLs by inherently current-less techniques like SKPM[13, 15, 28] excludes these problems, but still one must ensure that the substrate is completely covered. Incomplete coverage will result in intermediate results.

### 11.3.2 Considered mechanisms

To determine the nature of the work function reduction by PFN several models proposed in literature were considered first.[13, 15, 20] For each model we inspected its ability to explain the experimental findings reported here and in literature: the work function modification is i) dependent on the nature of the substrate: metallic, (organic) semiconducting or insulating; ii) independent on the work function of the substrate in the range 3.0 – 5.0 eV; iii) independent of the PFN layer thickness; iv) possible in absence of any semiconductor which can be electrochemically doped.[13]

Four models that can describe the work function reduction by the WML PFN are schematically shown in Figure 11.5: formation of an electric double layer (EDL) after doping of the WML (Figure 11.5a), charge transfer to or from the conductor (Figure 11.5b), spontaneous dipole orientation in the WML (Figure 11.5c) and the spontaneous dipole orientation at the interface (Figure 11.5d). A detailed discussion follows in the next paragraphs about these mechanisms and their ability to describe the observations from Figure 11.3 and Figure 11.4. Each of these mechanisms is found to have difficulties in explaining the complete series of findings described above. Therefore an alternative model is presented later on.

The first model (Figure 11.5a) describes electric double layer formation between a conductor and a doped material. In organics, doping can be achieved electrochemically by ions stabilizing electronic charges. Such behavior is e.g. the basis of light-emitting electrochemical cells.[29-31] In the polyelectrolytes studied here, mobile ions are present that can be used for electrochemical doping. Electrochemical doping is, however, not evident in the semiconductor PFN. Oxidation of tertiary aliphatic amines has nonetheless been reported and leads to the formation of a cationic compound.[32] Such cationic compounds can stabilize electrons on nearby semiconductors, i.e. electrochemical doping. The EDL that is formed in case doping is indeed present or takes place would result in a bias-dependent depletion of carriers in the doped semiconductor at the interface. The depletion width would range between 6 and 2 nm for (very high) doping densities of $10^{25}$ – $10^{26}$ $m^{-3}$, respectively, in case a change in built-in potential of 1 V is assumed. In our measurements no thickness dependence of work function modification by PFN is observed, which indicates that such a depletion layer is absent. Also the fact that PEIE,[13] an insulating tertiary aliphatic amine, can change the work function without any form of doping indicates that the work function change studied in this chapter is not due to doping and the resulting EDL formation. This however does not exclude that doping takes place in devices that contain polyelectrolytes.[20] The relatively low ionic mobility can result in slow transient behavior during device operation.[5]

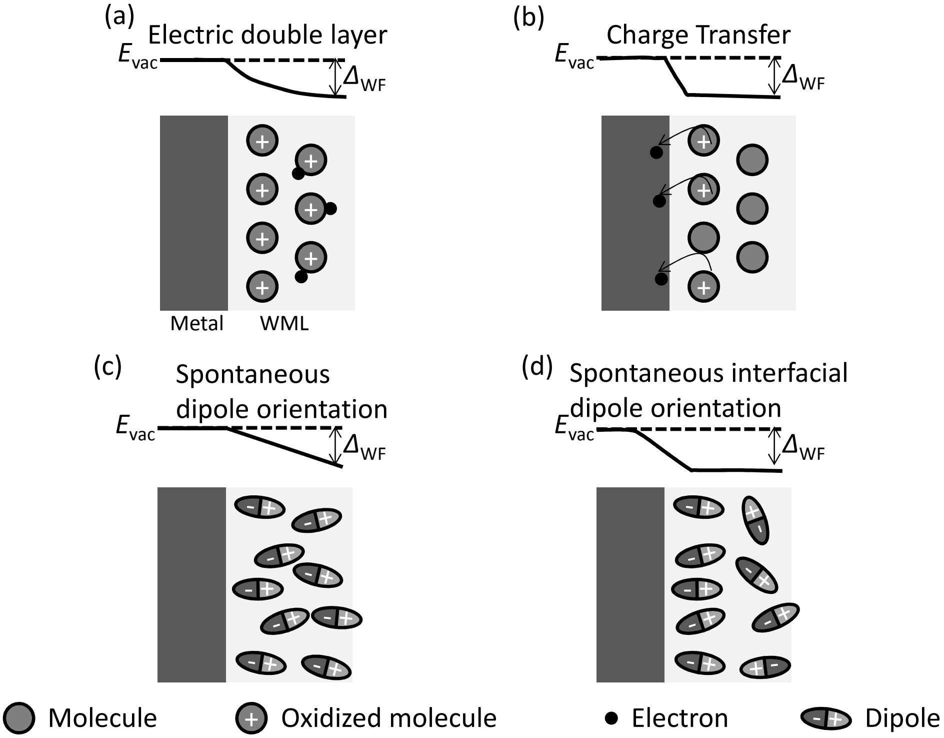

**Figure 11.5 Schematics of possible mechanisms to explain the work function (WF) modification by WMLs: (a) electric double layer formation, (b) charge transfer, (c) spontaneous dipole orientation in the bulk and (d) spontaneous dipole orientation at the interface. The corresponding vacuum levels are shown on top to indicate the spatial potential drop. A legend is shown below.**

Modification of the work function can also occur due to dipole formation induced by integer or partial charge transfer between the substrate and the WML (Figure 11.5b). Charge transfer can take place in a large variety of circumstances as reviewed by Braun *et al.* in Ref. 8. These can be divided in two classes: charge transfer after physisorption or chemisorption. The latter can occur in case the metal surface of the substrate is atomically clean, i.e. at pressures as low as $10^{-9}$ mbar. In contrast, the deposition of PFN reported here took place at atmospheric pressure. Nevertheless, in case a clean substrate surface is considered, specific interaction between the WML and the substrate can take place. Specific interactions are, however, not likely to explain the work function modification by PFN on conductors as it is shown to be a general effect for multiple, different substrate materials in Figure 11.3. In case of physisorption, charge transfer can still take place. Charge transfer is driven by filling empty, lower lying energy states in either the substrate or the WML itself. The cost of charge transfer is the electrostatic energy due to the formation of a dipole. In case of PFN deposited on a metal the sign of the work function change could be explained by electron transfer into the metal. Figure 11.3 shows however that PFN reduces the work function of low work function metals like Ca and Al as much as e.g. Au. This implies that the electron-donating energy level in PFN would have to lie above the Fermi level of Ca and Al. Then PFN would not be air-stable, which it in fact is. Charge transfer therefore cannot explain the general behavior of PFN on conductors shown in Figure 11.3. Significant work function modification by charge transfer already occurs after deposition of a monolayers on e.g. a metallic substrate,[33] which is in agreement with the absence of a thickness dependence of the work function modification by PFN.

A third mechanism to obtain a work function modification is the spontaneous orientation of dipoles in the WML deposited on top of the substrate. This spontaneous orientation of dipoles may either be throughout the complete layer (Figure 11.5c) or only at the interface (Figure 11.5d). In case the complete layer is polarized, a linear dependence of the work function on layer thickness is expected as observed in Ref. 15. Similar as in Ref. 16 we find no thickness dependence as illustrated by Figure 11.4. Another argument against this model lies in the fact that we observe a work function reduction of organic semiconductors by PFN as well. This means that the positive end of the dipole in the WML is directed away from the organic semiconductor in absence of a top contact. This is opposite to devices reported in literature[1] and reproduced by us where PFN deposition on the semiconductor is followed by deposition of Al. In these devices the dipole is directed towards the organic semiconductor as electron injection from Al is improved. This means that during or after deposition of Al the dipoles in the WML would have to be rotated by 180 degrees. Electric field-induced reorientation of polyelectrolytes has been reported.[19] Here, however, no external field was applied.

In case the dipole orientation occurs only at the interface of the WML, an abrupt change in work function is expected as a function of the layer thickness. This is in line with our experimental findings. Still this mechanism has difficulties in explaining the inversion in dipole orientation between metal/organic semiconductor/PFN and metal/organic semiconductor/PFN/metal, as discussed in the previous paragraph. Before deposition of the top metal layer, the PFN molecules are randomly oriented. During evaporation, reorientation of those molecules should then occur to achieve a significant work function reduction. This process seems unlikely.

### 11.3.3 Proposed mechanism

Based on our experimental findings in addition to the literature cited in this article, we suggest the following mechanism for work function modification by PFN. Consider a material with positively and negatively charged constituents contacted by a conductor as shown in Figure 11.6. Image charges of the positive and negative constituents are present in the conductor.[34] As the image charges are oppositely charged, each image charge exerts an attractive force on its respective, real charge. Consequently, both charged constituents want to lie as close as possible near the conductor. The final position with respect to the conductor, however, depends on the geometrical size and the ability of the charged constituents to move. A large difference in size and ability to move of the charged constituents then leads to a difference in final position relative to the electrode. In Figure 11.6 this is illustrated in case both constituent parts have a) an equal and b) an unequal ability to move. The result of this difference (Figure 11.6b) is that a dipole is created in the WML at the interface. This polarization follows a trade-off between the energy gain by approaching the metal surface and the energy loss of a net polarization. Note that the dipole of the image charges is in the same direction as the dipole of the real charges, enhancing the total dipole. This is due to the inverted sign of the charge of the image. In addition, the image dipole can enhance the effective polarizability of molecules at the interfaces of conductors.[35-36] Recently, similar behavior as described in this paragraph was found in a zwitterionic polyelectrolyte[18] and other polyelectrolytes[19].

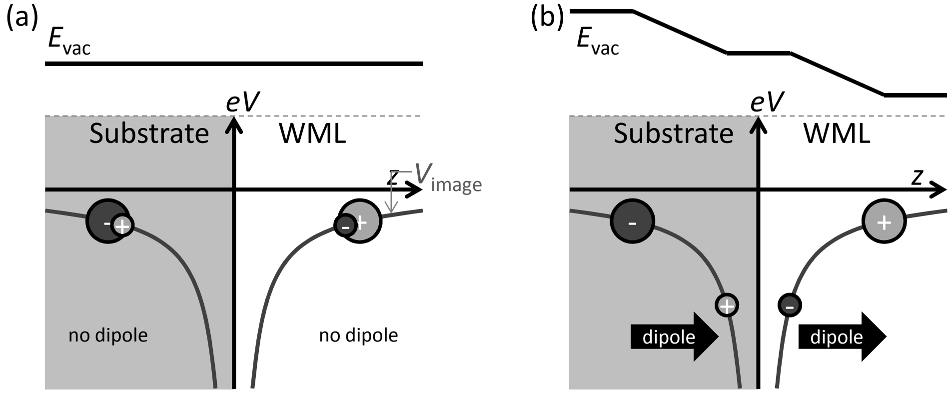

**Figure 11.6 Schematics of the formation of an interfacial dipole between a WML and the substrate by image charge attraction. The gray line indicates the image potential ($V_{image}$). (a) In case the charges in the WML have similar ability to move no dipole is formed. (b) In case the charges in the WML differ in movability, a dipole is formed as the more mobile charge has a smaller approach distance towards the interface. The image charges form a dipole as well, equal in size and**

**direction as the real dipole. The resulting work function modification is shown by the vacuum level indicated as black line on top.**

To understand the driving force of the work function modification, attraction by image charges in the substrate, the electrostatics of the system, the substrate and the WML should be taken into account.[37] When the WML is physisorbed on an insulator, the only electrostatic interaction is that between the charged constituents of the molecules of the WML itself. The small difference between the relative dielectric constants of the WML and the insulator results only in minor image force interaction. In this case a net polarization would only cost energy and therefore does not occur: no work function modification takes place as shown in Figure 11.7c. In case the WML is physisorbed[13] on a conductor an additional electrostatic interaction arises due to the formation of image charges. As discussed above, the interaction with these image charge makes it energetically favorable for (parts of) the physisorbed molecules to move closer to the metal (Figure 11.7a). This is a very short range interaction, hence the virtual absence of a layer thickness dependence. Furthermore, for this effect to take place no charge transfer from the WML to the metal or vice versa is required to take place. Consequently, the effect is independent of the work function of the conductor. For WMLs on semiconductors, the contrast in relative dielectric constant is similar as for insulators, i.e. small. However, semiconductors can hold compensation charges which can still stabilize a dipole. Hence energetically stable interface dipoles can be formed for WMLs physisorbed on semiconductors as shown in Figure 11.7b.

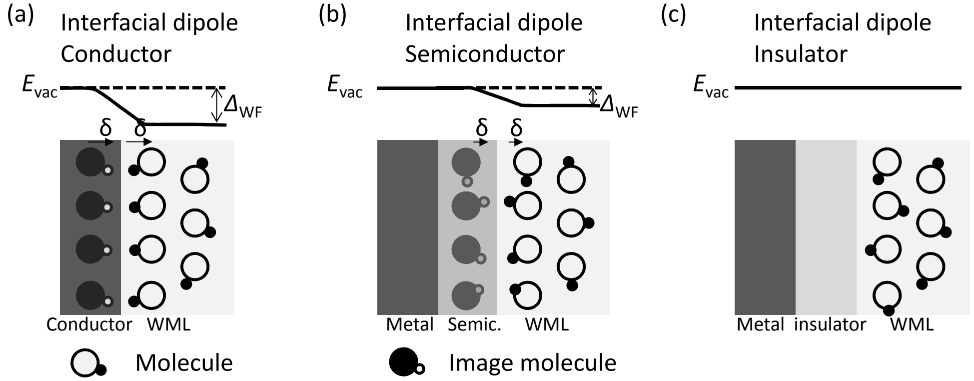

**Figure 11.7 Schematics of the proposed work function modification mechanism. Shown is the formation of an interfacial dipole (*δ*) between a WML and (a) a conductor, (b) a semiconductor and (c) an insulator. The full, partial, or absent stabilization by (image) charges in the substrate is also shown. The corresponding vacuum levels are shown on top to indicate the spatial potential drop. A legend is shown below.**

Our suggested mechanism to explain the experimental findings for PFN used as WML is based on the following facts. The independence of the work function reduction on the work function of the layer below, excludes that exchange of electrons with the metal is of importance. The layer thickness independence of the work function modification additionally indicates that the effect occurs close to the interface as expected (Figure 11.7). No work function shift is observed in case an insulating layer is inserted between a conductor and the PFN. So, despite the absence of electron exchange between electrode and WML, a (semi)conducting surface is needed to enable work function modification. This is in line with the proposed mechanism that image charges in the (semi)conductor contacting the WML drive the polarization at the interface.

The relevant, charged constituents in PFN are the nitrogen atom and its lone pair in a $sp^3$ orbital. The relatively small *s* character of the orbital results in a relatively large separation from the nucleus. The typical basicity of amines furthermore indicates that the lone pair of electrons is not delocalized over the molecule.[38] Therefore this lone pair can in principle easily be attracted towards the interface by its image charge in the substrate.

### 11.3.4 Work function increase by H-PSS and Nafion

The proposed mechanism for work function modification discussed in the previous paragraph is based on the basic ingredients of having a (semi)conductive surface covered by molecules with charged constituents that differ in size and ability to move. Next to PFN, many other materials may possess these properties. Especially, polyelectrolytes can be expected to show similar behavior as illustrated in Figure 11.6 and Figure 11.7. In literature quaternized ammonium derivatives of PFN have already been shown to improve electron injection similarly as PFN.[1, 6] To determine whether other polyelectrolytes show similar behavior as PFN in work function modification of conducting, semiconducting, and insulating substrates, similar measurements were performed with H-PSS and Nafion as WML. The results are shown in Figure 11.8 and Table 11.2 and Table 11.3.

In case H-PSS or Nafion are used as WML the work function is observed to be *increased* or to remain constant. Similar to PFN, the strongest work function changes are observed on conductors (black dots or pentagons for H-PSS and Nafion, respectively, in Figure 11.8) and are within experimental uncertainty independent of the work function of the conductor itself. On organic semiconductors (blue squares or diamonds for H-PSS and Nafion, respectively) only a small increase in work function is observed, whereas on insulators (red triangles for Nafion) a change in work function is absent. On semiconductors, the anionic polyelectrolytes (blue symbols in Figure 11.8) seem to result in a smaller work function modification as compared to PFN (blue symbols in Figure 11.3). This difference may be explained by the lesser ability of the used p-type semiconductors to provide an electron as compensation charge. Similar effects are also observed for the stabilization of ferroelectric polarization by organic semiconductors.[39-42] As the deposition of a layer of H-PSS or Nafion occurs from an acidic solution, it was checked whether spin coating instead with a 1 M $H_2SO_4$ solution on Au gave similar results. This step actually results in washing the electrode with an acidic solution. No work function increase of the Au (star in Figure 11.8) was observed.

**Table 11.2 Work function modification by H-PSS.**

| Work function (eV) | Pristine | With H-PSS |
|---|---|---|
| **ITO** | 4.4 | 5.0 |
| **Au** | 4.6 | 5.49 |
| **Ag** | 4.3 | 4.7 |
| **Al** | 3.07 | 4.1 |
| **ITO-PPV** | 4.47 | 4.64 |
| **Au-PC70BM:PCPDTBT** | 4.5 | 4.7 |
| **Au-PMMA** | 4.6 | 4.6 |

**Table 11.3 Work function modification by Nafion.**

| Work function (eV) | Pristine | With Nafion |
|---|---|---|
| **ITO** | 4.4 | 4.95 |
| **Au** | 4.6 | 5.1 |
| **PEDOT** | 4.85 | 5.25 |
| **Au-PFO** | 4.48 | 4.6 |
| **Au-PS** | 4.9 | 4.85 |
| **Au-PMMA** | 4.7 | 4.8 |

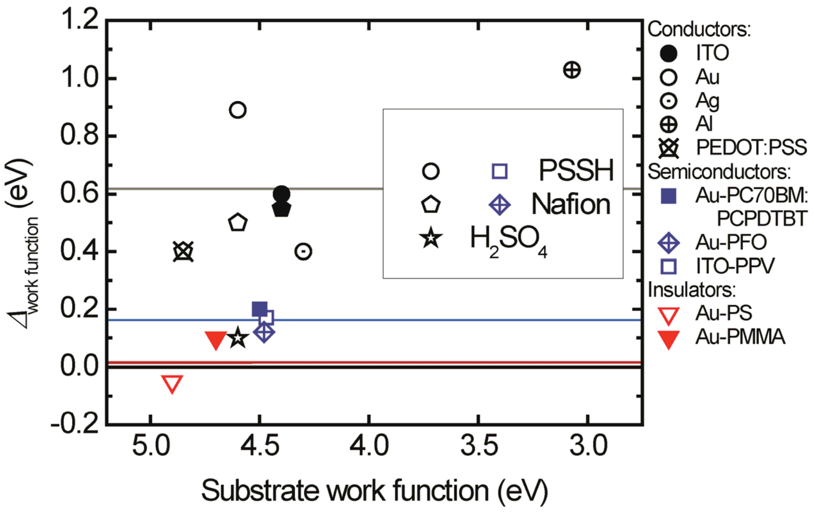

**Figure 11.8 Work function as measured by SKPM for substrates covered by ~10 nm H-PSS or Nafion. Substrates are categorized in clean conductors (black circles or pentagons for H-PSS and Nafion, respectively) and metals coated with a 5 – 10 nm thick film of semiconductor (blue squares or diamonds for H-PSS and Nafion, respectively) or insulator (red triangles for Nafion). The symbol filling indicates the specific substrate material as shown in the legend. The horizontal lines indicate the average change in work function for each substrate category. The data is also presented in Table 11.2 and Table 11.3.**

The results regarding PFN, H-PSS and Nafion shown in Figure 11.3 and Figure 11.8 show that despite using different materials, the work function modification behaves the same, dependent on the type of substrate used. Different is however the sign of the work function modification as PFN reduces the substrate work function, whereas H-PSS and Nafion enhance it. According to the proposed mechanism for PFN, the direction of the dipole in the WML at the interface is determined by the size of the constituent parts and their ability to move. In the anionic polyelectrolytes studied here the charged constituent parts are the ions within the $SO_3^-H^+$ group. As the $SO_3^-$ ion is covalently bound to a polymer backbone, it has more difficulty in reaching the interface than the small, ionically bound proton. Therefore mainly the proton approaches the interface, resulting in a dipole oriented towards the interface. These results therefore demonstrate that the proposed mechanism does not only apply to the work function modification by PFN, but also by polyelectrolytes like Nafion or H-PSS.

### 11.3.5 Ion size effects in WMLs

According to our proposed mechanism (Figure 11.6) the geometrical size of the charged constituents should strongly affect the size and direction of the induced interfacial dipole. To verify whether the ion size influences the magnitude of the work function modification, the work function modification by $X^+PSS^-$ with $X^+ = H^+$, $Li^+$, $Na^+$ was studied on Au. In addition the work function modification by quaternized ammonium salts was studied as well: a series of tetrabutylammonium halides, ($TBA^+Y^-$) with $Y^- = F^-, Cl^-, Br^-, I^-$; and salts ($TBA^+Z^-$) with $Z^- = BH_4^-, BF_4^-, PF_6^-$. Also the size of the alkyl group (methyl, butyl, or hexyl) in the ammonium ion was varied. The work function modification of Au by deposition of thin layers of approximately 10 nm is shown in Figure 11.9 as a function of the ion radius. The ionic radii were taken from literature.[43-46] The radius of the ion with an underlined name is connected to the horizontal axis. The general trend that is observed in all three series ($X^+PSS^-$; $TBA^+Y^-$; $TBA^+Z^-$) is that an increase in ion size is accompanied by a reduction in the magnitude of the work function modification. In $H^+PSS^-$ a work function increase is observed as the PSS- ion has a low movability due to its large relative size. Increasing the size of the positive counterion reduces this difference and clearly results in a reduced magnitude of the work function change. In the $TBA^+F^-$ and $TBA^+BH_4^-$ salts, the $TBA^+$ ion has the lowest movability compared to the counterions due to the four relatively large butyl chains. Consequently a work function reduction is expected and also observed in Figure 11.9. Increasing the size of the counterions again reduces the difference in movability. The experiment is in agreement with this as the magnitude of the work function reduction is reduced. That not only the ion-size is important regarding work function modification is illustrated by the stronger reduction in case the larger $BH_4^-$ ion is used opposed to $F^-$, $Cl^-$, or $Br^-$. Clustering and ordering of the salt molecules, which can strongly vary between the different series, is likely to play a large role as well. This is in line with earlier observations by Yang et al.,[47] where polyelectrolytes with larger ions used as interlayer were found to result in better in device performance. Furthermore, it should be noted that in devices, the performance is not only determined by the work function change due to a WML, but also by additional effects of the WML on electrical transport and injection. A change in magnitude of the ammonium constituent itself leads however to an oppositely expected effect: c.f. $TMA^+I^-$ vs. $TBA^+I^-$ and $TBA^+Br^-$ vs. $THA^+Br^-$ (see Figure 11.2i-k for the structural formulae). This may tentatively be explained by a change in salt density at the interface or the ability to block the counter ions from reaching the surface. Regarding the sign of the work function modification by the ammonium series, it is found to be opposite to the $PSS^-$ series. This corresponds to a dipole orientation such that the largest ion, $PSS^-$ and $TBA^+$, is the furthest away from the interface and the smaller counter ion is closest.

The dashed purple line in Figure 11.9 illustrates the work function modification by PFN to enable comparison with the polyelectrolytes. The work function reduction by PFN is similar in case $TBA^+F^-$ is used. If however $TBA^+PF_6^-$ is used, no work function reduction is observed. The latter was also observed in Ref. 13, where the work function modification by PEIE was measured as a function of the acidity of the solution from which it was deposited. The largest work function modification was obtained from a basic solution when PEIE with neutral amine groups was present. When using an acidic solution, by addition of $H^+PF_6^-$, part of the amines is protonated and electrostatically compensated by a $PF_6^-$ counterion. In that case the magnitude of the work function modification was observed to decrease. This is in line with our measurement of $TBA^+PF_6^-$ on Au shown in Figure 11.9 where no work function modification is observed.

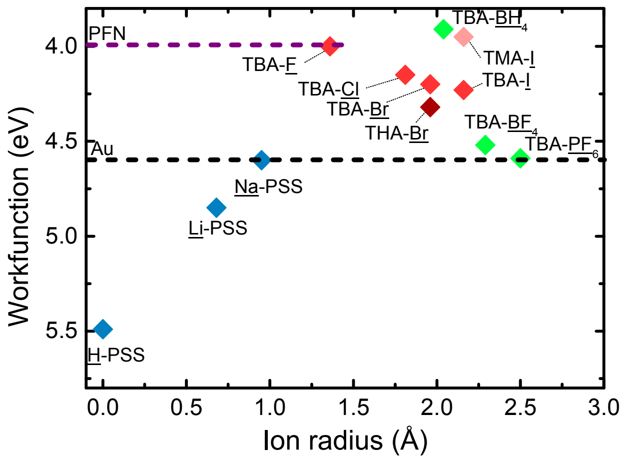

**Figure 11.9 Work function of an Au substrate covered by a thin layer (5-10 nm) of salt as measured by SKPM. The labels show the type of ion and the ion radius of the underlined ion corresponds to the horizontal axis. The dashed lines indicate the work function of a clean Au substrate and an Au substrate covered with PFN.**

## 11.4 General considerations

The general behavior of the interlayers described in the previous paragraphs allows a consistent description of the work function changes, but we note that these can be accompanied with effects which are specific for the materials used. For example, work function reduction by PFN on P3HT is expected but not observed experimentally. We tentatively attribute this to material specific effects that may be superimposed on, or interfere with the interface dipole formation as discussed in this chapter. It is known for example that PFN in combination with fullerenes results in doping of the fullerenes.[20] Another example is found in a recent paper by Wetzelaer et al.,[48] where an anionic electrolyte, stearate, with a relatively large counter ion, $Cs^+$, was shown to improve *electron* injection from Al to a comparable level as Ba. This result may be explained by the relatively large size of the $Cs^+$ ion which might make image charge screening of the negatively charged polymer more favorable. Alternatively, n-type doping by $Cs^+$ may explain the observed results as well in this specific case.[49]

In actual devices, where WMLs are typically sandwiched between an organic semiconductor and a metallic electrode, the situation is more complicated than the one studied here. In lowest order, oppositely directed dipoles are expected at both interfaces of the WML. Typically, the metal-WML interface dipole will be largest and improved injection may still be expected. However, the presence of substantial space charge in the semiconductor may destabilize the interfacial dipoles. Injection of electrons (holes) and the consequent formation of negative (positive) space charge in the organic semiconductor can destabilize a dipole pointed away from (towards) the semiconductor. This would be an interesting topic for further study.

## 11.5 Conclusion

In summary we have shown that WMLs based on tertiary aliphatic amines and polyelectrolytes, e.g. sulfonic acid based polymers or aliphatic quaternized ammonium salts, show similar behavior in work function modification. Work function modification occurs only on (semi-)conducting substrates and is independent of the substrate work function in the range of 3 to 5 eV. Additionally the work function modification does not depend on the WML thickness, but does depend on the relative size of the anion and cation and their respective ability to move.

The data supports a single mechanism for both work function reduction and enhancement by prompted formation of an interfacial dipole. This process is driven by the attraction of the positive and negative part of the dipole towards the interface by the image charge interaction in case the substrate is a (semi-)conductor. The geometrical size and movability of the positive and negative parts of the dipole determine which (partial) charge can get closest to the substrate, resulting in a net dipole orientation away from or towards the interface which modifies the work function. The large data set proves that the general work function modification by the WMLs studied here cannot be described by any doping mechanism, charge transfer, or spontaneous dipole orientation in the solid film after deposition. Although other mechanisms are not excluded for specific interlayer-substrate combinations, the prompted dipole formation mechanism is found to be universal for a large variety of interlayer materials deposited on a large variety of substrates and provides a guideline for developing new materials.

# References

[1] F. Huang, H. B. Wu, D. Wang, W. Yang, Y. Cao, Chem. Mater. 16 (2004) 708.

[2] A. K. K. Kyaw, D. H. Wang, V. Gupta, J. Zhang, S. Chand, G. C. Bazan, A. J. Heeger, Adv. Mater. 25 (2013) 2397.

[3] C. M. Zhong, C. H. Duan, F. Huang, H. B. Wu, Y. Cao, Chem. Mater. 23 (2011) 326.

[4] L. F. Lan, J. B. Peng, M. L. Sun, J. L. Zhou, J. H. Zou, J. Wang, Y. Cao, Org. Electron. 10 (2009) 346.

[5] C. V. Hoven, R. Q. Yang, A. Garcia, V. Crockett, A. J. Heeger, G. C. Bazan, T. Q. Nguyen, Proc. Natl. Acad. Sci. U S A 105 (2008) 12730.

[6] J. H. Seo, T. Q. Nguyen, J. Am. Chem. Soc. 130 (2008) 10042.

[7] J. Lee, H. Kang, J. Kong, K. Lee, Adv. Energy Mater. 4 (2014) 1301226.

[8] S. Braun, W. R. Salaneck, M. Fahlman, Adv. Mater. 21 (2009) 1450.

[9] H. Vazquez, F. Flores, A. Kahn, Org. Electron. 8 (2007) 241.

[10] A. Kahn, N. Koch, W. Y. Gao, J. Polym. Sci. Part B Polym. Phys. 41 (2003) 2529.

[11] L. Lindell, M. P. de Jong, W. Osikowicz, R. Lazzaroni, M. Berggren, W. R. Salaneck, X. Crispin, J. Chem. Phys. 122 (2005) 84712.

[12] D. E. Gardin, G. A. Somorjai, J. Phys. Chem. 96 (1992) 9424.

[13] Y. H. Zhou, C. Fuentes-Hernandez, J. Shim, J. Meyer, A. J. Giordano, H. Li, P. Winget, T. Papadopoulos, H. Cheun, et al., Science 336 (2012) 327.

[14] F. Huang, H. B. Wu, Y. Cao, Chem. Soc. Rev. 39 (2010) 2500.

[15] R. D. Xia, D. S. Leem, T. Kirchartz, S. Spencer, C. Murphy, Z. C. He, H. B. Wu, S. J. Su, Y. Cao, et al., Adv. Energy Mater. 3 (2013) 718.

[16] S. Liu, K. Zhang, J. Lu, J. Zhang, H.-L. Yip, F. Huang, Y. Cao, J. Am. Chem. Soc. 135 (2013) 15326.

[17] Y.-H. Kim, T.-H. Han, H. Cho, S.-Y. Min, C.-L. Lee, T.-W. Lee, Adv. Funct. Mater. 24 (2014) 3808.

[18] F. Lui, Z. A. Page, V. V. Duzhko, T. P. Russell, T. Emrick, Adv. Mater. 25 (2013) 6868.

[19] B. H. Lee, I. H. Jung, H. Y. Woo, H.-K. Shim, G. Kim, K. Lee, Adv. Funct. Mater. 24 (2014) 1100.

[20] C.-Z. Li, C.-C. Chueh, F. Ding, H.-L. Yip, P.-W. Liang, X. Li, A. K. Y. Jen, Adv. Mater. 25 (2013) 4425.

[21] T. W. Lee, O. Kwon, M. G. Kim, S. H. Park, J. Chung, S. Y. Kim, Y. Chung, J. Y. Park, E. Han, et al., Appl. Phys. Lett. 87 (2005) 231106.

[22] T. W. Lee, Y. Chung, O. Kwon, J. J. Park, Adv. Funct. Mater. 17 (2007) 390.

[23] M. Manceau, S. Berson, Nanotechnology 25 (2014) 014018.

[24] G. Greczynski, T. Kugler, M. Keil, W. Osikowicz, M. Fahlman, W. R. Salaneck, J. Electron. Spectrosc. Relat. Phenom. 121 (2001) 1.

[25] A. M. Nardes, M. Kemerink, M. M. de Kok, E. Vinken, K. Maturova, R. A. J. Janssen, Org. Electron. 9 (2008) 727.

[26] K. Zilberberg, S. Trost, H. Schmidt, T. Riedl, Adv. Energy Mater. 1 (2011) 377.

[27] J. Meyer, K. Zilberberg, T. Riedl, A. Kahn, J. Appl. Phys. 110 (2011).

[28] J. Lim, M. Park, W. K. Bae, D. Lee, S. Lee, C. Lee, K. Char, ACS Nano 7 (2013) 9019.

[29] Q. B. Pei, G. Yu, C. Zhang, Y. Yang, A. J. Heeger, Science 269 (1995) 1086.

[30] S. van Reenen, P. Matyba, A. Dzwilewski, R. A. J. Janssen, L. Edman, M. Kemerink, J. Am. Chem. Soc. 132 (2010) 13776.

[31] M. Lenes, G. Garcia-Belmonte, D. Tordera, A. Pertegas, J. Bisquert, H. J. Bolink, Adv. Funct. Mater. 21 (2011) 1581.

[32] K. Abbas, D. Marji, Z. Naturforsch. A 60 (2005) 667.

[33] P. C. Rusu, G. Giovannetti, C. Weijtens, R. Coehoorn, G. Brocks, Phys. Rev. B 81 (2010) 125403.
[34] H. Ishii, K. Sugiyama, E. Ito, K. Seki, Adv. Mater. 11 (1999) 972.
[35] W. C. Meixner, P. R. Antoniewicz, Phys. Rev. B 13 (1976) 3276.
[36] P. R. Hilton, D. W. Oxtoby, J. Chem. Phys. 72 (1980) 6346.
[37] B. L. Maschhoff, J. P. Cowin, J. Chem. Phys. 101 (1994) 8138.
[38] P. M. Dewick, *Essentials of Organic Chemistry*. John Wiley & Sons: West Sussex, 2006.
[39] R. C. G. Naber, J. Massolt, M. Spijkman, K. Asadi, P. W. M. Blom, D. M. de Leeuw, Appl. Phys. Lett. 90 (2007) 113509.
[40] J. J. Brondijk, K. Asadi, P. W. M. Blom, D. M. de Leeuw, J. Polym. Sci. Part B Polym. Phys. 50 (2012) 47.
[41] P. Wurfel, I. P. Batra, J. T. Jacobs, Phys. Rev. Lett. 30 (1973) 1218.
[42] P. Wurfel, I. P. Batra, Phys. Rev. B 8 (1973) 5126.
[43] A. L. Rohl, D. M. P. Mingos, Dalton Trans. (1992) 3541.
[44] Y. Nakamori, K. Miwa, A. Ninomiya, H. W. Li, N. Ohba, S. I. Towata, A. Zuttel, S. I. Orimo, Phys. Rev. B 74 (2006) 045126.
[45] J. C. Slater, J. Chem. Phys. 41 (1964) 3199.
[46] J. S. Huang, B. G. Sumpter, V. Meunier, Chem. Eur. J. 14 (2008) 6614.
[47] R. Q. Yang, H. B. Wu, Y. Cao, G. C. Bazan, J. Am. Chem. Soc. 128 (2006) 14422.
[48] G. A. H. Wetzelaer, A. Najafi, R. J. P. Kist, M. Kuik, P. W. M. Blom, Appl. Phys. Lett. 102 (2013) 053301.
[49] H. H. P. Gommans, M. Kemerink, G. G. Andersson, R. M. T. Pijper, Phys. Rev. B 69 (2004) 155216.

# **Chapter 12** Perspective on the future of LECs

## 12.1 Current view on operational mechanism of LECs

Great effort has been put in understanding, development and improvement of LECs by researchers dating back until the first report on LECs by Pei *et al.* in 1995.[1] As a result relatively high efficiencies[2-5] have already been reached from single layer devices which are ideal for large-scale, cheap processing methods.[6] Nevertheless, incomplete understanding of LEC device operation has obscured the possibilities and limits of LECs as well as the best routes to proceed for making the technology successful. The objective of this thesis was to remove this obscurity by endeavoring to conceptually and quantitatively understand the dominant processes in LEC operation. Operation starting from carrier injection, doping/ion dynamics, charge transport, charge recombination until the radiative exciton decay processes has been investigated by experiments and numerical modeling in polymer and iTMC based semiconductors.

First we identified that the electrical transport mechanism in polymer LECs is based on electrochemical doping of the organic semiconductor. A dynamic p-i-n junction structure is formed where light emission originates from the intrinsic region. A prerequisite for the formation of such a p-i-n junction is non-limited carrier injection, achieved by piling up ions at the contacts to form electric double layers. N-type and p-type doping then results from redistribution of cations and anions to opposite sides of the active layer to electrostatically compensate injected electrons and holes. The response time of LECs is related to this relatively slow ionic redistribution. The latter is however not limited by the relatively slow mobile ion transport, but rather to the (even) slower process of salt dissociation into free, mobile ions. The consequences of electrochemical doping on the electronic transport are the following:

i) Large electronic carrier densities are created in the active layer without the need to provide large electric fields, effectively improving the conductivity of the semiconductor;
ii) The electronic carrier mobility is improved significantly by the large doping density, improving the conductivity in the doped regions even more;
iii) The significantly improved conductivity enables low-voltage operation of devices with relatively thick active layers (>>$10^{-7}$ m);
iv) The doped regions result in near unity recombination efficiency by recombination of all carriers at the intrinsic region.

These effects are found to scale with the admixed salt density in the active layer of the LEC. So to optimize LECs for charge transport, while ignoring the effects of doping on the radiative efficiency, an as high as possible ion density is preferred, provided electronic carrier injection can follow the enhanced bulk conductivity. These effects were found to hold for LECs with relatively small (100 nm) and large (100 μm) active layer thicknesses.

In LECs based on ionic transition metal complexes highly similar electrical transport was observed despite the large difference in active layer components. N-type and p-type doped regions are also formed during operation, leaving an intrinsic region in between where the majority of the applied potential drops and where recombination takes place. To further test the similarity between polymer and iTMC-LECs the thermal activation of the turn-on of both types of devices was studied. The related thermal activation energy was found to be similar to the thermal activation energy of the ion conduction in the same device. This further confirms that ion redistribution is linked to the turn-on of polymer and iTMC-LECs, being in line with electrochemical doping during operation.

The tradeoff of the improved charge transport in LECs is a reduction of the luminescent efficiency by electrochemical doping, which was identified by two separate observations. Firstly, after switch-on of polymer and iTMC-LECs, the luminescent efficiency was found to roll off. Simultaneously the active layer was electrochemically doped, evidenced by a continuous enhancement of the current density and brightness of the LECs. Secondly, for polymer LECs in steady-state operation, an enhanced doping density was found to reduce the luminescent efficiency. The doping density was enhanced by admixing additional salt in the active layer. To explore the origin of the reduced luminescent efficiency, polaron-induced photoluminescence quenching was studied in conjugated polymers for varying doping density. Both Förster resonance energy transfer and charge transfer were determined as quenching mechanisms. The found quenching model was inserted in a numerical device model which reproduced qualitatively and quasi-quantitatively the reduction in luminescent efficiency in transient and steady-state operation. This proves that unlike the electrical transport, the luminescent efficiency is negatively affected by electrochemical doping which quenches the formed excitons. The optimal (polymer) LEC will therefore necessarily require a compromise between transport and recombination optimization.

Investigation of magnetic field effects on electrical transport and luminance in LECs showed that triplet excitons can improve both charge transport and luminescent efficiency. A large magneto-resistance of 12 % in fully doped LECs is explained by triplet excitons detrapping electrical charge carriers. Furthermore a reduction in magneto-efficiency is related to triplet-triplet annihilation, which is an additional source of singlet excitons. The contribution of delayed fluorescence to the total light output of the LEC is estimated to be roughly 10-20 %.

Besides electrochemical doping, thin films of electrolytes were furthermore observed to be able to enhance or reduce electrode work functions. This work function modification was found to be independent of the electrolyte layer thickness and work function of the electrode and dependent on the dielectric properties of the substrate on which it is deposited. This excludes possible mechanisms like charge transfer, electric double layer formation or spontaneous dipole orientation. The work function modification can, however, be described by dipole orientation at the interface induced by image charges of the electrolyte itself in the substrate. A requirement for this process to occur is asymmetry in size or side-groups of the oppositely charged constituents of the electrolyte.

The charge transport, recombination and radiative decay characteristics in LECs were successfully modeled by our numerical device model. Quasi-quantitative and qualitative agreement between experiments and simulations based on experimentally determined input parameters, proves that the basic processes for LEC operation are known and relatively well understood. Therefore we conclude that the combined use of ionic conductors and organic semiconductors in LECs enables great improvement of electrical transport and brightness at the cost of a reduced luminescent efficiency.

## 12.2 Future directions to improve LECs

The future and success of LECs to become a significant, global lighting technology highly depends on developments to improve the luminescent efficiency, response time and lifetime without significant compromises in the current advantages in processing and electrical transport. Below, the perspective of the author is given on possible future developments to improve the performance of LECs.

### 12.2.1 Emission engineering

To be able to take full advantage of the enhanced electrical transport in LECs and the concomitant brightness, the strong reduction in efficiency needs to be prevented. To address the root of the cause, exciton quenching must be avoided. Requirements for effective polaron-induced exciton quenching are i) exciton formation near a high density of polarons, ii) exciton diffusion, iii) spectral overlap for exciton emission and polaron absorption, and iv) a sufficient exciton lifetime. To avoid exciton quenching one or more of these requirements should *not* be fulfilled.

The use of dyes for light emission gives an opportunity to prevent exciton diffusion and/or spectral overlap between excitons and polarons. In case the dye has a lower bandgap compared to its host system, excitons can be energetically trapped in the dye, reducing exciton diffusion. As diffusion was found to be a main contributor to the quenching process, this could strongly reduce exciton quenching and enable the use of higher doping densities. The addition of large side-groups on such dyes[7] may furthermore enhance the distance between neighboring sites, to further reduce the probability of quenching. Especially regarding iTMC-LECs host-guest systems have already been reported.[8-10] Issues that may arise in such host-guest systems are for example unwanted emission from the host material[11] or asymmetrical carrier trapping. The latter may lead to imbalanced carrier transport, resulting in carrier recombination close to one of the electrodes where exciton quenching is relatively strong. Nevertheless, given the strong contribution of exciton quenching in polymer LECs, a recent promising report[12] and the fact this topic remains a relatively unexplored, dyes in LECs are highly promising to prevent exciton quenching and boost the luminescent performance. It furthermore solves the problem of synthesis of a single material with good transport and light emission properties.

Another method to reduce quenching is by enhancement of the radiative decay rate of excitons. By synthesis and selection of materials with an enhanced radiative decay rate, the contribution of the competing quenching process can be reduced. The radiative decay rate of singlet excitons can be determined from the Strickler-Berg relation.[13] A high dielectric constant and strong absorption at the relevant fluorescence wavelengths are required for a high decay rate, which is not so easily improved in typically low dielectric organic semiconductors like PPV. Enhancement of the dielectric constant may however improve the decay rate.

The radiative decay rate can also be enhanced by improving the fraction of the excitons with a singlet state. Our study on OMAR in PPV-based LECs proved that this fraction is worse than 0.25. Better understanding and control of the processes determining the final singlet exciton fraction should be able to lift it to 0.25 and perhaps beyond. Such a route is currently little explored in the field, but also not likely to be a short-term winner to improve the efficiency.

A more viable route is to turn the attention to triplet emitters, which have enhanced luminescent efficiency as all excitons can undergo radiative decay.[14] Although triplet emission in LECs is not new –iTMC-LECs based on iridium exhibit triplet emission- the origin of quenching is still relatively unexplored. We[15] and others[16] have shown that also here a roll-off in efficiency occurs, which is due to exciton quenching. This quenching likely takes place via a combination of triplet-triplet annihilation and triplet-polaron quenching. Both processes can be reduced by enhancement of the radiative decay rate. Haneder et al. reported that regarding triplet emitters, besides spin-orbit coupling between the excited $T_1$ and $S_1$ states, a small singlet-triplet splitting between $T_1$ and $S_1$ ($\Delta E_{ST}$) results in an enhanced radiative decay rate.[17] A small splitting is for example the case in iridium complexes and strongly depends on the ligands. Further enhancement of the radiative triplet exciton decay rate by specially designed materials[18] will help to reduce these quenching effects and may therefore be a promising route.

### 12.2.2 Reducing the response time

Another issue which requires attention is the relatively long response time in LECs, related to the slow redistribution of ions. Two approaches are reported in literature, being the use of a dedicated driving scheme for operation or fixation of doping during a pre-treatment of the LEC.

Attempts to fix doping are most notably by use of chemical reactions[19-22] or the strong temperature dependence of the ion mobility.[23-25] In either case the device is prebiased to allow ions to redistribute over the device forming a p-i-n junction. The doping can then be fixed by either lowering of the temperature or chemical reactions with (side-groups of) the ionic compounds. After removal of the bias the doping remains in place. Subsequent application of a bias voltage should then not result in ion transport to form new doping complexes. If that is the case, then the turn-on time depends solely on the response of the relatively mobile electronic carriers.

An alternative method to speed up the electrochemical doping process is by application of a larger driving voltage. Driving schemes[26-27] in which an initial, large bias voltage is used can therefore significantly speed up the doping in the device to quickly reach quasi-steady-state operation. Use of a constant current driving scheme is an even more elegant solution.[27-28]

Another, rather unexplored method is to address the intrinsic cause of the slow response speed, i.e. the slow salt dissociation in the active layer.[29] The salt dissociation rate depends on the binding energy between the ions and the ion capture rate. The latter is likely related to the ion mobility. Reduction of the salt binding energy and enhancement of the ion mobility can be achieved by enhancement of the dielectric constant: the dielectric constant is inversely proportional to the binding energy (which originates from electrostatic interaction) between ions. This means that an enhancement of the dielectric constant from e.g. PPV, ~3, to 10 may have significant effect.

To enhance the dielectric constant, alternative semiconducting materials could be considered. Note that in electroluminescent devices typically low dielectric materials are preferred due to the recombination rate being inversely proportional to the dielectric permittivity. In LECs the recombination efficiency is already (near) optimal, which means that enhancement of the dielectric constant does not necessarily harm the recombination efficiency. Today such semiconductors are mainly used for photovoltaic applications where recombination should be suppressed.[30-31] It should be noted that the relative dielectric constant of PEO, the material typically used to promote salt dissociation and ion mobility in LECs, is ~6.[32]

An additional advantage of the use of a high dielectric semiconductor is that the addition of PEO may no longer be required. Exclusion of PEO from the active layer would solve issues like phase separation, which likely has an effect on the current lifetime of LECs.[33]

Furthermore it would enable admixture of additional components like dyes in the active layer without creating a 4-component system.

The use of alternative salts may also be a possibility to reduce the response time. The binding energy is inversely proportional to the ionic bond length, so larger ions will likely have a smaller binding energy. This may, however, tradeoff in mobility as larger ions are more difficult to be transported through solid media.

# References

[1] Q. B. Pei, G. Yu, C. Zhang, Y. Yang, A. J. Heeger, Science 269 (1995) 1086.

[2] T. Hu, L. He, L. Duan, Y. Qiu, J. Mater. Chem. 22 (2012) 4206.

[3] Y. P. Jhang, H. F. Chen, H. B. Wu, Y. S. Yeh, H. C. Su, K. T. Wong, Org. Electron. 14 (2013) 2424.

[4] S. Tang, J. Pan, H. A. Buchholz, L. Edman, J. Am. Chem. Soc. 135 (2013) 3647.

[5] Y. Yang, Q. B. Pei, J. Appl. Phys. 81 (1997) 3294.

[6] A. Sandström, H. F. Dam, F. C. Krebs, L. Edman, Nat. Commun. 3 (2012) 1002.

[7] R. D. Costa, E. Orti, H. J. Bolink, S. Graber, C. E. Housecroft, E. C. Constable, Adv. Funct. Mater. 20 (2010) 1511.

[8] A. R. Hosseini, C. Y. Koh, J. D. Slinker, S. Flores-Torres, H. D. Abruna, G. G. Malliaras, Chem. Mater. 17 (2005) 6114.

[9] C. T. Liao, H. F. Chen, H. C. Su, K. T. Wong, Phys. Chem. Chem. Phys. 14 (2012) 1262.

[10] A. Pertegas, N. M. Shavaleev, D. Tordera, E. Orti, M. K. Nazeeruddin, H. J. Bolink, J. Mater. Chem. C 2 (2014) 1605.

[11] S. Coe, W. K. Woo, M. Bawendi, V. Bulovic, Nature 420 (2002) 800.

[12] G. Qian, Y. Lin, G. Wantz, A. R. Davis, K. R. Carter, J. J. Watkins, Adv. Funct. Mater. (2014).

[13] S. J. Strickler, R. A. Berg, J. Chem. Phys. 37 (1962) 814.

[14] F. C. Chen, Y. Yang, Q. Pei, Appl. Phys. Lett. 81 (2002) 4278.

[15] S. van Reenen, T. Akatsuka, D. Tordera, M. Kemerink, H. J. Bolink, J. Am. Chem. Soc. 135 (2013) 886.

[16] S. B. Meier, D. Hartmann, D. Tordera, H. J. Bolink, A. Winnacker, W. Sarfert, Phys. Chem. Chem. Phys. 14 (2012) 10886.

[17] S. Haneder, E. Da Como, J. Feldmann, J. M. Lupton, C. Lennartz, P. Erk, E. Fuchs, O. Molt, I. Munster, et al., Adv. Mater. 20 (2008) 3325.

[18] Q. Wang, I. W. H. Oswald, M. R. Perez, H. P. Jia, B. E. Gnade, M. A. Omary, Adv. Funct. Mater. 23 (2013) 5420.

[19] C. V. Hoven, H. P. Wang, M. Elbing, L. Garner, D. Winkelhaus, G. C. Bazan, Nat. Mater. 9 (2010) 249.

[20] S. Tang, L. Edman, Electrochim. Acta 56 (2011) 10473.

[21] J. M. Leger, D. B. Rodovsky, G. R. Bartholomew, Adv. Mater. 18 (2006) 3130.

[22] C. H. W. Cheng, M. C. Lonergan, J. Am. Chem. Soc. 126 (2004) 10536.

[23] J. Gao, G. Yu, A. J. Heeger, Appl. Phys. Lett. 71 (1997) 1293.

[24] J. Gao, Y. F. Li, G. Yu, A. J. Heeger, J. Appl. Phys. 86 (1999) 4594.

[25] J. H. Shin, S. Xiao, A. Fransson, L. Edman, Appl. Phys. Lett. 87 (2005) 043506.

[26] G. Yu, Y. Cao, C. Zhang, Y. F. Li, J. Gao, A. J. Heeger, Appl. Phys. Lett. 73 (1998) 111.

[27] J. F. Fang, P. Matyba, L. Edman, Adv. Funct. Mater. 19 (2009) 2671.

[28] D. Tordera, S. Meier, M. Lenes, R. D. Costa, E. Orti, W. Sarfert, H. J. Bolink, Adv. Mater. 24 (2012) 897.

[29] L. Holzer, F. P. Wenzl, S. Tasch, G. Leising, B. Winkler, L. Dai, A. W. H. Mau, Appl. Phys. Lett. 75 (1999) 2014.

[30] M. Lenes, F. B. Kooistra, J. C. Hummelen, I. Van Severen, L. Lutsen, D. Vanderzande, T. J. Cleij, P. W. M. Blom, J. Appl. Phys. 104 (2008) 114517.

[31] X. Liu, K. S. Jeong, B. P. Williams, K. Valchshouri, C. H. Guo, K. Han, E. D. Gomez, Q. Wang, J. B. Asbury, J. Phys. Chem. B 117 (2013) 15866.

[32] A. Munar, A. Sandstrom, S. Tang, L. Edman, Adv. Funct. Mater. 22 (2012) 1511.

[33] X. Y. Li, J. Gao, G. J. Liu, Org. Electron. 14 (2013) 2711.

# Appendix

# A Numerical model to describe operation of LECs

To model the device operation of light-emitting electrochemical cells a numerical model is used which describes carrier injection, transport and recombination in the active layer in the presence of mobile ions.[1-3] Two similar versions of the model were used, a 1D version based on the drift-diffusion equations and a 2D version based on the Boltzmann transport equation. Both models solve the carrier transport equations for electrons, holes, anions and cations, and Poisson's equation by forward integration in time. In the next paragraphs a detailed description is given of the methods to describe charge transport, carrier injection and carrier recombination. Additional, optional processes like i) a doping dependence in the carrier mobility, ii) a binding energy between the ions and iii) exciton quenching were included in the numerical model as well for part of the simulations presented in this thesis. Parameters that need to be defined for each calculation are shown in Table A.1.

**Table A.1 Input parameters for the numerical model of a light-emitting electrochemical cell.**

| Parameter | Symbol |
|---|---|
| **Mobility (electron/hole/anion/cation)** | $\mu_n$ / $\mu_p$ / $\mu_a$ / $\mu_c$ |
| **HOMO and LUMO of semiconductor** | $E_{HOMO}$ / $E_{LUMO}$ |
| **Density of states of semiconductor** | $N_0$ |
| **Salt density** | $c_0$ |
| **Work function of contacts** | $\varphi$ |
| **Drain voltage** | $V_{bias}$ |
| **Temperature** | $T$ |
| **Relative dielectric constant** | $\varepsilon_r$ |

## A.1 Charge transport

In the 1D model, transport of electrons, holes, anions and cations is described by the drift-diffusion equations:

$$J_n = nq\mu_n \frac{dV}{dx} + kT\mu_n \frac{dn}{dx}, \tag{A.1}$$

$$J_p = pq\mu_p \frac{dV}{dx} - kT\mu_p \frac{dp}{dx}, \tag{A.2}$$

$$J_a = aq\mu_a \frac{dV}{dx} + kT\mu_a \frac{da}{dx}, \tag{A.3}$$

$$J_c = cq\mu_c \frac{dV}{dx} - kT\mu_c \frac{dc}{dx}, \tag{A.4}$$

where *J* and *μ* refer to the current density and mobility of the charge carriers. *n*, *p*, *a* and *c* refer to electron, hole, anion and cation density, respectively, and as well denote the type of charge carrier when used as subscript. The electron and hole mobility could be chosen either dependent or independent of the doping density as described in the main text. $q$ is the absolute electron charge, $V$ is the electrostatic potential, $k$ is Boltzmann's constant and $T$ is the temperature. Einstein's relation between the diffusion constant and the mobility is assumed to hold. The ion current is zero at the electrodes, for the electrodes are ionically blocking. Electron and hole injection is explained in detail in Appendix A.2. The continuity equations are

$$\frac{dn}{dt} = \frac{1}{q}\frac{dJ_n}{dx} - R, \tag{A.5}$$

$$\frac{dp}{dt} = -\frac{1}{q}\frac{dJ_p}{dx} - R, \tag{A.6}$$

$$\frac{da}{dt} = \frac{1}{q}\frac{dJ_a}{dx}, \tag{A.7}$$

$$\frac{dc}{dt} = -\frac{1}{q}\frac{dJ_c}{dx}, \tag{A.8}$$

for electrons, holes, anions and cations, respectively. Here $R$ is the recombination rate which is discussed in Appendix A.5. The potential profile throughout the device is calculated from Poisson's equation:

$$\nabla^2 V = -\frac{q}{\varepsilon_0 \varepsilon_r}(p - n + c - a), \tag{A.9}$$

where $\varepsilon_0$ and $\varepsilon_r$ are the dielectric and the relative dielectric constant, respectively.

In the 2D model a rectangular grid is used with grid points at the corners of each cell. The areas of the cells are determined by the widths of the columns and rows which can be specified per row or column. For each cell a material type is specified, either gate, contact, dielectric or semiconductor. Calculations of current, recombination, etc. are performed on the grid points. The four cells surrounding the grid point are in equilibrium with each other, which is effectuated by area-average weighting. Consequently, a single quasi Fermi level is defined on each grid point.

Carrier transport is described by the following Boltzmann transport equations:

$$J_i = -q\mu_i i \nabla \psi_{F,i}, \tag{A.10}$$

where $\psi_{F,i}$ is the quasi Fermi energy for electrons ($i$ = $n$), holes ($i$ = $p$), anions ($i$ = $a$), or cations ($i$ = $c$) which is given by

$$\psi_{F,n} = \psi_L - \frac{kT}{q}\ln\frac{n}{N_0}, \tag{A.11}$$

$$\psi_{F,p} = \psi_H + \frac{kT}{q}\ln\frac{p}{N_0}, \tag{A.12}$$

$$\psi_{F,a} = V - \frac{kT}{q}\ln\frac{a}{N_0}, \tag{A.13}$$

$$\psi_{F,c} = V + \frac{kT}{q}\ln\frac{c}{N_0}, \tag{A.14}$$

where $\psi_L = E_{LUMO} + V$ and $\psi_H = E_{HOMO} + V$ and $V$ is the electrostatic potential. The Poisson and continuity equations as given for the 1D model were also used in the 2D model to calculate the electrostatic potential and maintain continuity in carrier transport.

## A.2 Carrier injection

To describe the injection of electrons and holes into the semiconductor, the following parameters are of importance: the HOMO and LUMO levels of the semiconductor; the Fermi level of the contacts; the grid point spacing at the interfaces; and the charge carrier density in the semiconductor at the interface. The injection models used for calculations reported in this thesis are called 'Fowler-Nordheim',[4] 'Emtage-O'Dwyer'[5] and 'modified Boltzmann'. The first assumes injection is mediated by tunneling through a triangular barrier. A more detailed description of this model as used in the numerical modeling can be found in Ref. 6. The Fowler-Nordheim injection model gives the carrier density *n* at the electrode as

$$n = \frac{j_{FN}}{q\mu_n F}, \tag{A.15}$$

$$j_{FN} = \frac{C}{q\varphi_n}F^2\exp\left(-B\frac{(q\varphi_n)^{3/2}}{F}\right), \tag{A.16}$$

$$B = \frac{8\pi\sqrt{2m_0}}{2.96hq}, \tag{A.17}$$

$$C = \frac{2.2q^3}{8\pi h}, \tag{A.18}$$

where $m_0$ is the free electron mass, $h$ is Planck's constant, $\varphi_n$ is the injection barrier height, $q$ is the absolute electronic charge and $F$ is the electric field at the contact plane.

The Emtage-O'Dwyer injection model includes the effect of the image-potential of the injected charge carrier which effectively reduces the injection barrier height $\varphi_n$ to $\varphi_n'$:[7]

$$\varphi_n' = \varphi_n - \sqrt{\frac{qF}{4\pi\varepsilon_0\varepsilon_r}}. \tag{A.19}$$

This injection barrier $\varphi_n'$ is subsequently used in a Boltzmann factor to give a boundary condition for the carrier density *n* at the electrode as

$$n = N_0 \exp\left(-\frac{q\varphi_n'}{kT}\right). \tag{A.20}$$

Relatively short grid point spacing is needed close to the electrodes to avoid undersampling. Undersampling at the interfaces namely leads to an unphysical reduction of the charge carrier injection rate for the Fowler-Nordheim and Emtage-O'Dwyer injection models. It namely increases the distance to be overcome by the injected carriers to reach the first grid point after the contact. The planar LECs studied in this thesis have an interelectrode spacing of e.g. 20 µm. Evasion of undersampling at the interfaces by use of a small grid point spacing leads to extremely long calculation times: this time scales with one over the smallest spacing of the numerical mesh to maintain numerical stability. In optimized LECs[2] injection, however, does not limit the current through the LEC. deMello,[8] for instance, solved this issue by making use of an adaptive-grid method-of-lines. In this thesis another solution was chosen by designing another injection model: the 'modified Boltzmann' injection model. It uses a Boltzmann factor to describe injection in the following manner taking into account the band bending just behind the first grid point:

$$n(1) = N_0 \exp\left(-\frac{q\varphi_n - q[V(2) - V(1)]}{kT}\right), \tag{A.21}$$

where *n*(1) is the electron density at the first grid point next to the electrode and *V*(*i*) the potential at grid point *i* (= 1, 2). Hence, the Boltzmann factor is effectively evaluated at the 2nd grid point. The potential at the first grid point *V*(1) is taken as a boundary condition for the potential and is thus constant, i.e. 0 or $V_{\text{bias}}$. The potential at the neighboring grid point however changes due to space-charge accumulated at the EDLs which facilitates injection of electron or holes. In this model injection is not affected by the grid point spacing and thus thicker devices can be simulated while not having to alter the number of grid points because of injection problems.

Simulations have been performed proving that all three injection models converge to the same result if small enough grid point spacing is chosen, i.e. $L(N-1) = 100/80$ nm in this case. The results are shown in Figure A.1. All relevant properties of the LEC are basically identical for the different injection models in these simulations. By increasing the grid point spacings for some of the injection models, e.g. Fowler-Nordheim tunneling injection, the injection rate becomes limited as shown in Chapter 2.[2] However, the results shown here indicate that the precise nature of injection does not influence the device physics. In contrary, only the resultant injection rate has influence on this.

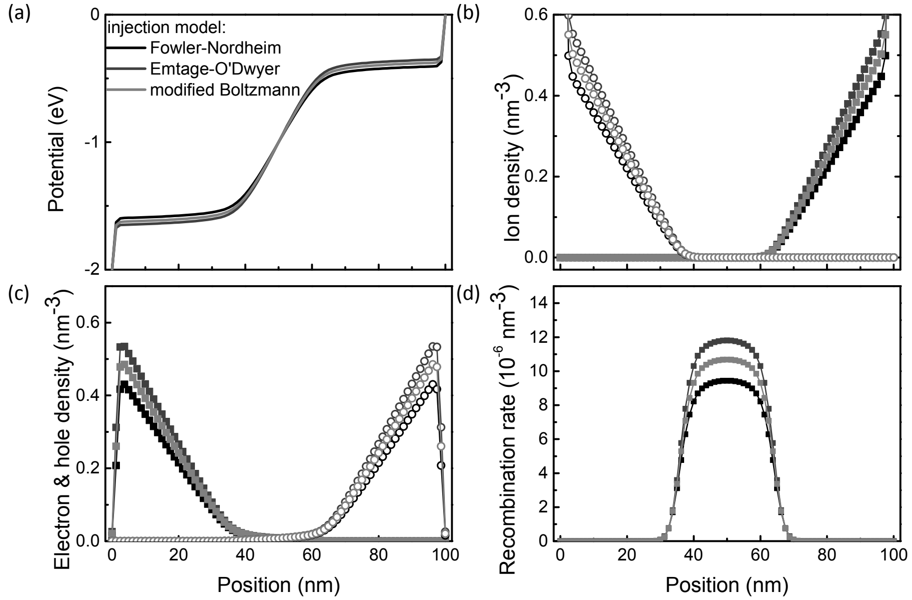

**Figure A.1 Simulation results for potential, carrier density and recombination rate distributions in LECs for different injection models. The black, dark gray and light gray graphs refer to the Fowler-Nordheim, Emtage-O'Dwyer and modified Boltzmann injection model respectively. (a) the potential distribution, (b) the ion density distribution, (c) the electron and hole density distributions and (d) the recombination rate distribution. In (b) and (c), the squares and circles refer to the positive and negative charge carriers respectively.**

## A.3 Electronic carrier mobility

For the implementation of a doping dependence in the charge carrier mobility experimental data was parameterized and implemented in the model. The qualitative doping dependence of the hole mobility found by electrochemical doping of P3HT by Shimotani et al. was used to construct the following model (see Figure A.2a and b):[9]

$$\mu_{p/n}(f) = \frac{\mu_{p/n,1}-\mu_{p/n,0}}{1+exp\left(\frac{f_0-f}{W}\right)} + \mu_{p/n,0}. \tag{A.22}$$

Here $f$ is the doping fraction which is equal to the carrier density divided by the density of states ($N_0$ = 0.3 nm$^{-3}$). This approximation of the doping fraction is justified by the observation that the net ion density always equals the net electronic charge density in the doped regions as shown in Figure A.1b and c. Regarding the other parameters, $\mu_{p/n,1}$ is the mobility at maximal doping ($f$ = 1), $\mu_{p/n,0}$ is the mobility in the absence of doping ($f$ = 0), and $f_0$ and $W$ are two parameters that set the transition from $\mu_0$ to $\mu_1$: $f_0$ determines at which doping fraction the mobility increases and *W* determines the range of doping fractions over which this increase occurs.

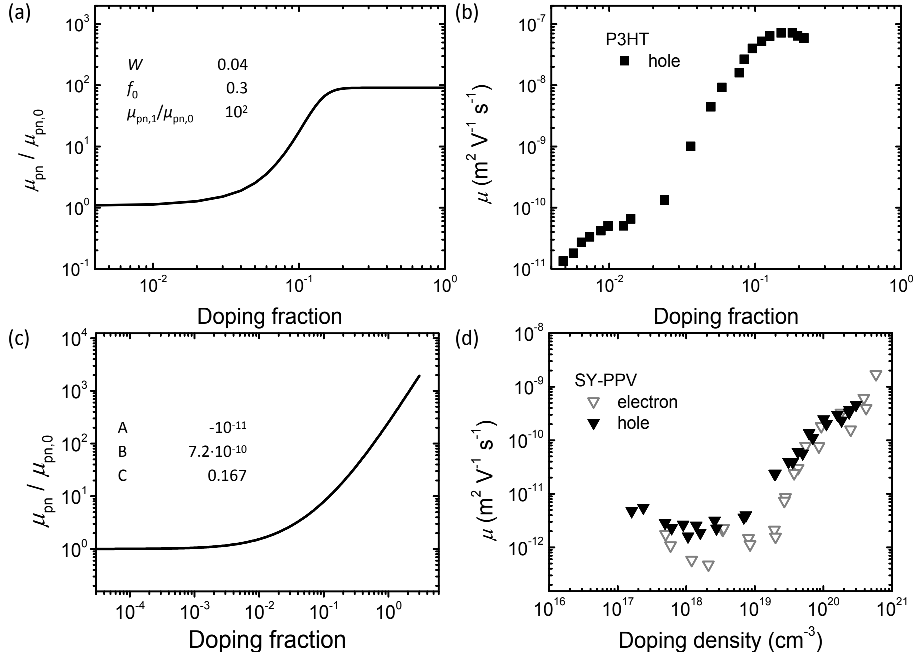

**Figure A.2 The electron/hole mobility as a function of the doping fraction or density. Experimentally determined graphs are shown in (b) for regioregular P3HT[9] and in (d) for Super Yellow PPV. Modeled graphs are shown in (a) based on Equation (A.22) and (c) based on Equation (A.23) for the parameters in the inset tables.**

The qualitative doping dependence of the carrier mobility in PPV (see Figure A.2d) can be described by the following model:

$$\mu_{p/n}(f) = \mu_{p/n,0}(A + B \cdot (f + C)^2), \tag{A.23}$$

where *A*, *B* and *C* are the parameters. In Figure A.2c a plot of this model is shown for $A = -1 \cdot 10^{-11}$, $B = 7.2 \cdot 10^{-10}$ and $C = 0.167$, as well as the doping density dependence measured in Super yellow PPV (see Figure 8.8b).

An optional field dependence of the carrier mobility is assumed to follow Poole-Frenkel behavior with exponential factor $\gamma$ in m$^{0.5}$ V$^{-0.5}$.[10-11] It is implemented by multiplication of the mobility by $\exp(\gamma \cdot \sqrt{F})$.

## A.4 Binding energy between ions

The binding energy between anions and cations was taken into account by introduction of a 5th type of carrier: the salt molecule. The binding energy between anion and cation is $E_s$ (>0).

The total anion-cation binding capture rate $C_i$ ($m^{-3}\,s^{-1}$) at each grid point *i* is

$$C_i = \gamma_c \cdot (n_{a,i} - n_{p,i}) \cdot (n_{c,i} - n_{n,i}), \qquad \textbf{(A.24)}$$

with $\gamma_c$ the capture coefficient ($m^3\,s^{-1}$) and $n_{x,i}$ the density at grid point *i* for anions (*x* = *a*), cations (*x* = *c*), holes (*x* = *p*) and electrons (*x* = *n*). Note that ions compensated by electrons or holes do not contribute to formation of salt. To describe dissociation of the salt the following detrapping rate $E_i$ ($m^{-3}\,s^{-1}$) was used:

$$E_i = K \cdot \gamma_d \cdot n_s, \qquad \textbf{(A.25)}$$

where $n_s$ is the salt density, *K* is the mass action law constant (here taken $10^{27}$ $m^{-3}$) and the coefficient $\gamma_d$ is related to the capture coefficient $\gamma_c$ via detailed balance:

$$\gamma_d = \gamma_c \cdot exp\left(-\frac{E_S}{kT}\right). \qquad \textbf{(A.26)}$$

Finally, the net ion binding rate $U_i$ ($m^{-3}\,s^{-1}$) is given by

$$U_i = C_i - E_i. \qquad \textbf{(A.27)}$$

Before each simulation the device was allowed to reach steady-state at $V_{bias}$ = 0 V to allow salt to form.

## A.5 Exciton formation and decay

In this model, electron and hole recombination is described by a Langevin process:

$$R = \frac{q(\mu_n + \mu_p)}{\varepsilon_0 \varepsilon_r} pn. \qquad \textbf{(A.28)}$$

In case the efficiency and luminance of the LEC needs to be calculated, also the decay of excitons can be included. Recombination of electrons and holes give rise in the model to singlet and triplet excitons according to a fraction $r_S$ and $r_T$. The excitons can subsequently diffuse with diffusion constant $D_{exc,S/T}$. For a given lifetime of the singlet and triplet excitons, $\tau_S$ and $\tau_T$, the singlet/triplet rate equations become

$$\frac{\partial S}{\partial t} = r_S R - \frac{S}{\tau_S} - D_{exc,S} \frac{d^2 S}{dx^2}, \qquad \textbf{(A.29)}$$

and

$$\frac{\partial T}{\partial t} = (1 - r_S)R - \frac{S}{\tau_T} - D_{exc,T}\frac{d^2T}{dx^2}, \tag{A.30}$$

where $S$ and $T$ are the singlet and triplet exciton densities.

To implement singlet exciton quenching by polarons, a model must be used to describe the density dependence of the quenching rate $k_{\mathrm{PQ}}$. The exciton quenching can then be implemented by the definition of

$$\frac{1}{\tau_S} = \frac{1}{\tau_{S,0}} + k_{PQ} \cdot (n + p), \tag{A.31}$$

where $\tau_{S,0}$ is the singlet exciton lifetime in absence of any quenchers. As the numerical model does not use the molecular sites for calculation but a rectangular grid, quenching models like Förster resonance energy transfer cannot be simply implemented. The method to implement exciton quenching by polarons is by use of obtained experimental data. The doping dependence of $k_{FL}/\left(k_{FL} + k_{PQ}\right)$ is measured as shown in Chapter 8, where $k_{\mathrm{FL}} = 1/\tau_{S,0}$. From this $k_{\mathrm{PQ}} \cdot (n+p)$ can be determined, parameterized and put into the model to give the quenching rate at each cell at a given polaron density. Excitons on site *i* do not interact with excitons on site $j \neq i$. Long range interactions are only mediated by the diffusion of excitons to another cell. As the timesteps in the calculation for charge transport are typically orders of magnitude larger than the lifetime of the excitons, $k_{FL}$ and $D_{\mathrm{exc}}$ are reduced by a factor $10^{-5}$, which slows down both processes equally. Such a delay may give rise to errors in the calculation of the transient behavior of the exciton decay processes. For transients which are limited by the movement of ions care is taken that the ion diffusion coefficient $D_{\mathrm{ion}} = \mu_{\mathrm{ion}}kT/q$ remains smaller than $D_{\mathrm{exc}}$ by at least a factor 10 to minimize this effect.

## A.6 Model operation (normal and impedance mode)

In this paragraph the general operation of the models is described. Initially the device only contains anions and cations which electrostatically compensate each other. No electrons or holes are present. Only at the contacts electrons and holes are present due to the boundary conditions imposed by the chosen injection model. In addition, the bias voltage is applied to one of the contacts, whereas the other contact is set at 0 V. From then on the model calculates the Fermi energy of all the carriers, followed by solving the Boltzmann transport equations or the drift-diffusion equations. Then electron-hole recombination is accounted for. Consequently the continuity equations are used to calculate the new carrier densities at each grid point. A steady-state solution is obtained when the current, which is determined by the sum of current through the contacts, becomes constant.

The model also handles impedance measurements. To model the admittance spectrum, the device is first allowed to reach steady-state. After this, a voltage step $V_{\mathrm{step}}$ is applied and the resulting step response of the current is calculated. The complex admittance spectra can then be derived by a Fast Fourier Transform of the derivative of the conductance.

# References

[1] S. van Reenen, P. Matyba, A. Dzwilewski, R. A. J. Janssen, A. Edman, M. Kemerink, Adv. Funct. Mater. 21 (2011) 1795.

[2] S. van Reenen, P. Matyba, A. Dzwilewski, R. A. J. Janssen, L. Edman, M. Kemerink, J Am Chem Soc 132 (2010) 13776.

[3] S. van Reenen, R. A. J. Janssen, M. Kemerink, Org. Electron. 12 (2011) 1746.

[4] R. H. Fowler, L. Nordheim, Proc. R. Soc. London Ser. A 119 (1928).

[5] P. R. Emtage, J. J. O'Dwyer, Phys. Rev. Lett. 16 (1966) 356.

[6] A. J. Campbell, D. D. C. Bradley, D. G. Lidzey, J. Appl. Phys. 82 (1997) 6326.

[7] J. J. M. van der Holst, M. A. Uijttewaal, R. Balasubramanian, R. Coehoorn, P. A. Bobbert, G. A. de Wijs, R. A. de Groot, Phys. Rev. B 79 (2009) 085203.

[8] J. C. deMello, Phys. Rev. B 66 (2002) 235210.

[9] H. Shimotani, G. Diguet, Y. Iwasa, Appl. Phys. Lett. 86 (2005) 022104.

[10] A. R. Buckley, Synth. Met. 160 (2010) 540.

[11] J. Frenkel, Phys. Rev. 54 (1938) 647.

# Summary

## Charge and ion dynamics in light-emitting electrochemical cells

Light-emitting electrochemical cells (LECs) are potential candidates for next-generation, low-cost, large-area lighting applications. LECs consist of a single, solution-processed active layer which contains an organic semiconductor as well as mobile ions. As such, two classes of LECs can be discerned. Polymer LECs have an active layer which is a blend of a polymer semiconductor and a solid polymer electrolyte which comprises mobile ions. In small molecule LECs electronic and ionic transport are enabled by a single material by use of ionic transition metal complexes (iTMCs). The merits of LECs are excellent processing characteristics without a large compromise in performance.

Following the first report on LECs by Pei *et al.* in 1995, researchers have put great efforts to understand, develop and improve LECs. As a result relatively high efficiencies have already been reached from single layer devices which are ideal for large-scale, cheap processing methods. Nevertheless, incomplete understanding of LEC device operation has obscured the possibilities and limits of LECs as well as the best routes to proceed for making the technology successful. The objective of this thesis is to remove this obscurity by endeavoring to conceptually and quantitatively understand the dominant processes in LEC operation. Operation starting from carrier injection to doping/ion dynamics, charge transport, charge recombination until the (non-)radiative exciton decay processes, has been investigated by experiments and numerical modeling in polymer and iTMC based semiconductors.

In Chapters 2-5 and 6-7 the electrical transport is studied in LECs based, respectively, on polymer and iTMC semiconductors. The electrical transport is studied in devices with large interelectrode gaps of $\sim 10^{-5}$ m, enabling characterization by mainly optical and scanning probe techniques, and in devices with small interelectrode gaps of $\sim 10^{-7}$ m, enabling characterization by electrical techniques. In Chapters 8-9 the luminescent properties of polymers in presence of electrochemical doping are investigated. Chapters 10 and 11, respectively, report on magnetic field effects in LECs and the use of ionic materials as interlayers in organic electronic devices to improve electrical transport. Below a more detailed summary is given per chapter.

For a long time two distinct models were used to describe the operational behavior of LECs: the electrochemical doping model and the electrodynamic model. Both models are supported by experimental data and numerical modeling in literature. In **Chapter 2**, we show that these models are essentially limits of one master model, separated by different rates of carrier injection. For ohmic non-limited injection, a dynamic p-i-n junction is formed, which is absent in injection limited devices. This unification is demonstrated by numerical calculations and measurement of the surface potential, the light emission profile and the doping profile in operational devices. An analytical analysis yields an upper limit for the ratio of drift and diffusion currents, having major consequences on the maximum current density through this type of device.

Incorporation of ions in the active layer of polymer LECs leads to attractive device properties like enhanced injection and improved carrier transport. In **Chapter 3**, the effect of the salt concentration on the operation of LECs is investigated using experiments and numerical calculations. The current density and light emission are shown to increase monotonously with increasing ion concentration over a wide range of concentrations. The increasing current is accompanied by an ion redistribution leading to a narrowing of the recombination zone. Hence, in absence of detrimental side reactions and doping-related electroluminescence quenching the ion concentration should be as high as possible. In Chapter 9 it will in fact be shown that the latter of these conditions is not fulfilled in typical LECs.

A major drawback of LECs is the long time scale associated with switching, during which ions redistribute in the active layer. In **Chapter 4**, a numerical modeling study is presented that gives fundamental insight in the dynamics during turn-on. The characteristic response of planar LECs to an applied bias is electrochemical doping of the active layer by doping fronts moving across the active layer. Formation and motion of such doping fronts are shown to be intimately related to both the electronic and ionic mobility and therefore provide useful information regarding charge transport in LECs. In particular, it is shown that the switch-on time in LECs is directly related to the time an ion needs to cross approximately half the device, enabling the extraction of the ion mobility from the switch-on time.

In **Chapter 5**, the operational mechanism of polymer LECs in sandwich geometry is studied by admittance spectroscopy and numerical modeling. Capacitance and conductance at different frequencies and bias voltages reflect the motion of ions, the formation of electric double layers, and the formation of a p-i-n junction, which is all in line with the electrochemical doping model. Numerical modeling shows that impedance measurements cannot be used to determine the actual junction width. In addition, the long settling time of polymer LECs is shown to be due to a slow process of salt dissociation that continues after p-i-n junction formation, rather than being due to ion conduction. This implies that in order to significantly decrease the response-time of LECs an electrolyte/salt combination with an as low as possible ion binding energy must be used.

In **Chapter 6** we switch focus to LECs based on ionic transition metal complexes. Using a planar electrode geometry, the operational mechanism of iridium(III) iTMC-based LECs is studied by a combination of fluorescence microscopy and scanning Kelvin probe microscopy (SKPM). Application of a bias to the LECs leads to the quenching of the photoluminescence (PL) in between the electrodes and to a sharp drop of the electrostatic potential in the middle of the device, far away from the contacts. The results shed light on the operational mechanism of iTMC-LECs and demonstrate that these devices work essentially the same as LECs based on conjugated polymers do, i.e. according to an electrochemical doping mechanism. Moreover, with proceeding operation time the potential drop shifts towards the cathode, coincident with the onset of light emission. During prolonged operation the emission zone and the potential drop both migrate towards the anode. This event is accompanied by a continuous quenching of the PL in two distinct regions separated by the emission line.

Two types of LECs are commonly distinguished, the polymer-based LEC (pLEC) and the ionic transition metal complex-based LEC. Apart from marked differences in the active layer constituents these LEC types typically show operational time scales that can differ by many orders of magnitude at room temperature. In **Chapter 7**, we demonstrate that despite these differences pLECs and iTMC-LECs show current, light output and efficacy transients that follow a universal shape. Moreover, we conclude that the turn-on time of both LEC types is dominated by the ion conductivity since the turn-on time exhibits the same activation energy as the ion conductivity in the off-state. These results demonstrate that both types of LECs are really two extremes of one class of electroluminescent devices. They also implicate that no fundamental difference exists between charge transport in small molecular weight or polymeric mixed ionic and electronic conductive materials. Additionally, it follows that the ionic conductivity is responsible for the dynamic properties of devices and systems using them. This likely extends to mixed ionic and electronic conductive materials used in organic solar cells and in a variety of biological systems.

An important loss mechanism in organic electroluminescent devices is exciton quenching by polarons. Gradual electrochemical doping of various conjugated polymer films was studied in **Chapter 8** to determine the doping density dependence of photoluminescence quenching. Electrochemical doping was achieved by contacting the film with a solid electrochemical gate and an injecting contact. A sharp reduction in photoluminescence was observed for doping densities between $10^{18}$ and $10^{19}$ $cm^{-3}$. The doping density dependence is quantitatively modeled by exciton diffusion in a homogeneous density of polarons followed by either Förster resonance energy transfer or charge transfer. Both mechanisms need to be considered to describe polaron-induced exciton quenching. Thus, to reduce exciton-polaron quenching in organic optoelectronic devices, both mechanisms must be prevented by reducing either exciton diffusion, spectral overlap of the exciton emission and polaron absorption spectra, doping density, or a combination thereof.

The admixed ions in LECs cause a trade-off between electrical transport and luminescent efficiency. Experiments and numerical modeling described in **Chapter 9** on thin film LECs prove that on the one hand carrier injection and transport benefit from electrochemical doping by mobile ions, whereas on the other hand the electroluminescent efficiency is reduced by exciton quenching by polarons involved in the doping. As a consequence the quasi-steady-state luminescent efficiency is found to decrease with increasing ion concentration. The transient of the luminescent efficiency furthermore shows a characteristic roll-off while the current still increases, attributed to ongoing electrochemical doping and the associated quenching. Both effects can be modeled by exciton polaron-quenching described by diffusion-assisted Förster resonance energy transfer. These results indicate that the tradeoff between efficiency and charge transport is fundamental in nature, suggesting that the application realm of future LECs should likely be sought in high-brightness, low-production cost devices, rather than in high-efficiency devices.

In **Chapter 10**, magnetic field effects in conductance and electroluminescence are studied to give insight in spin-dependent processes. Besides other effects a large negative magneto-conductance (MC) of 12% is observed in electrochemically doped LECs at sub-bandgap bias voltages. These effects indicate processes like delayed fluorescence from triplet-triplet annihilation and spin-mixing prior to exciton formation. The latter is found to result in a reduction in triplet exciton density which is argued to reduce detrapping of polarons in the recombination zone at low bias voltages, explaining the observed negative MC. Regarding organic magneto-resistance this study provides novel experimental data to verify existing models describing magnetic field effects in organic semiconductors which contribute to better understanding hereof. Furthermore we present indications of strong magnetic field effects related to interactions between trapped carriers and excitons, which specifically can be studied in electrochemically doped OLEDs. Regarding LECs, this work shows that delayed fluorescence from triplet-triplet annihilation substantially contributes to the electroluminescence and the device efficiency.

An alternative use of electrolytes, besides in the active layer of LECs, is as thin injection layers in organic electronics. The microscopic origin behind work function modification by such polyelectrolytes and tertiary aliphatic amines used as interlayers is however unclear. In **Chapter 11** we report on scanning Kelvin probe microscopy to determine the work function modification by thin layers of such materials on different substrates. Both reductions and increases in work function were found to follow a general mechanism. Such modifications are found to only take place when the work function modification layer (WML) is deposited on conductors or semiconductors. On insulators no effect is observed. Additionally, the work function modification is independent of the WML thickness or the substrate work function in the range of 3 to 5 eV. This data supports work function modification by dipole formation at the electrode interface, induced by interaction with its image dipole. Differences in size and side groups of the ionic constituents lead to differences in approach distance towards the surface. These differences determine magnitude and direction of the resulting dipole. This understanding facilitates design and synthesis of new air-stable and solution-processable WMLs for organic electronics.

**Chapter 12** summarizes the main findings and implications of this dissertation and on basis of that provides an outlook. The operation of LECs is governed by the formation of a dynamic p-i-n junction by mobile ions leading to electrochemical doping. We found that the electrochemical doping density improves transport of electronic charge carriers at the cost of luminescent efficiency. Charge carrier transport is improved by electrostatic compensation, resulting in larger carrier densities and mobilities. The luminescent efficiency is however reduced as excitons, formed in the intrinsic region between the doped regions, diffuse partially towards the doped regions and are quenched by the high doping density. To confirm this, numerical modeling was performed on the charge transport, recombination and radiative decay characteristics in LECs. Quasi-quantitative and qualitative agreement between experiments and calculations based on experimentally determined input parameters proves that the basic processes for LEC operation are known and relatively well understood. Therefore we conclude that the combined use of ionic conductors and organic semiconductors in LECs enables great improvement of electrical transport and brightness at the cost of a reduced luminescent efficiency. The outlook presents suggestions to reduce turn-on times and mitigate the efficiency loss due to exciton-polaron quenching.

# Samenvatting

## Dynamica van ladingen en ionen in lichtgevende elektrochemische cellen

Kunstmatig licht is in de huidige maatschappij een van de basisbehoeften van mensen en daarom alomtegenwoordig. Het wordt gebruikt in vele toepassingen als mobiele telefoons, televisies, maar ook voor verlichting in gebouwen of op straat. Om op de lange termijn het wereldwijde gebruik van dergelijke verlichting te kunnen faciliteren, zijn duurzame en betaalbare verlichtingstechnologieën nodig. Een mogelijke verlichtingstechniek die veelbelovend is voor goedkope productie van grote oppervlaktes is de lichtgevende elektrochemische cel (LEC). De LEC is een subklasse van de organische licht emitterende diode (OLED), welke weer een variant is op de anorganische LED, die momenteel wereldwijd beschikbaar is voor consumenten. Net als de LEC bestaat de OLED uit een actieve laag gebaseerd op organische materialen, die grotendeels bestaan uit koolstof. Dit element is ruimschoots aanwezig op aarde en is niet toxisch, hetgeen deze techniek potentieel duurzaam maakt. De koolwaterstof verbindingen in LECs en OLEDs zijn zogenaamde halfgeleiders die in principe elektriciteit efficiënt in licht kunnen omzetten. Om dit proces zo efficiënt mogelijk te laten verlopen, moeten in OLEDs vele dunne lagen met een precieze dikte van enkele tot tientallen nanometers op elkaar worden aangebracht. Deze voorwaarde is een grote uitdaging voor goedkope productie op grote schaal en is daarom een van de redenen waarom OLEDs momenteel relatief duur zijn.

LECs echter, bestaan uit een enkele actieve laag waarvan de dikte niet van cruciaal belang is. Deze actieve laag kan vanuit oplossing aangebracht worden, wat mogelijkheden biedt voor goedkope productietechnieken zoals inkjet printen of drukken. Een dergelijke techniek zou het mogelijk maken om LECs zoals een krant op de lopende band te produceren. Anders dan in de actieve laag van een OLED, bevat de actieve laag van een LEC ionen die vrij door de actieve laag kunnen bewegen. Hierdoor kan een enkele actieve laag in een LEC toch relatief efficiënt elektriciteit in licht omzetten. Hoe dit in z'n werk gaat wordt verderop uitgelegd.

Grofweg twee klassen LECs kunnen worden onderscheiden. De ene klasse is gebaseerd op een mengsel van een polymere halfgeleider, ionen ('opgelost zout'), en een ander polymeer. De polymere halfgeleider faciliteert elektrische stroom en de omzetting hiervan in licht. Het andere polymeer bevordert de oplosbaarheid van het zout en het transport van de resulterende ionen. De andere klasse van LECs is gebaseerd op kleine, halfgeleidende moleculen die zelf ionisch zijn, zogenaamde ionische transitie metaal complexen (iTMCs). Deze iTMCs kunnen daarom zowel elektrisch transport als ionisch transport faciliteren.

De eerste wetenschappelijke publicaties over dergelijke LECs dateren uit 1995. Sindsdien hebben wetenschappers veel energie gestoken in de ontwikkeling en verbetering van LECs alsook in het onderzoek naar de werking van LECs. Inzicht in de werking is cruciaal om te bepalen wat de mogelijkheden en grenzen zijn van deze technologie. Je kunt er bijvoorbeeld mee bepalen welke fundamentele processen de oorzaak zijn van ongewenste maar vaak voorkomende eigenschappen als een lage levensduur of een lage efficiëntie. Deze kennis kan vervolgens benut worden om gericht naar oplossingen te zoeken. De werking van LECs is echter voor een lange tijd onduidelijk geweest en dat heeft de verdere ontwikkeling ervan gehinderd. Het doel van dit proefschrift is om de onduidelijkheid over de werking van LECs weg te nemen door de belangrijkste processen in werkende LECs zowel kwalitatief als kwantitatief in kaart te brengen. De processen die onderzocht zijn, zijn i) de injectie van elektrische ladingsdragers in de organische halfgeleider; ii) het transport van ionen en de elektrostatische compensatie door deze ionen van geïnjecteerde lading, genaamd dotering. In dit proces vormt b.v. een negatief elektron samen met een positief ion een neutraal paar; iii) het transport van elektronische ladingsdragers door de resulterende gedoteerde organische halfgeleider; iv) de omzetting van elektrische ladingsdragers in elektron-gat paren, zogenaamde excitonen; v) het daarop volgende verval van deze excitonen onder de eventuele uitzending van licht. Deze processen zijn onderzocht in LECs gebaseerd op polymeren en iTMCs, met een combinatie van experimenten en numerieke berekeningen. Hieronder volgt een korte beschrijving van de inhoud van dit proefschrift per hoofdstuk.

In de wetenschappelijke literatuur werd de werking van LECs lange tijd geïnterpreteerd met twee fundamenteel verschillende modellen, het elektrodynamisch model en het elektrochemische doteringsmodel. In Figuur 1 staat een schematisch overzicht van beide modellen. Volgens het elektrochemische model gebeurt het volgende. De LEC wordt aangezet door een spanning over de elektrodes aan te leggen wat een elektrisch veld veroorzaakt in de actieve laag. Het gevolg is dat de ionen in de actieve laag richting de elektrodes bewegen; positieve ionen naar de negatieve elektrode en negatieve ionen naar de positieve elektrode. Doordat de ionen niet door de elektrodes heen kunnen bewegen, zullen ze opstapelen aan het grensvlak bij de elektrode, zoals weergegeven in Figuur 1b. De verzameling opgestapelde ionen bij een elektrode worden ook wel een elektrische dubbellaag (EDL) genoemd. Deze EDLs maken het eenvoudiger om elektrische ladingsdragers vanuit de elektrodes in de actieve laag te injecteren. De positieve ionen bij de negatieve elektrode helpen de injectie van elektronen, die negatief geladen zijn. Hetzelfde gebeurt bij de positieve elektrode, waar negatieve ionen de injectie van positieve ‘gaten’ bevorderen. Gaten zijn missende elektronen en te beschouwen als positief geladen deeltjes. De geïnjecteerde lading, op haar beurt, veroorzaakt lokaal ook elektrische velden die ionen aantrekken. Het gevolg is dat ionische en elektrische ladingen elkaars lading compenseren en daardoor bij elkaar blijven. Dit proces heet dotering en gebeurt aan beide kanten in het device zoals weergegeven in Figuur 1c. De elektrische lading wordt nu via de ionen doorgegeven zodat de elektronen en gaten naar de overkant van het device bewegen. Elektronen en gaten ontmoeten elkaar echter in het midden van het device en trekken elkaar aan. Recombinatie kan dan plaatsvinden, waarbij een nieuw neutraal complex gevormd wordt, een exciton (zie Figuur 1d). Dit gebeurt tussen de twee gedoteerde gebieden in. Het gevormde exciton in de organische halfgeleider kan vervolgens vervallen naar de grondtoestand, waarbij licht uitgezonden wordt en het elektron het gat opvult. Het elektrochemische doteringsmodel wordt gekenmerkt door de dotering die in vrijwel de gehele actieve laag optreedt waardoor een zogenaamde p-i-n junctie structuur ontstaat. Hierin vindt efficiënt ladingstransport plaats in de p- en n-type gedoteerde gebieden en recombinatie van lading in het intrinsieke (d.i. ongedoopte) gebied. Merk hierbij op dat de enkele actieve laag in een LEC ‘spontaan’, d.w.z. als een spanning wordt aangelegd, opdeelt in vijf lagen: twee lagen die de injectie van stroom bevorderen (de EDLs), twee lagen die het transport van stroom bevorderen (n- en p-type dotering) en een laag waarin recombinatie plaatsvindt (de intrinsieke laag). In een OLED moeten dit soort lagen een voor een met grote precisie aangebracht worden. Hierdoor kan een LEC in potentie veel goedkoper zijn dan een OLED.

Het andere model, het elektrodynamisch model, beschrijft de werking van LECs op een alternatieve manier. Ook dit model voorspelt de opstapeling van ionen bij het grensvlak van de elektrodes en de actieve laag (zie Figuur 1f). Volgens dit model gaat deze opstapeling echter verder totdat alle aangelegde spanning gecompenseerd wordt door de opgestapelde ionische lading bij de contacten (zie Figuur 1g). Het gevolg is dat in de rest van de actieve laag het elektrisch veld sterk gereduceerd is. De geïnjecteerde lading wordt daardoor niet meer door een elektrisch veld naar de tegenovergesteld geladen elektrode getransporteerd, maar door middel van diffusie. Op het moment dat een elektron een gat tegenkomt, recombineren deze en kan het vervolgens radiatief vervallen zoals weergegeven in Figuur 1h en beschreven in het elektrochemische doteringsmodel. Het karaketeristieke verschil tussen beide modellen is de aan- respectievelijk afwezigheid van gedoteerde gebieden in de bulk van het device: in het elektrodynamische model worden maar drie ‘sublagen’ gevormd, twee EDLs en een intrinsiek gebied. Het gevolg is een fundamenteel verschillende verdeling van de aangelegde spanning.

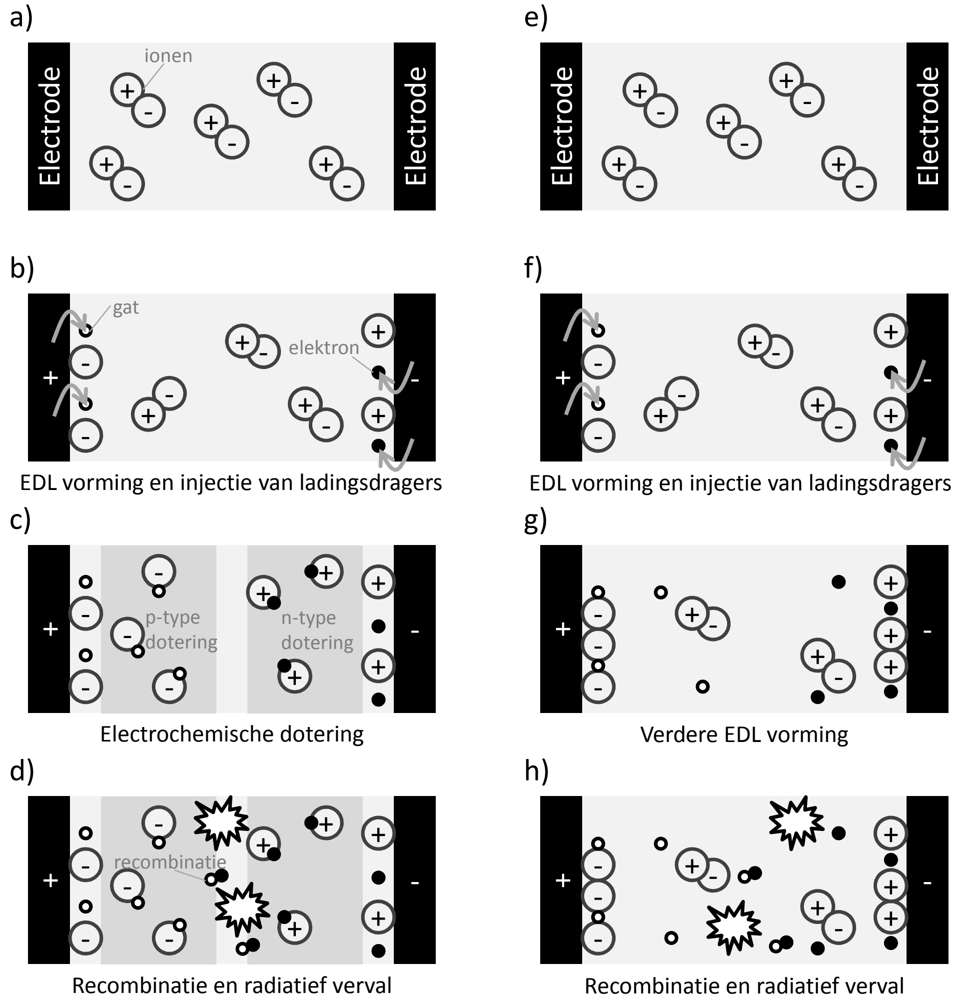

EDL vorming en injectie van ladingsdragers

EDL vorming en injectie van ladingsdragers

Electrochemische dotering

Verdere EDL vorming

Recombinatie en radiatief verval

Recombinatie en radiatief verval

**Figuur 1 Schematisch overzicht van (a-d) het elektrochemische doteringsmodel en (e-h) het elektrodynamisch model.**

In **Hoofdstuk 2** van dit proefschrift wordt met behulp van experimenten en numerieke berekeningen aangetoond dat beide modellen kloppen en kunnen voorkomen in LECs. Welk model door de LEC gevolgd wordt, blijkt af te hangen van de injectiesnelheid van ladingsdragers vanuit de elektrodes in de actieve laag. In het geval waarin de injectiesnelheid relatief hoog is zal de hoeveelheid ladingsdragers in de actieve laag toenemen waardoor ze samen met de ionen de actieve laag elektrochemisch doteren, zoals hierboven uitgelegd voor het elektrochemische doteringsmodel. In het geval de injectiesnelheid, ondanks de ophoping van ionen aan het grensvlak tussen elektrode en actieve laag, laag blijft, zal de ophoping van ionen doorgaan totdat er geen elektrisch veld meer is in de actieve laag. Dit resulteert in werking volgens het elektrodynamische model.

Om dit experimenteel te verifiëren hebben we LECs gemaakt met relatief goed en slecht contact tussen de elektrodes en de actieve laag. Beide LECs, gemaakt van grofweg dezelfde bestandsdelen, volgden daardoor ofwel het elektrochemische doteringsmodel, ofwel het elektrodynamisch model. Dit is gemeten in LECs met een actieve laagdikte van ongeveer 100 micrometer met onder andere een atoomkracht microscoop die de verdeling van de aangelegde spanning tussen de elektrodes meet. Numerieke berekeningen bevestigden dat inderdaad de injectiesnelheid van ladingsdragers uit de contacten bepaalt welk model gevolgd wordt door de LEC.

De aanwezigheid van ionen is het voornaamste verschil tussen OLEDs en LECs alsook de reden dat een LEC met slechts een enkele actieve laag relatief efficiënt kan functioneren. In **Hoofdstuk 3** is het effect van de hoeveelheid ionen in de actieve laag onderzocht. Experimenten tonen aan dat deze hoeveelheid een groot effect heeft op het elektrisch transport in LECs. Als er meer ionen aanwezig zijn in de actieve laag, dan zijn er meer ionen beschikbaar om op te stapelen bij de contacten en om geïnjecteerde ladingsdragers elektrostatisch te compenseren. Deze toename in dotering zorgt ervoor dat transport van ladingsdragers eenvoudiger wordt en dus toeneemt. Er lopen hogere stromen. De consequentie is dan dat meer elektrische lading recombineert en er dus in principe meer licht opgewekt kan worden. Op basis van deze resultaten kan dus gesteld worden dat om het elektrisch transport te verbeteren de ionconcentratie in LECs zo hoog mogelijk moet zijn. Het optreden van zijreacties en verlies van elektroluminescente efficiëntie (d.i. efficiëntie van omzetting van elektriciteit in licht) zullen echter wel optreden bij hoge ionconcentraties en moeten voorkomen worden.

Een van de voorname nadelen van mobiele ionen in LECs is de relatief lange schakeltijd. Dit is de tijd tussen het aanleggen van een spanning over de contacten en de emissie van licht. In **Hoofdstuk 4** wordt de dynamica van de ionen en geïnjecteerde lading onderzocht met behulp van numerieke simulaties. In een LEC met een actieve laag van ongeveer 100 micrometer dikte, vindt elektrochemische dotering van de actieve laag plaats door doteringsfronten die vanaf de contacten door de actieve laag heen schuiven. Op het moment dat deze fronten elkaar raken, wordt een p-i-n junctie gevormd waarbij licht geëmitteerd wordt vanuit het intrinsieke (i) gebied. Dit doteringsproces is gemodelleerd door een specifieke relatie tussen de mobiliteit van de ionen en de geïnjecteerde lading te gebruiken –de mobiliteit is een maat voor de snelheid waarmee deeltjes bewegen onder invloed van een elektrisch veld. Om een front te vormen, moet de mobiliteit van de geïnjecteerde lading groter zijn dan de mobiliteit van de ionen in de gedoopte gebieden. Buiten het gedoteerde gebied moet deze mobiliteit juist kleiner zijn dan die van de ionen. Deze resultaten bewijzen tevens dat de mobiliteit van geïnjecteerde lading door dotering sterk toeneemt, wat geleiding in gedoopte gebieden verder bevordert in LECs.

In de Hoofdstukken 2-4 zijn LECs bestudeerd met een afstand tussen de elektrodes van ongeveer 100.000 nanometer. Deze afstand noemen we de effectieve laagdikte. Zulke LECs zijn interessant voor de bestudering van de werking, maar niet praktisch voor toepassingen. LECs met een (echte) laagdikte van rond de 100 nanometer tussen de elektrodes zijn dat wel. In **Hoofdstuk 5** is onderzocht of zulke dunne LECs hetzelfde werken als de LECs met grotere (effectieve) laagdiktes. Door de frequentie-afhankelijkheid van de elektrische respons van een LEC op een variërende aangelegde spanning te meten, kan de tragere dynamica van de ionen gescheiden worden van de veel snellere dynamica van de geïnjecteerde lading. Met behulp van numerieke simulaties kunnen deze metingen geïnterpreteerd worden. Zo konden we informatie verkrijgen over de iongeleiding, de opstapeling van ionen aan de contacten en de vorming van een p-i-n junctie. Daarnaast bleek dat de relatief lange schakeltijd van de bestudeerde LECs niet zozeer door het transport van ionen gelimiteerd wordt, maar door een proces daarvóór. De mobiele ionen moeten namelijk eerst gevormd worden door dissociatie van gebonden anion-kation paren –het splitsen van het zout leidt tot vorming van mobiele ionen. Om de schakeltijd van LECs te verbeteren moet deze dissociatie dus versneld worden.

In **Hoofdstuk 6** wordt de focus verlegd van polymeren LECs naar LECs met een actieve laag van ionische transitie metaal complexen (iTMCs). Net als in Hoofdstuk 2 is onder andere de plaatsafhankelijke elektrostatische spanning aan het oppervlak van een LEC gemeten voor cellen met een grote effectieve laagdikte tussen 5 en 20 micrometer. Uit de metingen volgt dat het elektrisch veld zich concentreert in een klein gebied tussen de elektrodes. Dit gebied verschuift langzaam in de tijd. Optische metingen laten zien dat lichtemissie plaatsvindt vanuit ditzelfde gebied. Dit bewijst dat de werking van iTMC-LECs, net als polymere LECs, beschreven kan worden met het elektrochemisch doteringsmodel.

Vervolgens is in **Hoofdstuk 7** onderzocht of iTMC-LECs ook met een dunne actieve laag van ongeveer 100 nanometer hetzelfde werken als polymere LECs. Naast het verschil in bestandsdelen van de actieve laag werken deze LECs typisch op andere tijdsschalen. Een polymere LEC schakelt aan binnen enkele seconden, terwijl een iTMC-LEC minuten of zelfs uren nodig heeft. Metingen laten echter zien dat in beide typen LECs, afgezien van grote kwantitatieve verschillen, de tijdsafhankelijkheid van de stroom, de lichtemissie, en de efficiëntie kwalitatief gelijk zijn. Verder is de schakeltijd van beide typen LECs sterk afhankelijk van de temperatuur. De iongeleiding in beide typen vertoont dezelfde temperatuursafhankelijkheid. Dit bewijst dat de schakeltijd en de iongeleiding in beide typen LECs, gerelateerd zijn aan elkaar. Polymere LECs en iTMC-LECs zijn dus twee extremen van dezelfde klasse.

Na het elektrisch transport te hebben bestudeerd in de Hoofdstukken 2-7, is in **Hoofdstuk 8** de lichtemissie in gedoteerde materialen onderzocht. Lichtemissie ondervindt namelijk sterke hinder van dotering omdat dit niet-radiatief (= zonder uitzending van licht) verval van excitonen bevordert. Dit impliceert voor LECs dat dotering de lichtemissie kan verminderen. Om dit te onderzoeken is een dunne laag van een polymere halfgeleider geleidelijk gedoopt, terwijl gelijktijdig de fotoluminescentie gemeten is. Dit laatste is gedaan door het polymeer te beschijnen met licht zodat excitonen gevormd worden, die vervolgens weer vervallen tot de grondtoestand via dezelfde radiatieve of niet-radiatieve vervalprocessen als in een LEC. De verhouding tussen radiatief en niet-radiatief blijkt sterk af te hangen van de doteringsconcentratie in de polymere halfgeleider. Doteringsconcentraties boven $10^{18} – 10^{19}$ $cm^{-3}$ resulteren in voornamelijk niet-radiatief verval. Dit zijn concentraties die in LECs typisch bereikt worden in de gedoopte gebieden. Modellering aan de metingen laat daarnaast zien dat het niet-radiatieve verval door dotering een combinatie is van twee processen. Enerzijds kan het exciton energetisch vervallen door energieoverdracht naar een (optische overgang van een) doteringscomplex. Anderzijds kan het gebonden elektron-gat paar het elektron of gat verliezen door recombinatie met de elektrische lading van een doteringscomplex. De kans dat een van beide processen plaatsvindt, hangt af van de kans dat een exciton een doteringscomplex tegenkomt. Daardoor is de doteringsdichtheid van belang. Verder wordt de kans op niet-radiatief verval verhoogd door diffusie (spontane thermische beweging) van het exciton door de halfgeleider.

Het belang van dit niet-radiatieve verval van excitonen in LECs wordt beschreven in **Hoofdstuk 9**. In LECs vindt excitonvorming plaats in een niet-gedoteerd gebied. Dit exciton kan echter door diffusie getransporteerd worden naar de naburige gedoteerde gebieden, alwaar het niet-radiatief kan vervallen. Experimenten in Hoofdstuk 9 tonen aan dat LECs met hogere ion concentraties lagere elektroluminescente efficienties hebben. Numerieke berekeningen tonen aan dat de oorzaak van de lagere efficiëntie inderdaad het niet-radiatieve excitonverval is t.g.v. wisselwerking met de dotering. Anderzijds verbeteren hogere doteringsconcentraties het elektrisch transport, zoals ook eerder beschreven in Hoofdstuk 3. Deze resultaten betekenen dat de toepassing van de huidige generatie LECs gezocht moet worden in goedkope verlichting met hoge lichtsterkte, waarbij de efficiënte niet optimaal is.

De stroom en de lichtsterkte van werkende LECs blijken in **Hoofdstuk 10** sterk afhankelijk van magnetische velden. Bij zwakke magnetische velden blijkt de lichtsterkte toe te nemen. Met behulp van een model wordt dit toegeschreven aan een verandering in de verhouding van quantummechanische spin-toestanden van de excitonen. Slechts 1 van de mogelijke 4 toestanden, een singlet toestand, kan namelijk leiden tot radiatief verval van het exciton. Door een magnetisch veld aan te leggen ontstaan verhoudingsgewijs meer singlet spin-toestanden. Dit verklaart de toename in lichtsterkte. Tegelijkertijd is waargenomen dat de stroomsterkte afneemt met 12%, wat voor organische materialen een groot effect is. Deze afname kan verklaard worden door energie-overdracht van excitonen in een triplet spin-toestand (3 van de mogelijke 4 toestanden) naar geïnjecteerde ladingsdragers. Deze extra energie bevordert transport van deze ladingsdragers wat een hogere stroomsterkte oplevert. Een derde effect, waarbij de lichtsterkte juist afneemt bij relatief sterke magnetische velden, duidt op de aanwezigheid van vertraagde fluorescentie door de annihilatie van twee elektron-gat paren in triplet spin-toestanden. Dit betekent dat in LECs ook elektron-gat paren in de triplet toestand een bijdrage leveren aan de uiteindelijke lichtsterkte en elektroluminescente efficiëntie.

Naast het gebruik in LECs kunnen zouten ook gebruikt worden als dunne laagjes tussen de actieve laag en de elektrodes in organische elektronica en bij het op smaak brengen van gerechten. Zulke zogenaamde ‘tussenlagen’ modificeren de ‘werkfunctie’ van de contacten zodat deze gemakkelijker elektronen of gaten kunnen injecteren in de actieve laag. Tot op zekere hoogte is dit vergelijkbaar met het effect van de hierboven beschreven EDLs. Hoe deze werkfunctieverandering precies teweeg wordt gebracht, was echter onduidelijk. In **Hoofdstuk 11** wordt dit proces onderzocht door metingen van de werkfunctieverandering door verschillende tussenlagen, aangebracht op verschillende elektrodes. Verhoging en verlaging van de werkfunctie bleek eenzelfde, algemeen mechanisme te volgen. De interlaag kan namelijk een dipool (een plus- en minlading naast elkaar) aan het grensvlak met de elektrode vormen. Deze vorming wordt bepaald door de interactie van de ionen in de tussenlaag met hun beeldlading (‘spiegelbeeld’) in de elektrode. Deze interactie zorgt ervoor dat ionen graag zo dicht mogelijk bij de elektrode willen liggen. De uiteindelijke afstand tot het grensvlak hangt echter af van de grootte van het ion en van eventuele zijgroepen die het ion kunnen tegenhouden. Het verschil in grootte en de aanwezigheid van zijgroepen tussen anionen (-) en kationen (+) in een zout, bepalen daardoor of de negatieve, dan wel de positieve ionen het dichtst bij het grensvlak komen te liggen. Het verschil veroorzaakt een netto polarisatie, d.w.z. een dipool met een welbepaalde oriëntatie. Deze dipool houdt een lokaal elektrisch veld in stand wat de injectie van ofwel elektronen ofwel gaten bevordert –vergelijkbaar met bovengenoemde EDLs.

**Hoofdstuk 12** is een samenvatting van de belangrijkste conclusies van dit proefschrift en geeft daarnaast ook een vooruitzicht op mogelijkheden voor verder wetenschappelijk onderzoek aan LECs. Cruciaal voor de werking van LECs is de vorming van een dynamische p-i-n junctie door elektrochemische dotering. Elektrochemische dotering verbetert transport van elektronische ladingsdragers ten koste van de elektroluminescente efficiëntie. Transport van elektronische ladingsdragers wordt verbeterd door elektrostatische compensatie door tegenovergesteld geladen ionen. Dit verhoogt de dichtheid en mobiliteit van de elektronische ladingsdragers. De elektroluminescente efficiëntie neemt echter af doordat een significant deel van de gerecombineerde elektronen en gaten naar de gedoteerde gebieden diffunderen, alwaar ze geen licht opleveren. Dit beeld wordt in het proefschrift naast experimenten ondersteund door numerieke berekeningen waarmee de werking van LECs kwalitatief en quasi-kwantitatief correct gemodelleerd is. Daarom kan geconcludeerd worden dat de combinatie van ionische en elektronische geleiders in LECs het elektrisch transport en de lichtsterkte sterk verbetert, ten koste van de elektroluminescente efficiëntie. De toepassing van LECs moet dus in deze richting gezocht worden, tenzij onder andere het verlies van de elektroluminescente efficiëntie voorkomen kan worden. Een mogelijk veelbelovende manier om dit laatste te bereiken is de toevoeging van een extra component, een kleurstof, waarin excitonen met hoge efficiëntie radiatief vervallen en niet-radiatief verval voorkomen wordt.

# About the author

Stephan van Reenen was born on the 6th of March 1987 in Eindhoven, the Netherlands. After finishing his high school cum laude in 2005 at the Christian Huygens College in Eindhoven, he studied Applied Physics at the Eindhoven University of Technology. In 2008 he obtained his Bachelor degree in Applied Physics, combined with a minor in Chemical Engineering. During the Master phase of his studies, Stephan did an internship in the "Multilayer Devices & Coatings" group at TNO Industry & Technology and in the "Supramolecular Systems" group at the Humboldt Universität in Berlin under daily supervision of dr. Sibe Mennema. He investigated the inherently existing interfaces between dissimilar materials in organic (opto-) electronic devices. His graduation project was carried out in the Molecular Materials & Nanosystems group of prof. dr. ir. René Janssen under daily supervision of prof. dr. ir. Martijn Kemerink on light-emitting electrochemical cells. The results were published and in 2010 Stephan received his Masters degree cum laude. After the successful gradation project, he continued his work in the same group on light-emitting electrochemical cells of which the most important results are presented in this dissertation. Part of this work was also conducted for four months in the group of dr. Henk Bolink at the University of Valencia. Stephan presented his work at international conferences in Boston, Barcelona, Atlanta, San Fransisco, London, and Turku.

# List of publications

## Publications in scientific journals

1. S. van Reenen, S. Kouijzer, R. A. J. Janssen, M. Wienk, M. Kemerink, Origin of work function modification by ionic and amine-based interface layers, *accepted for publication in Adv. Mater. Interfaces*

2. S. van Reenen, M. Kemerink, Correcting for contact geometry in Seebeck coefficient measurements of thin film devices, *Org. Electron.* 10 **(2014)** 2250

3. S. van Reenen, M. V. Vitorino, R. A. J. Janssen, S. C. J. Meskers, M. Kemerink, Photoluminescence quenching in films of conjugated polymers by electrochemical doping, *Phys. Rev. B* 89 **(2014)** 205206

4. S. van Reenen, S. P. Kersten, S. H. W. Wouters, M. Cox, P. Janssen, B. Koopmans, P. A. Bobbert, M. Kemerink, Large magnetic field effects in electrochemically doped organic light-emitting diodes, *Phys. Rev. B* 88 **(2013)** 125203

5. S. B. Meier, S. van Reenen, B. Lefevre, D. Hartmann, H. J. Bolink, A. Winnacker, W. Sarfert, M. Kemerink, Dynamic doping in planar ionic transition metal complex-based light-emitting electrochemical cells, *Adv. Funct. Mater.* 23 **(2013)** 3531

6. D. Di Nuzzo, S. van Reenen, R. A. J. Janssen, M. Kemerink, S. C. J. Meskers, Evidence for space-charge-limited conduction in organic photovoltaic cells at open-circuit conditions, *Phys. Rev. B* 87 **(2013)** 085207

7. T. G. J. van der Hofstad, D. Di Nuzzo, S. van Reenen, R. A. J. Janssen, M. Kemerink, S. C. J. Meskers, Carrier recombination in polymer fullerene solar cells probed by reversible exchange of charge between the active layer and electrodes induced by a linearly varying voltage, *J. Phys. Chem. C* 117 **(2013)** 3210

8. S. van Reenen, T. Akatsuka, D. Tordera, M. Kemerink, H. J. Bolink, Universal transients in polymer and ionic transition metal complex light-emitting electrochemical cells, *J. Am. Chem. Soc.* 135 **(2013)** 886

9. S. van Reenen, R. A. J. Janssen, M. Kemerink, Dynamic processes in sandwich polymer light-emitting electrochemical cells, *Adv. Funct. Mater.* 22 **(2012)** 4547

10. S. van Reenen, R. A. J. Janssen, M. Kemerink, Doping dynamics in light-emitting electrochemical cells, *Org. El.* 12 **(2011)** 1746

11. S. van Reenen, P. Matyba, A. Dzwilewski, R. A. J. Janssen, L. Edman, M. Kemerink, Salt concentration effects in planar light-emitting electrochemical cells, *Adv. Funct. Mater.* 21 **(2011)** 1795

12. S. van Reenen, P. Matyba, A. Dzwilewski, R. A. J. Janssen, L. Edman, M. Kemerink, Unifying model for the operation of light-emitting electrochemical cells, *J. Am. Chem. Soc.* 132 **(2010)** 13776

# Manuscripts in preparation

1 S. van Reenen, R. A. J. Janssen, M. Kemerink, Understanding the efficiency in light-emitting electrochemical cells, *manuscript in preparation*

2 S. van Reenen, M. Scheepers, K. van de Ruit, R. A. J. Janssen, M. Kemerink, Explaining the effects of processing on the electrical properties of PEDOT:PSS, *manuscript in preparation*

# Publications on international conferences

1 S. van Reenen, S. Kouijzer, R. A. J. Janssen, M. M. Wienk, M. Kemerink, Origin of work function modification by ionic and amine-based interface layers, *International conference on synthetic metals* in Turku, Finland, **(2014)**; **contributed talk**

2 S. van Reenen, S. P. Kersten, S. H. W. Wouters, M. Cox, P. Janssen, B. Koopmans, P. A. Bobbert, R. A. J. Janssen, M. Kemerink; Large magnetoresistance in electrochemically doped organic light emitting diodes; *European conference on molecular electronics* in London, UK, **(2013)**; poster presentation; **(poster prize)**

3 S. van Reenen , S. B. Meier, T. Akatsuka, D. Tordera, W. Sarfert, M. Kemerink, H. J. Bolink; Universal operation of polymer and ionic Transition Metal Complex light-emitting electrochemical cells; *Materials Research Society Conference* in San Fransisco, USA, **(2013)**; **contributed talk**

4 S. van Reenen, R. A. J. Janssen, M. Kemerink; Doping dynamics in light-emitting electrochemical cells; *International conference on synthetic metals* in Atlanta, USA, **(2012)**; poster presentation

5 S. van Reenen, P. Matyba, A. Dzwilewski, R. A. J. Janssen, L. Edman, M. Kemerink; Design rules for light-emitting electrochemical cells; *Materials Research Society Conference* in Boston, USA, **(2011)**; poster presentation

6 S. van Reenen, P. Matyba, A. Dzwilewski, R. A. J. Janssen, L. Edman, M. Kemerink; Operational modes of light-emitting electrochemical cells; *European conference on molecular electronics* in Barcelona, Spain, **(2011)**; poster presentation

7 S. van Reenen, P. Matyba, A. Dzwilewski, R. A. J. Janssen, L. Edman, M. Kemerink; A unifying model for the operation of light-emitting electrochemical cells; *Materials Research Society Conference* in Boston, USA, **(2010)**; **contributed talk**

# Dankwoord

Het werk gepresenteerd in dit proefschrift, is uiteindelijk tot stand gekomen met hulp en steun van veel mensen om mij heen. Hier wil ik hen graag persoonlijk voor bedanken.

Tijdens het afstudeerjaar van mijn Master Technische Natuurkunde stond ik voor de moeilijke keuze tussen twee interessante promotieplaatsen, waarvan een onder de begeleiding van mijn huidige promotor Martijn. Na bijna vier jaren, die veel te snel voorbij zijn gegaan, heb ik helemaal geen spijt van de keuze die ik toen gemaakt heb. Martijn, je hebt me de mogelijkheid gegeven om zelf richting te geven aan mijn onderzoek en met veel mensen en andere onderzoeksgroepen samen te werken. Daarnaast heb je me geleerd kritisch na te denken over planning en resultaten, alsook de communicatie van resultaten naar buiten toe door publicaties in wetenschappelijke tijdschriften en presentaties op conferenties. Bedankt daarvoor!

René, ik wil je bedanken dat je ondanks je overvolle agenda, toch altijd tijd kon vrijmaken om mijn voortgang te bespreken of een manuscript van commentaar te voorzien. Daarbij gaf je altijd weer nieuwe inzichten en ideeën die ik goed kon gebruiken om mee verder te gaan. De vergaderingen met jou en Martijn op maandagochtend waren altijd erg inspirerend voor de rest van de week.

Besides my doctoral supervisors I also would like to thank Henk Bolink, Ludvig Edman, Paul Blom, Bert Koopmans and Reinder Coehoorn for being part of my thesis committee and for valuable input on the contents of this thesis. I am very grateful, Henk, that I was part of your research group in Valencia for 4 months, where I learned a lot from you and your students. The dedicated group dinners were outstanding, not only because of the excellent food. Ludvig, the great collaboration with you and Piotr jumpstarted my PhD in short time, for which I am very grateful. I was pleased to hear that you and Martijn will continue to collaborate on what is also the main topic of this thesis, LECs. I also would like to thank Peter Bobbert for his interest in my work and the valuable contributions to chapter 10.

Daarnaast hebben mijn collega's ervoor gezorgd dat ik naast veel succesvolle samenwerkingsverbanden ook een gezellige tijd heb gehad de afgelopen 4 jaar. Christian, we zijn ongeveer tegelijkertijd begonnen en zijn nu ook allebei bijna klaar. Daardoor zaten we telkens in dezelfde periode van onze promotie en hebben we veel samen kunnen doen. De conferenties naar San Francisco, Barcelona, Atlanta, en London, en je afkeer van moderne kunst, tot weerzin van Martijn, zal ik niet vergeten. Ook jij, Sandra, bent bijna klaar met je proefschrift. Dankzij onze gezamenlijke inspanningen is hoofdstuk 11 tot stand gekomen waar ik je zeer dankbaar voor ben. Daniele en Tom wil ik bedanken voor het werk dat we gezamenlijk verricht hebben aan organische zonnecellen waaruit enkele papers voortgekomen zijn. Matthijs, Steinar, Paul, en Sander dank ik voor de leuke samenwerking aan LECs in magnetische velden waaruit hoofdstuk 10 is voortgekomen. Verder wil ik ook mijn dank in helaas te weinig woorden uitspreken voor andere (oud-)collega’s van M2N-natuurkunde, Alessia, Andrey, Andrzej, Duncan (bedankt voor je tips voor mijn Rubicon voorstel), Erik, Erwin, Gerard, Harm, Joris, Kees, Kevin, Le, Marco (2x), Matěj, Mohammed, Niels, Rein (2x), Richard, Seva (спасибі за пивом), Simon, Wijnand (2x), Willem, Zuhal, M2N-scheikunde, Alice, Benjamin, Dhritiman, Dominique, Gijs, Hans, Jolanda, Koen, Martijn, Martina, Serkan, Stefan O, Stefan M, Veronique, Weiwei, Wenshan. I also would like to thank my friends and colleagues with whom I worked at the University of Valencia, Dani, Takeo, Toni, Olga, Christina, Manuel, Angel, Jorge and others as well as Sebastian from the University of Erlangen. Especially the trip by car with Takeo, Olga and Christina to Cuenca where we nearly ran out of fuel on a long deserted road will remain in my memory. Ook wil ik Bob, Mellany, Ralph, en Sandra bedanken voor de gezellige vergaderingen voor de voorbereidingen van het SMO groepsuitje in 2011. Max, Miguel en Wessel wil ik bedanken, omdat ik hen tijdens hun bachelor eindproject of stage heb mogen begeleiden.

Verder wil ik ook Bas, Chiel, Karel, Pim en Steinar bedanken voor de gezellige avonden die we doorgebracht hebben met een onuitputtelijke hoeveelheid bord/kaartspellen. Ook al gaan we allemaal steeds verder uit elkaar wonen, hoop ik dat we dit nog vaak blijven doen.

Ook dank ik mijn familie en schoonfamilie –Aris & Ada, Vincent, Alexander & Janine, Jan & Nelly, Patrick & Clarice, Dimitry & Richelle- voor jullie liefde, steun en interesse in mij en mijn werk. Helaas is het moeilijk om in detail uit te leggen wat ik precies gedaan heb, maar hopelijk kan dit boekje en de bijbehorende promotiezitting het allemaal wat duidelijker maken.

Alexander, ik voel me bevoorrecht dat ik jou als tweelingbroer heb en daarmee iemand ken die in veel opzichten hetzelfde is als ik. Dat wij van jongs af aan zoveel hebben kunnen delen met elkaar is een van de belangrijkste redenen dat ik uiteindelijk tot hier, het afwerken van mijn proefschrift, gekomen ben.

Van alle mensen ben jij, Synthia, het belangrijkst voor mij geweest. Jij motiveert me, en bent er voor me als het goed gaat, maar ook als het slecht gaat. Ik ben zielsblij dat we elkaar op 31 mei 2011 het jawoord hebben gegeven en zie onze toekomst, wat er ook gebeurt, gelukkig en samen verbonden tegemoet.

Ten slotte wil ik God bedanken voor de voorspoed die Hij mij gedurende mijn leven tot nu toe gegeven heeft en daarmee de mogelijkheden om dit werk succesvol te volbrengen. Ik ben me bewust dat daar geen verzekering voor is, ook niet voor een christen zoals te lezen in de Bijbel over Job, die alles op aarde verloor, behalve zijn vertrouwen in U. Ik bid dat ik met Uw hulp met eenzelfde vertrouwen mag blijven geloven.